Neutrino Interaction Cross-section Ratios Measured with the T2K Near Detector

Iain Alexander Lamont

Lancaster University

September 2016

Submitted in partial fulfilment of the requirements for the degree of

Doctor of Philosophy in Physics at Lancaster University

Abstract

The T2K near detector, ND280, is used to compare electron and muon neutrino interaction cross sections by measuring the ratio of the Charged-Current Quasi-Elastic (CCQE or CC0π) to the total Charged-Current (CC) interaction cross section for both flavours. The double ratio of these is taken to study the differences between electron and muon neutrino interactions. A charged-current interaction with no final state pions is also studied in place of the CCQE topology to provide a less model dependent result. In either case, no significant deviation from the NEUT and GENIE Monte Carlo generators was found showing that the current models accurately predict the relative amount of CCQE and CC0π to CC interactions for electron and muon neutrinos.

A series of studies are presented regarding the ND280 ECals. An energy-equalisation calibration is applied to bars in the ECals and found to considerably improve the consistency of the detector. In addition, the rate of degradation of the ECal scintillator bars was found to be well modelled by an exponential decay with a $\approx 3\%$ loss of energy recorded per year. The systematic uncertainties associated with matching tracks between a TPC and an ECal are calculated and found to be $\approx 1\%$.

Declaration

No part of this thesis has been previously submitted for the award of a higher degree.

Acknowledgements

Firstly, I'd like to thank Dr. Jaroslaw Nowak for supervising me and having the patience to deal with my quirks. Thanks also to Dr. Laura Kormos who supervised me through the first year of my Ph.D and to Dr. Alex Finch who helped me through many software problems. The data and fake data shown in this thesis was produced by a collaboration of over 500 people who have all in some way contributed to the work shown here.

I'd like to also show my appreciation to the people I shared an office with, who made the whole experience much more enjoyable.

Lastly, I'd like to thank my friends and family who've supported me through my Ph.D in a variety of ways. It meant more to me than they probably realised.

Contents

List of Figures

List of Tables

Chapter 1

Introduction

1.1 Current Status of Neutrino Physics

1.1.1 Neutrino Oscillations

The phenomenom of neutrino oscillations was first proposed to reconcile puzzling features in data from several experiments. The first of these was the Homestake Experiment which observed a deficit in the flux of electron neutrinos originating from the Sun [1]. This result was later confirmed by other experiments including the Kamiokande experiment [2]. Other strange results followed, including a deficit in the ratio of muon neutrino to electron neutrino flux from neutrinos created in the Earth's atmosphere observed by the Kamiokande experiment [3].

The interpretation of these results as neutrino oscillations was proposed in [4]. Shortly after, several experiments confirmed the hypothesis including the SNO experiment which published results giving strong evidence of flavour change in neutrinos [5] showing that the Homestake result could be explained in this context. The Super Kamiokande experiment provided precise measurements of the atmospheric oscillations [6] to confirm the results of its predecessor experiment as being consistent with neutrino oscillations.

The mathematical formalism that describes such oscillations was laid out by Maki, Nakagawa, and Sakata in 1962 [7]. This is parameterised by three mixing angles, θ_{12}, θ_{23}, and θ_{13}; and two mass splittings Δm^2_{21} and Δm^2_{32}. The Particle Data Group [8] has the most up to date values of these parameters by combining results from many experiments. The most notable of these are the Super Kamiokande experiment [9], the SNO experiment [10], the KamLAND experiment [11], the IceCube experiment [12], the Daya Bay experiment [13], and the RENO experiment [14]. The measurement of these parameters is affected by the hierarchy of the neutrino mass eigenstates. It is unknown whether $m_3 > m_2 > m_1$, known as normal hierarchy, or $m_2 > m_1 > m_3$, known as inverted hierarchy. This can be seen in Fig 1.1.1.

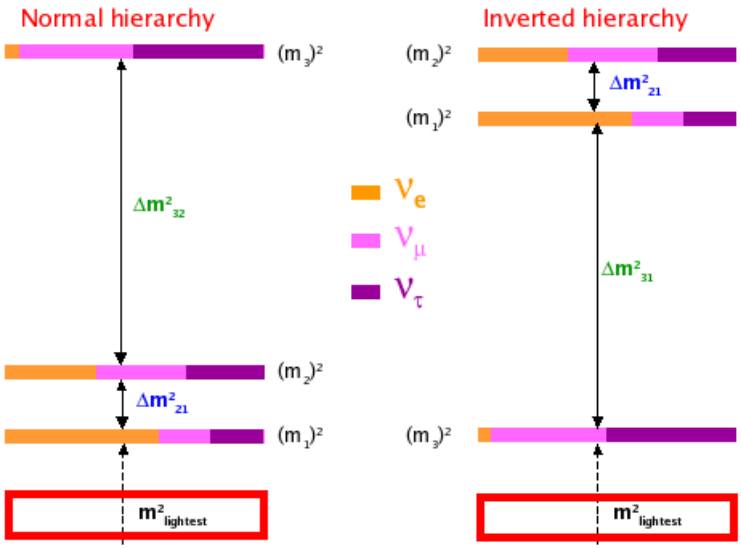

Figure 1.1.1: A diagram showing the different possible mass hierarchies for the neutrino mass eignenstates. The left shows normal mass heirarchies and the right shows inverted hierachy [15].

A summary of the value of the oscillation parameters is shown in Tab 1.1.1. The angle θ_{12} is pertinent for solar neutrinos, θ_{23} has been measured using neutrinos created in the upper atmosphere, and θ_{13} is best measured using nuclear reactors.

Parameter	Value
$\sin^2(\theta_{12})$	0.304 ± 0.014
$\sin^2(\theta_{23})$	$0.514^{+0.055}_{-0.056}$
$\sin^2(\theta_{13})$	$(2.19 \pm 0.12) \times 10^{-2}$
Δm^2_{21}	$(7.53 \pm 0.18) \times 10^{-5}$ eV^2
Δm^2_{32}	$(2.44 \pm 0.06) \times 10^{-3}$ eV^2

Table 1.1.1: The current best knowledge of neutrino oscillation parameters (assuming normal hierarchy) taken from the Particle Data Group [8]

A global review of neutrino oscillation data can be found in [16].

1.1.2 Neutrino Interactions

Uncertainties on neutrino interaction cross sections play a large role in studying neutrino oscillations, often being the dominant uncertainty on the results. To combat this, many experiments have made measurements of these cross sections. Of particular interest here are muon and electron neutrinos interacting with a carbon target. The T2K experiment recently published a series of papers measuring these cross sections, such as those in Figs 1.1.2 1.1.3 1.1.4. These show the muon neutrino charged current quasi-elastic interaction cross section [17], the electron neutrino total charged current interaction cross section [18], and the muon neutrino total charged current interaction cross section respectively [19].

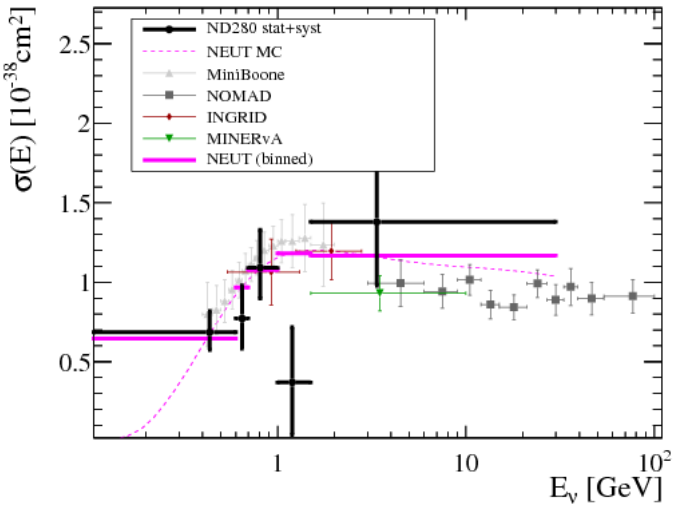

Figure 1.1.2: The muon neutrino charged current quasi-elastic interaction cross section per target neutron on carbon [17]

Other experiments have published measurements of interaction cross sections. Of particular note are the MiniBooNE, MINERνA, NOMAD and MINOS experiments which have provided measurements on a variety of targets.

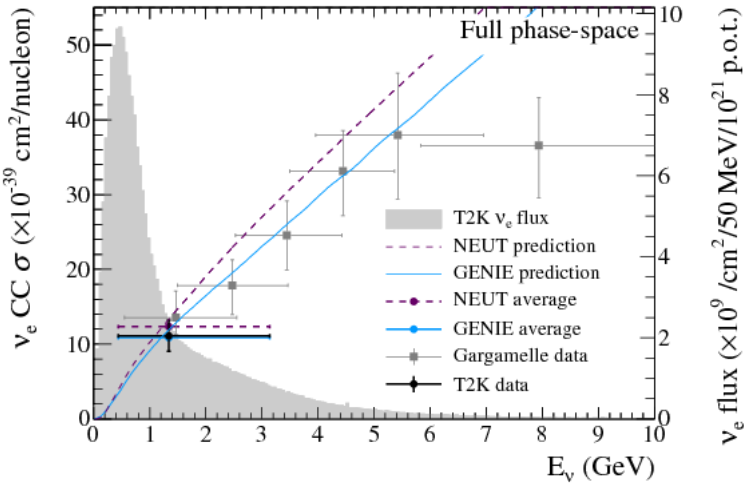

Figure 1.1.3: The electron neutrino total charged current interaction cross section on carbon [18]

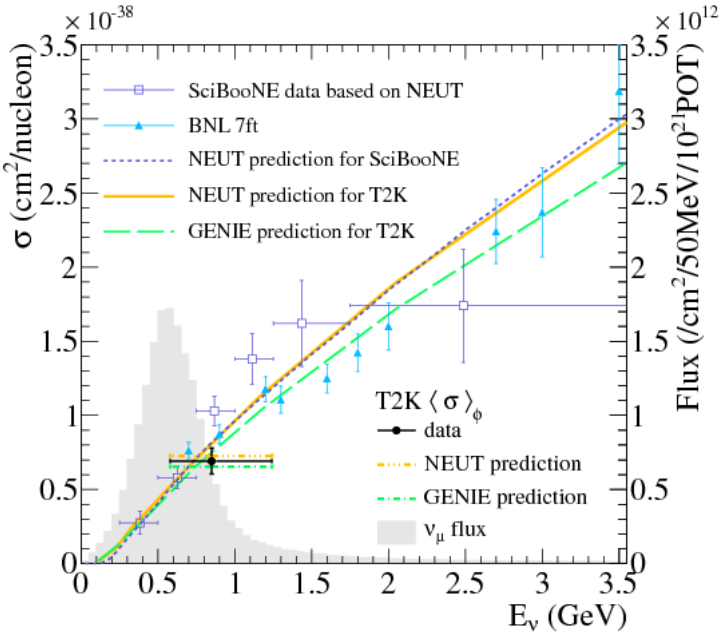

Figure 1.1.4: The muon neutrino total charged current interaction cross section on carbon [19]

1.2 The Analysis

The main focus of this thesis is an analysis to compare ν_e and ν_μ interaction cross sections on carbon as a target. Two interaction cross sections are studied; the total Charged Current interaction cross section (CC), and the Charged Current Quasi-Elastic (CCQE) cross section. Since most previous cross section measurements have large uncertainties assoicated with them, the ratios of cross sections are used instead in the hopes that there will be some cancellation of the uncertainties.

In practice, it is difficult to determine whether an event is truly a CCQE interaction or a non CCQE interaction with nuclear processes causing particles other than the lepton to not leave the nucleus. Extracting a CCQE cross section then requires these processes to be well understood. To combat this, the ratios are calculated for a CCQE signal and an interaction with only the lepton and no mesons exiting the nucleus ($\nu_\ell + {}^{12}C \rightarrow \ell + 0\pi$) to give a result without needing these models. In either case, the selection criteria are the same, only the signal changes.

The ratios studied are CCQE/CC for ν_e and ν_μ and the double ratio of the two to give a ν_e/ν_μ comparison, these are detailed in Eqs 1.2.1a - 1.2.1c. This allows for a measurement of how likely a neutrino will undergo a CCQE interaction relative to the total CC interaction probability, and the difference between this quantity for ν_e and ν_μ. The interactions shown in these equations are on a Carbon as the target for neutrino interactions used for this analysis is comprised mostly of Carbon.

$$R_e = \frac{\sigma(\nu_e + {}^{12}C \rightarrow e + 0\pi)}{\sigma(\nu_e + {}^{12}C \rightarrow e + X)} \tag{1.2.1a}$$

$$R_\mu = \frac{\sigma(\nu_\mu + {}^{12}C \rightarrow \mu + 0\pi)}{\sigma(\nu_\mu + {}^{12}C \rightarrow \mu + X)} \tag{1.2.1b}$$

$$DR = \frac{R_e}{R_\mu} \tag{1.2.1c}$$

The results are parameterised in terms of several kinematical variables such as lepton momentum, lepton angle, neutrino energy, and the four-momentum transfered in the interaction. Reconstructed variables such as outgoing lepton momentum and angle, are studied to try to make a model independent measurement. Model dependent variables like neutrino energy or four-momentum transferred are also studied as they are more intrinsic to the cross section and can be compared directly to Monte Carlo (MC) predictions and theoretical models.

1.3 Motivation

The previous interaction cross section results published by the T2K collaboration [17] [18] [19] have systematic uncertainties associated with them $\mathcal{O}(20\%)$. Some of these results are described and shown in Sec 1.1.2. The large uncertainties in these previous results have meant that it has not been possible to extract differences in ν_e and ν_μ interactions. By taking the ratios of cross sections, some of the systematic uncertainties partially cancel out. This provides better information on neutrino interaction differences between flavours, and could therefore be used to test or refute different theoretical models. Other reasons why these ratios are interesting include using them as a tool to reduce uncertainties on oscillation measurements and providing a test of lepton universality. These are detailed in the following sections.

1.3.1 Reducing Uncertainties in Oscillation Experiments

The interaction cross sections play a vital role in neutrino oscillation experiments. Many of the experiments that study neutrino oscillations, such as the T2K experiment, use a near detector to sample the neutrino beam and a far detector to study the oscillated beam. For a beam of muon neutrinos, Eq 1.3.1 shows the expected number of reconstructed ν_e events at a far detector, N_e, that have oscillated from ν_μ (with probability $P_{\nu_\mu \to \nu_e}$). φ_μ is the flux of ν_μ as measured in the

near detector, L_{Far} is the distance to the far detector from the beam production point, σ_e is the ν_e cross section and ϵ_e is the efficiency for reconstructing ν_e events in the far detector. The uncertainties on both the flux and the interaction cross section are large, meaning that the prediction of N_e has large uncertainties.

$$N_e = \frac{\varphi_\mu}{L^2_{\text{Far}}} P_{\nu_\mu \to \nu_e} \sigma_e \epsilon_e \tag{1.3.1}$$

Alternatively, the flux as measured in the near detector can be written down as in Eq 1.3.2, which depends on the ν_μ interaction cross section. The number of ν_μ events in the near detector is given by N_μ, σ_μ is the ν_μ interaction cross section, and ϵ_μ is the efficiency for reconstructing ν_μ events in the near detector.

$$\varphi_\mu = N_\mu \frac{L^2_{\text{Near}}}{\sigma_\mu \epsilon_\mu} \tag{1.3.2}$$

This results in an expression for the predicted number of ν_e events in the far detector, Eq 1.3.3, that does not rely on the flux model, but instead has the ratios of the ν_e and ν_μ cross sections.

$$N_e = N_\mu \frac{L^2_{\text{Near}}}{L^2_{\text{Far}}} \frac{\sigma_e}{\sigma_\mu} \frac{\epsilon_e}{\epsilon_\mu} P_{\nu_\mu \to \nu_e} \tag{1.3.3}$$

Understanding this well could help reduce uncertainties on measurements of the oscillation probability and the CP violating phase.

1.3.2 Tests of Lepton Universality

Measuring the ratios of ν_e and ν_μ interaction cross sections could provide a useful test of lepton universality. Once kinematic differences and differences due to nuclear effects have been taken into account, the cross sections are expected to be the same for all three species of neutrino. Any significant differences not due to these effects would be indicative of New Physics [20].

Possible new Physics differences in ν_e and ν_μ cross sections are Second Class Current (SCCs) described in Sec 2.1.7.3, radiative corrections described in Sec 2.1.7.1 or extensions to the Standard Model that add extra gauge bosons, described in Sec 2.1.7.4.

1.4 Summary of My Work

The work I have performed for the T2K experiment falls into two categories; the analysis of interaction cross section ratios, and the service work involving the ND280 Electromagnetic Calorimeters (ECal).

The service work involved calibration of the ECals to ensure a universal response of the detector, described in Sec 3.1. It also entailed a study of the degradation of the scintillator bars in the ECal with time and calculating corrections for this effect as well as extrapolating this to the future. This work is described in Sec 3.2. I also performed studies on the systematic uncertainty associated with matching a reconstructed object in the ECal with an object in one of the Time Projection Chambers (TPC). These uncertainties are propagated through the selections used in the cross section ratio work and used in several other T2K analyses. This work is described in Sec 3.3. Lastly, I was an onsite expert for the ECal during my long term attachement in Tokai. The work associated with this is not included here.

The cross section ratio analysis involved brief studies on optimising the ν_e selection that are not included here as it was superseded by work performed by other collaborators. Performing the analysis involved using both the selections for ν_e and ν_μ CC and CCQE interactions in ND280 and creating a framework to calculate the ratios for a variety of reconstructed variables and to unfold to other variables that are difficult to reconstruct. This is detailed in Sec 4.6. The main body of the work was calculating the cancellation of the systematic uncertainties, detailed in Sec 4.7.

Chapter 2

Theory and the T2K Experiment

2.1 Theory

2.1.1 Overview

The Standard Model of Particle Physics (SM) describes all known elementary particles, such as quarks and leptons, and the fundamental forces that govern how they behave [21] [22]. The Standard Model is a Quantum Field Theory (QFT) with internal symmetries described by Eq 2.1.1.

$$SU(3)_c \otimes SU(2)_L \otimes U(1)_Y \tag{2.1.1}$$

Each group in Eq 2.1.1 represents a force with the indices c, L, and Y, representing the quantity the force couples to. $SU(3)_c$ represents the strong nuclear force coupling to colour, $SU(2)_L$ represents the weak nuclear force coupling to left-handed particles and $U(1)_Y$ represents the Electromagnetic force coupling to Hypercharge. A chart of the particles included in the SM is given in Fig 2.1.1.

The normal procedure for working with these fields and particles is to define a Lagrangian density for the field, $\mathcal{L}$, a quantity that determines how the system evolves. For any system, the Lagrangian is simply the kinetic energy of the system, T, minus the potential energy of the system, V, and the Lagrangian is the integral of the Lagrangian density over all space-time. These relations are shown in Eqs 2.1.2 2.1.3 [23].

$$L(x^\mu, \partial_\mu x) = T - V \tag{2.1.2}$$

$$L = \int d^4x \mathcal{L}[\phi, \partial_\mu \phi] \tag{2.1.3}$$

In this formulism, x^μ are the coordinates describing a point in the system, ϕ is a field, and μ is a Lorentz index running over the three dimensions of space

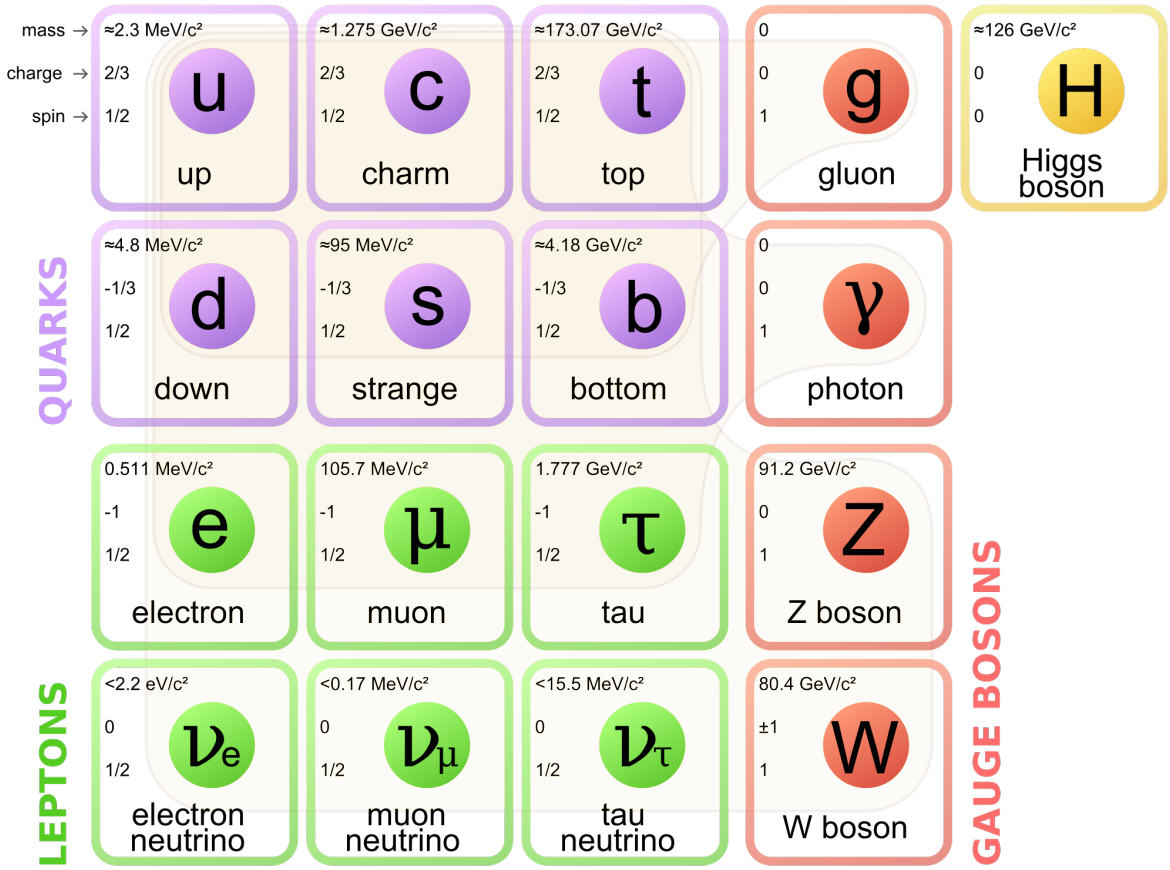

Figure 2.1.1: A table of Standard Model particles, broken down into the quarks, leptons, gauge bosons and the Higgs boson. The mass, spin and electric charge of each particle is also shown. [8]

and one dimension of time. Essentially meaning that the Lagrangian density is a quantity that depends only on the field and its space-time derivatives. From the Lagrangian, it is possible to derive the Feynman rules and determine the interaction properties of neutrinos.

2.1.2 Neutrinos in the Standard Model

Left-handed neutrinos form part of an SU(2) doublet with their corresponding charged lepton. Only the particles with left-handed chirality form part of the doublet, as the weak force does not couple to right-handed particles. Conversely, the weak force only couples to right-handed anti-particles. The particles that do not interact via the weak interaction form singlet states, a summary of these are shown in Eq 2.1.4 [24].

$$\begin{pmatrix}\nu_e\\ e\end{pmatrix}_L \quad \begin{pmatrix}\nu_\mu\\ \mu\end{pmatrix}_L \quad \begin{pmatrix}\nu_\tau\\ \tau\end{pmatrix}_L \quad (e)_R \quad (\mu)_R \quad (\tau)_R \tag{2.1.4}$$

This is built into the standard model as suggested by experimental results rather than a deeper theory.

2.1.3 The Weak Interaction

The electroweak Lagrangian, $\mathcal{L}_{\mathrm{EW}}$, contains interaction terms for particles that allow them to couple to various fields. Shown in Eqs 2.1.5 2.1.6 2.1.7 are the parts of the electroweak Lagrangian describing Electromagnetic interactions (EM), Neutral Current interactions (NC), and Charged Current interactions (CC) respectively for electron and neutrino scattering [25].

$$\mathcal{L}_{\mathrm{EM}} = q(\bar{e}\gamma_\mu e)A^\mu \tag{2.1.5}$$

$$\mathcal{L}_{\mathrm{NC}} = -\frac{g}{2\cos(\theta_W)}\Big[\bar{\nu}\gamma_\mu\frac{1}{2}(1-\gamma_5)\nu - \bar{e}\gamma_\mu\frac{1}{2}(1-\gamma_5)e + 2\sin^2(\theta_W)\bar{e}\gamma_\mu e\Big]Z^\mu \quad (2.1.6)$$

$$\mathcal{L}_{\mathrm{CC}} = -\frac{g}{\sqrt{2}}\Big[\bar{\nu}\gamma_\mu\frac{1}{2}(1-\gamma_5)eW^{+\mu} + \bar{e}\gamma_\mu\frac{1}{2}(1-\gamma_5)\nu W^{-\mu}\Big] \quad (2.1.7)$$

Where A^μ, Z^μ, $W^{+\mu}$ and $W^{-\mu}$ are fields. The excitations of these fields correspond to the photon, the Z^0 boson, and the $W^\pm$ bosons respectively. Terms with these fields describe interactions between the spinors ν, $\bar{\nu}$, e and $\bar{e}$, which describe neutrinos and leptons. The quantities g, θ_W, and q are related to the coupling strength between particles. The spinors that describe neutrinos do not appear in the electromagnetic component of the electroweak Lagrangian. The interactions discussed in this thesis are all charged current interactions, so this is the part of the Lagrangian of interest when discussing interaction cross sections. The only bosonic fields in $\mathcal{L}_{\mathrm{CC}}$ are the W^+ and W^-, this is representative of the fact that a neutrino charged current interaction must exchange charge. An Feynman diagram of such a process is shown in Fig 2.1.3.

The fields that describe the weak interaction act as a linear combination of vector and axial-vector fields, taking the form $V - A$. Consequently, the currents describing the W and Z bosons, J^W_μ and J^Z_μ, take the forms shown in Eq 2.1.8 and 2.1.9 respectively. Here, the spinors u and $\bar{u}$ correspond to the particles the boson couples to. Due to its $V - A$ nature, the weak interaction can violate parity. This was first shown in [26] by studying the β decay of Cobalt nuclei.

$$J^W_\mu = \frac{-ig_W}{2\sqrt{(2)}}\bar{u}(\gamma^\mu - \gamma^\mu\gamma^5)u \quad (2.1.8)$$

$$J^Z_\mu = \frac{-ig_Z}{2}\bar{u}(g_V\gamma^\mu - g_A\gamma^\mu\gamma^5)u \quad (2.1.9)$$

To calculate a cross section for a weak interaction process, a term describing the propagator in the Feynman diagram is needed. This is done most simply using the Feynman rules [27]. For a particle of mass M, the propagator term is given by Eq 2.1.10. At energies similar to that of the T2K neutrino beam, it is reasonable to make the approximation that $q^2 \ll M^2$ and the propagator term reduces to Eq 2.1.11.

$$-i\frac{g_{\mu\nu} - \frac{q_\mu q_\nu}{M^2}}{q^2 - M^2} \tag{2.1.10}$$

$$-i\frac{g_{\mu\nu}}{M^2} \tag{2.1.11}$$

Using the matrix element and the propagator term, the coupling strength of the boson can be related to the Fermi constant, G_F, and the mass of the boson as in Eq 2.1.12.

$$G_F = \frac{g^2}{4\sqrt{2}M_W^2} \tag{2.1.12}$$

This shows why the weak interaction couples so weakly, the large mass of the W and Z bosons suppresses the interactions by a factor of approximately M_W^2.

2.1.4 Neutrino Oscillations

Neutrino oscillations are a purely quantum mechanical effect caused by neutrinos having mass. Specifically, the neutrino mass eignestates are non-zero, non-degenerate and not aligned with the weak (flavour) eigenstates. The differences in the mass eigenstates are the fundamental cause of neutrino oscillations because a phase difference occurs from wavepackets within a flavour eigenstate propagrating at different speeds due to their different masses. The relationship between the mass and flavour eigenstates is shown in Eq 2.1.13. The matrix, U_{PMNS}, that relates these states is known as the Pontecorvo-Maki-Nakagawa-Sakata (PMNS)

matrix, based on the work in [7]. Each set of flavour and mass eigenstates is orthonormal and so the transformation that relates them must be unitary. Thus, the PMNS matrix takes the form of three rotation matrices that include a complex phase. The most common parameterisation of this is shown in Eq 2.1.14. $\nu_{1,2,3}$ are the mass eigenstates and $\nu_{e,\mu,\tau}$ are the flavour eigenstates. The fact that neutrinos can change flavour was the first evidence that neutrinos have mass.

$$\begin{pmatrix} \nu_e \\ \nu_\mu \\ \nu_\tau \end{pmatrix} = \begin{pmatrix} U_{e1} & U_{e2} & U_{e3} \\ U_{\mu 1} & U_{\mu 2} & U_{\mu 3} \\ U_{\tau 1} & U_{\tau 2} & U_{\tau 3} \end{pmatrix} \begin{pmatrix} \nu_1 \\ \nu_2 \\ \nu_3 \end{pmatrix} \tag{2.1.13}$$

$$U_{\text{PMNS}} = \begin{pmatrix} 1 & 0 & 0 \\ 0 & c_{23} & s_{23} \\ 0 & -s_{23} & c_{23} \end{pmatrix} \begin{pmatrix} c_{13} & 0 & s_{13}e^{-i\delta_{CP}} \\ 0 & 1 & 0 \\ -s_{13}e^{i\delta_{CP}} & 0 & c_{13} \end{pmatrix} \begin{pmatrix} c_{12} & s_{12} & 0 \\ -s_{12} & c_{12} & 0 \\ 0 & 0 & 1 \end{pmatrix} \tag{2.1.14}$$

In Eq 2.1.14, the terms s_{ij} and c_{ij} are shorthands for $\sin\theta_{ij}$ and $\cos\theta_{ij}$. The angles θ_{ij} quantify mixing between the ij^{th} mass eigenstates, and δ_{CP} is the CP violating phase, which determines the asymmetry between matter and anti-matter neutrino oscillations.

The neutrino mass eigenstates ν_1, ν_2, ν_3 propagate according to the Dirac equation with solutions that describe plane-waves. The probability for oscillation from state α to state β is then given by the square of the wavefunction as shown in Eq 2.1.15 for distance travelled from the production of the neutrino, L.

$$P(\nu_\alpha \to \nu_\beta) = |\, \langle \nu_\beta(L) | \nu_\alpha(0) \rangle \,|^2 \tag{2.1.15}$$

The oscillation probabilities can be calculated as in Eq 2.1.16, this shows the probability of a neutrino of flavour α oscillating to flavour β.

$$P(\nu_\alpha \to \nu_\beta) = \delta_{\alpha\beta} - 4\sum_{i>j} \Re(U^*_{\alpha i}U_{\beta i}U_{\alpha j}U^*_{\beta j}) \sin^2\left(\frac{\Delta m^2_{ij}L}{4E}\right) + 2\sum_{i>j} \Im(U^*_{\alpha i}U_{\beta i}U_{\alpha j}U^*_{\beta j}) \sin\left(\frac{\Delta m^2_{ij}L}{2E}\right) \quad (2.1.16)$$

The mixing angles relate to the amplitude of the oscillations whilst the differences in the masses squared relate to the frequency. These parameters can be measured by experiments but do not give any information on the absolute value of the neutrino masses, these have yet to be measured.

2.1.5 Interaction Types

Using the weak interaction Lagrangian described in Sec 2.1.3 the properties of the interactions can be modelled. In practice, a neutrino can scatter off an atomic electron, a group of nucleons, a single nucleon, or a single quark. The types of interaction a neutrino can undergo can be broken down into four distinct categories, leading to a large variety of possible final states:

- Elastic scattering: A neutrino scatters off a nucleon, either a proton or a neutron, via a Z^0 boson (neutral current). A Feynman diagram showing an example of this process is shown in Fig 2.1.2. This can result in the ejection of the target nucleon from the nucleus. Neutral current elastic scattering can occur at any neutrino energy with a peak in the interaction cross section at roughly 1 GeV.

- Quasi-elastic scattering: A neutrino scatters off a nucleon via a W^+ boson (charged current) producing the associated lepton. This can result in the ejection of the target nucleon from the nucleus. In the case of neutrino (not anti-neutrino) scattering, the nucleon must be a neutron in order to conserve electric charge. A Feynman diagram showing a Charged-Current

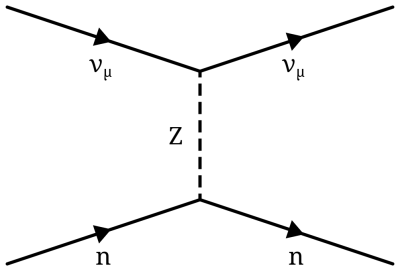

Figure 2.1.2: A Feynman digram showing an elastic scattering interaction between a muon neutrino and a neutron.

Quasi-Elastic interaction is given in Fig 2.1.3. Quasi-elastic scattering is the dominant process below about 1 GeV in neutrino energy.

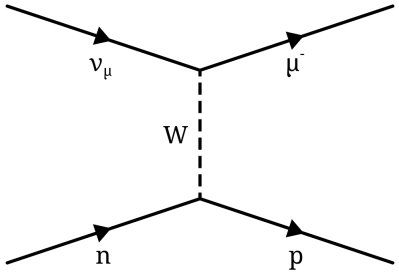

Figure 2.1.3: A Feynman digram showing a Charged-Current Quasi-Elastic (CCQE) interaction between a muon neutrino and a neutron producing a muon and a proton.

- Resonance production: A neutrino excites a target nucleon to a higher mass resonance state ($p \to \Delta$, $n \to N^*$). This then decays back to a proton or neutron producing additional mesons. A Feynman diagram showing an example of this process is shown in Fig 2.1.4. These processes are dominant in the energy range of 1 GeV - 5 GeV. Calculations of resonance production cross sections were recently improved in [28].

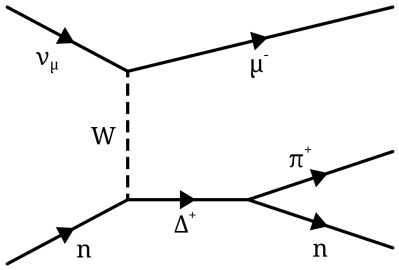

Figure 2.1.4: A Feynman digram showing resonance pion production by the decay of an excited state into a neutron and a charged pion.

- Deep Inelastic Scattering: At high enough energies, the de Broglie wavelength of the neutrino is of a similar size to an individual quark in a nucleon. The neutrino can then scatter off the quarks producing hadrons. Deep inelastic scattering becomes the dominant interaction over resonance at energies above about 5 GeV, as shown in Fig 2.1.5.

The interaction cross sections for the individual components described above are shown in Fig 2.1.5 with the total charged current cross section overlaid. This shows at which energies the different processes dominate and will be useful when considering the ratios of cross sections. The CCQE cross section as measured by the MiniBooNE [29] and NOMAD [30] experiments is shown in Fig 2.1.6 [31].
The total charged current cross section is very difficult to model on its own. Instead, the individual different components are modelled and the total charged current cross section calculated as the incoherent sum of them. These individual components are CCQE, resonance production, and deep inelastic scattering. The resulting expression for the total Charged Current cross section is shown in Eq 2.1.17 with σ_{RES} and σ_{DIS} being the cross sections for a neutrino charged current resonance and deep inelastic scattering processes respectively.

$$\sigma_{\mathrm{CC}} = \sigma_{\mathrm{CCQE}} + \sigma_{\mathrm{RES}} + \sigma_{\mathrm{DIS}} \tag{2.1.17}$$

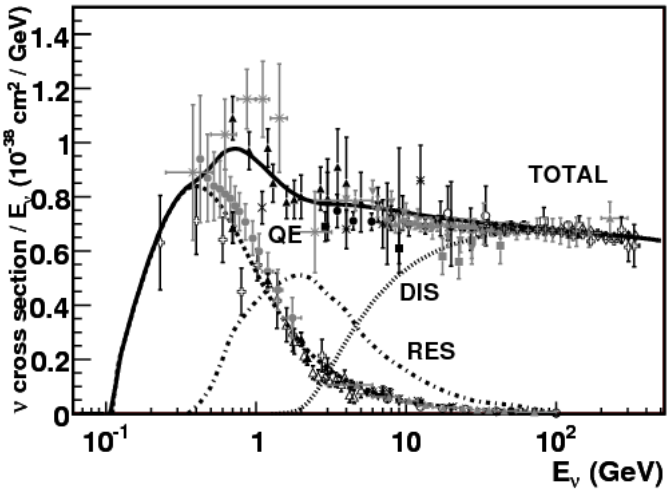

Figure 2.1.5: The contributions of the different interaction types to the total charged current cross section. The data are from several different experiments with the plot taken from [32].

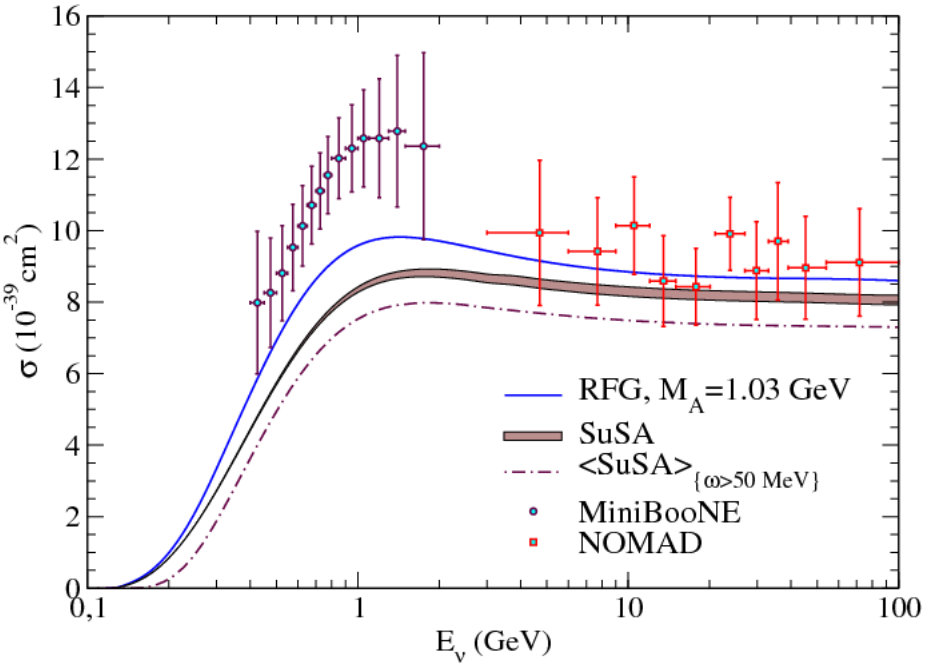

Figure 2.1.6: The ν_μ CCQE interaction cross section measured by the MiniBooNE [29] and NOMAD [30] experiments with predictions based on a Relativistic Fermi Gas (RFG) model and SusperScaling Approximations (SuSA) laid on top [31].

Consequently, the CC inclusive cross section is difficult to quantify. Instead, Monte Carlo generators will be used to form predictions for the cross sections and the ratios of cross sections. Details on this will be given in Sec 4.3.

2.1.6 Cross Sections

A cross section is a quantity that describes how likely a particle is to interact. The interaction cross section depends on the energy of the neutrino and what the neutrino is interacting with.

To study neutrino cross sections from a theoretical perspective, it is much simplier to separate the problem into different energy ranges as different processes dominate. For instance, at energies below the mass of the lepton corresponding to the neutrino, only neutral current processes are possible. In principle, one could simply use the electroweak Lagrangian to get a formula for the cross section across all energy ranges. However, initial conditions, final state interactions and nuclear corrections make this calculation very difficult [32].

In general, the cross section between an incoming neutrino and a stationary lepton in terms of the 4-momentum transfer, q^2, is given by Eq 2.1.18 [33]. $\mathcal{M}$ is the matrix element describing the interaction type and the particles involved. It is determined from the interaction Lagrangian. The rest of the terms are kinematic; s and u are Mandelstam variables given in Eqs 2.1.19 2.1.20 which encode the kinematics of scattering between two particles with initial momenta p_1 and p_2, and final momenta p_3 and p_4. m_ℓ and m_ν are the masses of the lepton and neutrino respectively.

$$\frac{d\sigma}{dq^2} = \frac{1}{16\pi} \frac{|\mathcal{M}|^2}{(s-(m_\ell+m_\nu)^2)(s-(m_\ell-m_\nu)^2)} \tag{2.1.18}$$

$$s = (p_1+p_2)^2 = (p_3+p_4)^2 \tag{2.1.19}$$

$$u = (p_1 - p_4)^2 = (p_2 - p_3)^2 \tag{2.1.20}$$

The neutral current and charged current Lagrangians used to calculate the matrix elements, $\mathcal{M}$, are shown in Eq 2.1.6 and Eq 2.1.7 respectively. The resulting matrix elements are shown in Eq 2.1.21 and Eq 2.1.22 [32]. For simplification, these equations use the assumption that the 4-momentum of the interaction boson is much smaller than its mass ($q^2 \ll M^2$) and so can be neglected.

$$\mathcal{M}_{CC} = -\frac{G_F}{\sqrt{2}}\{[\bar{\ell}\gamma^\mu(1-\gamma^5)\nu_\ell][\bar{\nu}_e\gamma_\mu(1-\gamma^5 e)]\} \tag{2.1.21}$$

$$\mathcal{M}_{NC} = -\sqrt{2}G_F\{[\bar{\nu}_\ell\gamma^\mu(g_V^\nu - g_A^\nu\gamma^5)\nu_\ell][\bar{e}\gamma_\mu(g_V^f - g_A^f\gamma^5)e]\} \tag{2.1.22}$$

The g_V and g_A terms are vector and axial-vector coupling constants respectively. The same formulation can be used to describe neutrino-quark interactions.

As with neutrino-lepton scattering, a complete formula can be found to describe neutrino-quark interactions. However, quarks are only seen in bound states (hadrons) and so modelling these interactions becomes much more difficult. For extended objects like these, the neutrino-nucleon interaction depends largely on the wavelength of the interacting boson, which is dependant on the 4-momentum transfered, $Q^2 = -q^2$. This results in Eq 2.1.23 for CCQE scattering, which was written down by Llewellyn-Smith in [27].

$$\frac{d\sigma}{dQ^2} = \frac{G_F^2 M^2 |V_{ud}|^2}{8\pi E_\nu^2}\left(A \pm \frac{(s-u)}{M^2}B + \frac{(s-u)^2}{M^4}C\right) \tag{2.1.23}$$

In Eq 2.1.23, M is the nucleon mass, E_ν is the neutrino energy, and A, B and C are functions of Q^2 and the nucleon form factors given by Eq 2.1.24 2.1.25 2.1.26. For brevity, $\zeta = Q^2/4M^2$. The $\pm$ sign in Eq 2.1.23 is $(-)$ for antineutrino-quark scattering and $(+)$ for neutrino-quark scattering. The situation is further complicated when considering the practical situation of neutrino-nucleus scattering due to the energy and momentum distributions of the nucleons inside the nucleus not

being well understood. The most common description uses a Fermi gas model, with the formalism being laid out in [67].

$$\begin{aligned} A &= \frac{(m^2+Q^2)}{M^2}\Bigg[(1+\zeta)F_A^2-(1-\zeta)F_1^2+\zeta(1-\zeta)F_2^2+4\zeta F_1F_2 \\ &\quad -\frac{m^2}{4M^2}\left((F_1+F_2)^2+(F_A+2F_P)^2-\left(\frac{Q^2}{M^2}+4\right)F_P^2\right)\Bigg] \qquad (2.1.24) \\ B &= \frac{Q^2}{M^2}F_A(F_1+F_2) \qquad (2.1.25) \\ C &= \frac{1}{4}(F_A^2+F_1^2+\zeta F_2^2) \qquad (2.1.26) \end{aligned}$$

The functions F_1, F_2, F_A and F_P are form factors that determine the properties of the interaction. F_1 and F_2 are the Dirac and Pauli electromagnetic vector form factors of the first class current that describe the distributions of the electric charge inside the nucleon at a given four-momentum transfer. They can be accurately measured using charged lepton scattering as in [34]. F_A and F_P are the axial and pseudo-scalar form factors for the first class currents. F_A is not well known as previous experiments have found inconsistent results. F_P can be measured in pion electroproduction studies as in [35].

2.1.7 Ratios of Interaction Cross Sections

It is important to understand the cross sections described in Sec 2.1.6 for electron and muon neutrinos in order to interpret the results of the cross section ratios. In principle, it is possible to write out very long formulae for the cross section ratios but these are very complicated and difficult to extract any information from. However, kinematic arguments can be used to predict a general trend for each of the ratios whilst Monte Carlo (MC) generators can be used to generate more quantitative predictions, as in Sec 4.3. The possible causes of differences

between ν_e and ν_μ interactions are also discussed here.

As shown in Eq 2.1.17, the CCQE cross section is, by definition, smaller than the CC inclusive cross section for both ν_e and ν_μ. Therefore, the CCQE to CC MC ratio must be less than or equal to 1. The threshold neutrino energy required to undergo a CCQE interaction is the mass of the produced lepton. Since there is not enough energy to produce additional particles at energies just above the lepton mass, the cross section ratio will be 1. At higher energies, extra particles can be produced and the ratio decreases. As the phase space for producing these extra particles increases, the CCQE process becomes subdominant and the ratio continues to get smaller with higher energies.

The double ratio, given in Eq 2.1.27, involves comparing the differences in the CCQE to CC ratio for ν_e and ν_μ. These should follow a similar pattern with the drop from 1 coming slighly later for the ν_μ ratio. Consequently, the double ratio should be 1 at the point where there is not enough energy for either ν_e or ν_μ to undergo a reaction other than CCQE. The double ratio should then drop at the point where a ν_e can produce additional particles and the ν_μ cannot. Above this point, the double ratio should level out at 1 again once the difference in lepton masses becomes small compared to the neutrino energy.

$$DR = \frac{\frac{\sigma(\nu_e \text{ CCQE})}{\sigma(\nu_e \text{ CC})}}{\frac{\sigma(\nu_\mu \text{ CCQE})}{\sigma(\nu_\mu \text{ CC})}} \tag{2.1.27}$$

The shapes of these ratios can be seen in Fig 2.1.7. This shows calculations of the cross section ratios on Carbon (C^{12}) performed by the GENIE Monte Carlo generator. More detail on these calculations is given in Sec 4.3.

It is important to quantify any possible sources of difference betweem ν_e and ν_μ cross sections to identify the causes of any deviations from the expectations when taking the ratios. The possible sources are differences in final state lepton mass,

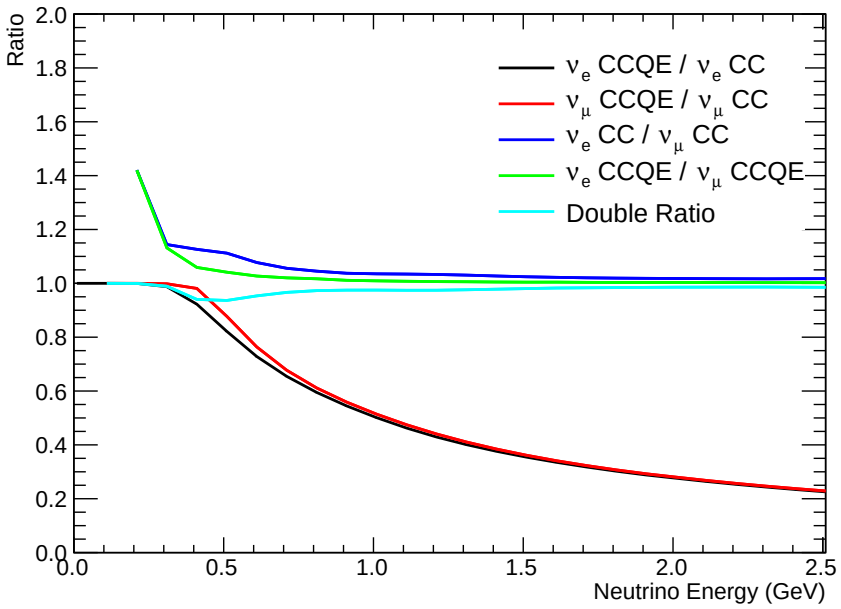

Figure 2.1.7: Calculations of the five cross section ratios performed by the GENIE Monte Carlo generator.

radiative corrections to the tree level process, uncertainties in the nucleon form factors, second class currents, and low mass W bosons. See [38] for a review of these for CCQE processes.

2.1.7.1 Radiative Corrections

The Feynman diagrams shown in Sec 2.1.5 show first order scattering processes. Radiative corrections are higher-order contributions to the tree-level process that involve the emission of photons. These can either be reabsorbed and so only affect the size of the cross section or end up in the final state and so change the topology of the event. These are shown as diagrams that contain loops or Bremsstrahlung photons. Fig 2.1.8 shows the possible processes that involve radiation of photons and Fig 2.1.9 shows the fractional difference in cross section due to these. The first and fourth processes (the two leftmost) can only go via the neutral current interaction as charge would not be conserved. The others can go by either the charged or neutral current process. The effects of these corrections could show up as about a 10% difference between the ν_e and ν_μ cross sections [39] and enhance the CCQE to CC ratio by increasing the CCQE interaction cross section. Radiative corrections to neutrino-lepton processes have been calculated in [40], [41], [42] and [43] for neutrino-nucleon scattering.

2.1.7.2 Uncertainties in the Nucleon Form Factors

The form factor F_A can cause differences in ν_e and ν_μ cross sections via a change in the effective axial mass of a nucleon, m_A. The nucleon axial mass is a quantity that describes the charge radius of a nucleon and affects neutrino-nucleon cross-sections considerably. F_1 and F_2 affect the axial mass but these are too well measured at the relevant values of Q^2 to result in a significant difference [34]. On the other hand, F_A is poorly measured. Fig 2.1.10 shows the difference in ν_e and ν_μ cross section due to various changes in m_A, within the experimental limits compared with a nominal value of axial mass, m_A, = 1.1 GeV. The variation allowed is small, at about 1% at low energies and drops at increasing energies

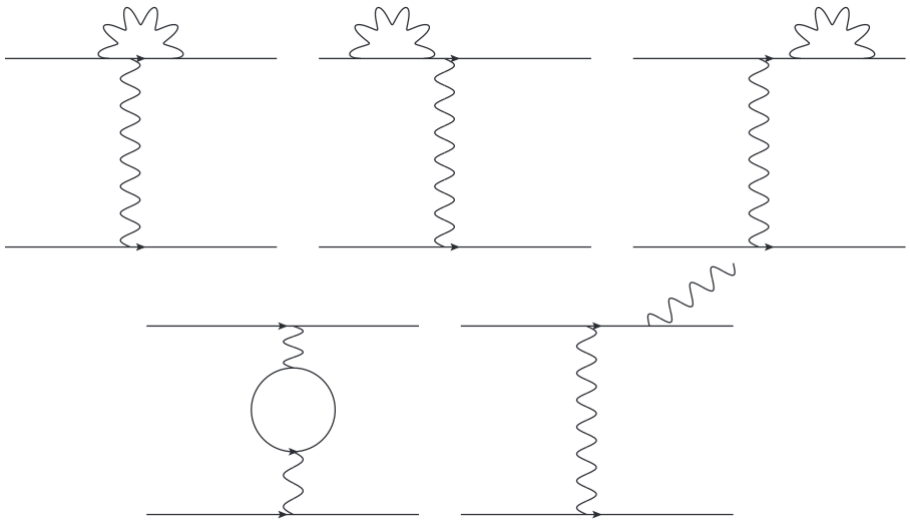

Figure 2.1.8: Feynman diagrams showing possible radiative corrections to the tree level diagrams [39].

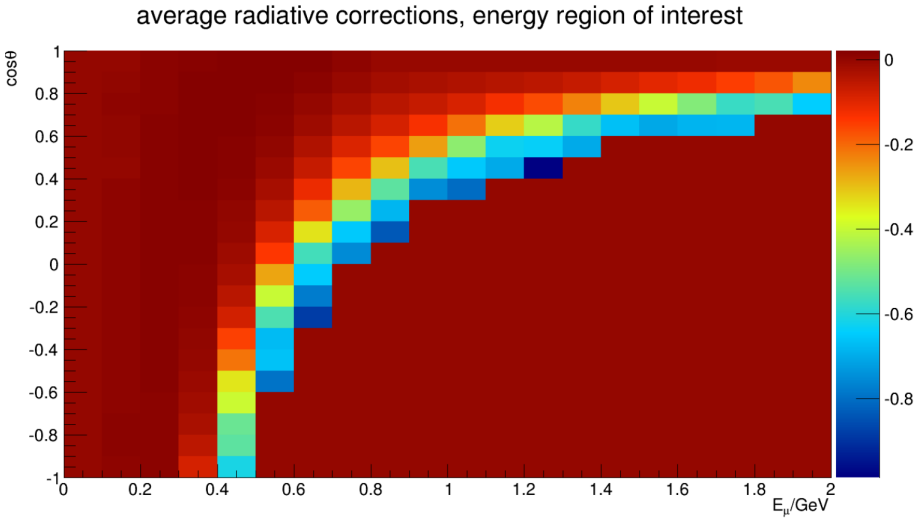

Figure 2.1.9: The fractional difference in cross section due to radiative corrections as a function of neutrino energy and lepton angle [39]. The z-axis shows the fractional difference between the CCQE cross section with radiative corrections and the cross section for CCQE interactions only.

[38]. These possible differences are significantly smaller than those associated with radiative corrections.

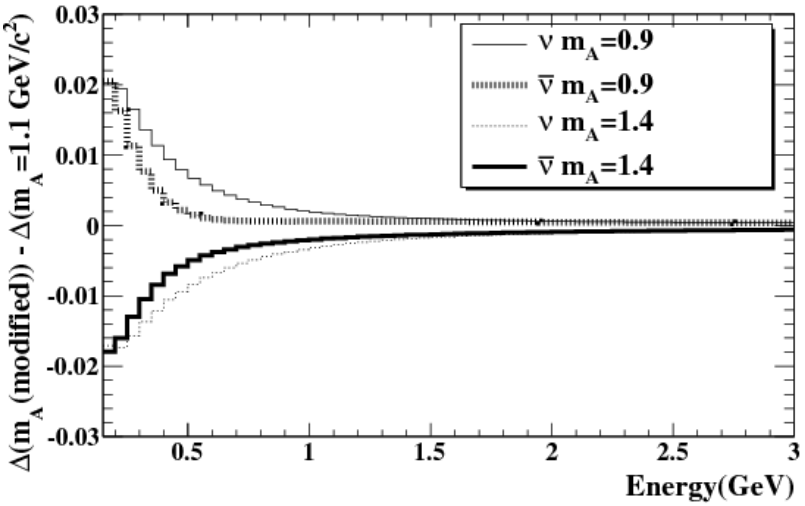

Figure 2.1.10: The size of the predicted change in the difference of ν_e and ν_μ cross section due to changes in m_A [38].

2.1.7.3 Second Class Currents

The currents that describe the W and Z bosons are given in Eq 2.1.8 and Eq 2.1.9. These can be split into two types, depending on their G-Parity. First class currents have quantum numbers, $J^{PG} = 1^{+-}, 1^{-+}$ and second class currents have $J^{PG} = 1^{++}, 1^{--}$ [44] [45]. The CCQE cross section shown in Eq 2.1.23 depends on the second-class current form factors, F_{3^A}, and F_{3^V}, through the parameters B and C. Eqs 2.1.25 2.1.26 do not include this as second class currents would violate charge or time symmetry and so are assumed to not exist. The full equations are shown in Eq 2.1.28 and Eq 2.1.29 with second class currents having the most impact through B.

$$B(Q^2) = \frac{Q^2}{M^2} F_A(F_1+F_2) - \frac{m^2}{M^2}\left[(F_1 - \zeta F_2)\, F_{3^V} - \left(F_A - \frac{Q^2 F_P}{2M^2}\right) F_{3^A}\right] \quad (2.1.28)$$

$$C(Q^2) = \frac{1}{4}\left(F_A^2 + F_1^2 + \zeta F_2^2 + 4\zeta F_{3^A}^2\right) \tag{2.1.29}$$

By studying β decays it is possible to determine both F_{3^A} and F_{3^V}. F_{3^A} is measured in [36] and a limit on F_{3V} is calculated in [37].

The F_{3^V} term always enters the cross section formula suppressed by terms in m/M (lepton mass over nucleon mass) and so only play a significant role in ν_μ scattering. It is difficult to constrain F_{3^V} experimentally [37], and so there is room for big differences in the ν_e / ν_μ cross section ratio due to this. On the other hand, F_{3^A}, is well constrained [46] and consistent with zero and so cannot affect the cross sections significantly. These terms can change the interaction cross sections via altering the effective axial mass of the neutrino. Fig 2.1.11 shows the predicted effect of including second class currents with the maximally allowed value of F_{3V} as constrained by experiments [37].

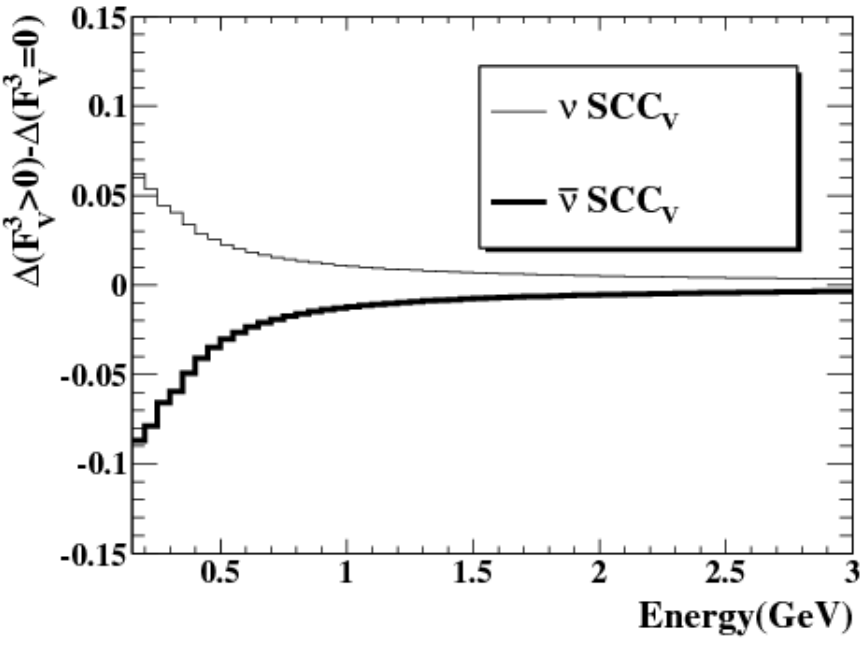

Figure 2.1.11: The size of the predicted change in the difference of ν_e and ν_μ cross section due to second class currents with $F_{3^V}(Q^2) = 4.4F_1(Q^2)$ [38].

2.1.7.4 Low Mass Ws

There are several extensions to the Standard Model, such as the little Higgs model [47], that include a second SU(2) group which would mix with the standard SU(2) group. This would mean there exist additional bosons, W' and Z', as well as the standard Ws and Z, enhancing both the ν_e and ν_μ cross sections. The effect would be bigger for the ν_e cross section due to the larger phase space to produce an electron. Therefore, such an extension could increase the ν_e / ν_μ cross section ratios.

Although several potential causes of difference from what may be expected in these ratios are discussed. In practice, it could be difficult to determine which of these (if any) is responsible.

2.2 The T2K Experiment

2.2.1 Overview

The T2K experiment makes use of a neutrino beam produced at the J-PARC facility in Tokai-Mura, on the east coast of Japan. The beam is sent through a suite of near detectors located at J-PARC towards the Super Kamiokande detector (SK) 295 km from the beam production point. The neutrino flux is measured at both the near detector suite, before the neutrinos in the beam have had a chance to oscillate, and at SK. Comparisons of these measurements allows for calculations of several of the parameters involved in neutrino oscillations. A schematic of this arrangement is shown in Fig 2.2.1.

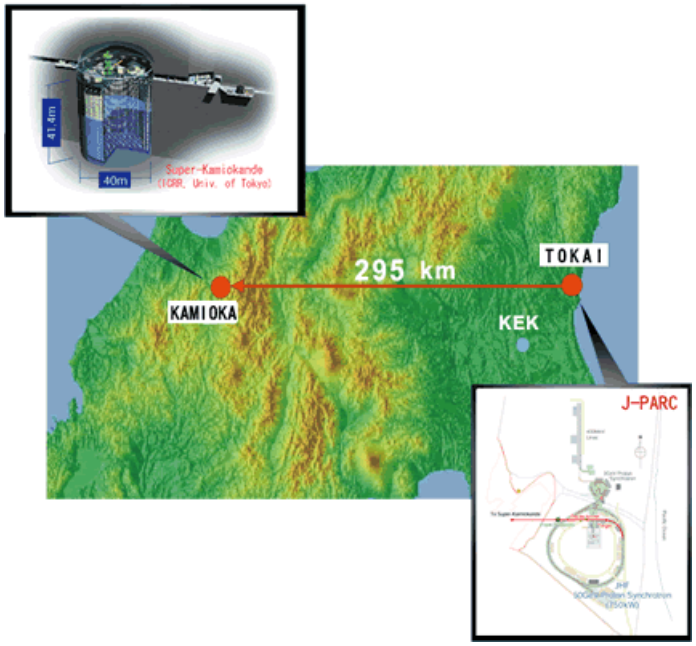

Figure 2.2.1: The layout of the T2K experiment. The neutrino beam is sent from J-PARC, across Japan, to the Super Kamiokande far detector. [48]

The near detector suite consists of two main detectors; INGRID and ND280. INGRID is an on-axis detector, used to measure the beam profile. It is described

in more detail in Sec 2.2.14. ND280 and SK are both off-axis detectors, and are described in Sec 2.2.5 and Sec 2.2.15 respectively. The analyses presented in this thesis were performed with the ND280 detector, and so it is given more focus here.

2.2.2 The J-PARC accelerator

The neutrino beam used by T2K is created at the J-PARC facility (Japanese Proton Accelerator Research Complex) by firing a proton beam into a graphite target. The proton beam is created by first accelerating a H^- beam to 400 MeV in a LINAC. This beam is then stripped of electrons to create a H^+ beam before being sent through a rapid-cycling synchotron (RCS) which accelerates it up to 3 GeV. The proton beam is then injected into the main ring and accelerated up to 30 GeV before being fired at the target to create the neutrino beam. A diagram of this layout is shown in Fig 2.2.2. The proton beam is delivered to the target in spills, one spill contains eight bunches of protons in the main ring.

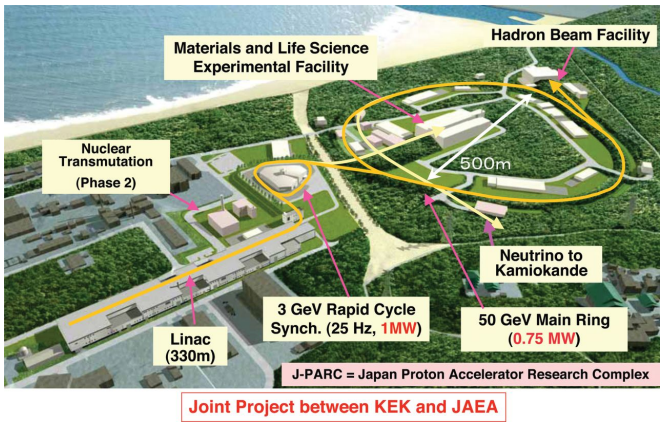

Figure 2.2.2: The J-PARC facility, with the main components to accelerate the proton beam up to 30 GeV labelled. [49]

2.2.3 The T2K Neutrino Beam

The proton is fired into a graphite target to create a secondary beam composed of pions and kaons. Magnetic horns then focus either the positively or negatively charged pions and kaons to point 2.5 ° away from the Super Kamiokande far detector. The pions travel through a 96 m long decay volume where they decay into muons and muon neutrinos, with a small contamination from electrons and electron neutrinos. For a neutrino beam, the magnetic horns focus the positively charged particles, whilst for an anti-neutrino beam the negatively charged particles are focused. The electrons and muons created in these decays are sent into a beam dump to stop them reaching the near detector complex [48]. A schematic of this layout is shown in Fig 2.2.3.

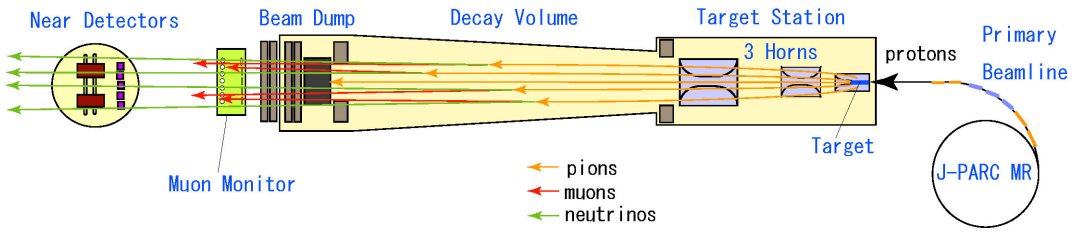

Figure 2.2.3: A schematic of the target station, decay volume, beam dump and near detector suite. The process of creating a neutrino beam from a proton beam is illustrated. [50]

The neutrino beam energy was carefully chosen such that SK lies at the oscillation maximum for $\nu_\mu \rightarrow \nu_e$. To achieve this for a 295 km baseline, a 600 MeV beam is needed. A neutrino beam with peak energy around 1 GeV is produced but is pointed slightly off-axis (2.5 °) from ND280 and SK. This has the effect of narrowing the beam energy spectrum and lowering the peak energy at the detectors to 600 MeV, at the cost of reducing the flux of neutrinos. A plot showing how the beam energy changes with off-axis angle is shown in Fig 2.2.4.

The energy of a neutrino from the decay of a pion to a muon and muon neutrino as a function of the angle of the outgoing neutrino with respect to the muon (θ)

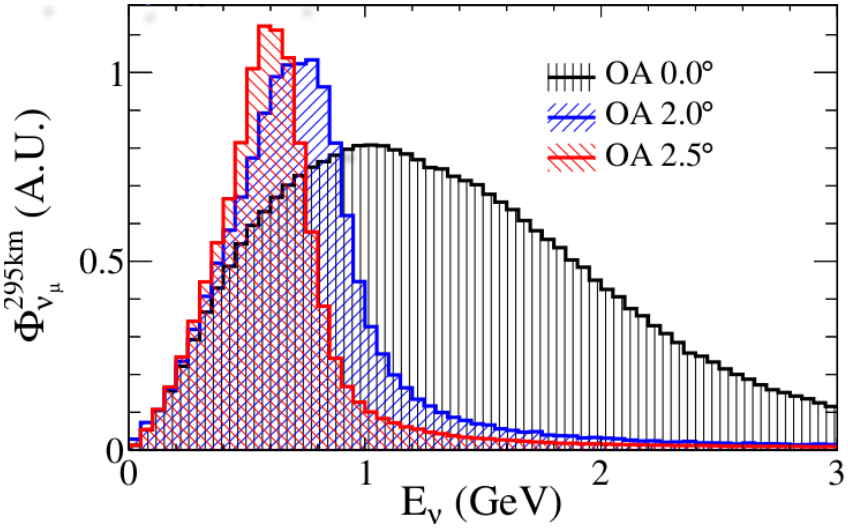

Figure 2.2.4: A plot showing how the T2K neutrino beam energy spectrum at the far detector changes with off-axis angle. ND280 and Super-Kamiokande are located 2.5 ° off-axis and have a peak neutrino energy at 600 MeV [51]. The y-axis shows the flux of neutrinos, φ, in arbritary units at the far detector.

and pion energy (E_π) is described by Eq 2.2.1.

$$E_\nu = \frac{m_\pi^2 - m_\mu^2}{2(E_\pi - p_\pi \cos\theta)} \tag{2.2.1}$$

The resulting beam consists of mainly muon neutrinos with a 1% contamination of electron neutrinos [52]. Fig 2.2.5 shows the energy spectra for electron and muon neutrinos broken down into the different parent particle of the neutrinos. The electron neutrinos peak at a higher energy than the muon neutrinos, as a large fraction of the electron neutrinos come from kaon decays, whereas most muon neutrinos come from the less massive pion decay.

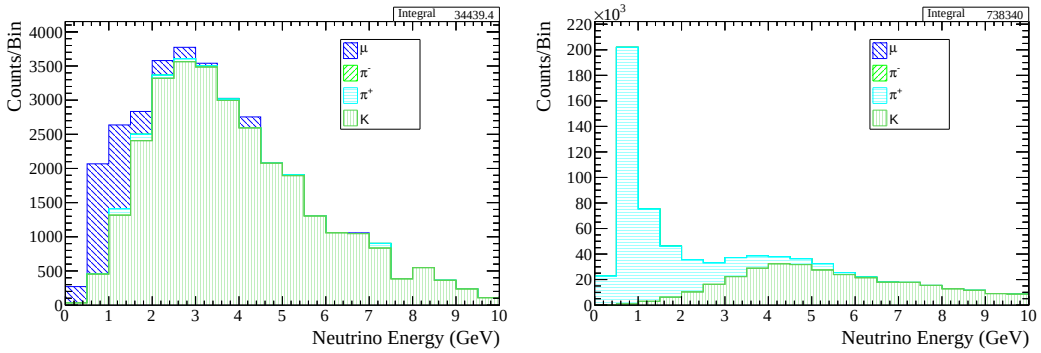

(a) ν_e flux **(b)** ν_μ flux

Figure 2.2.5: The energy spectrum of the ν_e and ν_μ of the beam, broken down into the particle type that decayed to produce the neutrinos.

2.2.4 T2K Data

The data taking for the T2K experiment is split into seven distinct runs. The first four runs took data in neutrino mode only. Runs 5, 6 and 7 took data in a mixture of neutrino mode and anti-neutrino mode. The Protons On Target (POT) and beam power during these periods are shown in Fig 2.2.6. The long time period between run 2 and run 3 was due to the 2012 earthquake which struck Japan, the gap between run 4 and run 5 was due to an accident in the hadron facility.

2.2.5 The ND280

The ND280 off-axis detector is composed of a suite of smaller subdetectors working together to optimise the reconstruction of neutrino interactions. It is located 280 m from the target in order to study the unoscillated neutrino beam. A schematic of the layout of the ND280 detector is shown in Fig 2.2.7.

For most analyses, two Fine Grained Detectors (FGDs) act as target mass for the incident neutrino beam. The two FGDs are sandwiched between a total of three Time Projection Chambers (TPCs) that are designed for studying the kinematics

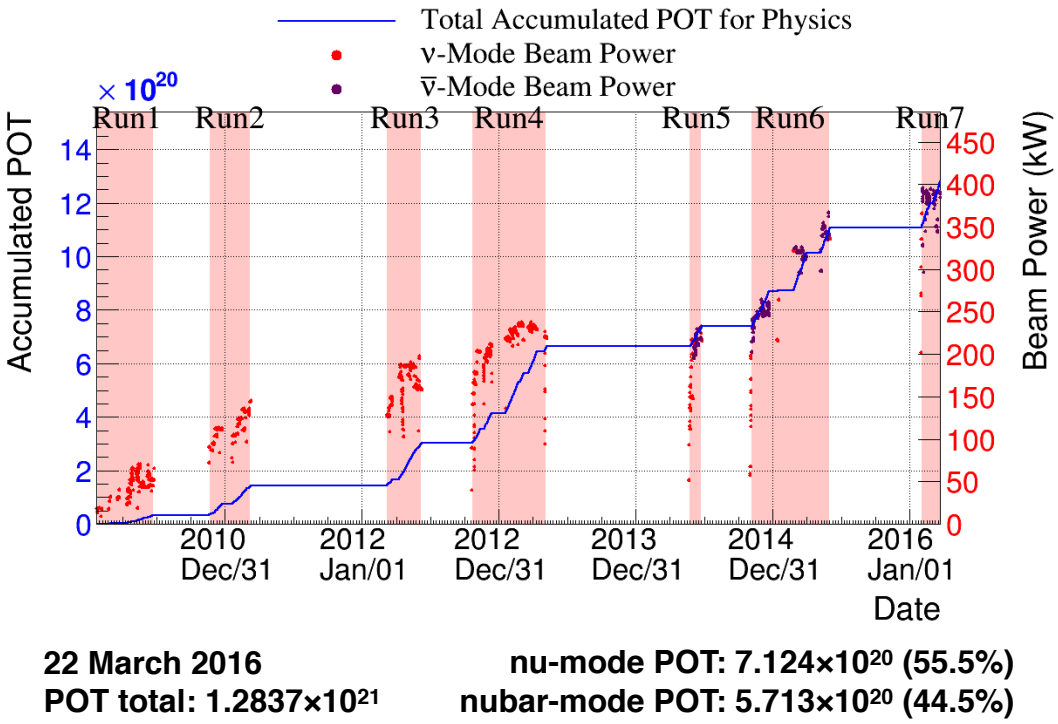

Figure 2.2.6: The accumulated POT for the T2K experiment as a function of time. The red points show the power of the beam for data taken in neutrino mode, the purple points are for anti-neutrino mode.

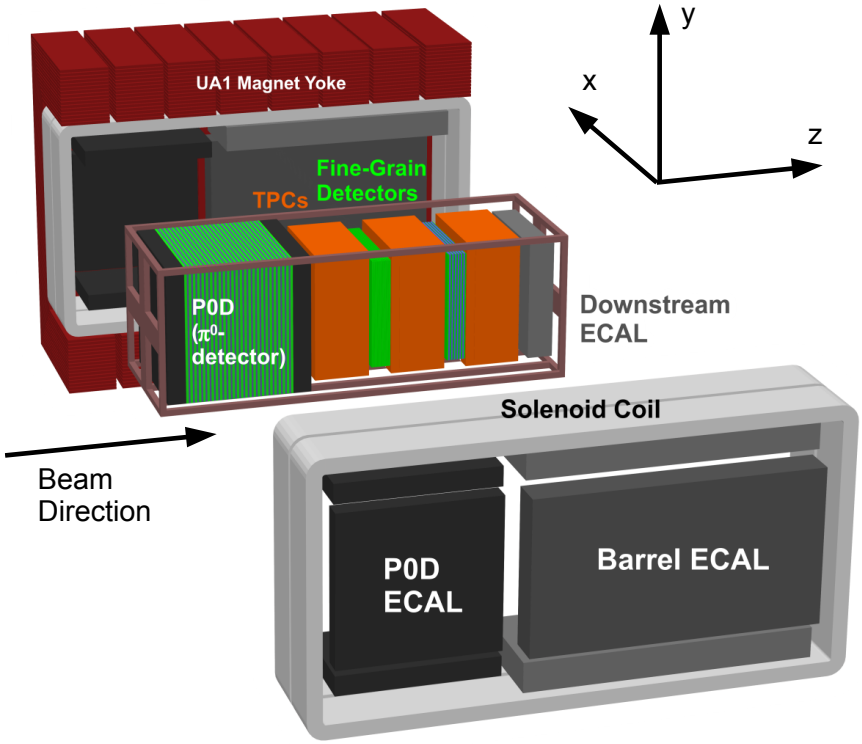

Figure 2.2.7: An exploded schematic of the ND280 off-axis detector [53]

of charged particles. Further upstream of the FGDs and TPCs is the Pi Zero detector (PØD). This was designed to study events containing a π^0 and to measure neutrino interaction cross sections on water. The FGDs, TPCs and the PØD are almost completely surrounded by a series of Electromagnetic Calorimeters (ECals). The goal of the ECals is to compliment the particle identication procedures from the other detectors with a particular focus on detecting and measuring the properties of photons.

The collection of FGDs, TPCs and ECals is known as the tracker region of the ND280. In order to aid the tracker in determination of the momenta and identity of charged particles, a 0.2 T magnet surrounds the tracker. Finally, a Side Muon Range Detector (SMRD) is built into the magnet. This acts as a veto on cosmic rays and particles entering the detector due to neutrino interactions in the surrounding rock whilst also recording tracks leaving the detector at high angles.

2.2.6 ND280 Electronics

Most of the subdetectors in the ND280 complex make significant use of scintillator and wavelength shifting fibre technologies. Excitation photons from charged particles passing through a scintillator bar are captured by wavelength shifting fibres running through the centre of each bar. The scintillation photons are then recorded by multi pixel photon counters (MPPCs). The light collection efficiency of the MPPCs peaks at a wavelength of 440 nm [54]. The fibres shift the frequency of the light passing to 510 nm to be closer to the peak collection efficiency. More detail on the MPPCs can be found in [55].

INGRID, the P0D, the SMRD and the ECals all use identical electronics to read out the MPPC information. The signals from 64 MPPCs are sent to a Trip-T Front end Board (TFB), which integrates the recorded charge from each MPPC and sends the information along to a Readout Merger Module (RMM). As many as 48 TFBs are read by an RMM (although the number varies). The RMMs send

trigger signals to the TFBs and receives the data back. The RMM then sends the data to a computer that collects and processes it.

A Master Clock Module (MCM) is used to receive signals from the accelerator when a neutrino spill will arrive in order to synchronise the electronics. The MCM is also connected to cosmic trigger modules (CTMs) which receive signals from the TFBs (or crate master boards for the FGD [56]) and determines whether a cosmic event has occured in the detector and triggers the readout.

2.2.7 ND280 Software and Data Processing

The information recorded by the ND280 during data taking is processed by several software packages before it is used by analysers. The three main steps taken, in order, are calibration, reconstruction and then reduction.

1. Calibration - When electric charge is deposited at a scintillator bar or TPC node, it is called a hit. The energy deposited by a particle is calculated based on the measured deposited charge. For each bar or node, calibrations are applied to every hit to offset the differences in performance of the bars, the readout and the electronics. Information on how one is these calibrations, the energy equalisation calibration for the ECals, is performed is given in Sec 3.1.

2. Reconstruction - All the hits from within a beam window are then processed by reconstruction software. Tracks and showers from particles, and vertices from neutrino interactions or secondary processes are formed for each subdetector based on the pattern of hits. These are locally reconstructed objects. Lastly, the information from all the subdetectors is combined to fully reconstruct the interactions within the ND280. This creates global tracks that may cross multiple subdetectors.

3. Reduction - The output files from the reconstruction are huge as they contain all the hit information. Consequently, they are processed through a

final software package to reduce the information to a smaller, and more useable format. These are the files used in the cross section ratio analysis.

For Monte Carlo (MC) simulated data, additional steps are required. The neutrino beam and detector response are simulated with custom packages, with the neutrino interactions in the detector handled by either NEUT or GENIE Monte Carlo generators. An illustration of the software chain that processes data and Monte Carlo is given in Fig 2.2.8.

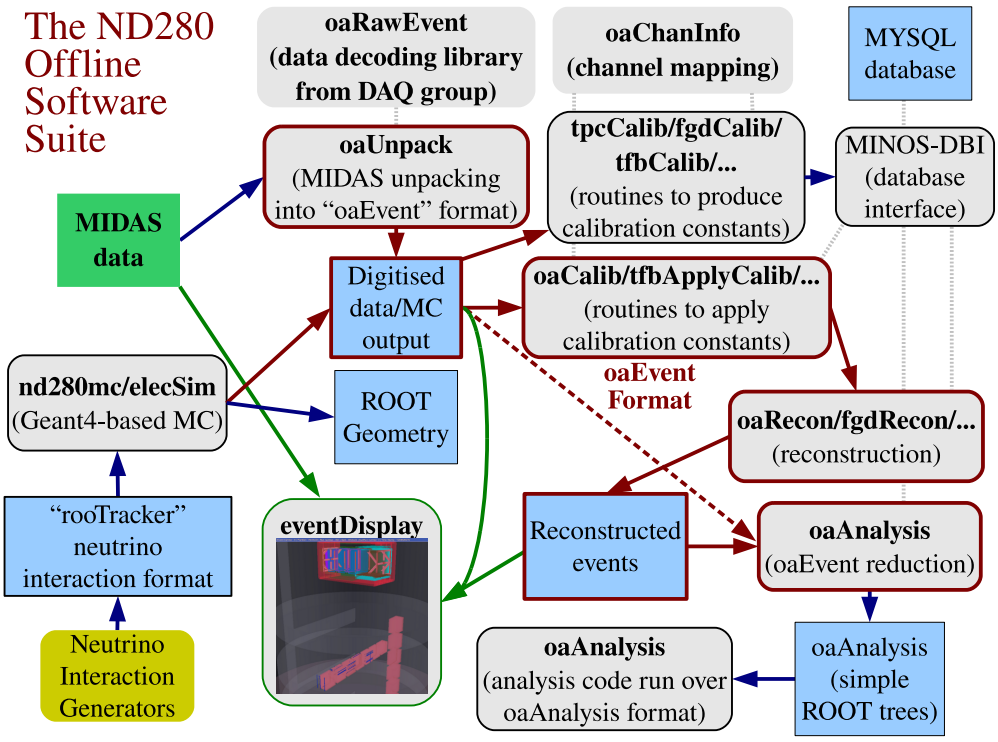

Figure 2.2.8: An illustration showing how the main software packages process data and Monte Carlo. For greater detail on these packages, see [53]

Lastly, the Monte Carlo simulated data can have weights applied to the properties of events based on a random number generator to create so-called toy experiments. For instance, the reconstructed energy can be weighted for many toys to calculate the effect it has on a particular type of event. This is done many times when evaluating systematic uncertainties.

2.2.8 ND280 Magnet

The ND280 off-axis detector is encased in the recycled UA1/NOMAD magnet from CERN. This provides a 0.2 T dipole manetic field in order to curve the trajectories of charged particles travelling through the ND280 detector, allowing for measurement of the momenta and charge with good resolution. The two half yokes of the magnet consist of eight C-shaped elements designed, when combined, to provide a fairly uniform magnetic field across the detector. The magnetic flux density for a weaker field of 0.07 T in the TPC region is shown in Fig 2.2.9 which scales linearly to 0.2 T [53]. This shows a roughly homogenous field near the centre of the TPC with slightly larger deviations nearer the edges.

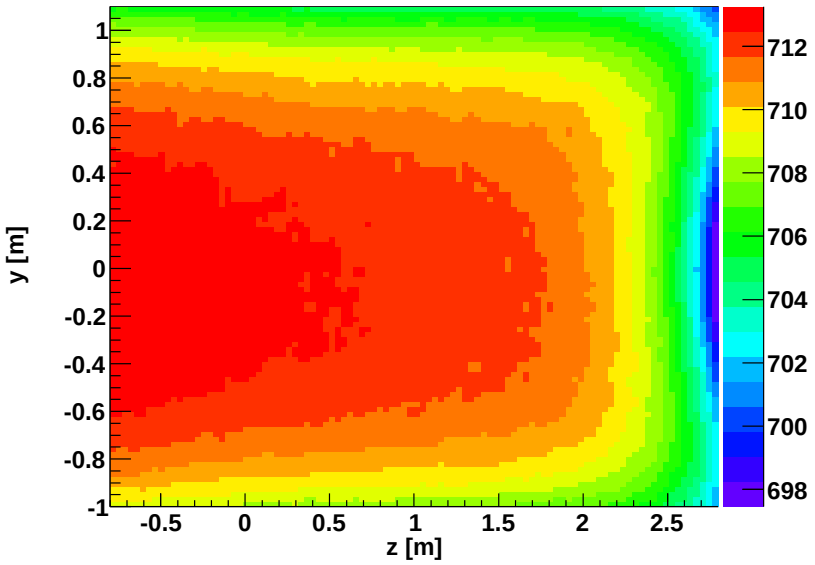

Figure 2.2.9: The mapped magnetic field of the central basket region of the TPC. The colours shown represent the strength of the magnetic field, with values given on the z-axis in units of Gauss. The neutrino beam enters the TPC from the negative z-direction [53]. These measurements were taken with a magnetic field strength of 0.07 T compared to 0.2 T during data taking. The shape of the magnetic field distribution remains the same at higher values. For reference, the TPCs are 2.4 m long in the y-direction and 1.0 m in the z-direction.

2.2.9 Fine Grained Detectors

The ND280 off-axis detector has two fine grained detectors (FGDs) that act as target mass for incoming neutrinos, as well as the tracking of charged particles coming from neutrino interactions. The FGDs consist of layers of extruded polystyrene scintillator (doped with 1 % PPO and 0.03 % POPOP [56]) oriented perpendicular to the beam direction. The layers alternate between bars oriented in the x and y directions, to facilitate the tracking of charged particles. When a charged particle passes through a scintillator bar, it excites the molecules and de-excitation photons are emitted. These photons are captured by wavelength shifting fibres that run down the centre of each bar. One end of these fibres is mirrored and the other leads to a MPPC, which records the signal produced from scintillation in the bar and sends the information along to the read-out electronics.

Both FGDs are 1.1 tonnes of effective neutrino target and have dimensions 2.300 m $\times$ 2.400 m $\times$ 0.365 m (width $\times$ height $\times$ depth in the beam direction) [56]. The most upstream FGD (FGD1) has 30 layers of bars totalling 5,760 scintillator bars whilst the second FGD (FGD2) only has 14 layers. FGD2 is the same overall size as FGD1 but with water in between each layer of scintillator, with half as many layers as FGD1. The water will also act as a target for neutrino interactions. A subtraction of measured interaction cross sections on FGD2 and FGD1 allows for measurements of interaction cross sections on carbon and on water. An image of an FGD is shown in Fig 2.2.10.

2.2.10 Time Projection Chamber

The two FGDs are separated by a time projection chamber (TPC), with an additional TPC before and after the FGDs to make a total of three. These were conceived to have multiple functions; determining the number and orientation of charged particles traversing the detector, measuring the momentum and charge of the particles, and as a means of identifying the types of the particles.

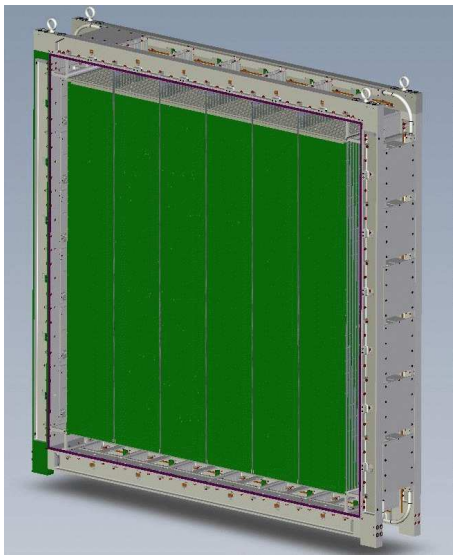

Figure 2.2.10: View of an FGD without the cover. Running perpendicular to the beam direction are the scintillator modules (green) [53]

The TPCs use argon gas that acts as a drift gas. This is stored in an inner box, insulated by an outer box filled with carbon dioxide gas. A central cathode panel creates a uniform electric field across the drift volume of the TPC that is roughly aligned with the field produced by the magnet [57]. The argon gas produces ionisation electrons when a charged particle passes through. Due to the electric field from the central cathode, these electrons drift through the gas away from the cathode towards one of the readout planes. The drift electrons are then sampled and multiplied with micromegas detectors [58]. The micromegas detectors are grouped into 72 modules, with the central cathode placed after the first 36 modules. A schematic of a TPC is shown in Fig 2.2.11, the outer dimensions are 2.3 m $\times$ 2.4 m $\times$ 1.0 m.

The pattern and timing of the signals is used to form a 3D image of the charged particle crossing the detector. The curvature of the trajectory in the magnetic field is used to establish the charge of the particle that created it and calculate its momentum. In addition to this, the number of electrons recorded at each module can be used to calculate the rate of energy loss of the particle. Combining all this

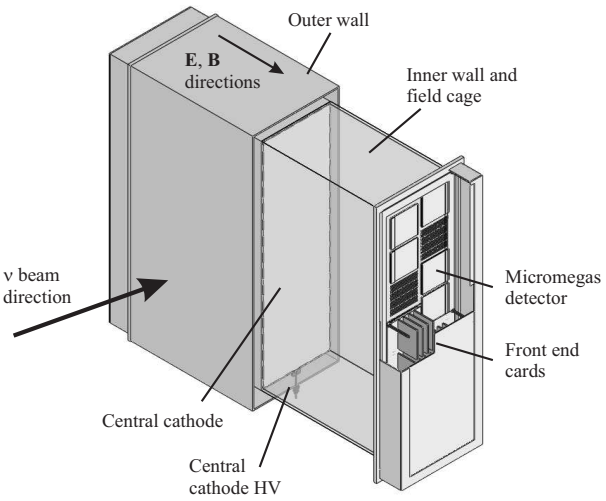

Figure 2.2.11: Drawing showing a simplified layout of a TPC [53]

information means that the TPCs prove very powerful at identifying the particles that travel through them.

2.2.11 Electromagnetic Calorimeters

The description of the electromagnetic calorimeters is more detailed than the other subdetectors to accomodate the calibration work described in Sec 3.1 and Sec 3.2.

The electromagnetic calorimeters (ECals) surround the FGDs, TPCs and the PØD. Like the FGDs, the ECal uses plastic scintillator bars. The primary goal of the ECal is to identify photons and to measure their direction and energy as they leave the tracker area of the detector. This is particularly useful for the detection of $\pi^0 \rightarrow \gamma\gamma$, since the TPCs are insensitive to neutrally charged particles. A secondary function of the ECals is to compliment the particle identification performed by the TPCs, the most improvement being found at energies where certain particles have similar rates of energy loss (i.e. muons and pions or elec-

trons and protons). The combination of all ECal modules provides near complete coverage of particles leaving the inner detectors.

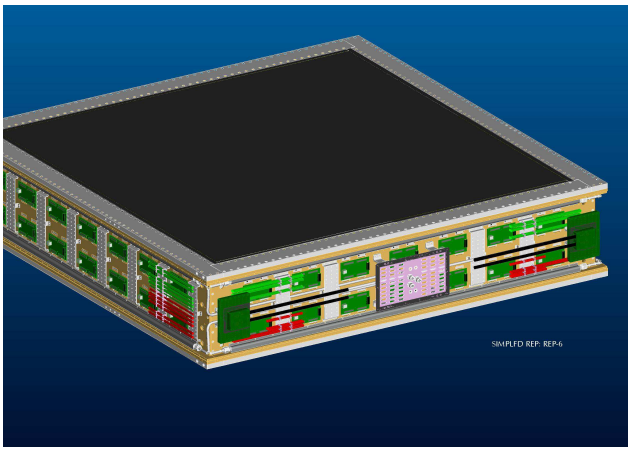

Figure 2.2.12: An external view of an ECal module. The scintillator bars are alligned in the horizonal direction [53]

The ECal can be broken down into three different types: the Barrel ECal containing six modules with 31 layers of scintillator bars, the PØD ECal containing six modules with 6 scintillator layers, and the downstream ECal (DS ECal) consisting of one module with 34 scintillator layers. One of these modules is shown in Fig 2.2.12. The bars in the ECal modules are mixtures of double and single-ended bars [54]. The double-ended bars have a readout MPPC at both ends of the bar, the single-ended bars are mirrored at one end and are read out by an MPPC at the other end.

The Barrel ECal modules use bars in the x, y, and, z directions to surround the tracker on the sides parallel to the beam to catch particles escaping perpendicular to the beam direction. The bars in the z direction are 3.84 m long and use a double-ended readout. The bars in the x and y directions are 1.52 m and 2.36 m long respectively, and both utilise a single-ended readout.

The DS ECal uses only double-ended bars that have alternate layers in the x and y directions. The bars run perpendicular to the beam direction in order to catch

particles escaping downstream of the tracker. All the bars in the DS ECal are 2.04 m long.

The PØD ECal modules use single-ended readout bars only, which are arranged parallel to the beam (z) direction. These surround the PØD instead of the tracker and are 2.34 m long.

2.2.12 Pi Zero Detector

The Pi Zero Detector (PØD) was designed with the aim of helping to understand one of the largest backgrounds at the Super Kamiokande detector; neutral current events that produce a π^0 i.e. $\nu_\mu + N \rightarrow \nu_\mu + N + \pi^0$. To achieve that understanding, a water target was needed for the PØD, the same as in SK. The PØD uses planes of scintillator bars in the x and y directions. In between these layers are fillable water bags and lead and brass sheets that act as targets [59]. This allows for a subtraction method between water-in and water-out to determine the cross sections on water. The scintillator bars, like the FGDs, are read out at one end using wavelength shifting fibres.

The PØD has a total of 40 layers with 134 bars running in the y direction and 126 in the x direction. This arrangement has a fine enough segmentation to reconstruct charged particle tracks, and electromagnetic showers due to $\pi^0 \rightarrow \gamma\gamma$. The active region of the PØD has dimensions 2.1 m $\times$ 2.2 m $\times$ 2.4 m and is located upstream of the FGDs and TPCs.

2.2.13 Side Muon Range Detector

The Side Muon Range Detector (SMRD) is built into the magnet of the ND280 detector, and so surrounds the ECals and the tracking detectors. The SMRD has three primary functions: record and measure the momenta of muons exiting the

inner detectors, trigger cosmic rays entering the ND280, and identify tracks entering the ND280 from beam neutrinos interacting in other materials surrounding the ND280 [60].

The SMRD uses 440 scintillator modules inserted in the air gaps between the steel plates of the magnet flux return yokes. There are 16 of these flux return yokes and they form a ring that surrounds the inner detectors on four sides. As with the other ND280 subdetectors, the SMRD scintillators are read out using wavelength shifting fibres attached to Multi Pixle Photon Counters (MPPCs).

2.2.14 INGRID

The INGRID detector (Interactive Neutrino GRID), is an on-axis detector designed to monitor the beam centre and intensity. At nominal beam intensity, this is acheived daily using high-statistics samples of neutrino interactions on the iron in INGRID. The measurement of the beam centre is achieved at 0.4 mrad precision at the near detector pit 280 m downstream of the beam production point. Unlike the other detectors in the near detector complex, INGRID is not magnetised, meaning that charge discrimination is not possible.

INGRID is made up of 14 identical modules arranged in a cross shape along the x and y directions, with two additional modules located away from the beam center, as shown in Fig 2.2.13. These two additional modules check the axial symmetry of the beam. All 16 modules use alternating layers of tracking scintillator planes and iron plates, surrounded by veto scintillator plates to reject interactions from outside the detector. The total mass of each module is 7.1 tonnes, allowing for the high-statistics samples needed to achieve INGRID's Physics goals.

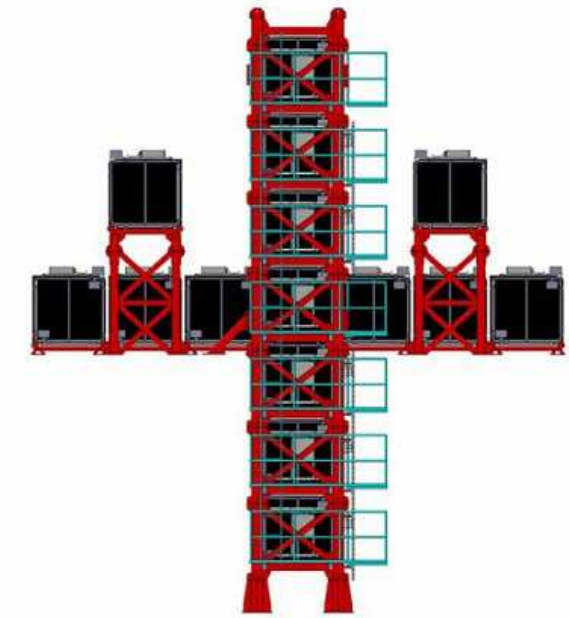

Figure 2.2.13: A schematic of the INGRID on-axis detector [53]

2.2.15 Super Kamiokande

The T2K far detector, Super Kamiokande (SK), is located 295 km away from the beam production point, 1,000 m below ground, in a mine under Mount Kamioka. Being so far underground means that the flux of cosmic rays entering the detector is reduced significantly. SK uses Cherenkov radiation to detect charged particles created by neutrino interactions on water within the detector. A schematic of the detector is shown in Fig 2.2.14.

The SK detector contains 50,000 tonnes of ultra pure water housed in a large cylindrical vessel, which acts as target for neutrino interactions. The detector is made of two parts; an inner and outer detector, divided by a cylindrical support structure. The inner detector holds 36,000 tonnes of ultra pure water and has 11,146 inward facing Photo Multiplier Tubes (PMTs) [61]. The outer part acts as a veto on incoming charged particles and has 1885 outward facing PMTs.

When a charged particle travels through the water in SK faster than the speed of

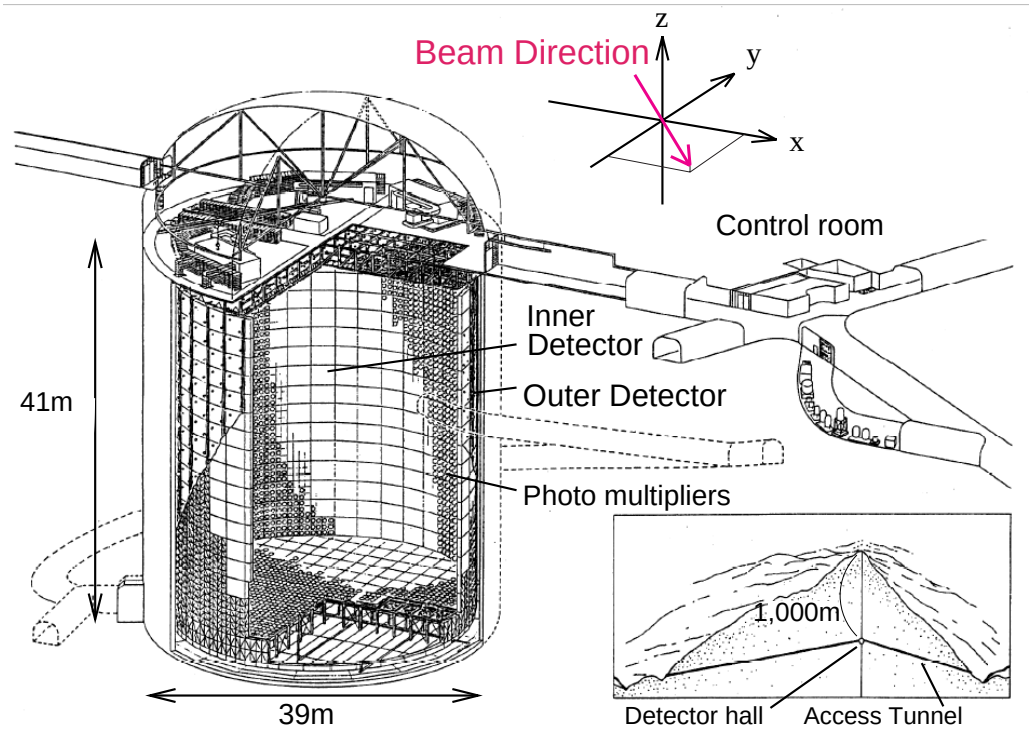

Figure 2.2.14: A schematic of the Super Kamiokande experiment [53]

light in water, it produces Cherenkov radiation in a cone centred on the direction of the charged particle. This cone of light can be detected by the PMTs, creating a ring image for contained events. The properties of each ring can be used to determine the type of particle that produced it, and the energy and direction of the particle. Fig 2.2.15 shows the differences between muon-like rings (left) and electron-like rings (right). As the electrons are more likely to scatter in the detector, they produce more diffuse rings, whereas the rings produced by muons are clearer. This can be used to distinguish between the two particles, whilst the amount of light emitted can be used to calculate the energy of the particle.

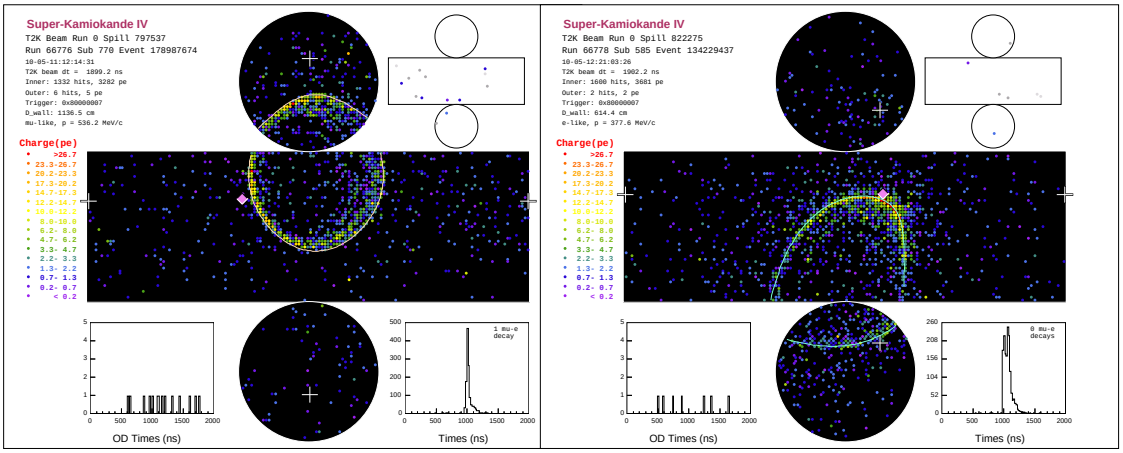

Figure 2.2.15: A muon-like event (left) and an electron-like event (right) in the Super Kamiokande detector. The electron-like ring is fuzzier than the muon-like ring due to electrons having a shorter mean free path than muons [53]

The SK detector has other goals beyond T2K, such as searches for proton decay, studying solar and atmospheric neutrinos, and supernovae relic neutrinos.

Chapter 3

Studies with Electromagnetic Calorimeter

3.1 ECal Calibration

3.1.1 Overview

All the subdetectors in the ND280 detector require calibrating to ensure that each bar or node in the subdetector performs consistently with the others. The focus here will be the energy equilisation calibration of the ND280 ECals. For the relevant detail on the detector, refer to Sec 2.2.11.

The purpose of this calibration is to ensure that all the scintillator bars in the ECals record the same amount of energy for a particle passing through. This is necessary as slight differences in each bar could result in different amounts of energy recorded, which in turn could affect the measurements performed by the ND280.

3.1.2 Data Sample

To measure the differences between each bar, a well understood control sample with high statistics is needed. Cosmic muons are ideal for this as they are abundant and act like MIPs (Minimum Ionising Particle), meaning that they deposit a roughly equal amount of energy in each bar as they pass through. To select MIP-like tracks, only cosmic tracks that go all the way through an ECal are used. A schematic showing a charged particle passing through multiple bars is shown in Fig 3.1.1.

The energy recorded for each hit needs two corrections applied to it; one for the angle from perpendicular of the track passing through the bar and the other for the distance the hit was from the MPPC at the end of the bar. The correction for track angle is necessary as a particle that travels through the bar at a high angle will have a longer path in the scintillator and so will deposit more energy. The correction is calculated by determining the path length of the particle inside the bar. The correction for the distance the hit was from the sensor is required as

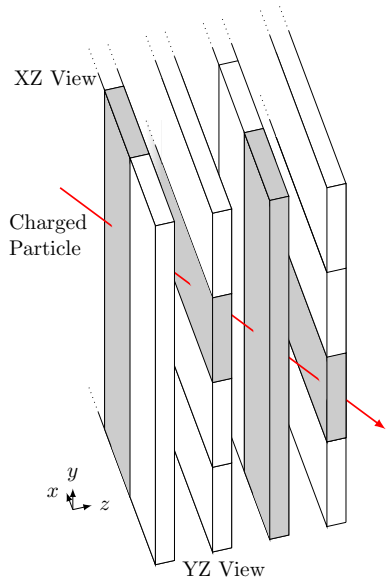

Figure 3.1.1: A schematic showing a charged particle traversing an ECal.

the light travelling down the fibre in the bar attenuates and so hits further from the sensor will have a lower recorded energy. The average energy recorded in bins of distance from the sensor is plotted and fitted with a double exponential [54]. The fit equation is shown in Eq 3.1.1 for current recorded by an MPPC, I_{MPPC}, due to a hit x m from the sensor. The other parameters are free parameters used in the fits and are used to calculate the correction.

$$I_{\text{MPPC}} = A\left(\frac{1}{(1+R)}e^{-x/\lambda_1} + \frac{R}{(1+R)}e^{-x/\lambda_2}\right) + B \tag{3.1.1}$$

The method for the energy equalisation calibration was inherited from the ND280 calibration group who also performed this calibration for T2K runs 1-3.

3.1.3 Procedure

The energy spectrum for each bar is plotted by recording the energy of all hits (corrected for path and attenuation) originating from cosmic muons. An exmple

of this is shown in Fig 3.1.2 for a bar in the DS ECal. The energy of a hit in these plots is given in Photon Equilivent Units (PEU), which is related to the number of photons recorded by the MPPCs. The energy spectrum for each bar is fitted with a Landau-Gaussian distribution and the most probable value of the fit is used as a measure of the response (the average energy recorded) of that bar, $\mathcal{E}$. This quantity can be calculated for a single bar, or groups of bars. A Landau-Gaussian is used to take into account both the energy spectrum of cosmic muons, described by a Landau distribution, and the response of the bar, described by a Gaussian distribution.

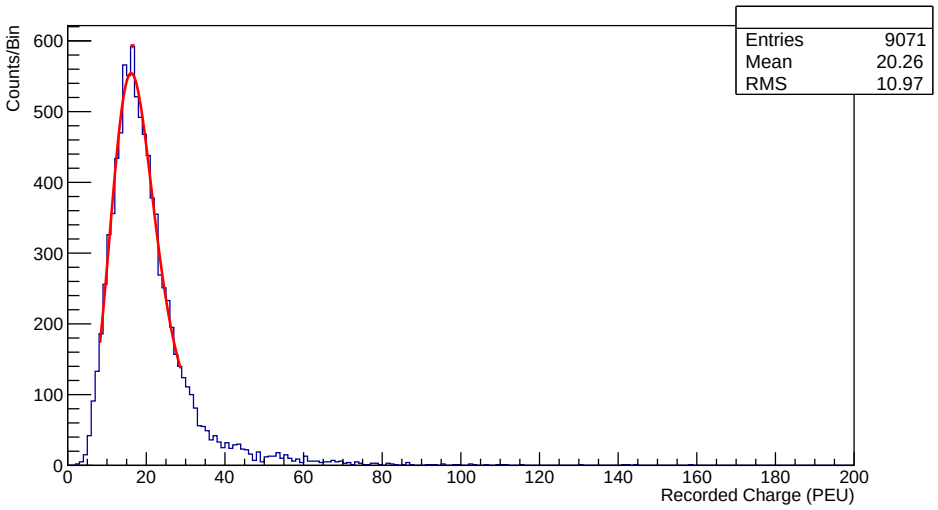

Figure 3.1.2: The energy spectrum for cosmic muons shown in the blue histogram as measured by a bar in the ECal. The red curve is a fitted Landau-Gaussian distribution, the parameters of which determine the response of the bar.

The equation for the probability density function, $p(x)$, for a Gaussian distribution and Landau distribution are given in Eq 3.1.2 and Eq 3.1.3 respectively. The fit to the energy spectrum is the convoluted sum of these two distributions. The parameters μ and σ are the mean and standard deviation of the Gaussian distribution.

$$p(x) = \frac{1}{2\pi\sigma^2} e^{-\frac{(x-\mu)^2}{2\sigma^2}} \tag{3.1.2}$$

$$p(x) = \frac{1}{\pi} \int_0^\infty e^{-t\log t - xt} \sin(\pi t) dt \tag{3.1.3}$$

For each bar, i, a fractional correction, c_i, is calculated by finding the average energy recorded by that bar, $\mathcal{E}_i$ and dividing by the average energy recorded for all the bars of the same orientation and module, $\mathcal{E}_T$, as shown in Eq 3.1.4.

$$c_i = \frac{\mathcal{E}_i}{\mathcal{E}_T} \tag{3.1.4}$$

These calibration constants are calculated using through-going cosmic muons and applied to beam data on a hit-by-hit basis.

3.1.4 Energy Equalisation

As a check of the procedure, the calculated constants are applied back to the energy spectra for each bar, as in Eq 3.1.5.

$$E' = \frac{E}{c_i} \tag{3.1.5}$$

The response of all the bars should be much more uniform with these applied. The results of this are shown in Fig 3.1.3 for T2K runs 5 and 6. The green points represent the spread in response for different bars in the ECals before the bar equalistaion calibration is applied. The blue points show the spread after the calibration is applied. The horizontal blocks in channel ID correspond to different RMMs while the two different groupings in bar response correspond to double or single-ended bars. The two missing RMMs correspond to the P0D ECal RMMs that are not calibrated with this method.

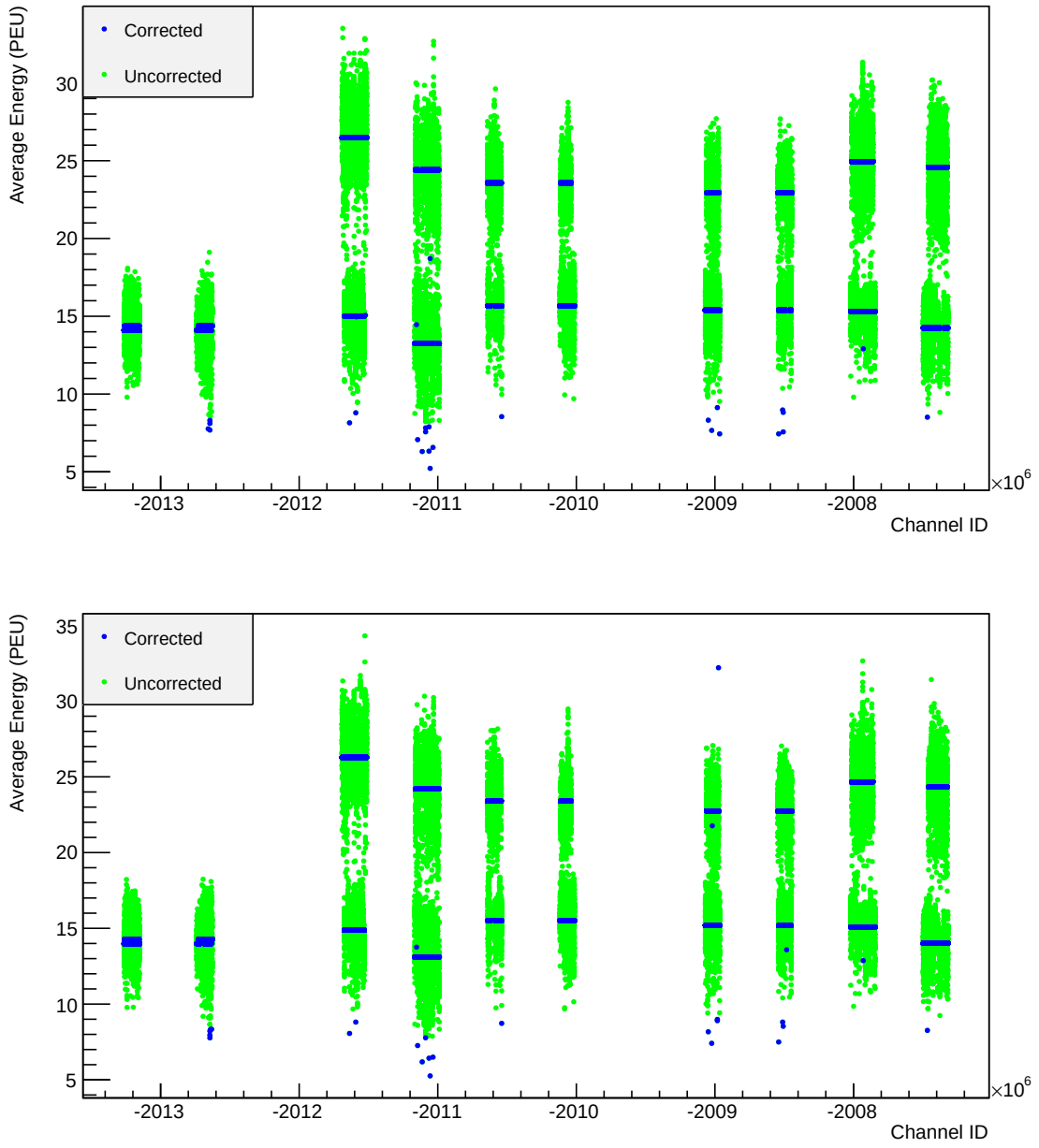

Figure 3.1.3: The average energy recorded for each bar (shown as channel ID) is shown as a scatter in green. The blue points show the same distributions with the calibration constants applied. The top plot was created using run 5 data whilst the bottom plot was made using run 6 data. The blocks in channel ID correspond to the different RMMs (RMM 2 and 7 are missing as these are for the P0D ECal). The RMMs with two areas of response are those that contain a mixture of double and single-ended bars, with the single-ended bars collecting more energy on average.

A more robust test of the energy equalisation calibration is to apply them at the hit level instead of to the whole distribution. The constants are applied back to a statistically independent sample of cosmic muons as a better cross check. Additional corrections are also applied to take into account the differences between double and single-ended bars and the differences in the modules. Each module is scaled to have the same average response as the DS ECal as it has been the most stable during running. The distribution shown in Fig 3.1.4 shows the spread in uncalibrated responses and Fig 3.1.5 shows the calibrated responses, verifying the procedure.

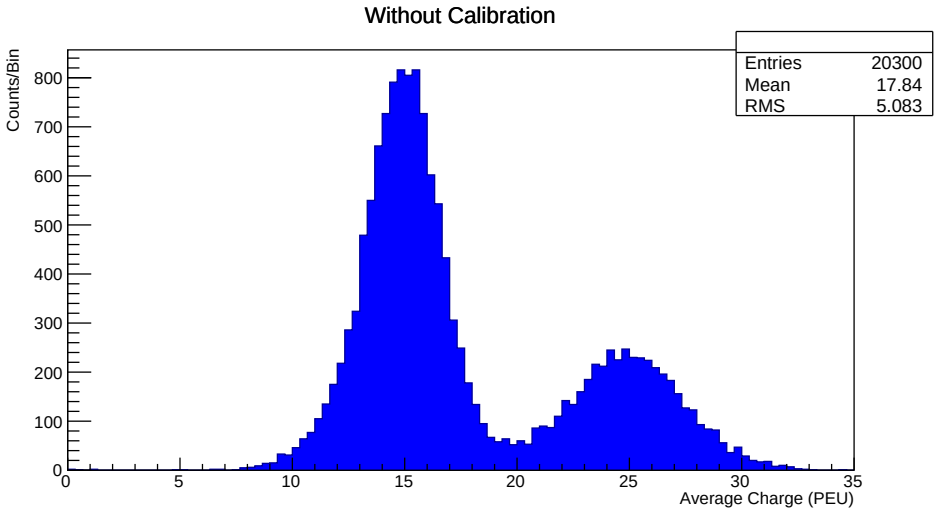

Figure 3.1.4: The average response for all the bars with no calibrations applied. The two different peaks correspond to bars with single and double-ended readouts.

A final check of the stability of the calibration constants is performed by comparing one set of constants with another. This is shown in Fig 3.1.6. The red and blue histograms show the 1 - run 5 and 1 - run 6 calibration constants respectively for all the bars in the barrel ECal and DS ECal. These are the constants that are applied to the data. The black histogram shows the difference between the run 5 and run 6 constants (normalised to the run 5 constants). The narrow peak

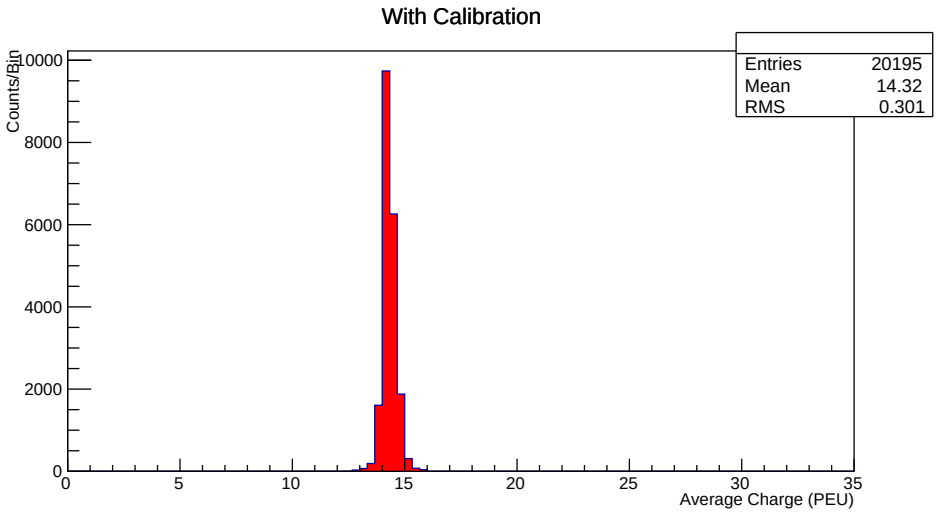

Figure 3.1.5: The average response for all the bars with the bar equalisation calibration applied and additional calibrations to equalise the different modules and bar types.

for the difference in these constants shows the stability of these constants across different runs.

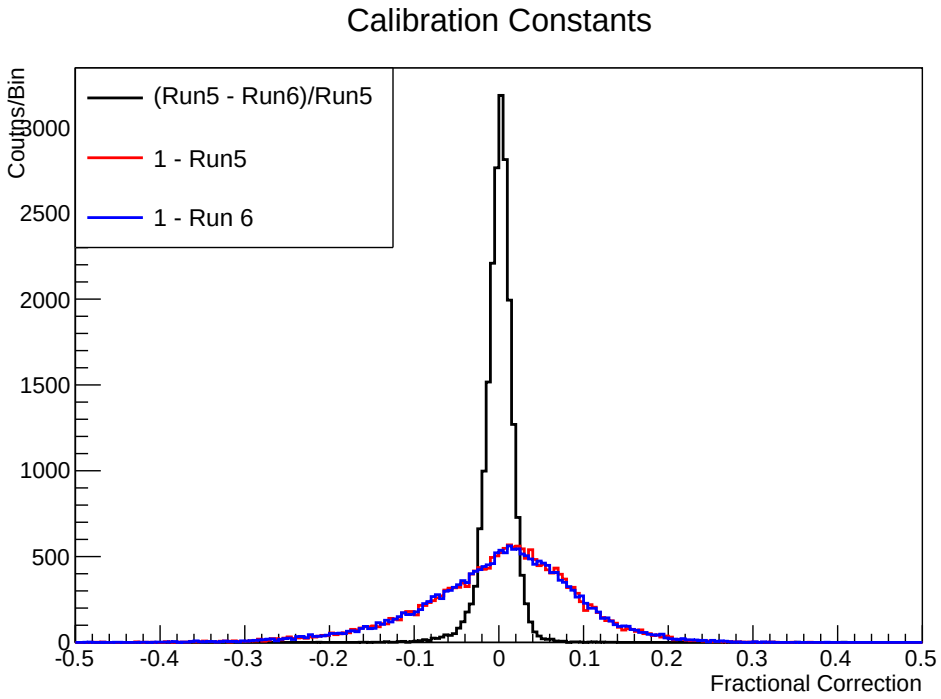

Figure 3.1.6: The run 5 calibration constants (blue) compared with the calibration constants for run 6 (red). The black histogram shows the calculation of (run 5 - run 6)/run 5 calibration constants.

3.2 ECal Scintillation Degradation

3.2.1 Overview

The ECal scintillator bars were made at FNAL from extruded polystyrene doped with organic fluors at concentrations of 1% PPO and 0.03% POPOP [54]. The performance of these bars is expected to gradually decrease with use and time. This effect needs to be parameterised to correct for reduced amounts of energy recorded per hit in later T2K runs. The different modules have bars constructed to have varying lengths, with some modules having double ended readout and others having single ended readout. For this reason, and the fact that the degredation of the bars is heavily dependent on the temperature, the different bar types are treated separately in this study. More detail on the bars can be found in the ECal JINST paper [54].

The degredation of the bars can be attributed to several effects [62]:

1. Thermo-oxidative chemical reactions resulting in the creation of peroxides which absorb scintillating radiation, essentially making the bars more opaque.

2. Mechanical degradation due to chemical stress which can cause surface cracks that disrupt light transmission.

3. Diffusion of low molecular components of the formulation which can cause both surface and internal defects. This can cause yellowing of the scintillator increasing opacity. Cracking can also arise that may disrupt light transmission.

More information on the processes behind the ageing can be found in [63]. Which of these cause the degradation in the ND280 ECal bars is not discussed here. Instead a parameterisation is given such that the effects can be extrapolated to the future and a correction can be applied to any data taken to normalise to a chosen

date. The temperature dependance of the scintillator ageing is discussed in [62]. Scintillator bars were held at a constant temperature for an extended period to test the ageing as a function of temperature. This was done for 45 °C, 65 °C and 85 °C with a significantly higher rate of light loss recorded at 85 °C.

A similar study has already been performed by the MINOS collaboration which uses the same scintillator technology as the ND280 detector. They report a 3.5% loss of light yield per year in the near detector and 3.0% in the far detector over a seven year period with the two detectors running at different temperatures. The loss of light yield follows an exponential form and the temperature dependence was found to be 0.2 ± 0.06 %/ °C in the near detector and 0.4 ± 0.07 %/ °C in the far detector [64].

3.2.2 Procedure

The sample used for studying the ageing of the scintillator bars is the same as is used for the energy equalisation. This sample was described in Sec 3.1.2.

After being corrected for the path and attenuation of the track, the recorded charge of all hits for a particular bar type is plotted. This distribution is then fitted with a Landau-Gaussian function, the MPV (Most Probable Value) of which gives the average recorded charge by that bar type in Photo-Equivilent Units (PEU). An example of the charge distribution and the fitted Landau-Gaussian function is shown in Fig 3.2.1.

This procedure is repeated for different time periods and the Laundau Gaussian fit parameters are studied for each period to test for variations with time. The MPV and width of the distribution are of particular interest to describe the rate of degredation and the affects this has on the data. The uncertainty on the MPV is calculated by dividing the fit width, w, by the square root of the total number of hits, as shown in Eq 3.2.1. The average charge recorded as a function of T2K

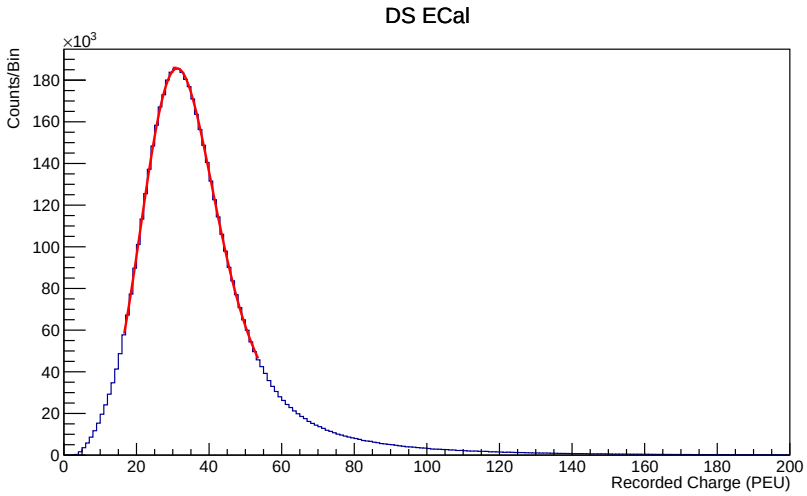

Figure 3.2.1: The recorded charge distribution for run 1 cosmic muons for all bars in the DS ECal, fitted with a Landau-Gaussian. The MPV of the fit is used as a measure of the average charge recorded. This spectrum can in principle be found for a single bar or group of bars.

run is shown in Fig 3.2.2.

$$\sigma = \frac{w}{\sqrt{N}} \tag{3.2.1}$$

The procedure is then repeated for bins of hit time since the T2K runs do not correspond to actual times.

3.2.3 Results

To get a clear picture of the characteristics of the ECal scintillator bar degradation, examine the parameters of the fits to the charge distributions for different bins of time. Fig 3.2.3 shows the average response of the ECal modules as a function of time. Each time bin corresponds to roughly one month.

It is possible to see by eye that the response gradually decreases with time, as would be expected. To quantify this, the plots are fitted with a line (as shown in

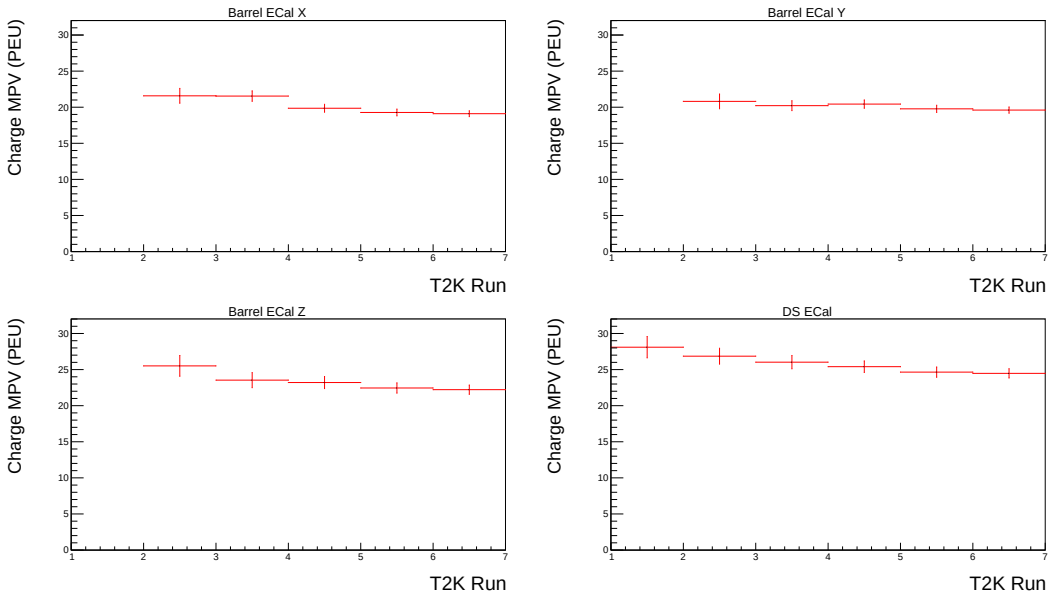

Figure 3.2.2: The average recorded charge per T2K run, calculated by finding the MPV of a Landau-Gaussian fit to the charge distribution for each run. Note that the Barrel ECal modules were not in place during run 1.

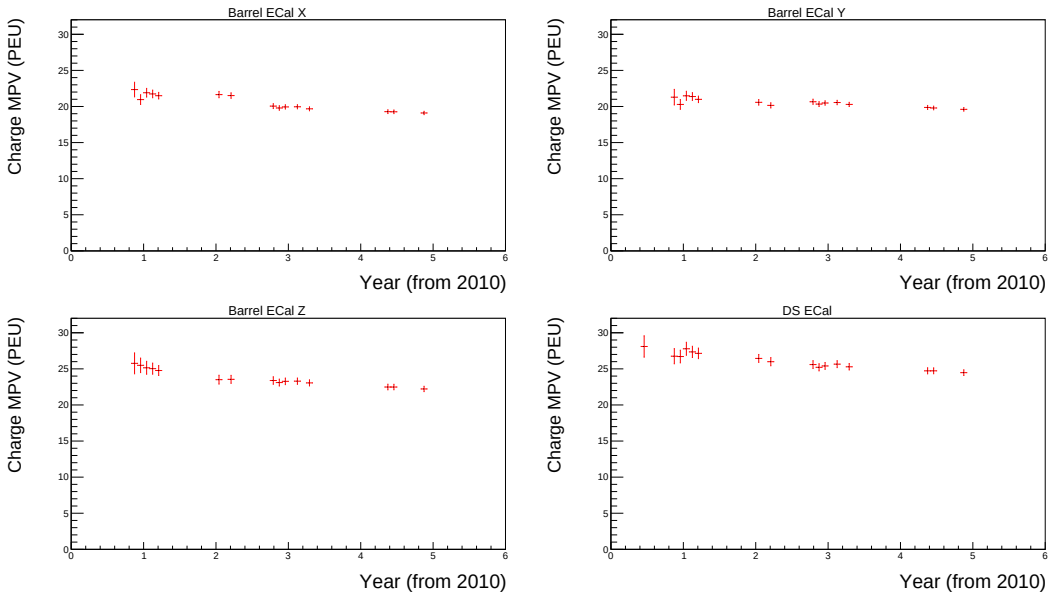

Figure 3.2.3: The average recorded charge for different time periods. Each data point corresponds to roughly a month. The bars are grouped by module and orientation.

Fig 3.2.4) and an exponential (shown in Fig 3.2.5). These fit parameters can be used to estimate the ECal response in the future or to apply a hit-level correction to the recorded charge. The fitted equations are shown in Eq 3.2.2 and Eq 3.2.3 (where $\bar{Q}$ is the average charge recorded and t is the number of years from 2010) with fit parameters and their uncertainties shown in Tab 3.2.1 and Tab 3.2.2 for the straight line fits and exponential fits respectively.

$$\bar{Q}_{\text{lin}} = A + Bt \tag{3.2.2}$$

$$\bar{Q}_{\text{exp}} = A + Be^{kt} \tag{3.2.3}$$

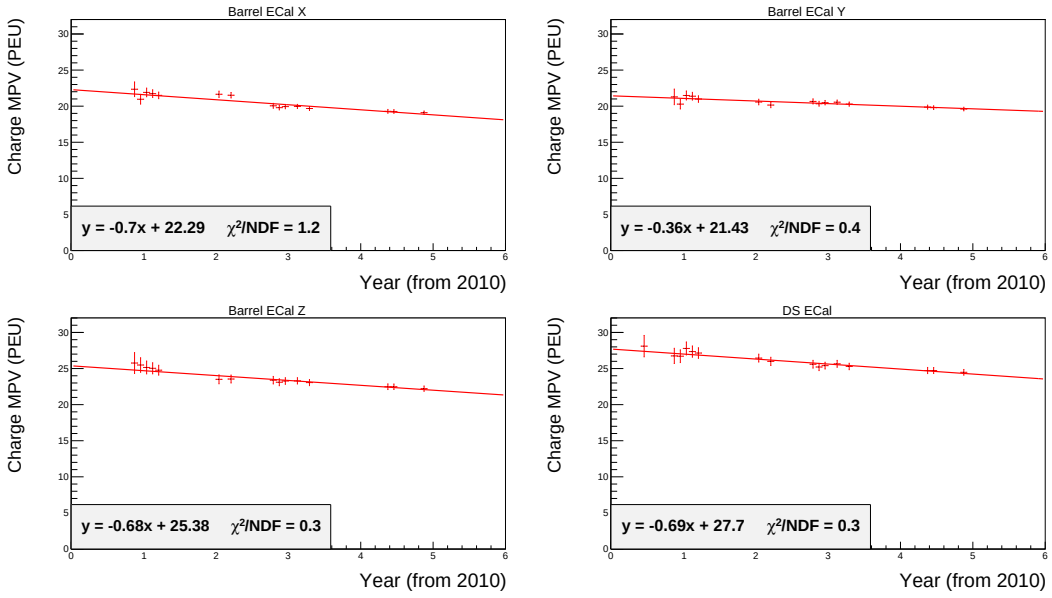

Figure 3.2.4: The average recorded charge for different time periods. Fitted with a straight line to parameterise the rate of degredation.

There should be a small amount of correlation between the data points since the temperature the ND280 operates at changes over the course of a year, which affects the rate of degradation. This analysis does not take these correlations into account when fitting the light yields as a function of time. This will result in the χ^2 of the fits slightly smaller than they would be otherwise.

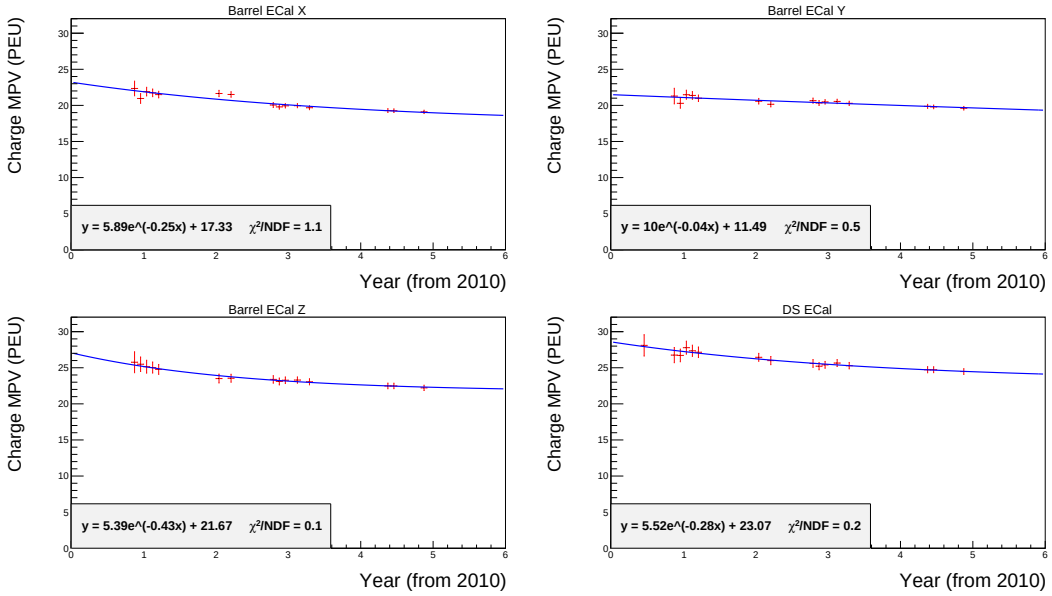

Figure 3.2.5: The average recorded charge for different time periods. Fitted with an exponential to parameterise the rate of degredation.

Module	A	B	χ^2/NDF
DS ECal	27.72 ± 0.38	-0.70 ± 0.11	0.2
BrECal X	22.34 ± 0.27	-0.71 ± 0.08	1.1
BrECal Y	21.51 ± 0.27	-0.38 ± 0.08	0.3
BrECal Z	25.25 ± 0.40	-0.64 ± 0.11	0.2

Table 3.2.1: The fitted parameters to the average charge distributions for the straight line fits. The parameters A and B are explained in Eq 3.2.2

Module	A	B	k	χ^2/NDF
DS ECal	23.29 ± 2.30	5.53 ± 1.63	-0.31 ± 0.24	0.1
BrECal X	17.90 ± 1.70	5.92 ± 1.22	-0.34 ± 0.15	0.8
BrECal Y	2.77 ± 1.78	18.80 ± 12.18	-0.02 ± 0.004	0.3
BrECal Z	21.57 ± 1.12	5.29 ± 0.93	-0.40 ± 0.28	0.1

Table 3.2.2: The fitted parameters to the average charge distributions for the exponential fits. The parameters A, B and k are explained in Eq 3.2.3

Over the plotted time period, it is difficult to fully distinguish the linear and exponential hypothesis. However, a previous study with similar bars recorded an exponential loss in light yield in time [62], and so this is expected to also be the case for the ECal scintillator.

Using these fit parameters it is possible to calculate the percentage drop in response from to 2010 to 2015 for both the line and exponential hypotheses and also estimate the drop in response in future years simply using the fit equation. However, this method will not take into account the large correlation between fit parameters and so will lead to very large uncertainties. Instead, it is better to use these fits to extrapolate to the future simply by extending the fit range and calculating the confidence intervals to give an estimate of the uncertainty on the future response. This is shown in Fig 3.2.6 and Fig 3.2.7 for the linear and exponential fits respectively. This method has the advantage that it will take the parameter correlations into account and the numeric values can be extracted from the fits and limits. The results of this are summarised in Tab 3.2.3.

The other fit parameter of interest is the width of the Landau-Gaussian distribution. This can be informative as to whether the shape of the charge distribution is changing with time. Fig 3.2.8 shows the width against time and Fig 3.2.9 shows the MPV divided by width. There are greater fluctuations in these plots compared to the MPV plots as these variables are less immediately affected by the ageing. This means that for some of the modules, the fits are not good represen-

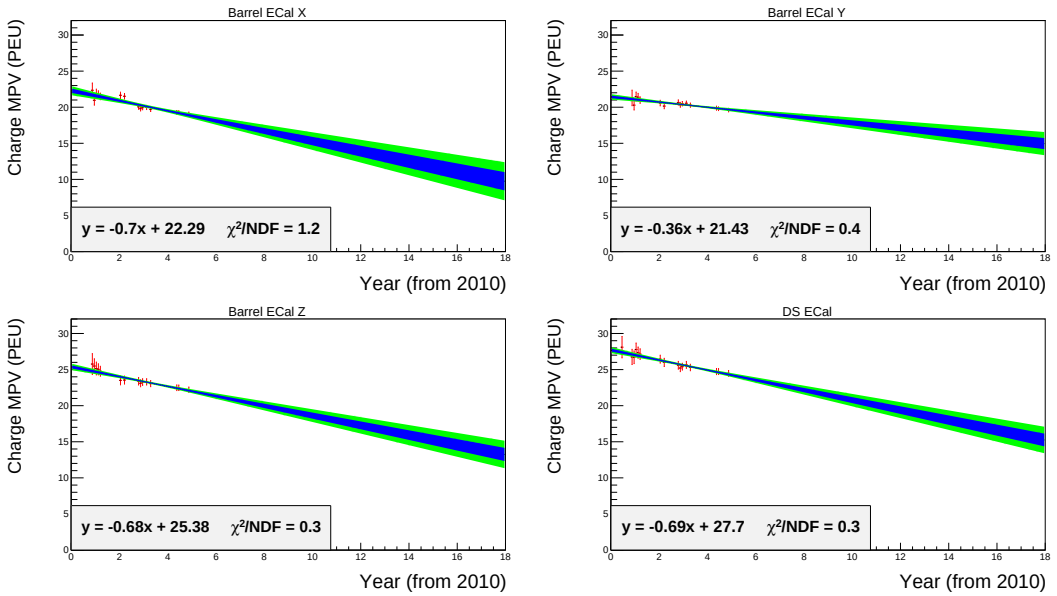

Figure 3.2.6: The linear fits for the ageing extrapolated up to 2028. The blue band shows a 95% confidence interval on this extrapolation and the green band shows a 68% confidence interval.

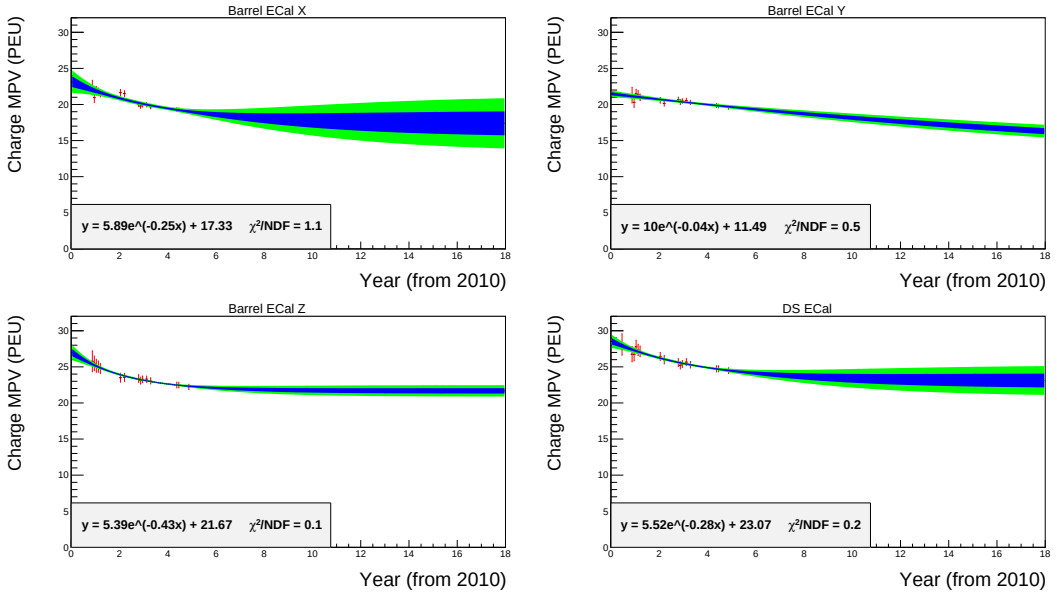

Figure 3.2.7: The exponential fits for the ageing extrapolated up to 2028. The blue band shows a 95% confidence interval on this extrapolation and the green band shows a 68% confidence interval.

Module	$\bar{Q}$ 2010	$\bar{Q}$ 2015 (% drop)	$\bar{Q}$ 2020 (% drop)	$\bar{Q}$ 2025 (% drop)
Linear Fit				
DS ECal	27.7 ± 0.2	24.2 ± 0.1 (87%)	20.7 ± 0.4 (75%)	17.3 ±0.7 (62%)
BrECal X	22.3 ± 0.3	18.8 ± 0.2 (84%)	15.3 ± 0.6 (69%)	11.8 ± 1.0 (53%)
BrECal Y	21.4 ± 0.2	19.6 ± 0.1 (92%)	17.8 ± 0.4 (83%)	16.0 ± 0.6 (75%)
BrECal Z	25.3 ± 0.2	22.0 ± 0.1 (87%)	18.6 ± 0.4 (74%)	15.2 ± 0.7 (60%)
Exponential Fit				
DS ECal	28.5 ± 0.4	24.4 ± 0.1 (86%)	23.4 ± 0.6 (82%)	23.2 ± 0.9 (81%)
BrECal X	23.2 ± 0.8	19.0 ± 0.2 (82%)	17.8 ± 1.0 (77%)	17.5 ± 1.5 (75%)
BrECal Y	21.5 ± 0.2	19.6 ± 0.1 (91%)	18.1 ± 0.3 (84%)	16.9 ± 0.4 (79%)
BrECal Z	27.0 ± 0.4	22.3 ± 0.1 (83%)	21.7 ± 0.3 (80%)	21.7 ± 0.4 (80%)

Table 3.2.3: The average charge recorded at different times in Photon Equivalent Units (PEU) for the different bar types in the ECal using a linear fit and an exponential fit. The values for 2020 and 2025 are calculated by extrapolating the fit range to later times. The percentage response compared to 2010 (roughly when T2K started taking data) is also given.

tations of the data. However, there is still a reasonably clear downward trend in the fitted widths, corresponding to the charge distribution narrowing with time. Looking at Fig 3.2.9 it seems that this is roughly at the same rate as the MPV is decreasing, shown by the relative flatness of the fits.

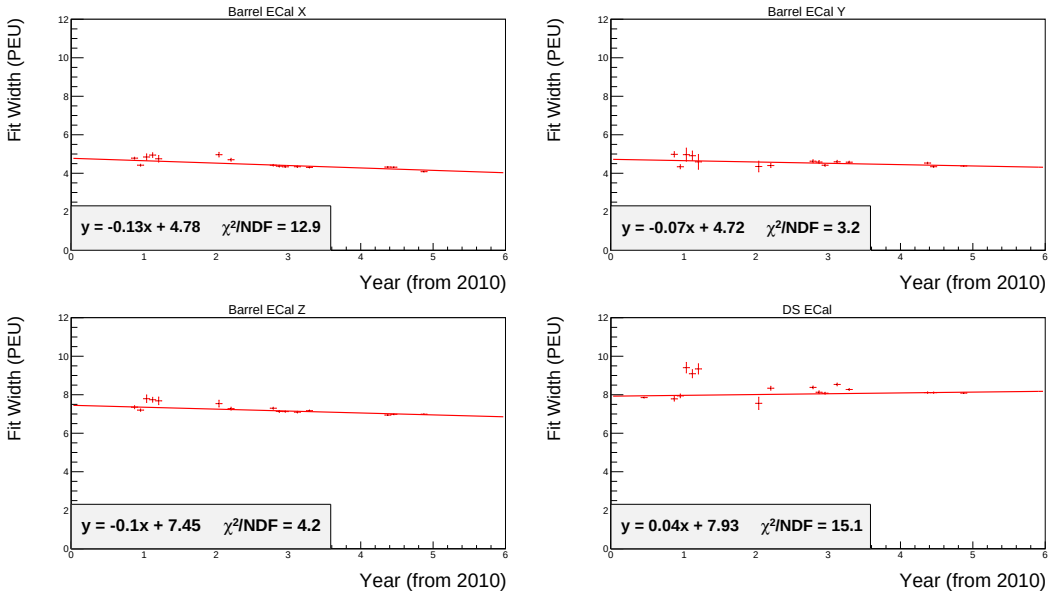

Figure 3.2.8: The width of the Landau-Gaussian fit to the recorded charge distribution for different time periods. Fitted with a straight line to parameterise the rate of degredation. The general downward trend in the data shows that the charge spectrum recorded by the scintillator bars is narrowing as they age.

3.2.4 Summary of Ageing Study

The scintillator ageing can be clearly parameterised by both a linear and an exponential fit. The exponential fit seems to model the data more closely with a lower fit χ^2 and is the model predicted by the literature [62] and previous results [64]. The fit parameters can be used to correct for the affects of the ageing in T2K data by scaling to a particular date. This correction is not currently implemented in T2K analyses but will be in the near future. Additionally, the fits can be used to predict the effectiveness of the ECal modules in the future which can help determine whether they can be reused in future experiments. On

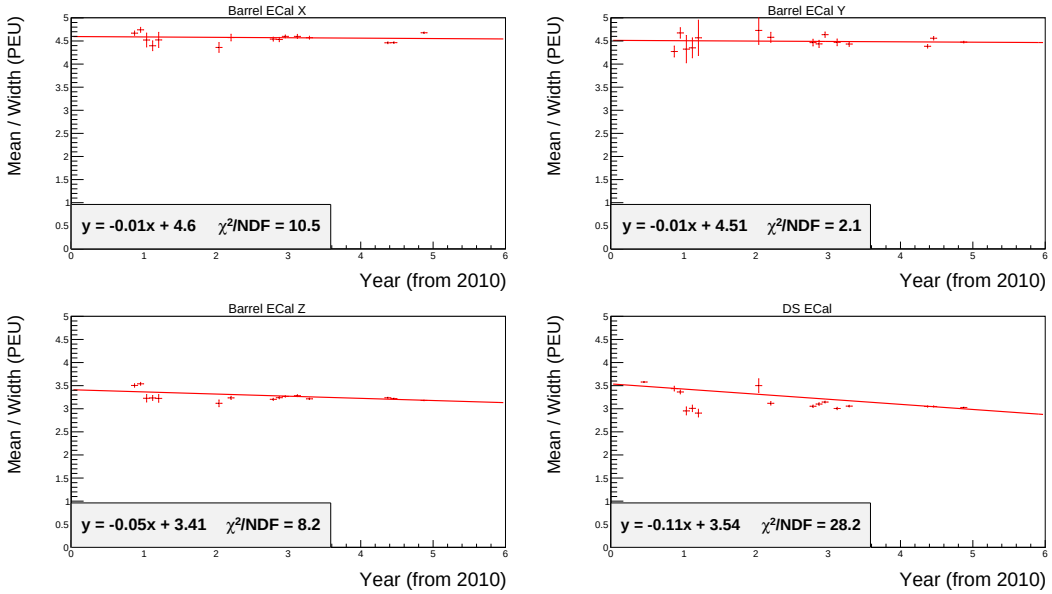

Figure 3.2.9: The MPV divided by width of the Landau-Gaussian fit to the recorded charge distribution for different time periods. Fitted with an straight line to parameterise the rate of degredation. The relative flatness of the fits shows that the MPV of the charge distribution is decreasing at a similar rate to the width.

the time scale of the Hyper-Kamiokande Experiment, the scintillator bars, for all types, are only expected to have roughly 30% loss of light collection efficiency assuming the exponential model. This is significant, but well understood, so it should be possible to properly take this into account and reuse the ECals in the future [65]. As T2K continues to take data, the fits should improve, allowing for a better parameterisation of the scintillator ageing.

3.3 TPC to ECal track matching Uncertainties

3.3.1 Introduction

If there is a difference in efficiency between data and Monte Carlo for matching components of a track between a TPC and an ECal, then the number of events in a selection using a TPC object that appears to enter an ECal will be different for data and Monte Carlo. This could mean counting extra or missing events in several T2K selections. This would have an impact on many T2K analyses. To take this into account, a systematic uncertainty is calculated for tracks entering the barrel ECal or the downstream ECal from a TPC.

The topology of interest is shown in Fig 3.3.1. This is a schematic of the ND280 detector with a muon neutrino interacting in FGD1, producing a muon that enters TPC2 and then the Barrel ECal.

3.3.2 Procedure

The fractional systematic uncertainty, σ, is calculated by taking the difference in track matching efficiency across the TPC and ECal for data and Monte Carlo simulation. This is combined with the uncertainties on the calculated efficiencies, as shown in Eq 3.3.1, ϵ is the measured efficiency whilst $\delta\epsilon$ is the statistical uncertainty on the efficiency. This basic procedure was first outlined in [52] and improved upon in this analysis by combining neutrino and anti-neutrino data, and by studying the systematic uncertainties in terms of two variables simultaneously. The samples used in this study are as follows: neutrino data with Protons On Target (POT) $= 5.5 \times 10^{20}$, neutrino NEUT MC fake data with 4.5×10^{21} POT, anti-neutrino data with 2.9×10^{19} POT and the anti-neutrino NEUT MC fake data with 1.0×10^{21} POT. The normalisations of these samples does not matter when calculating the efficiencies, but the MC samples having greater statistics will mean a smaller value of $\delta\epsilon^2_{MC}$ compared to $\delta\epsilon^2_{data}$.

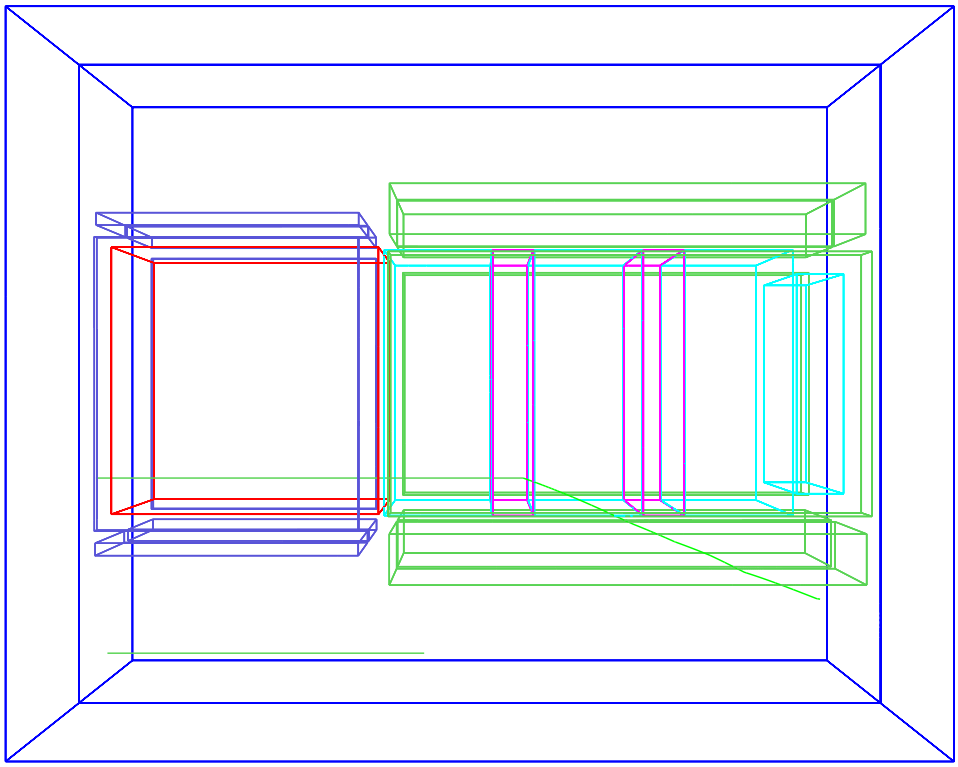

Figure 3.3.1: A schematic of the ND280 with a simulated neutrino interaction producing a track that travels through TPC1 and into the Barrel ECal. The neutrino enters from the left, travels through the PØD and TPC1 and then interacts in FGD1.

$$\sigma = \sqrt{(\epsilon_{data} - \epsilon_{MC})^2 + \delta\epsilon^2_{data} + \delta\epsilon^2_{MC}} \tag{3.3.1}$$

The efficiencies for both data and Monte Carlo are calculated using tracks that appear to enter an ECal from a TPC based on an event selection described in Sec 3.3.3. These events are used as a signal event, whilst any global track with both a TPC segment and an ECal segment is considered as passing the cuts. As discussed in Sec 2.2.7, a global track is a reconstructed track that uses information from multiple subdetectors. Eq 3.3.2 gives the calculation of the efficiency whilst Eq 3.3.3 is the formula that describes the calculated statistical error on the efficiencies based on binomial statistics. n is the number of tracks that reconstructed with matched TPC and ECal segments. The true matching efficiency is not used as it would not be possible to calculate this for data.

$$\epsilon = \frac{\text{Global track has TPC and ECal segments and passes cuts}}{\text{Global track has TPC and ECal segments}} \tag{3.3.2}$$

$$\delta\epsilon = \sqrt{\frac{\epsilon(1-\epsilon)}{n}} \tag{3.3.3}$$

A large statistical uncertainty on the efficiencies would also mean a large systematic uncertainty (see Eq 3.3.1). In order to minimise this, neutrino data is combined with anti-neutrino data into a single sample; and likewise for the Monte Carlo. Due to the differences in cross section between neutrinos and anti-neutrinos, the samples cannot simply be added. Instead, a weight is applied to the anti-neutrino events before they are combined, as shown in Eq 3.3.4.

$$\text{Total} = n(\nu) + w \times n(\bar{\nu}) \tag{3.3.4}$$

The event weights are calculated by taking the ratio of anti-neutrino mode data events to neutrino mode events that pass the event selections described in Sec 3.3.3 after the samples have been scaled to the same number of protons on target. The

same procedure is also applied to the Monte Carlo samples. The calculation of the event weights is shown in Eq 3.3.5.

$$w = \frac{\bar{\nu}(\text{POT})}{\nu(\text{POT})} \times \frac{\nu(\text{Events})}{\bar{\nu}(\text{Events})} \tag{3.3.5}$$

The uncertainties on the event weights are calculated using the square root of the number of events and propagated through to the uncertainties on the efficiencies and subsequently contributing to the systematic uncertainty. This increase is not as large as the decrease associated with the reduced statistical uncertainty, as shown in Sec 3.3.4.

3.3.3 Event selection

The event selection is split into two cases; either the track appears to enter the barrel ECal or the downstream ECal. The selection is applied to any TPC track, whilst further requirements can be added to assess the systematic uncertainty for different particle types. The cuts were first detailed in [52], with the slight difference that there is no momentum requirement on the tracks entering the ECal in order to study the systematic uncertainty as a function of track momentum. The cuts are as follows:

1. Good data quality - All the ND280 subdetectors, beam monitors and magnetic horns must be working correctly during the beam spill. The interaction must occur within the timing window for beam events.

2. Track Quality - The track is required to have at least 18 hits in a TPC. This is to ensure that the track is reconstructed well enough for the particle identification to work.

3. FGD vertex - An interaction vertex reconstructed within the FGD1 fiducial volume. At least one track from this vertex must be reconstructed as entering a TPC.

The following cuts are applied to select tracks entering the downstream ECal:

4. The position of the track as it exits the most downstream TPC satisfies:

   - -920 $< x <$ 920 mm.
   - -910 $< y <$ 930 mm. The requirements on the x and y position mean that the track is in the centre of the TPC. The z direction is the beam direction. 0 mm is the centre of the TPC, which is 2.3 m wide in x and 2.4 m in y.
   - $z >$ 2665 mm so the track ends near the back of TPC3. The DS ECal starts at z = 2855 mm. This is so the track is heading towards the DS ECal as it exits the TPC.

5. The angle as the track exits the most downstream TPC is less than 40^o from the z-axis.

The following cuts are applied to select tracks entering the barrel ECal:

6. The position of the track as it exits the most downstream TPC satisfies:

   - Outside -890 $< x <$ 890 mm or 920 $< y <$ 1085 mm. So that the TPC track end is near the barrel ECal.
   - Inside 600 $< z <$ 2600 mm. The barrel ECal starts at z = -663.97 mm and ends at z = 3216 mm.

7. The angle as the track exits the most downstream TPC is greater than 35^o from the z-axis.

8. The absolute value of the azimuthal angle as the track exits the most downstream TPC is less than 160^o.

The events that pass these selections are classified as events that appear to enter an ECal. The results of these selections are shown in Figs 3.3.2 and 3.3.3.

To calculate the systematic uncertainty for different particles, the track must be compatible with that particle type in the most downstream TPC. $\mathcal{P}$(particle) is an identification variable known as pull, defined in Eq 3.3.6. The pulls are based

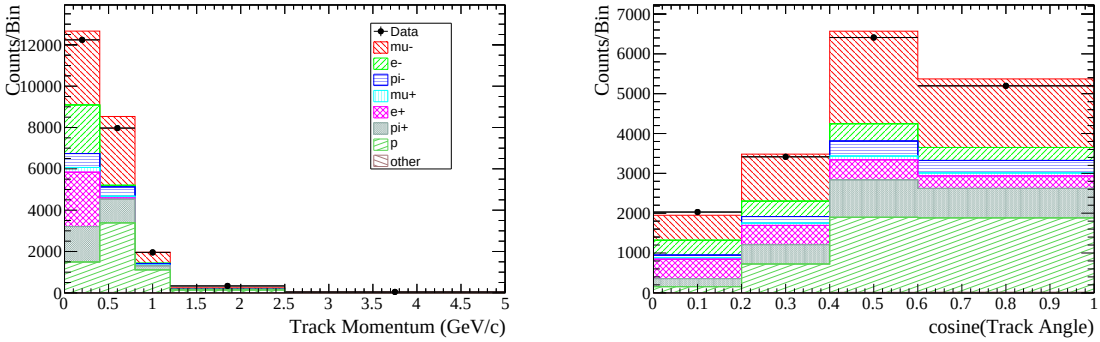

Figure 3.3.2: Events that appear to enter the barrel ECal. The Monte Carlo sample is normalised to the data POT. Both samples are for neutrino mode. Tracks that enter the barrel ECal from an FGD and through a TPC tend to enter at high angles and have low track momentum, as they have to bend in the magnetic field.

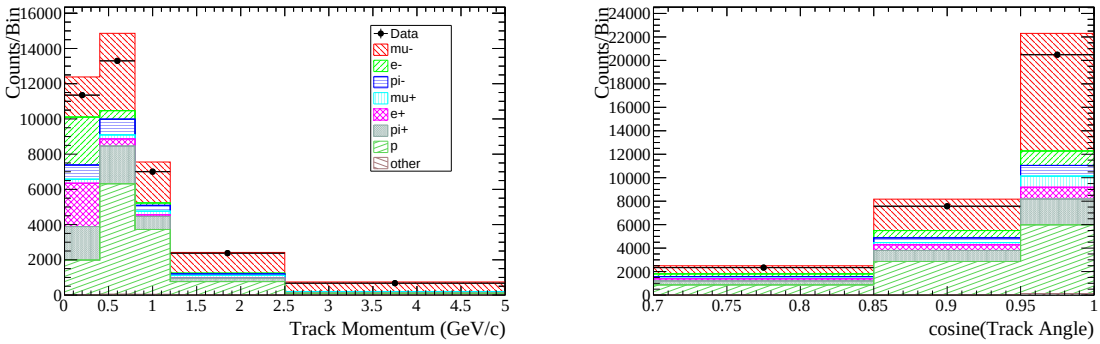

Figure 3.3.3: Events that appear to enter the downstream ECal. The Monte Carlo sample is normalised to the data POT. Both samples are for neutrino mode. Tracks originating from an FGD that enter the DS ECal are very forward going and cannot be bent significantly by the magnetic field, meaning they tend to have higher momentum than tracks entering the barrel ECal.

on the rate of energy loss of the track, dE/dx, as measured in a TPC and the expected value based on the measured momentum of the track and an assumption of the particle type. This leads to different values of $\mathcal{P}$ for different particle hypotheses which can discriminate between particle types. For a track created by an electron, $\mathcal{P}$ for the electron hypothesis should be close to 0. The uncertainty on dE/dx is given by $\sigma_{\mathrm{dE/dx}}$.

$$\mathcal{P} = \frac{(dE/dx)_{\mathrm{meas}} - (dE/dx)_{\mathrm{exp}}}{\sigma_{\mathrm{dE/dx}}} \tag{3.3.6}$$

For electron-like tracks, the track must satisfy cuts on the TPC pull:

- -1 $< \mathcal{P}(e) <$ 2
- $\mid \mathcal{P}(\mu) \mid > 2.5$
- $\mid \mathcal{P}(\pi) \mid > 2$

For muon-like tracks, the track must be compatible with the muon hypothesis in the most downstream TPC:

- -2 $< \mathcal{P}(\mu) <$ 2
- $\mathcal{P}(e) > 2$ or $\mathcal{P}(e) <$ -1

The events that pass the selection criteria and are electron-like are shown in Figs 3.3.4 and 3.3.5 whilst muon-like tracks that pass the selection criteria are shown in Figs 3.3.6 and 3.3.7.

The same selections can be applied to the anti-neutrino data and Monte Carlo samples. Since there is no charge discrimination in the selections, similar distributions are expected for neutrino data and Monte Carlo compared to anti-neutrino data and Monte Carlo. These checks are done in order to ascertain the validity of combining the samples. The data plotted against the Monte Carlo for anti-neutrino running is shown in Fig 3.3.8 to show that there are no large differences

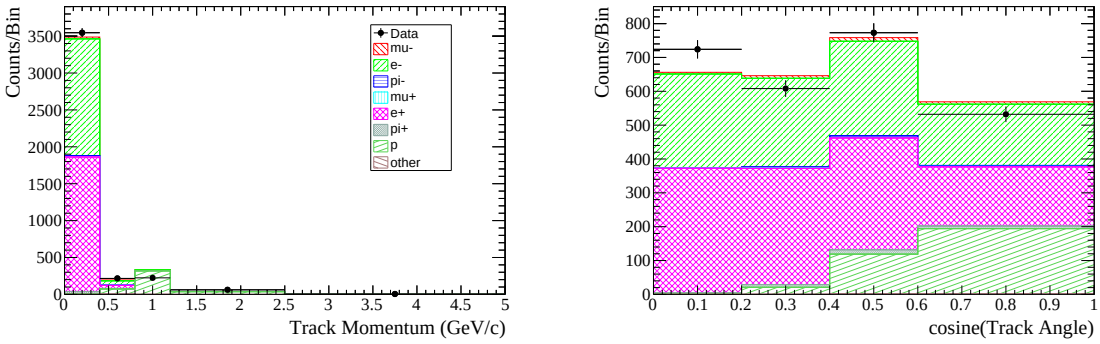

Figure 3.3.4: Electron-like events that appear to enter the barrel ECal. The Monte Carlo sample is normalised to the data POT. Both samples are for neutrino mode.

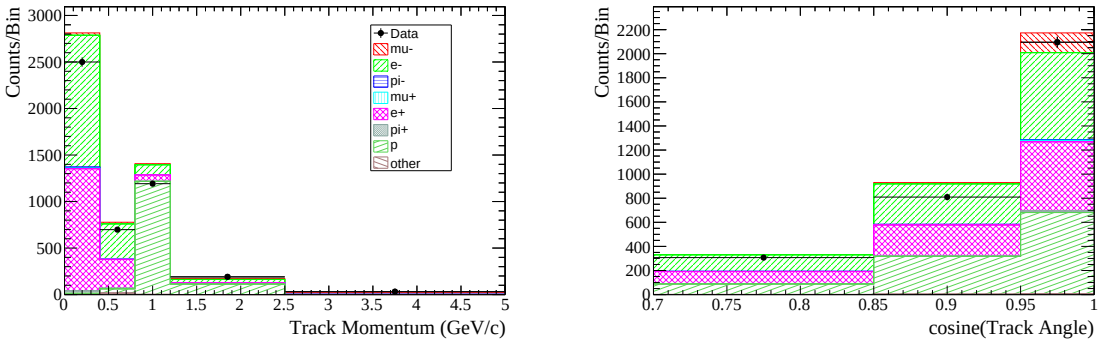

Figure 3.3.5: Electron-like events that appear to enter the downstream ECal. The Monte Carlo sample is normalised to the data POT. Both samples are for neutrino mode. The peak at around 1 GeV track momentum is due to protons that have similar rate of energy loss as electrons of the same momentum.

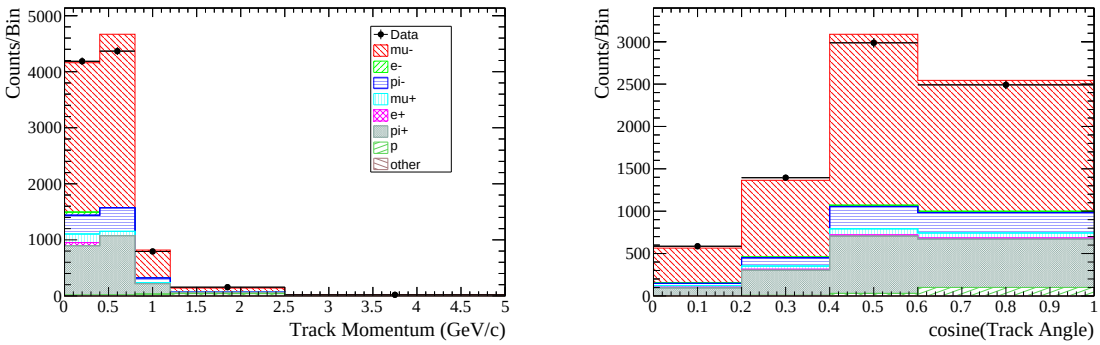

Figure 3.3.6: Muon-like events that appear to enter the barrel ECal. Both samples are for neutrino mode.

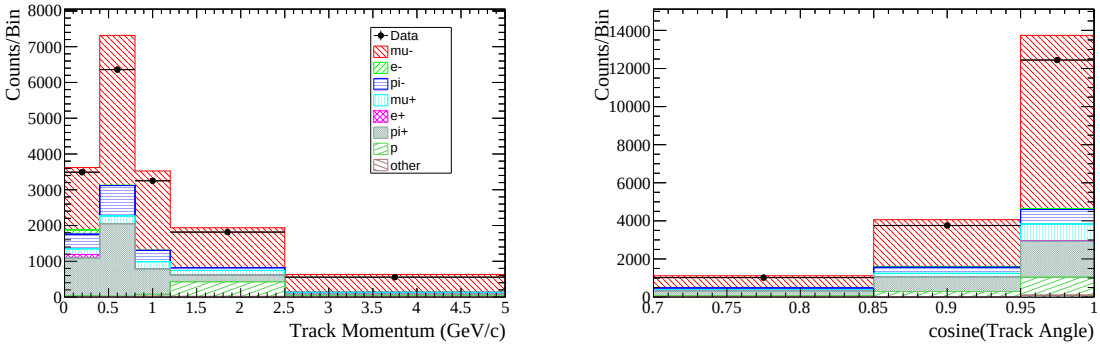

Figure 3.3.7: Muon-like events that appear to enter the downstream ECal. Both samples are for neutrino mode.

in shape between the two. The normalisations of the samples is less important, as this will cancel out when calculating the efficiencies. The selections shown are for all types of particle, with no requirements to distinguish between electrons and muons.

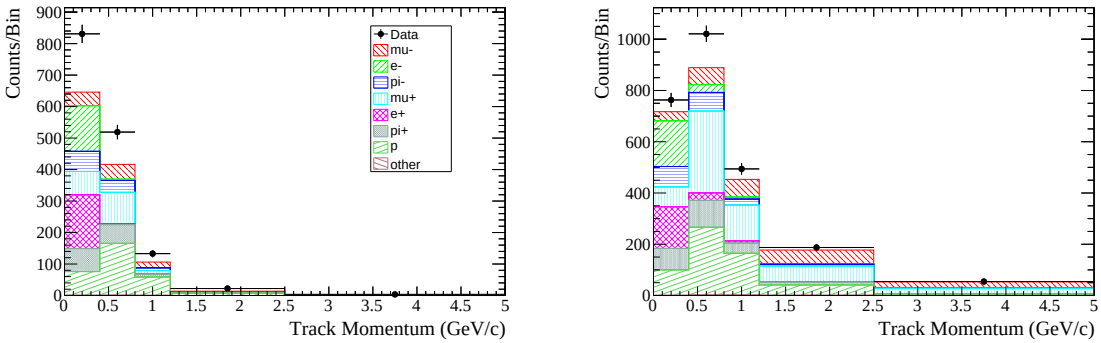

Figure 3.3.8: The selections applied to the anti-neutrino samples. The left plot shows tracks appearing to enter the barrel ECal whilst the right plot shows tracks appearing to enter the downstream ECal. The plots are normalised to have the same POT.

Finally, the neutrino data is plotted against anti-neutrino data in Fig 3.3.9 and the neutrino Monte Carlo is plotted against the anti-neutrino Monte Carlo in Fig 3.3.10. These plots are area normalised due to the differences in cross sections between the two samples and serve to demonstrate that the shapes of the distributions are similar. These plots are also shown for all types of particles

with no extra cuts applied. The similarities in the shape of these distributions, with statistical fluctuations, confirms the validity of combining the neutrino and anti-neutrino samples.

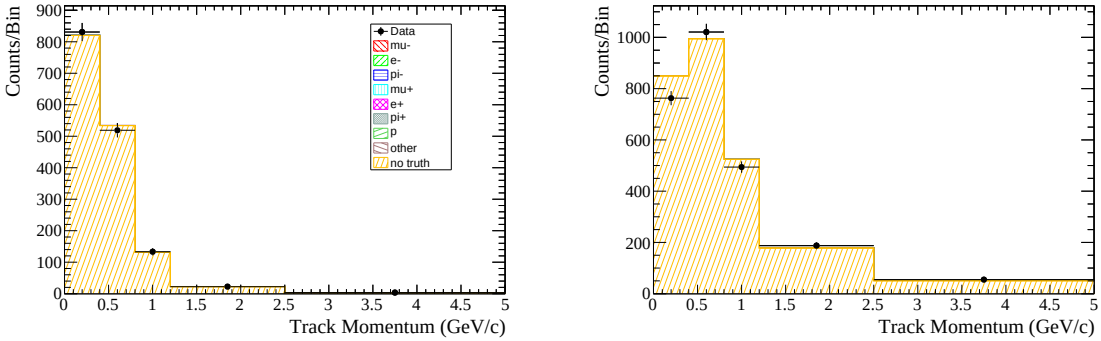

Figure 3.3.9: A comparison between neutrino data (histogram) and anti-neutrino data (points). The distributions are normalised to have the same area due to the differences in cross sections between neutrinos and anti-neutrinos. The plot on the left is for events that appear to enter the barrel ECal whilst the plot on the right is for events that appear to enter the downstream ECal.

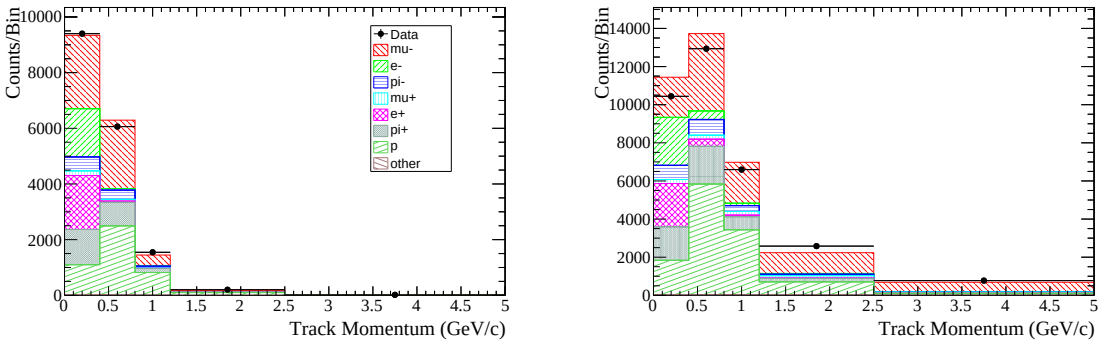

Figure 3.3.10: A comparison between neutrino Monte Carlo (histogram) and anti-neutrino Monte Carlo (points). The distributions are normalised to have the same area due to the differences in cross sections between neutrinos and anti-neutrinos. The plot on the left is for events that appear to enter the barrel ECal whilst the plot on the right is for events that appear to enter the downstream ECal.

3.3.4 Systematic Uncertainties

The event weights calculated for adding the anti-neutrino samples to the neutrino samples are shown in Fig 3.3.11. These weights are the ratio of the number of neutrino events divided by the number of anti-neutrino events after scaling to the same POT. The weights are expected to be a little under 3, due to the fact that there is an exact ratio of three for charged-current quasi-elastic interactions between neutrino and anti-neutrinos. Including all interaction types reduces the expected weights, particularly at higher neutrino energies. The plots show that the event weights are as expected. The discrepancies between data and Monte Carlo for the event weights are attributed to a convolution of several possible effects; such as mismodelling of background events or a poor understanding of the flux or cross section. For the purpose of the event weights, it is more important that the distributions of events for neutrino Monte Carlo compared with anti-neutrino Monte Carlo and neutrino data compared with anti-neutrino data are consistent, as shown in Figs 3.3.9 3.3.10.

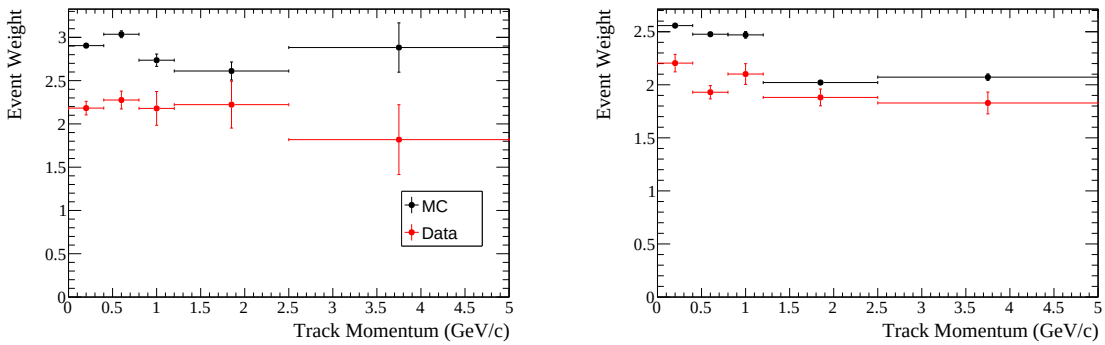

Figure 3.3.11: The event weights used to combine the neutrino and anti-neutrino samples. The left plot shows the weights for events that appear to enter the barrel ECal, the right plot shows events that appear to enter the downstream ECal. The red points are for data and the black points are for Monte Carlo.

Using the event selections described in Sec 3.3.3 and Eq 3.3.2 the track matching efficiencies can be calculated. Fig 3.3.12 shows the efficiency as a function of track momentum in the TPC (left) and as a function of track angle as it exits the TPC (right) for the downstream ECal. Whilst Fig 3.3.13 shows the same

for the Barrel ECal whilst both figures are for all particles types. The errors on these efficiencies are calculated using Eq 3.3.3.

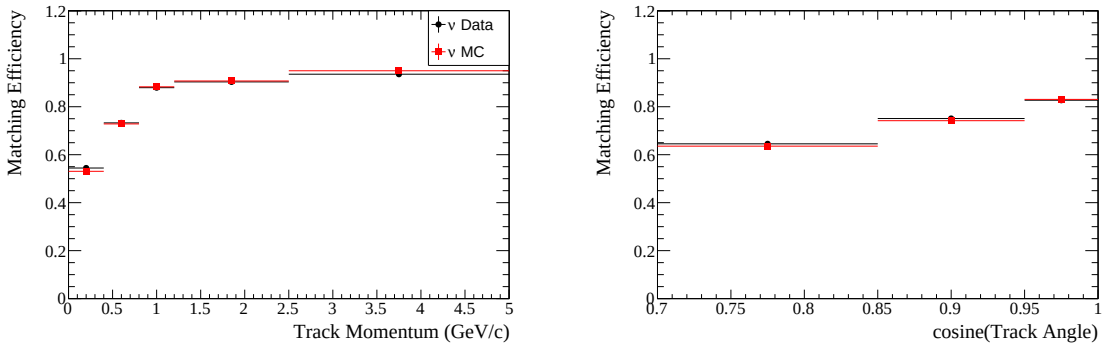

Figure 3.3.12: The efficiency of sucessfully matching a track that has passed through a TPC and entered the downstream ECal.

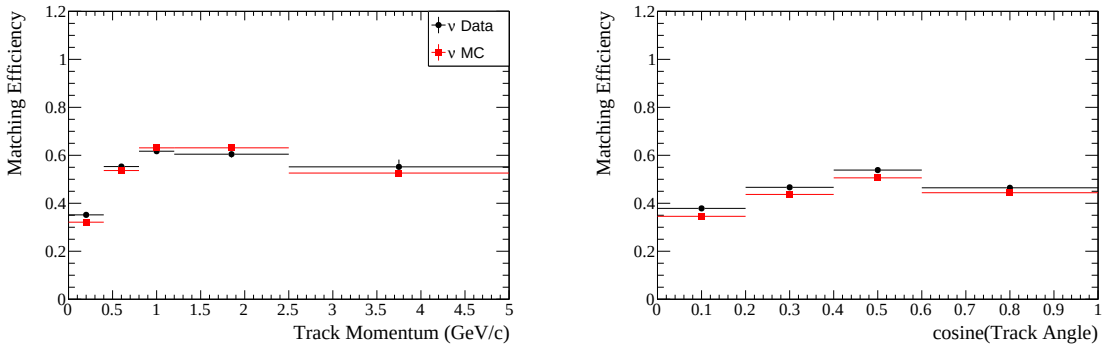

Figure 3.3.13: The efficiency of sucessfully matching a track that has passed through a TPC and entered the barrel ECal.

As a final check on the validity of combining samples, the track matching efficiency for neutrino and anti-neutrino mode are compared. This is shown in Fig 3.3.14. The results for all four samples appear similar, within the statistical errors. The dip in efficiency at low track momentum is due to particles that leave only a very small amount of activity in the ECal or are stopped by the TPC casing and so cannot be reconstructed. For the barrel ECal, the efficiency tends to be lower as the tracks tend to enter at a steeper angle and so are more difficult

to reconstruct correctly.

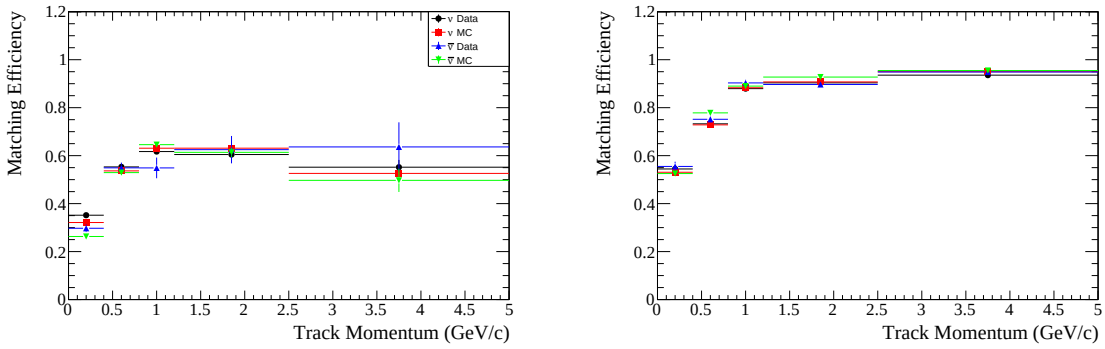

Figure 3.3.14: The efficiency of track matching for all four samples, neutrino data, anti-neutrino data, neutrino Monte Carlo and anti-neutrino Monte Carlo. Left shows the efficiency of matching a TPC track to an object in the barrel ECal, right shows for the downstream ECal.

The corresponding systematic uncertainties for the barrel ECal and downstream ECal are shown in Figs 3.3.15 and 3.3.16 respectively. The systematic uncertainty is calculated using Eq 3.3.1 and using events from the neutrino and anti-neutrino samples. The black points show the calculated systematic uncertainty using only neutrino mode, whilst the red points show the systematic uncertainty calculated from the combined samples. This includes the uncertainty on the event weights, which are propagated through and combined into the total systematic uncertainty. The distributions are characterised by considering both the difference in efficiency between data and Monte Carlo and the uncertainties on the efficiencies. The bins with the largest systematic uncertainty are those where the data and Monte Carlo do not agree or where the number of selected events are low. The added statistics gained by including the anti-neutrino samples is enough to reduce the systematic uncertainty despite the uncertainty on the event weights.

The efficiencies and systematic uncertainties can also be presented in two dimensions. This allows for a full understanding of the uncertainty with respect to all track dynamics. The efficiency for the combined neutrino and anti-neutrion samples as functions of track angle as it exits the TPC and the measured momentum

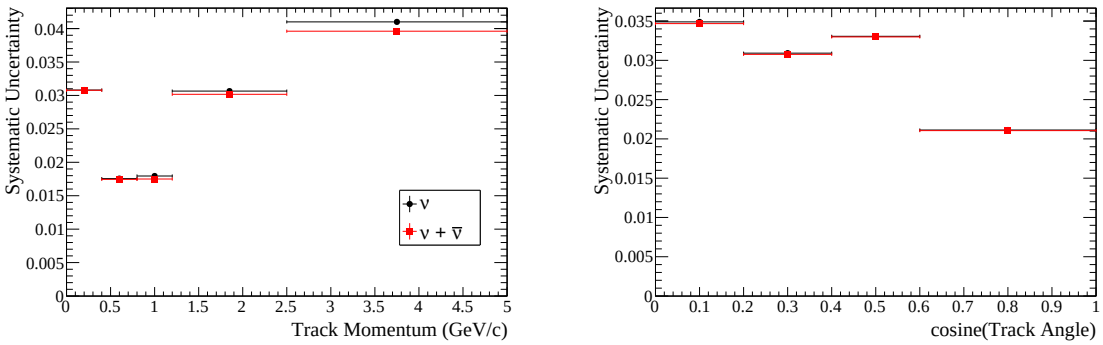

Figure 3.3.15: The systematic uncertainty associated with matching tracks that have passed through a TPC and entered the barrel ECal.

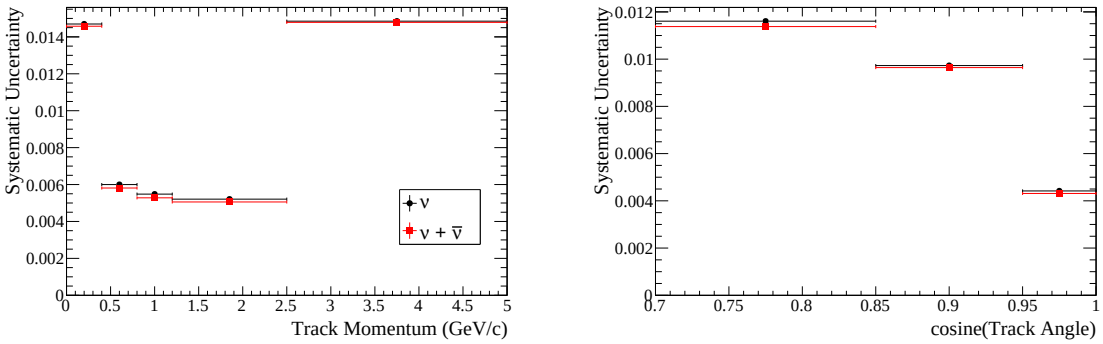

Figure 3.3.16: The systematic uncertainty associated with matching tracks that have passed through a TPC and entered the downstream ECal.

are shown in Fig 3.3.17 for tracks entering the barrel ECal and Fig 3.3.18 for tracks entering the downstream ECal. The corresponding systematic uncertainty is presented in Fig 3.3.19. As would be expected, the track matching efficiency improves with higher momentum tracks and tracks that hit the ECal straight on. The systematic uncertainties increase with two dimensional binning, due to the decreased statistics in each bin.

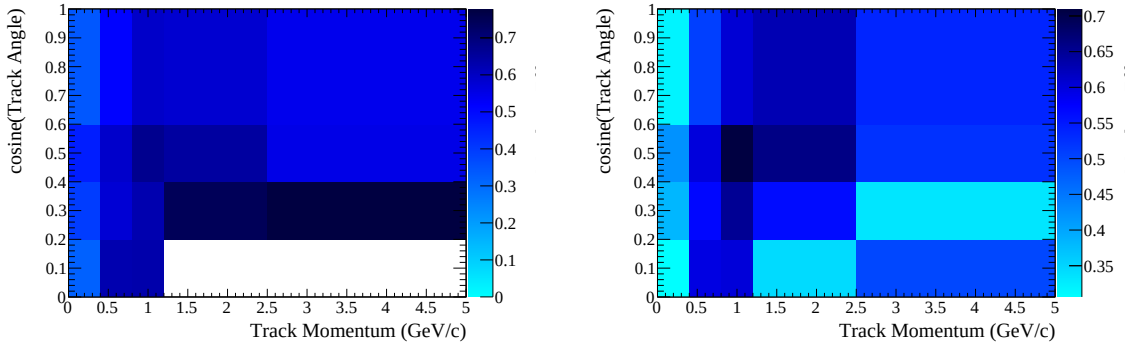

Figure 3.3.17: The efficiency of matching a track from a TPC to the barrel ECal. The left plot shows ND280 neutrino mode data and anti-neutrino mode data combined whilst the right plot shows neutrino mode Monte Carlo and anti-neutrino mode Monte Carlo combined.

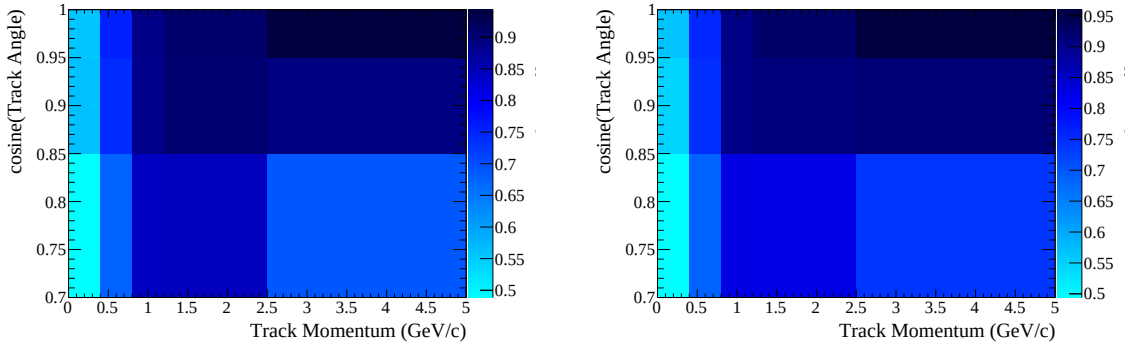

Figure 3.3.18: The efficiency of matching a track from a TPC to the downstream ECal. The left plot shows ND280 neutrino mode data and anti-neutrino mode data combined whilst the right plot shows neutrino mode Monte Carlo and anti-neutrino mode Monte Carlo combined.

Finally, the efficiencies and systematic uncertainties are presented for electron-like and muon-like tracks. These plots are not broken down into the two dimensional

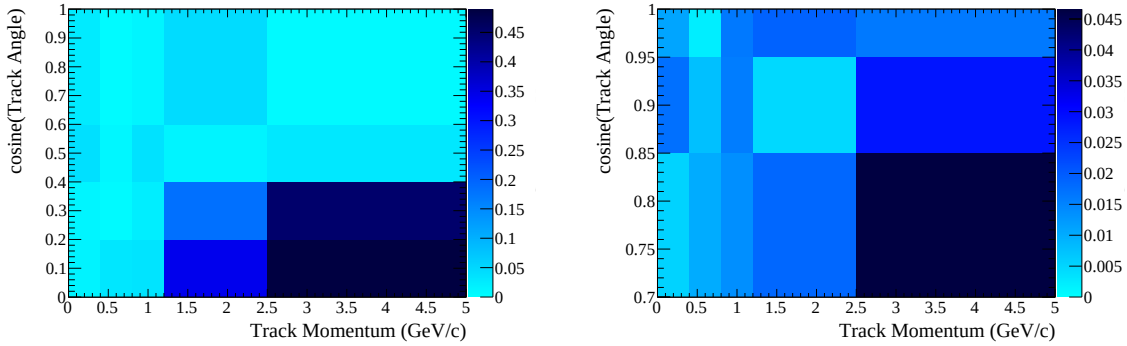

Figure 3.3.19: The systematic uncertainty of matching a track from a TPC to the downstream ECal based on the efficiencies shown in Figs 3.3.17 and Figs 3.3.18. The left plot shows the results for the Barrel ECal whilst the right plot shows for the downstream ECal.

cases as the extra requirements needed to select these tracks further limit the statistics, reducing the usefulness of these plots. Fig 3.3.20 shows the track matching efficiency from a TPC to the barrel ECal and the downstream ECal for electron-like tracks with the corresponding systematic uncertainties presented in Fig 3.3.21. The same plots are shown for muon-like tracks in Figs 3.3.22 and 3.3.23. All these plots are created using the combined neutrino mode and anti-neutrino mode, for data and Monte Carlo. The statistical uncertainties on the efficiencies are included in the systematic uncertainties, and so these plots are shown without error bars.

There is some significant bin-to-bin fluctuations in Figs 3.3.21 and 3.3.23. This is mostly due to small differences between data and Monte Carlo having a significant effect on the systematic uncertainty. Consequently, statistical fluctuations on the efficiencies create the fluctuations seen. This effect should be minimised in future as T2K continues to take data.

The efficiencies, their statistical uncertainties and the associated systematic uncertainties for each selection are summarised in Tab 3.3.1 with no binning applied. The values for the efficiencies and systematic uncertainties for specfic momentum and angle ranges are shown in Tab 3.3.2 for the barrel ECal and Tab 3.3.3 for the

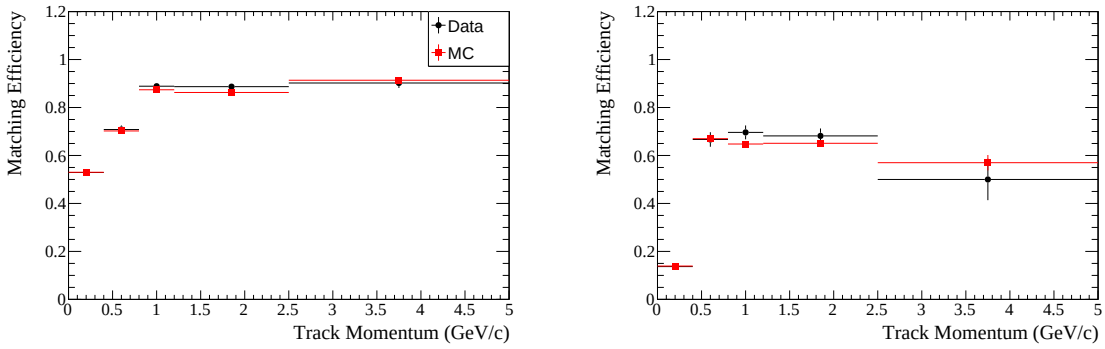

Figure 3.3.20: The efficiency of matching a track from a TPC to an ECal for electron-like tracks. The left plot shows for the downstream ECal whilst the right plot shows for the barrel ECal.

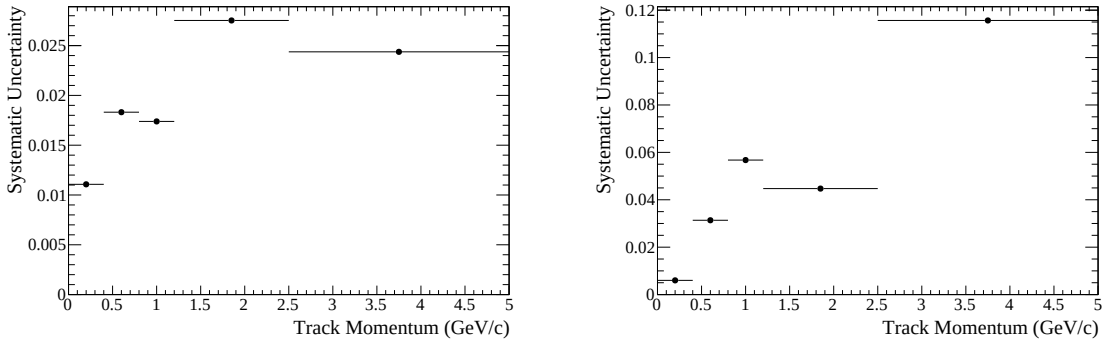

Figure 3.3.21: The systematic uncertainty associated with matching electron-like tracks from a TPC to an ECal. Left shows for the downstream ECal, right shows for the barrel ECal.

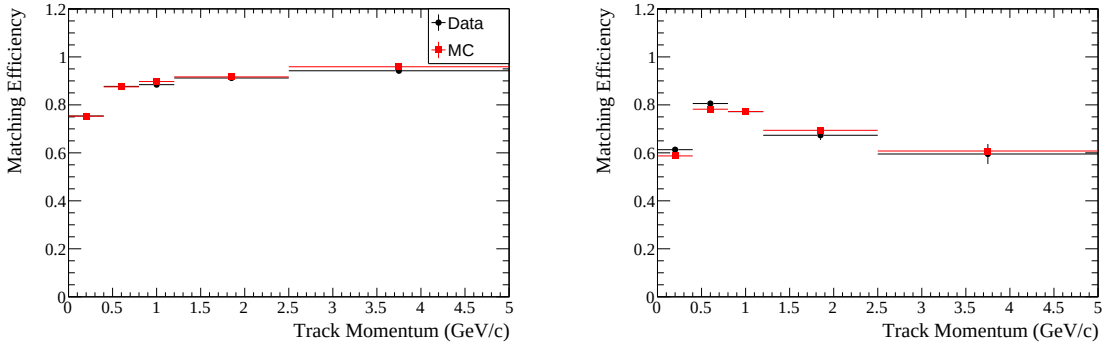

Figure 3.3.22: The efficiency of matching a track from a TPC to an ECal for muon-like tracks. The left plot shows for the downstream ECal whilst the right plot shows for the barrel ECal.

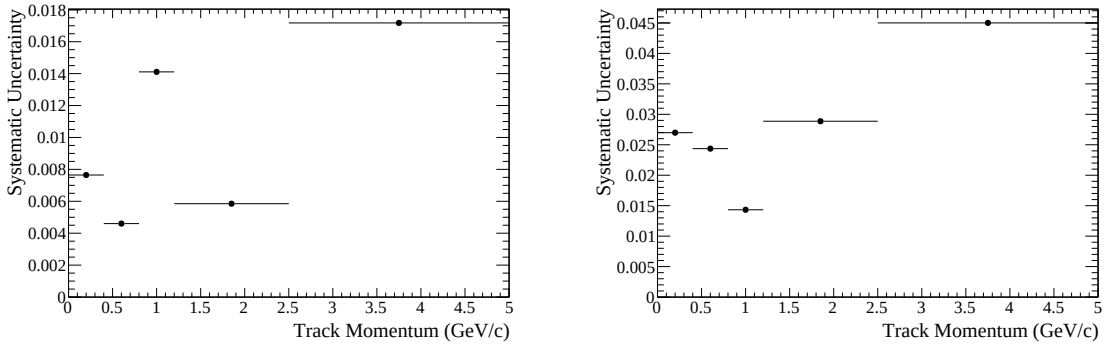

Figure 3.3.23: The systematic uncertainty associated with matching muon-like tracks from a TPC to an ECal. Left shows for the downstream ECal, right shows for the barrel ECal.

downstream ECal. These numbers are for events with no requirements to select particular particles.

Particle	Detector	Data Eff	Data Err	MC Eff	MC Err	Systematic (%)
All	Barrel	0.456	0.003	0.446	0.001	1.0%
	DS	0.774	0.002	0.779	0.001	0.6%
Ele	Barrel	0.223	0.006	0.223	0.002	0.7%
	DS	0.713	0.007	0.711	0.002	0.7%
Muon	Barrel	0.771	0.005	0.766	0.002	0.7%
	DS	0.923	0.002	0.940	0.001	1.7%

Table 3.3.1: The efficiencies of matching a track between a TPC and an ECal for data and Monte Carlo, their errors and the associated systematic uncertainties broken down into different types of particle and all particle types. No binning is applied.

Momentum (GeV/c)	Data Eff	Data Err	MC Eff	MC Err	Systematic (%)
0 - 0.4	0.351	0.004	0.322	0.001	3%
0.4 - 0.8	0.552	0.006	0.535	0.002	1.8%
0.8 - 1.2	0.618	0.011	0.629	0.004	1.6%
1.2 - 2.5	0.605	0.015	0.629	0.006	2.8%
2.5 - 5	0.554	0.030	0.505	0.014	5.9%
Angle (2π rad)					
0 - 0.2	0.378	0.011	0.345	0.004	3.5%
0.2 - 0.4	0.466	0.009	0.436	0.003	3.1%
0.4 - 0.6	0.538	0.006	0.504	0.002	3.5%
0.6 - 1.0	0.464	0.005	0.444	0.002	2.1%

Table 3.3.2: The efficiencies of matching a track between a TPC and the barrel ECal for data and Monte Carlo, their errors and the associated systematic uncertainties. No requirements are added to the tracks to select different types of particle.

Momentum (GeV/c)	Data Eff	Data Err	MC Eff	MC Err	Systematic (%)
0 - 0.4	0.544	0.005	0.532	0.002	1.3%
0.4 - 0.8	0.733	0.004	0.728	0.001	0.7%
0.8 - 1.2	0.879	0.004	0.883	0.001	0.6%
1.2 - 2.5	0.904	0.003	0.905	0.001	0.4%
2.5 - 5	0.936	0.004	0.951	0.001	1.6%
Angle (2π rad)					
0.70 - 0.85	0.645	0.006	0.635	0.002	1.3%
0.850 - 0.950	0.751	0.004	0.743	0.001	0.8%
0.95 - 1.00	0.827	0.003	0.830	0.001	0.4%

Table 3.3.3: The efficiencies of matching a track between a TPC and the downstream ECal for data and Monte Carlo, their errors and the associated systematic uncertainties. No requirements are added to the tracks to select different types of particle.

3.3.5 Summary

The matching uncertainty for the barrel ECal as a whole is 1.0% and 0.6% for the downstream ECal. The numbers separated into particle type are shown in Tab 3.3.1 and for different momentum or angle bins are shown in Tabs 3.3.2 for the barrel ECal and 3.3.3 for the downstream ECal. Figs 3.3.15 and 3.3.16 show that including the anti-neutrino samples does reduce the systematic uncertainties but not by much. However, the tools now exist so that further running in anti-neutrino mode should provide a more significant gain by including these samples. With more data, the systematic uncertainties can be reduced further or additional studies can be carried out to look at into systematic uncertainty in terms of other quantities.

Chapter 4

Differences in ν_e and ν_μ Interactions

4.1 Motivation

It is important to understand the differences in ν_e and ν_μ interactions for a variety of reasons. Firstly, a precise knowledge of the ratio of ν_e to ν_μ cross sections can be used as a means of reducing the uncertainties and biases on future oscillation measurements. This knowledge could also improve the prediction of the number of neutrino appearance events in future experiments. Also, a difference in ν_e and ν_μ cross sections not due to different lepton masses, would be indicative of New Physics and could also provide a test of lepton universality. More details on these ideas are presented in Sec 1.3.1 and Sec 1.3.2.

Comparing the measured cross section ratios with the predictions given in Sec 4.3 would also provide a good test of the models. This would compliment the normal method of testing the models which is to compare the measured cross sections directly with the predictions. With the systematic uncertainties partially cancelling in the ratios, the ratios could actually provide a more accurate test.

Lastly, there are currently no published measurements of any neutrino interaction cross section ratios for ν_e and ν_μ. The MINERvA collaboration is working towards a comparison of ν_e and ν_μ CCQE cross sections [66]. Any of the other ratios presented in this thesis would be the worlds first measurement of the neutrino cross section ratios.

4.2 Signal Definition

With four separate selections used it is important to clearly distinguish the different signals. In principle, it would be best to use CCQE and CC interactions for studying the differences in ν_e and ν_μ interactions. However, due to secondary interactions inside the nucleus and the limits of detectors to fully reconstruct neutrino interactions, it is difficult to determine experimentally whether an event is a true CCQE interaction. A further problem is that to determine the number of CCQE interactions nuclear models have to be used. To deal with this, a

CCQE signal is used as well as a second signal for interactions that appear to be CCQE interactions, i.e. an interaction with only the lepton and no mesons leaving the nucleus. This topology is referred to as CC0π interactions. The focus of this thesis will be the ratios using the CC0π topology. It is also important to consistently define the signals between the ν_e and ν_μ selections and to ensure that the CCQE and CC0π events are a subset of the CC inclusive events.

The signal definitions for the four selections are as follows:

- ν_e CC - Any ν_e charged current interaction within the FGD1 fiducial volume.
- ν_e CCQE - Any ν_e charged-current quasi-elastic interaction within the FGD1 fiducial volume.
- ν_e CC0π - A ν_e charged current interaction within the FGD1 fiducial volume where one track exiting the nucleus must be an electron with no mesons exiting the nucleus.
- ν_μ CC - Any ν_μ charged current interaction within the FGD1 fiducial volume.
- ν_μ CCQE - Any ν_μ charged-current quasi-elastic interaction within the FGD1 fiducial volume.
- ν_μ CC0π - A ν_μ charged current interaction within the FGD1 fiducial volume where one track exiting the nucleus must be a muon with no mesons exiting the nucleus.

The difference between the CCQE and CC0π signals will change the analysis when dealing with background events and missed events, and when generating the response matrix for unfolding. All the other steps will remain unchanged. The affects of this change in signal should be small, as most CC0π events will be CCQE interactions.

4.3 Monte Carlo Predictions

The predictions for the cross sections and ratios are calculated using NEUT (5.3.3) and GENIE (2.8.0) Monte Carlo generators. Both generators can explicitly calculate neutrino cross sections as a function of energy for different targets and different neutrino flavours. Four selections are used in the analysis, so four cross sections can be calculated. The cross section is calculated for a neutrino interacting with a Carbon (^{12}C) target since the FGD1 is composed mostly of Carbon. Calculations of the cross section ratios on other nuclear targets produced identical results as Carbon, making them independent of target. This may not be true for data.

Both NEUT and GENIE model the nucleus as a Relativistic Fermi Gas (RFG) with each nucleon being a spin-half fermion (see [67] for the specific model used by NEUT and [68] for the GENIE model). The generators both make use of the Llewellyn-Smith model [27], as discussed in Sec 2.1.6, to calculate the neutrino-nucleon CCQE cross section. Other models are used to calculate different interaction modes [69] [70]. The RFG model is then used to calculate the cross section for the nucleus as a whole for any specified target. The computed cross sections can be used when generating simulated data.

For more information on these two generators see [69] and [70] for NEUT and GENIE respectively with comparisons between the generators discussed in [71]. The main difference between the generators that will affect the cross section predictions is a different value of axial mass (effective charge radius of a nucleon), M_A, used. For instance, when generating CCQE interactions NEUT uses a value of $M_A = 1.2$ GeV whereas GENIE uses $M_A = 0.99$ GeV. Other differences include the RFG model used for the nucleus and the approximations used in the models.

As mentioned previously, a CC0π topology is also used as a signal to search for interactions that look like CCQE interactions. The generators do not calculate the cross sections in terms of final state topologies and so the predictions are calculated only in terms of the CCQE cross sections. The interaction cross sections

for the four signals are shown in Fig 4.3.1 with NEUT shown in red and GENIE shown in blue. The total charged current cross sections increase almost linearly with increasing neutrino energy at the relevant energies for this analysis. The CCQE cross section increases with energy up to ≈ 0.5 GeV then levels out as other processes become dominant.

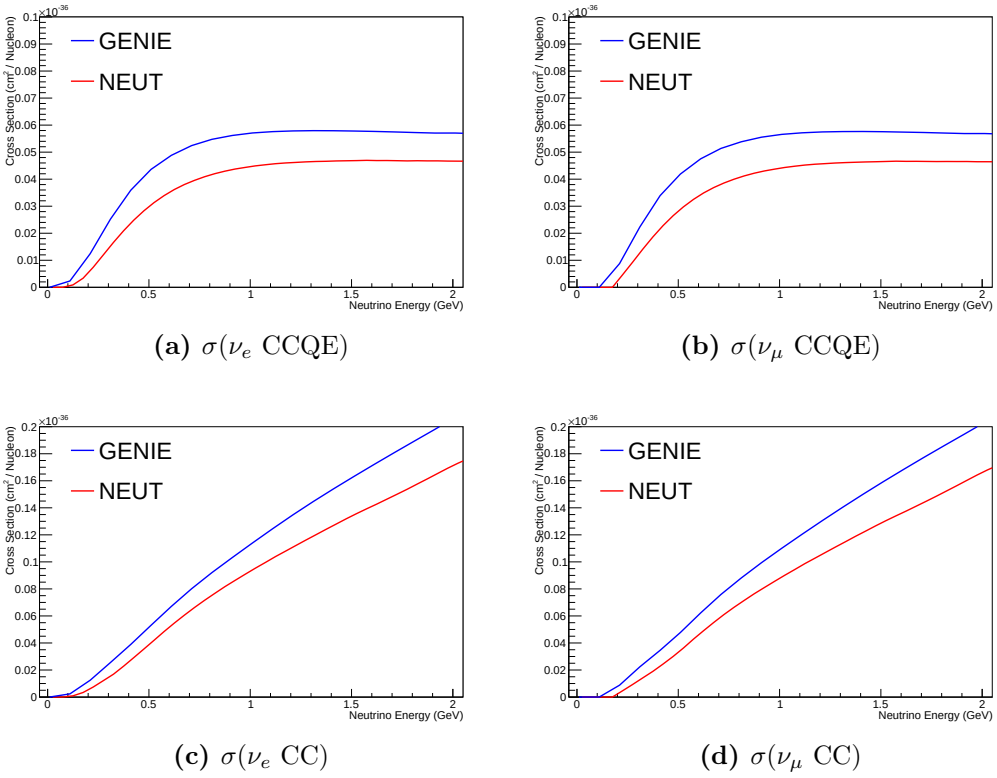

(a) $\sigma(\nu_e$ CCQE) **(b)** $\sigma(\nu_\mu$ CCQE)

(c) $\sigma(\nu_e$ CC) **(d)** $\sigma(\nu_\mu$ CC)

Figure 4.3.1: The cross sections for ν_e and ν_μ CCQE and CC interactions calculated by the NEUT (red) and GENIE (blue) Monte Carlo generators as a function of neutrino energy.

The predictions are calculated for specific energies. To generate the predictions for the ratios, a simple division is used on the values of the predictions for the individual cross sections. The results of this is shown in Fig 4.3.2. For an interpretation of the shape of these predictions, refer back to the kinematic arguements given in Sec 2.1.7. The agreement between the NEUT and GENIE calculations is good, with the threshold for producing charged-current interactions other than

CCQE being the same for both generators. The slight differences are attributed to the different values of M_A used.

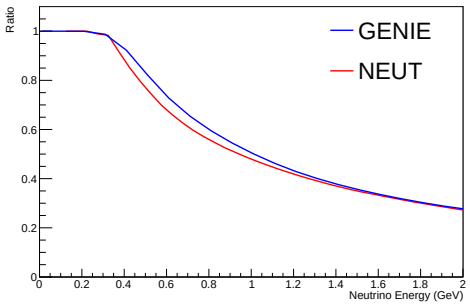

(a) $\sigma(\nu_e$ CCQE) / $\sigma(\nu_e$ CC)

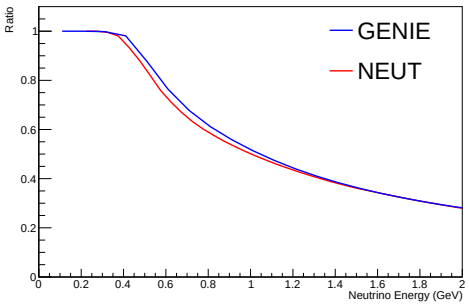

(b) $\sigma(\nu_\mu$ CCQE) / $\sigma(\nu_\mu$ CC)

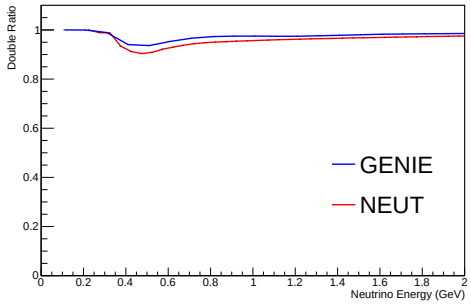

(c) Double Ratio of (a) to (b)

Figure 4.3.2: The cross section ratios as calculated by the NEUT (red) and GENIE (blue) Monte Carlo generators in terms of interaction type and reaction topology as a function of neutrino energy.

4.4 Data Samples

Three types of data set are used for this analysis; real data taken with the ND280, and simulated neutrino interactions within the ND280 from the NEUT and GENIE Monte Carlo generators. Each of the samples was processed with production 6B of the ND280 software [48].

The NEUT Monte Carlo sample is used as a training sample for selecting ν_e and ν_μ interactions and for determining the number of background events and missed events. The GENIE sample is used as a control sample for unfolding. The Monte Carlo samples can also be used for testing the analysis method by extracting the cross sections and cross section ratios from an independent sample and comparing with the calculated values. A good agreement is indicative of a valid methodology. Lastly, the real data is used to extract a real measurement of the neutrino interaction cross section ratios. This can be compared to the Monte Carlo results and predictions.

The Monte Carlo events simulated by NEUT and GENIE as well as the data samples used for this analysis and the total Protons On Target (POT) for each are summarised in Tab 4.4.1. The difference between the water and air samples is whether water bags in the PØD were filled or not. With water in the PØD acting as extra target material, the rate of background interactions coming from the PØD will be higher. For this reason, the samples are kept separate.

Sample	Data POT	NEUT MC POT	GENIE MC POT
run2 air	2.08×10^{19}	9.14×10^{20}	5.76×10^{20}
run2 water	2.89×10^{19}	1.15×10^{21}	1.28×10^{21}
run3c air	1.56×10^{20}	9.98×10^{20}	2.87×10^{20}
run4 air	1.76×10^{20}	3.49×10^{21}	3.57×10^{20}
run4 water	1.63×10^{20}	3.32×10^{21}	1.09×10^{21}
Total	5.45×10^{20}	9.87×10^{21}	3.60×10^{21}

Table 4.4.1: A summary of the Protons on Target (POT) for each of the data and Monte Carlo fake data samples used.

4.5 Event Selections

The event selections used to calculate the cross section ratios were inherited from the ND280 ν_e and ν_μ analyses. The samples were developed for the oscillation analyses and have also been used for cross section analyses. The cuts are detailed extensively in [52] for the ν_e selections and [72] for the ν_μ selections.

The basis of the two selections are similar; both search for an interaction in FGD1 with the lepton leaving a track in TPC2. Many of the additional criteria are similar between the selections, this helps with the cancellation of the systematic uncertainties. More details on the selections are given in the following sections.

One of the most powerful particle identification (PID) tools available is the rate of energy loss of the track (dE/dx) as measured by a TPC. A pull variable, $\mathcal{P}$, is constructed based on the expected rate of energy loss (exp) for a particle hypothesis calculated using the Bethe-Bloch formula and measuring the momentum of the track. The pull is then the expected dE/dx minus the measured dE/dx, normalised to the energy resolution of the TPCs for the particle hypothesis, σ, as shown in Eq 4.5.1.

$$\mathcal{P} = \frac{(dE/dx)_{\text{meas}} - (dE/dx)_{\text{exp}}}{\sigma} \tag{4.5.1}$$

This is used heavily in both the ν_e and ν_μ selections.

4.5.1 Selecting ν_e Events

The criteria for the ν_e CC selection are as follows.

1. Good data quality - All the ND280 subdetectors, beam monitors and magnetic horns must be working correctly during the beam spill. The interaction must occur within the timing window for beam events.

2. FGD vertex - An interaction vertex reconstructed within the FGD1 fiducial volume. At least one track from this vertex must be reconstructed as entering TPC1.

3. Negatively charged track - The highest momentum track associated with the vertex must be reconstructed as being negatively charged. This is the candidate lepton track. The probability of a track being reconstructed with the incorrect charge is low, and the uncertainty on this discussed in Sec 4.7.4.

4. Track Quality - If the candidate lepton track enters an ECal, then it is required to have at least 18 hits in a TPC. If the lepton candidate does not enter an ECal, then the requirement is at least 36 hits in a TPC. This is to ensure that the track is reconstructed well enough for the particle identification to work.

5. High Momentum - The momentum of the candidate track must be at least 200 MeV. Without this cut, a large background is introduced due to photons pair producing an electron and positron in the FGD. If the positron track is missed or reconstructed as a proton, then this will mimick the signal.

6. Electron PID - A complicated series of cuts are applied to the track on the pull given different particle hypotheses in order to select electron-like tracks. These are detailed in Eqs 4.5.2 - 4.5.4 in the case where the track doesn't enter an ECal. The results of these cuts are shown in Fig 4.5.1.

$$-1 > \mathcal{P}(e) \text{ or } \mathcal{P}(e) > 2 \tag{4.5.2}$$

$$-2.5 < \mathcal{P}(\mu) < 2.5 \tag{4.5.3}$$

$$-2.5 < \mathcal{P}(\pi) < 2.5 \tag{4.5.4}$$

If the track enters an ECal, these conditions are relaxed slightly to the condition given in Eq 4.5.5 and further criteria are applied using ECal variables. The results of the relaxed TPC criteria are shown in Fig 4.5.2.

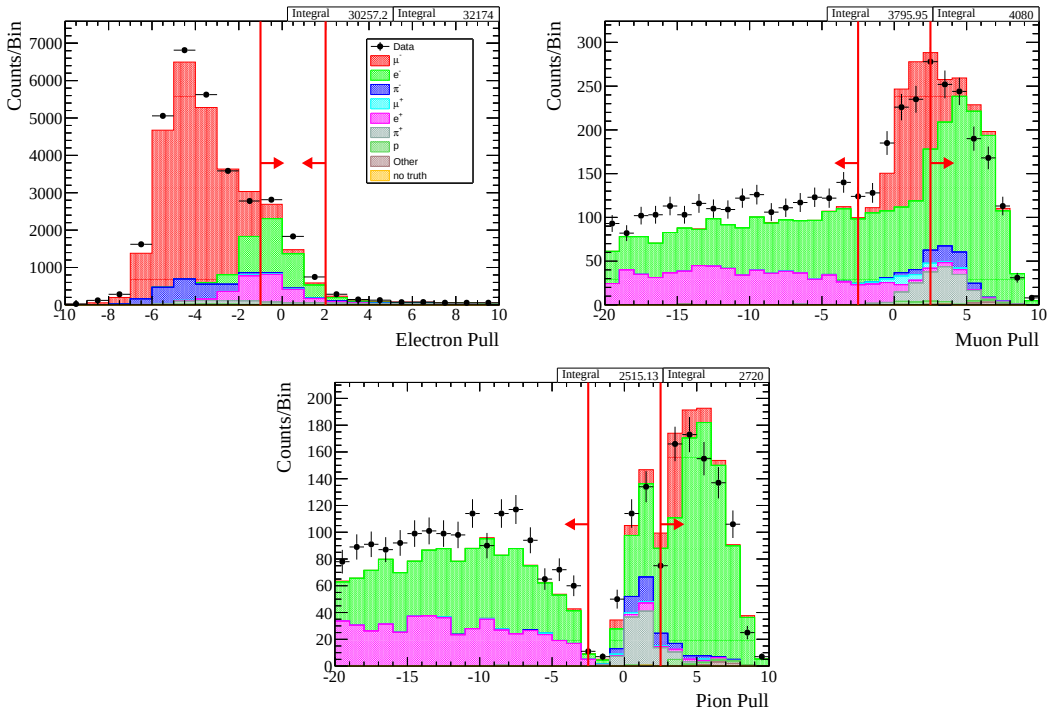

Figure 4.5.1: The results of the pull cuts on the selection of events after the first five cuts have been applied. These cuts are only applied to tracks that do not enter an ECal. The green histograms show electron tracks in the Monte Carlo. The red arrows point towards the events that are kept after the cuts are applied. For the plot showing the muon pull cut, the events shown have had the electron pull cuts already applied. Likewise, for the plot showing the pion pull cut, the electron and muon pull cuts have already been applied.

The two ECal variables used for particle identificaiton are the energy deposited in the ECal, and a log-likelihood variable, L, for determining tracks from showers. The power of these variables depends on the momentum of the track and whether the ECal object is contained or not. For tracks entering an ECal, require that $L > 0$ (i.e. the object is shower-like) if the track momentum as it exits the TPC is less than 1000 MeV or the ECal object is not contained. For contained ECal objects with momentum greater than 1000 MeV, require that the energy deposited is greater than 1100 MeV. The results of these cuts are shown in Fig 4.5.3.

$$-2 > \mathcal{P}(e) \text{ or } \mathcal{P}(e) > 2.5 \tag{4.5.5}$$

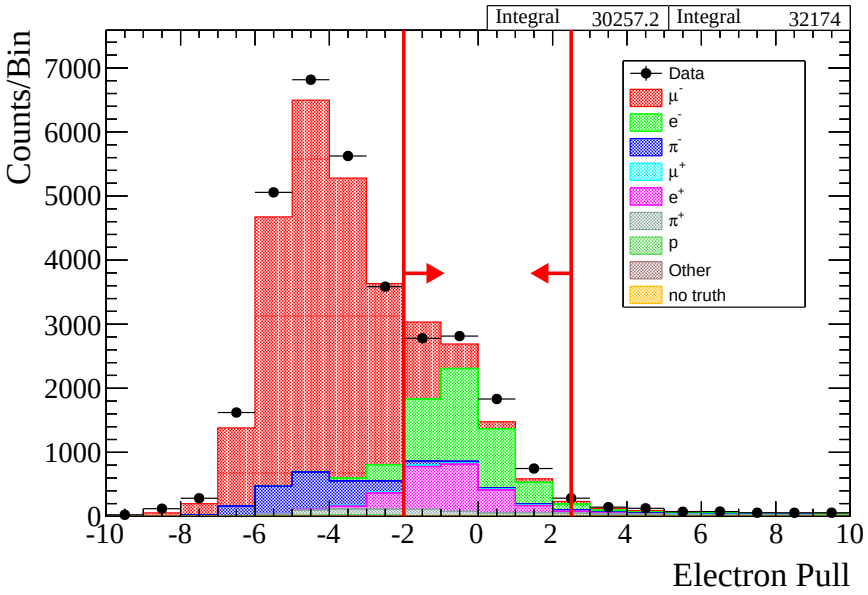

Figure 4.5.2: The results of the pull cuts applied for tracks that enter an ECal. The red arrows point to events that are kept by the cuts. The green histograms show electron tracks in the Monte Carlo.

7. 2nd PID - If the track enters a second TPC, further requirements on the pull as calculated by the second TPC are implemented to reject muons. These are detailed in Eq 4.5.6

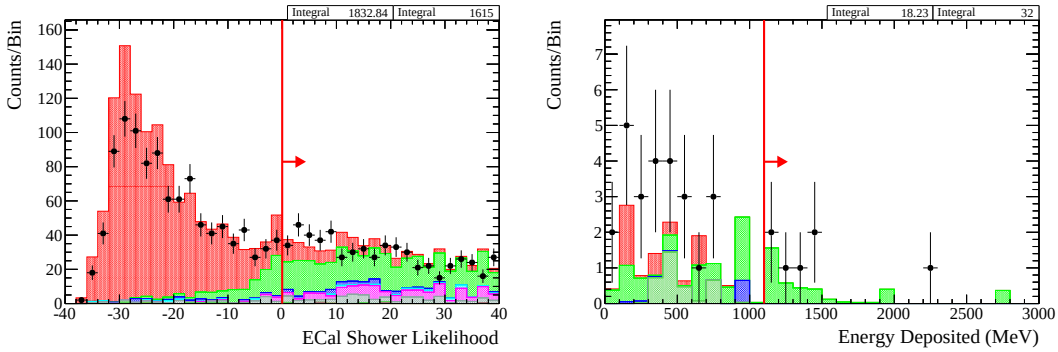

Figure 4.5.3: The criteria applied to tracks that use the ECals. The events shown already have the pull cuts in Eq 4.5.5 applied. The left plot shows events which are not contained or have track momentum less than 1000 MeV as the track exits the TPC. A cut on the likelihood variable that discriminates tracks and showers is applied to these events to select electron tracks. The right plot shows events that are contained in the ECal and have track momentum greater than 1000 MeV. A cut is applied to these events on the energy deposited in the ECal. The red arrows point towards events that are kept after the cuts are applied.

$$-2.5 < \mathcal{P}(\mu) < 2.5 \tag{4.5.6}$$

8. TPC veto - If a track is reconstructed in TPC1 and the end position is within 10 cm of the candidate lepton track then the event is rejected. This is to throw away events where the electron in FGD1 is not created by a neutrino interacting in FGD1.

9. Invariant mass - If there is an additional track exiting the interaction that is reconstructed as being positively charged and electron-like (based on pull cuts), then the invariant mass of the pair is calculated. If this is less than 100 MeV then the event is rejected. This is a further cut designed to remove events where the electron was not created in a neutrino interaction but instead by a secondary photon pair producing.

10. PØD veto - Reject any event if a track is reconstructed in the PØD or PØD ECal. Most of the background events caused by photon pair production in the FGD originate from the PØD and PØD ECal. This cut is implemented to try and reduce this background.

11. ECal veto - If there is an ECal object upstream of the candidate lepton track, then the event is rejected if the ECal object either starts or ends within 10 cm of the candidate track start. This cuts helps reject backwards going tracks mimicking the signal.

Additional requirements are made to select ν_e CC0π interactions. This means that the events that pass the ν_e CC0π selection are a subset of the events that pass the ν_e CC selection, which will mean there should be a significant amount of cancellation of the systematic uncertainties in the CC0π / CC ratio. These additional requirements are detailed below.

12. No Michel electron - The candidate lepton track cannot appear to decay into an electron. This is based on a time delay for a stopping muon to decay and by looking for kinks in the candidate lepton track where a muon may have decayed into an electron.

13. One proton track - In the case of only one track associated with the vertex, the track must be the candidate lepton track. If there are two tracks associated with the vertex then the second highest momentum track must be consistent with a proton based on pull cuts. The cuts to select proton-like tracks are detailed in Eqs 4.5.7 - 4.5.9.

$$-0.5 < \mathcal{P}(\mu) < 2 \tag{4.5.7}$$

$$-1.5 < \mathcal{P}(\pi) < 2.5 \tag{4.5.8}$$

$$-1.5 > \mathcal{P}(p) \text{ or } \mathcal{P}(p) > 10 \tag{4.5.9}$$

4.5.2 Selecting ν_μ Events

The criteria for the ν_μ CC selection are significantly simpler than those for the ν_e selections due to the greater flux of ν_μ in the beam meaning there is relatively a smaller background. The requirements are as follows.

1. Good data quality - As described for the ν_e selection.

2. FGD/TPC track - At least one track reconstructed in a TPC comming from a vertex in FGD1 is required. The highest momentum negatively charged track is selected as the candidate lepton track.

3. Veto track - If the highest momentum TPC track that isn't the candidate lepton track starts within 15 cm upstream of the candidate track, then the event is rejected. This is to reduce backgrounds caused by neutrino interactions upsteam of FGD1.

4. Isolated FGD veto - Reject the event if there is an isolated object in FGD1 that is not associated with the candidate neutrino interaction vertex.

5. Muon PID - To select muon-like tracks a likelihood variable is calculated based on the track pull. Cuts are then applied to this based on the reconstructed momentum of the candidate track. This provides excellent separating power between muon tracks and electron, pion or proton tracks. The likelihood variable, ℓ, is calculated by comparing the computed pull for a particular hypothesis and the sum of all the calculated pulls (for electron, muon, pion and proton). This is shown in Eq 4.5.10. An additional likelihood variable, ℓ_{MIP}, to distinguish pions from muons is calculated using the values of ℓ for different particle types. This is given in Eq 4.5.11.

$$\ell = \frac{e^{-\mathcal{P}^2}}{\sum_i e^{-\mathcal{P}_i^2}} \tag{4.5.10}$$

$$\ell_{\mathrm{MIP}} = \frac{\ell_\mu + \ell_\pi}{1 - \ell_p} \tag{4.5.11}$$

The cuts to select muon tracks are based on the likelihood variable as calculated for the four different particle hypotheses. An event will pass the selection if $\ell_\mu > 0.05$ and either the reconstructed momentum is greater than 500 MeV or $\ell_{\mathrm{MIP}} > 0.8$. The results of these cuts are given in Fig 4.5.4 and Fig 4.5.5 showing good separation of muon tracks with other particles.

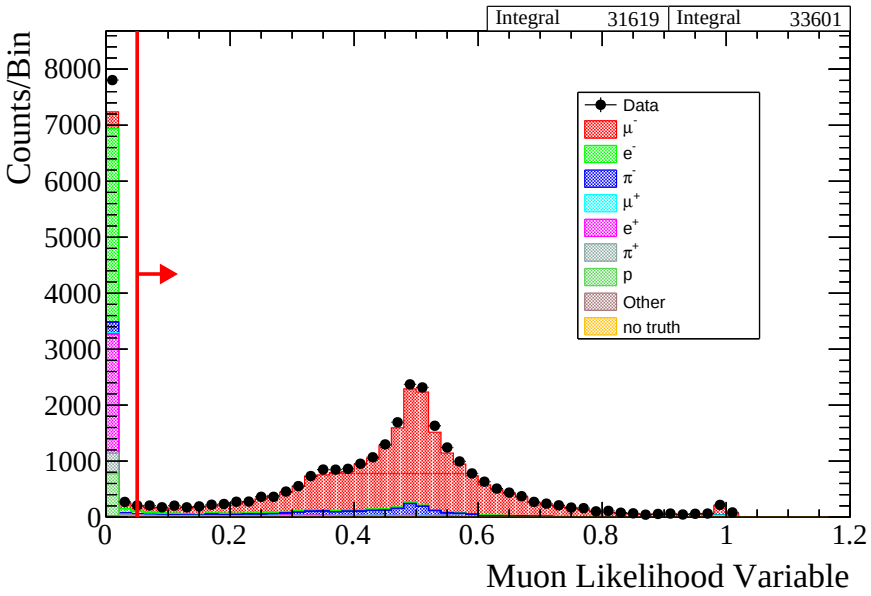

Figure 4.5.4: The distribution of events in terms of the muon likelihood variable for the highest momentum track, which must enter a TPC, originating from a vertex reconstructed within FGD1. The red line points towards events that are kept after the cut at $\ell_\mu > 0.05$ to select muon tracks.

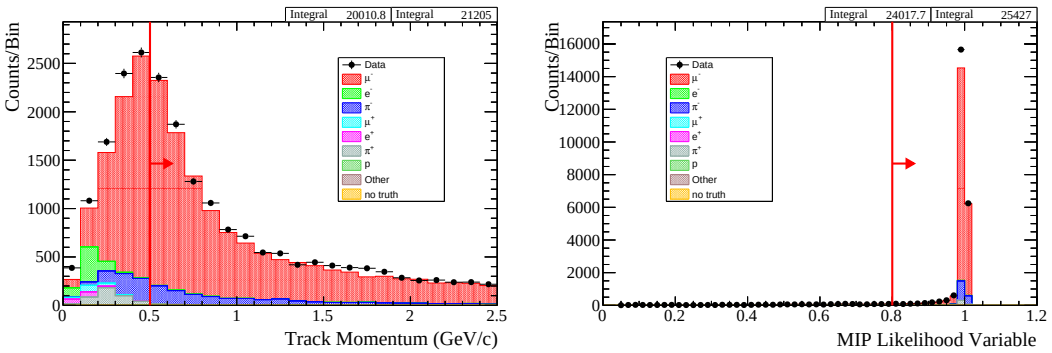

Figure 4.5.5: The distribution of events that pass the cut on $\ell_\mu > 0.05$ in terms of track momentum and ℓ_{MIP}. These tracks must have either reconstructed momentum greater than 0.5 GeV/c or $\ell_{\text{MIP}} > 0.8$. The red arrows show the events that are kept by these cuts.

As with the ν_e selections, the CC0π selection is an extension to the CC selection and so these events are a subset. The additional cuts to select CC0π are detailed below.

6. One negative track - Reject any event with more than one negative track associated with the candidate vertex.

7. No Michel electron - Reject any event with a Michel electron reconstructed inside the FGD1 fiducial volume. The Michel electron does not have to be associated with the candidate vertex or the candidate lepton i.e. if an electron is identified in the FGD1 ≈ 2 μs after the beam spill, the event is rejected. This is to remove background events caused by a neutrino interaction upstream of the FGD.

8. ECal π^0 veto - To reduce the CCπ^0 background, remove any event with an isolated ECal object that is shower-like (due to a photon).

9. Proton cut - Several different topologies are searched for regarding protons leaving the candidate vertex. Firstly, the candidate lepton track must start in FGD1 and enter TPC1. The four possibilities for protons are listed below.

    - No reconstructed proton tracks, the candidate muon track is the only track associated with the candidate vertex.
    - A single isolated proton-like track in FGD1. The track must stop in FGD1 and apart from the candidate lepton track there must be no other tracks associated with the candidate vertex.
    - A single proton-like track in FGD1 that enters TPC1. Apart from the proton track and the candidate lepton track there must be no other tracks associated with the candidate vertex.
    - A single proton-like track in TPC1 with no proton tracks in FGD1. This is to select events where the proton is missed in the FGD.

4.5.3 Event Distributions

The backgrounds to the selections are broken down into five categories. These are detailed below.

- NC - A neutral current interaction of a neutrino of any flavour interacting within the FGD1 fiducial volume. NC interactions cannot produce the charged lepton that is required by the selections, so this background is relatively small for the ν_μ selection but has a larger contribution to the ν_e selection, as it is more likely to produce secondary electrons than muons.

- ν_μ/ν_e - A neutrino of the wrong flavour undergoing a charged current interaction within the FGD1 fiducial volume. For the ν_μ selections, this background is very low as there are far more ν_μ than ν_e in the beam. On the other hand, there is a significant contribution to the ν_e selections from ν_μ for the same reason.

- OOFV - A neutrino interaction outside of the fiducial volume (OOFV) of the FGD which looks like a neutrino interaction inside the FGD. For the ν_e selection this is broken down into two types.

  - OOFV γ - This background primarily concerns the ν_e selections. A photon travels though TPC1, which cannot detect electrically neutral particles, and pair produces an e^+e^-. If the e^+ is missed by the reconstruction then the e^- will mimick the signal. These photons are normally created by a neutrino interaction upstream of FGD1 (most commonly the PØD) where a π^0 is produced, which decays to a pair of photons. The large contribution of this background is due to the relatively large number of ν_μ to ν_e in the beam and the large number of interactions in the PØD and other upstream detectors.
  - OOFV Other - The other OOFV events are mostly caused by positively charged particles travelling backwards, usually starting in the barrel or DS ECal, that stops in FGD1. This is reconstructed as a forward-going negatively charged particle starting in FGD1. Since these are reconstructed incorrectly, the particle identification is often

also incorrect. Thus, the most common backwards going particle that mimicks the electron or muon is a positively-charged pion. There is a very small number of events than happen within FGD1 but outside the fiducial volume and are reconstructed as occuring within the fiducial volume. This background is also classified as OOFV Other.

- CC Other - This is only for the CC0π samples. A charged current interaction of a neutrino of the correct flavour in the FGD1 fiducial volume with more than just the lepton and proton leaving the interaction nucleus.

The distributions of the selected events are shown in Fig 4.5.6 in terms of the reconstructed momentum and angle of the candidate lepton track. In all of these plots, the signal, as defined in Sec 4.2, is shown in blue and the points show data. These two quantities are chosen because they can be directly measured in the detector and the data can be compared with the simulation. The selections shown are broken down into the desired signal events, and the different types of background event.

The event distributions are slightly different between ν_e and ν_μ. The ν_e in the beam tend to be higher energy than the ν_μ, this means that the lepton momentum is peaked at higher energies and are more forward boosted for signal events. The electron being lighter than the muon further increases the peak at low angles in the ν_e selection compared to ν_μ. A significant background of out of fiducial volume events also plays a role in the event distributions for ν_e, causing a broader and lower peak in the momentum spectrum.

Fig 4.5.7 shows the same events as the ν_e and ν_μ CC0π selections in Fig 4.5.6 but with a CCQE signal instead of CC0π. The raw numbers of events passing the selection are unchanged, but the amount of background and missed events are different.

For studying the ratios of neutrino interaction cross sections, other quantities like neutrino energy and four-momentum transfer, Q^2, are more interesting. Using the truth information for the Monte Carlo, the distributions of the selected

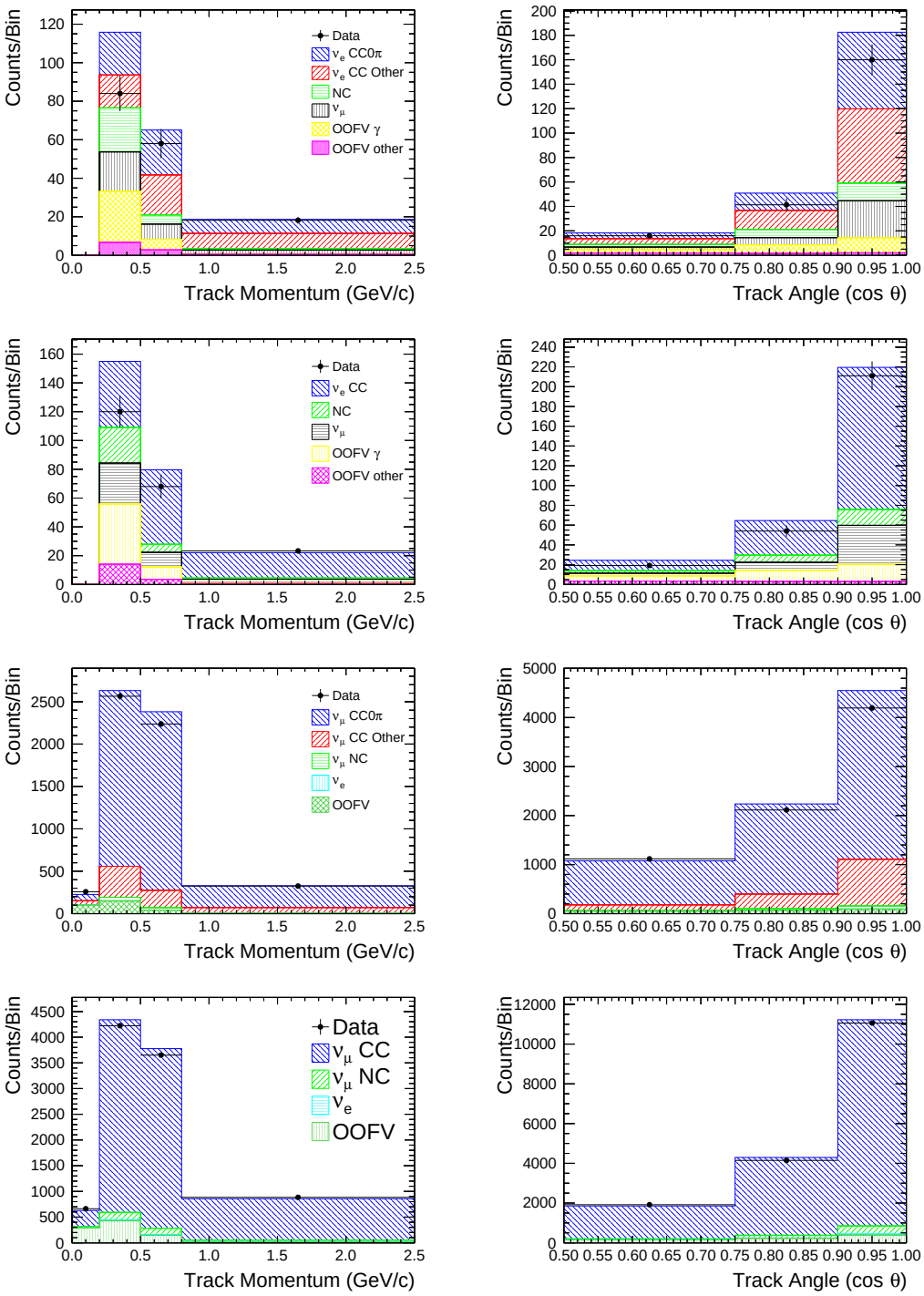

Figure 4.5.6: The distribution of events for NEUT Monte Carlo and data for the four selections shown in terms of the reconstructed momentum and angle of the candidate lepton track. The two plots in the first row are for the ν_e CC0π selection, the second row shows the ν_e CC selection and the third and fourth rows show the ν_μ CC0π and ν_μ CC selections respectively.

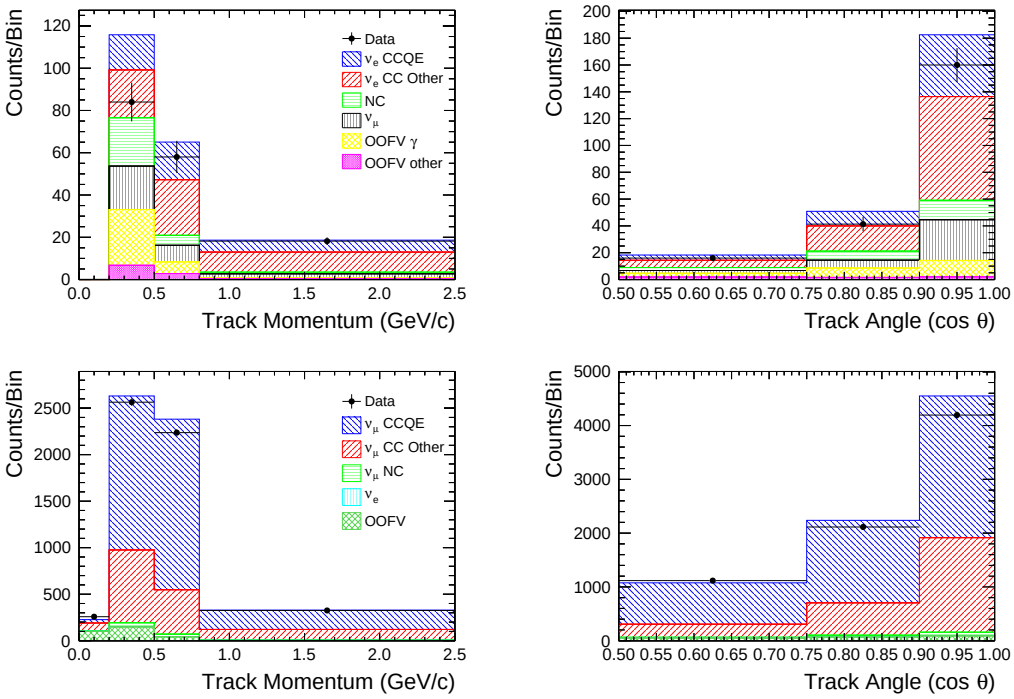

Figure 4.5.7: The distribution of events for NEUT Monte Carlo and data for the CCQE selections shown in terms of the reconstructed momentum and angle of the candidate lepton track. The first row shows the ν_e CCQE selection and the second row shows the ν_μ CCQE selection. The numbers of selected events are identical as the CC0π selections in Fig 4.5.6 but with the signal and backgrounds defined differently.

events can be studied for these quantities. It is also possible to look at the true momentum and true angle of the candidate lepton track to compare with the distributions shown in Fig 4.5.6. These are shown in Figs 4.5.8 - 4.5.11 for the ν_e CC, ν_e CC0π, ν_μ CC and ν_μ CC0π selections respectively. The neutrino energy and Q^2 are more interesting to study but require the use of a model to extract them in data. The method to do this will be described later.

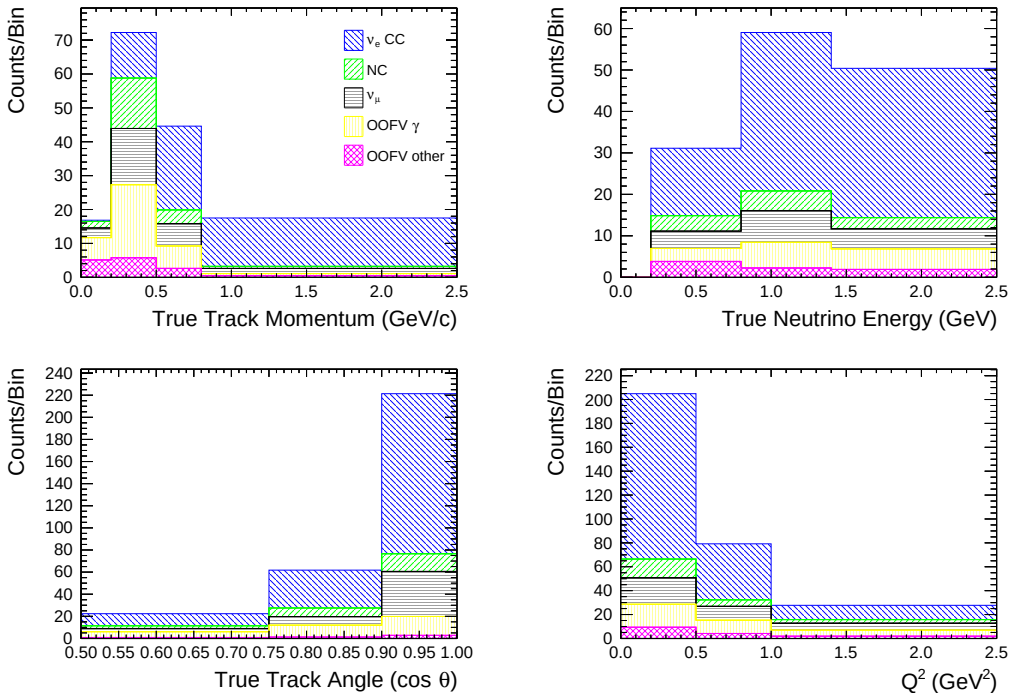

Figure 4.5.8: The distribution of NEUT Monte Carlo events for the ν_e CC selection shown in terms of the several variables. These are the true momentum and angle of the electron produced in the interaction, the energy of the interacting neutrino and the four-momentum transfered in the neutrino interaction. These rely on the Monte Carlo truth information and so data can not be added to these plots.

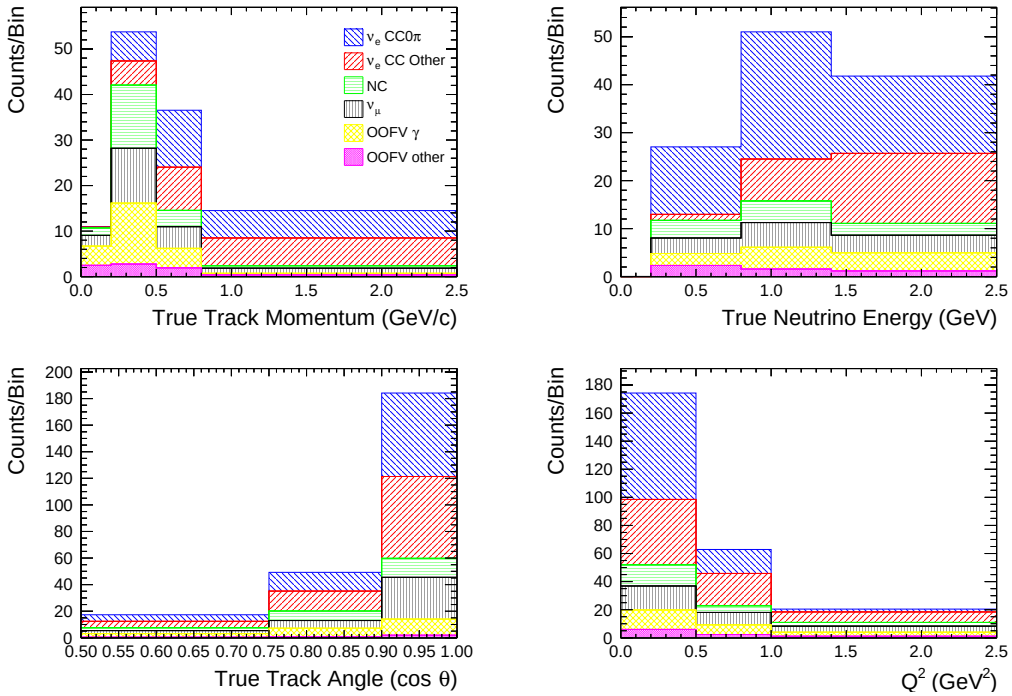

Figure 4.5.9: The distribution of NEUT Monte Carlo events for the ν_e CC0π selection shown in terms of the several variables. These are the true momentum and angle of the electron produced in the interaction, the energy of the interacting neutrino and the four-momentum transfered in the neutrino interaction. These rely on the Monte Carlo truth information and so data can not be added to these plots.

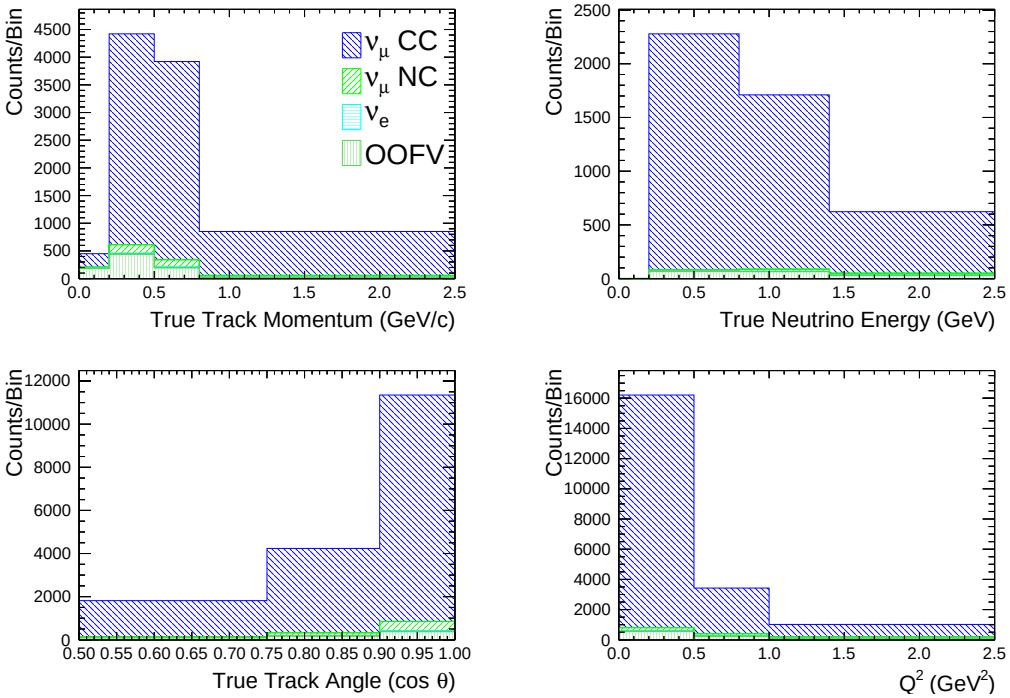

Figure 4.5.10: The distribution of NEUT Monte Carlo events for the ν_μ CC selection shown in terms of the several variables. These are the true momentum and angle of the muon produced in the interaction, the energy of the interacting neutrino and the four-momentum transfered in the neutrino interaction. These rely on the Monte Carlo truth information and so data can not be added to these plots.

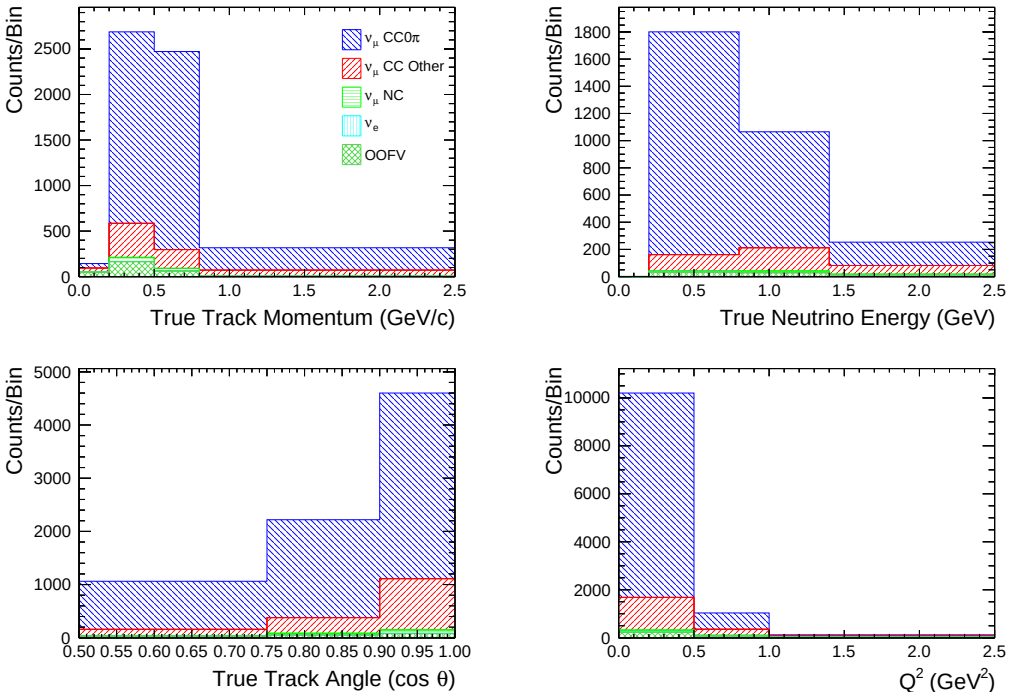

Figure 4.5.11: The distribution of NEUT Monte Carlo events for the ν_μ CC0π selection shown in terms of the several variables. These are the true momentum and angle of the muon produced in the interaction, the energy of the interacting neutrino and the four-momentum transfered in the neutrino interaction. These rely on the Monte Carlo truth information and so data can not be added to these plots.

The shapes of the event distributions for the ν_e CC selection in Figs 4.5.8 are strongly influenced by the shape of the backgrounds. The two largest backgrounds, the muon background and out of fiducial volume photon background, are both largest at low neutrino energies, low track momentum, and low four-momentum transfer. There is a strong preference for signal events to be very forward going due to the forward boosting of the beam, leading to a peak in the distribution at high values of $\cos(\theta)$. The background events have a less peaked distribution with respect to the angle of the candidate track. This is because the background tracks are often a secondry track from a neutrino interaction or from a secondary interaction and so tend to have a larger range of angles.

The events in the ν_e CC0π sample are a subset of those in the ν_e CC sample and the CC other interactions have similar distributions. Consquently, the distribution of these events are similar for both samples. The main difference is due to CC0π interactions being dominant at lower neutrino energies and so the distributions of events in terms of track momentum, neutrino energy and Q^2 are all peaked at lower values for the ν_e CC0π samples than the ν_e CC samples. The background from ν_e CC other interactions increases with energy, track momentum, and Q^2, as these interactions require more energy.

The ν_μ CC selection has a significantly lower rate of background interactions than the ν_e CC selection. This is primarily due to two reasons. Firstly, the flux of muon neutrinos in the beam is much higher than electron neutrinos so the relative amount of background events with no selections applied is much lower. Secondly, muons tend to travel much further into the detector and so are easier to identify than electrons, meaning the background rejection rate is higher. Due to this, the event distributions are dominated more by the signal events than the background events. The distributions are similar to those for the ν_e CC selection. The main differences arise from the energies of muon neutrinos in the beam being less than the energy of electron neutrinos. This means that distributions in terms of track momentum, neutrino energy and Q^2 are lower for the ν_μ sample.

As with the ν_e selections, the events in the ν_μ CC0π are a subset of those in the ν_μ CC sample with similar distributions for CC other to CC0π. This means that the distributions of events are similar for the two samples. The same arguments as used to describe the differences in the ν_e CC0π and ν_e CC samples apply and the result is distributions that are peaked at lower values of track momentum, neutrino energy and Q^2. The CC other background is the largest background to the ν_μ CC0π distribution, with the most contamination at larger values of neutrino enregy.

4.5.4 Purities and Efficiencies

To quantify how well the selections perform, the purities, ρ, and efficiencies, ϵ, are calculated. The purity is a measure of the proportion of selected events that are signal events, it is calculated in Eq 4.5.12. The efficiency is a measure of the number of signal events selected compared to the total number of signal events. Purity multiplied by efficiency is used as a measure of the performance of a selection as both should be maximised. Both purity and efficiency are dimensionless quantities.

$$\rho = \frac{\text{Number of signal events selected}}{\text{Total number of events selected}} \tag{4.5.12}$$

$$\epsilon = \frac{\text{Number of signal events selected}}{\text{Total number of signal events}} \tag{4.5.13}$$

The purities, efficiencies, and purities multiplied by efficiencies of the four selections are shown in Figs 4.5.12 - 4.5.15 for the ν_e CC, ν_e CC0π, ν_μ CC and ν_μ CC0π selections respectively. These are shown in terms of the same variables used to study the event distributions with the same binning.

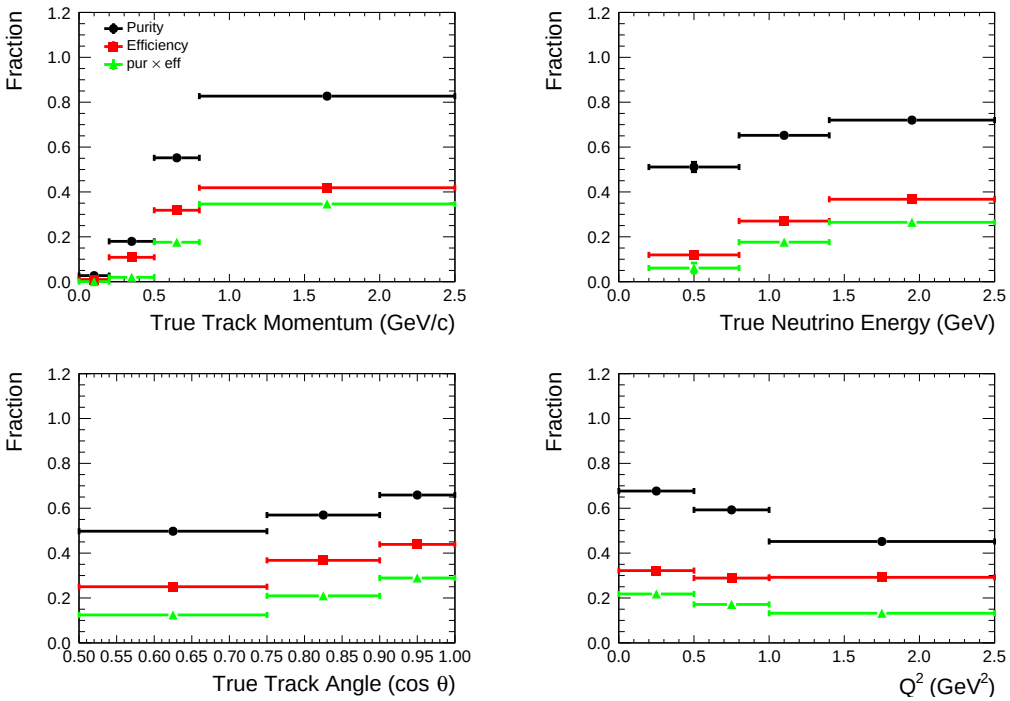

Figure 4.5.12: The purities and efficiencies of the ν_e CC selection using the same parameterisation as in Fig 4.5.8. The black points show the purities of each bin of the selection, the red points show the efficiencies and the green points show the product of the purities and efficiencies.

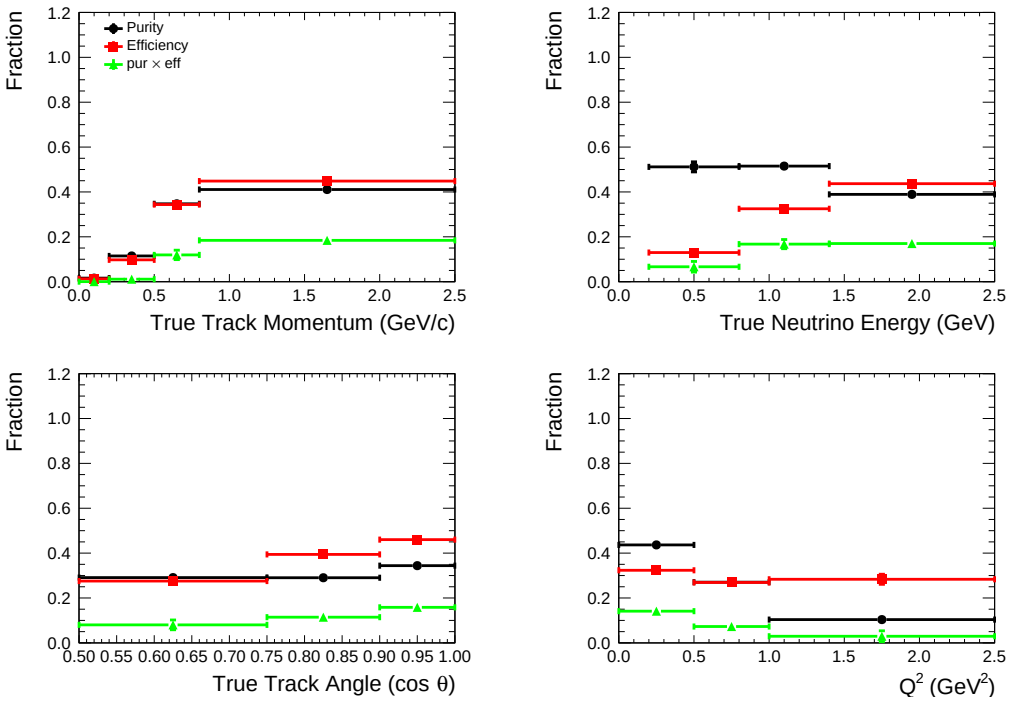

Figure 4.5.13: The purities and efficiencies of the ν_e CC0π selection using the same parameterisation as in Fig 4.5.9. The black points show the purities of each bin of the selection, the red points show the efficiencies and the green points show the product of the purities and efficiencies.

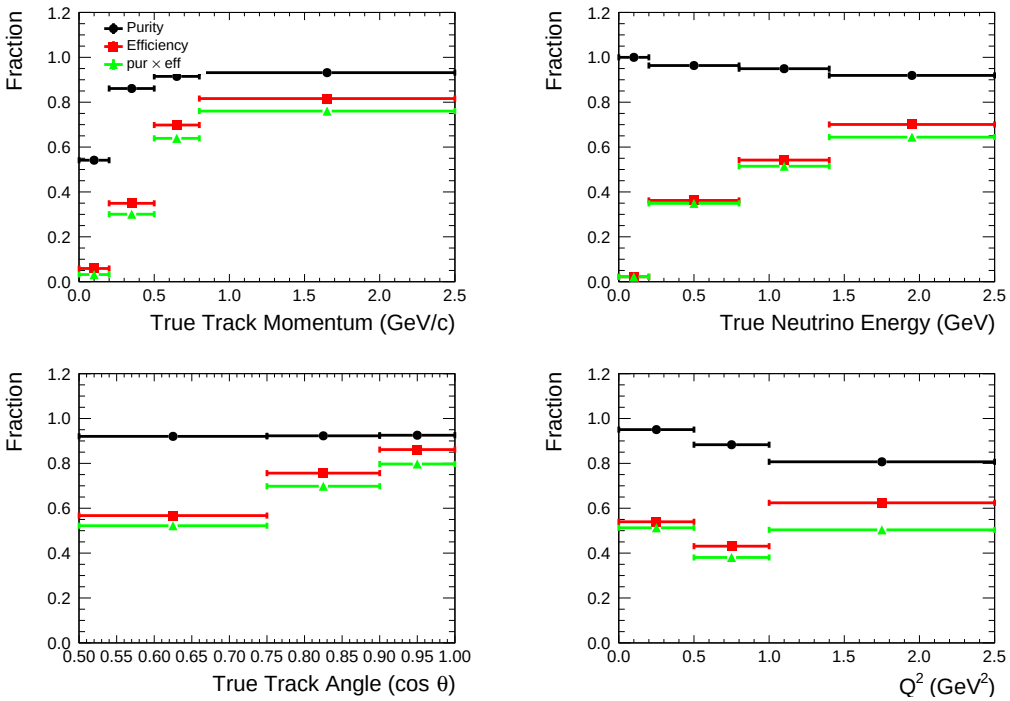

Figure 4.5.14: The purities and efficiencies of the ν_μ CC selection using the same parameterisation as in Fig 4.5.10. The black points show the purities of each bin of the selection, the red points show the efficiencies and the green points show the product of the purities and efficiencies.

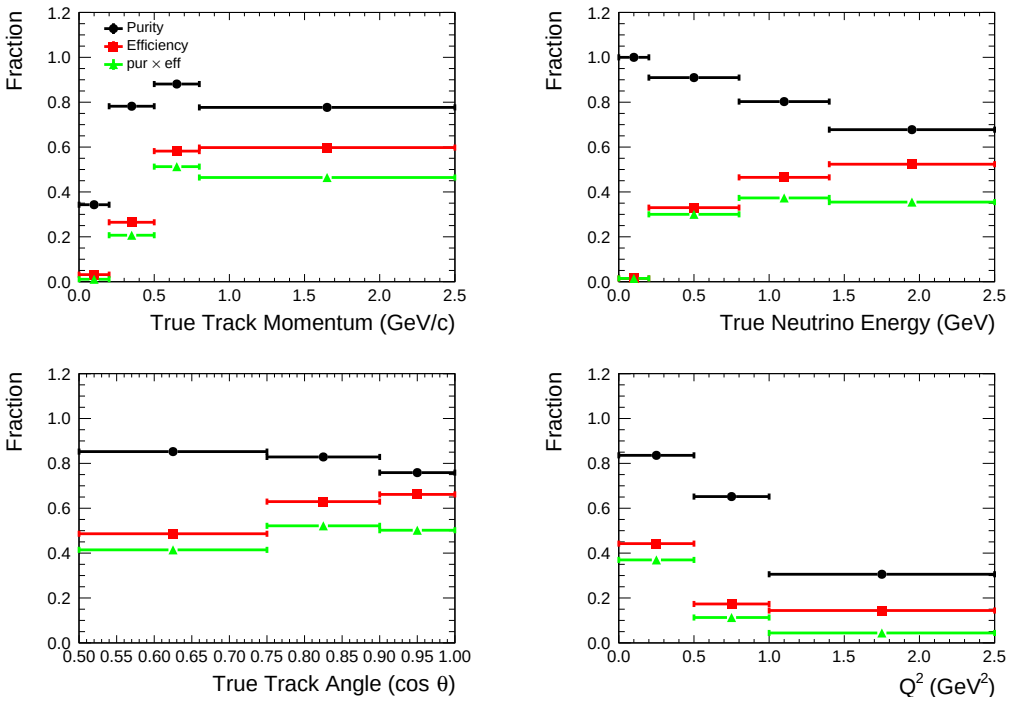

Figure 4.5.15: The purities and efficiencies of the ν_μ CC0π selection using the same parameterisation as in Fig 4.5.11. The black points show the purities of each bin of the selection, the red points show the efficiencies and the green points show the product of the purities and efficiencies.

The purity of the both the ν_e selections increases with track momentum. This is because the OOFV photon and ν_μ backgrounds tend to be low energy and so low track momentum. At higher track momentum, it is easier to differentiate muons from electrons. Due to how the OOFV photon events are produced, most of the initial neutrino energy doesn't go to the electron. The efficiency of the ν_e selections increases with track momentum and neutrino energy because low momentum electrons curve significantly in the magnetic field making them difficult to reconstruct accurately. At higher momentum, the tracks are easier to reconstruct and the efficiency improves. This means that above ≈ 0.6 GeV/c the reconstruction and identification of electron tracks doesn't improve much. Both the purity and efficiency suffer in the first bin, this is due to the cut on reconstructed track momentum at 0.2 GeV/c leading to very few events in this bin. Since these events have been badly reconstructed, they are more likely to be background events.

The purity and the efficiency of the ν_μ CC selection increases with track momentum for the same reasons as the ν_e selections; as these events are easier to reconstruct. For the ν_μ CC0π selection, the purity and efficiency initially increase with track momentum as the events are reconstructed more accurately. At higher momenta (above 1 GeV/c) the amount of charged current interactions that aren't CC0π interactions increases and the purity drops. Also the cuts to remove these events become less effective and the efficiency drops.

The purity of the ν_e selections increases with more forward angles. This is because the OOFV photon backgrounds tend to have a large spread in angles whereas the signal is peaked more at more forward angles. The efficiency of the ν_e selections also increases with more forward angles. This is because more forward going tracks tend to traverse more of the TPC, which helps with reconstruction.

The efficiency of the ν_μ CC and ν_μ CC0π selections increases with more forward angles as these events are easier to reconstruct as they will leave a longer path in a TPC. The neutral current background producing a single charged pion is strongly peaked at forward angles for the same kinematic reasons as the case of

the lepton produced in a charged current interaction. This has the affect that the purity decreases for very forward boosted tracks. For the CC0π sample, the largest background is CC other interactions. These also tend to be more forward boosted as the events that are incorrectly tagged as CC0π tend to only have one high-momentum track which tends to be forward going. This means the ν_μ CC0π sample has a lower purity than the ν_μ CC sample, particularly for forward going tracks.

4.6 Method

The interaction cross sections are calculated by first taking the event distributions described in Sec 4.5.3 and calculating a scaling factor to account for missed signal events (efficiency) and selected background events (purity). This scaling factor, f, is given by Eq 4.6.1 where ρ and ϵ are the purity and efficiency of a selection as calculated in Sec 4.5.4.

$$f = \frac{\rho}{\epsilon} \tag{4.6.1}$$

Another factor, φ, is needed for each bin to take into account the the fluxes of electron and muon neutrinos. A description of how this factor is calculated is given in Sec 4.6.1. The interaction cross section, σ, is then given by Eq 4.6.2 for the number of selected events x and the number of targets within the Fiducial Volume, N.

$$\sigma = \frac{\rho}{\epsilon} \cdot \frac{x}{\varphi N} \tag{4.6.2}$$

The ratio of two interaction cross sections, R, is then given by Eq 4.6.3 for x_1 and x_2 selected events. The number of targets cancels in the ratios and there will be partial cancellation in the flux weight that needs to be applied, this is described in Sec 4.6.1. The description of the correlations between the samples and how

the statistical uncertainties are calculated is given in Sec 4.7.1.

$$R = \frac{\varphi_2}{\varphi_1} \cdot \frac{\rho_1 \epsilon_2}{\rho_2 \epsilon_1} \cdot \frac{x_1}{x_2} \tag{4.6.3}$$

To calculate the cross sections and ratios of cross sections in terms of quantities that aren't directly accessible in data, such as neutrino energy or four-momentum transfer, an unfolding procedure is used. This also takes into account events migrating between bins due to errors in reconstruction. Unfolding uses a control sample to convert the distribution of events from one variable to another. The full methodology is described in Sec 4.6.2. The cross section calculated for an unfolded variable is given by Eq 4.6.4 where $\mathcal{U}(x_i)$ represents unfolding selected events in terms of variable x with bins i into another variable, y, with bins j. The purity is calculated in terms of the pre-unfolding variable ρ_i and applied to the selected events. Then the purity-weighted sample is unfolded and the efficiency and flux weight are calculated in terms of the post-unfolding variable and applied to the unfolded distribution. Lastly, because the data is binned, the width of each bin, w_j, needs to be taken into account too.

$$\left(\frac{d\sigma}{dy}\right)_j = \frac{\mathcal{U}(x_i \rho_i)_j}{\epsilon_j \varphi_j w_j N} \tag{4.6.4}$$

The cross section ratio in terms of an unfolded variable is then given by Eq 4.6.5. The width of the bins cancels out in this equation. However, the distribution of events within each bin will still play a role in the final result.

$$R_j = \frac{\mathcal{U}(x_i \rho_{i1})_j}{\mathcal{U}(x_i \rho_{i2})_j} \cdot \frac{\epsilon_{j2} \varphi_{j2}}{\epsilon_{j1} \varphi_{j1}} \tag{4.6.5}$$

4.6.1 Flux Weighting

When comparing ν_e and ν_μ cross sections, the different amount of ν_e and ν_μ in the beam needs to be taken into account. For the CC0π / CC ratios the flux

of signal events will cancel out as these interactions will be from the same neutrino species. This means the flux factor will be 1. However, due to slightly different backgrounds and thus slightly different proportions of ν_e and ν_μ in these selections, the flux will not cancel entirely. The correction for this needs to be calculated for each bin of the selection.

A weight for each event can be calculated for Monte Carlo using the flux histograms provided by the beam group. These show the number of each type of neutrinos in the beam as a function of neutrino energy for different runs. The ν_e and ν_μ fluxes, and the ratio of them, are shown in Fig 4.6.1 for the run2 beam with equivalent histograms existing for all T2K runs. In later runs, the beam power increased (refer back to Fig 2.2.6) leading to larger fluxes. Also, the beam width and position change slightly across runs and so each run must be treated separately.

These histograms are used to generate a weight for each event, w, in Monte Carlo by finding the value of the flux based on the energy and flavour of the interacting neutrino. A weight to be applied to each bin, φ, is calculated by summing the weights for each event, as in Eq 4.7.4 for n selected events in that bin.

$$\varphi = \frac{1}{n}\sum_{i=0}^{n} w_i \tag{4.6.6}$$

This weight can then be applied to the data or Monte Carlo. For data there is an extra complication; because the weight is calculated using Monte Carlo, the weight has to be scaled by the ratio of data events to Monte Carlo events in the bin to ensure that the weighting is applied for the correct number of events. This should then take into account the different numbers of ν_e and ν_μ in the beam when calculating a cross section or taking a ratio of them.

It was found that the flux weights for the CC0π and CC selections are very similar to each other such that their ratios are very close to 1. The weights for the ratios not being exactly one is due to different proportions of different neutrino

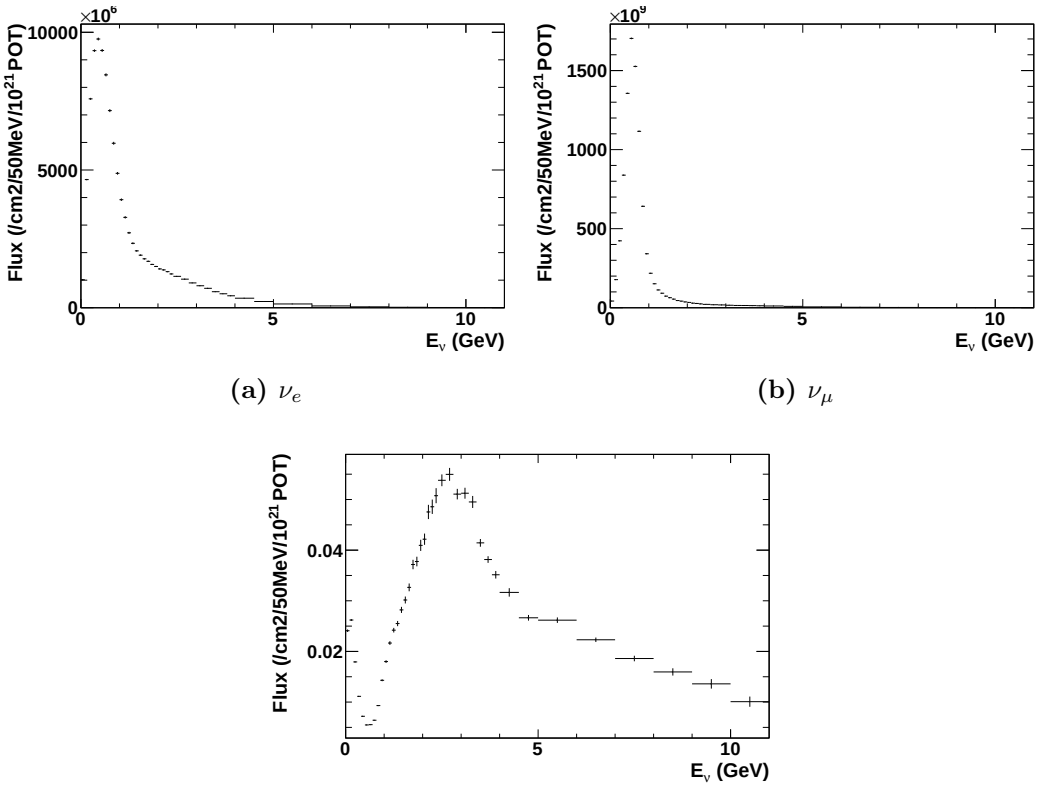

(a) ν_e **(b)** ν_μ

(c) ν_e / ν_μ

Figure 4.6.1: The flux of ν_e and ν_μ in the beam during run 2 per 50 MeV per cm^2 per 10^{21} protons on target.

flavours in the backgrounds to the selections. An example of the actual weights applied can be seen in Fig 4.6.2 for the ν_e CC0π / ν_e CC ratio.

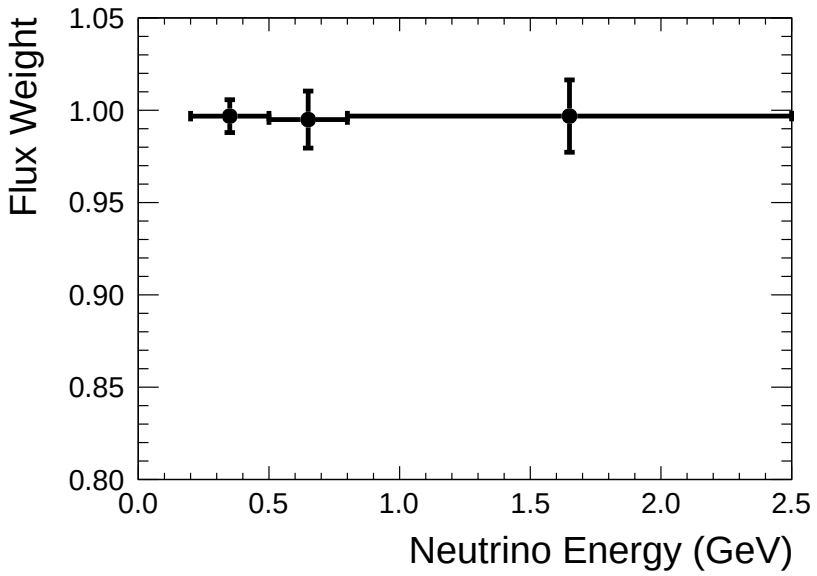

Figure 4.6.2: The flux weights that need to be applied to take into account the different amounts of ν_e and ν_μ in the beam for the ν_e CC0π / ν_e CC ratio. The weights not being exactly 1 is a consequence of slightly different backgrounds in the selections. The weights are calculated for the selections unfolded from candidate track momentum to neutrino energy.

4.6.2 Unfolding

A Bayesian unfolding technique [73] is used to take into account detector inefficiencies and reconstruction failures. Unfolding is a procedure that uses estimates of the probability of an event with some true value being measured with some reconstructed value to unsmear distributions in data. This method can be used to convert a reconstructed quantity to a "true" quantity, such as reconstruced track momentum to "true" lepton momentum or neutrino energy.

These probability estimates come from a statistically independent Monte Carlo sample. A response matrix encoding these probabilities, R_{mt}, is calculated based on event distribution n_m and true distribution μ_t^{MC} for reconstructed bins m and true bins t as shown in Eq 4.6.7.

$$n_m = \sum_t R_{mt} \ \mu_t^{MC} \tag{4.6.7}$$

An unsmearing matrix can be calculated using Bayes Theorem, for T true bins, as shown in Eq 4.6.8.

$$Я_{tm}^{(1)} = \frac{R_{mt} \ \mu_t^{MC}}{\sum_{i=0,T} \ R_{mi} \ \mu_i^{MC}} \tag{4.6.8}$$

The unsmearing matrix can then be applied to the reconstructed distribution to get a representation of the true distribution, as shown in Eq 4.6.9.

$$\hat{\mu}_t^{(i+1)} = \sum_m Я_{tm}^{(i+1)} \ n_m \tag{4.6.9}$$

A statistically and systematically independent sample is needed as a control sample. Otherwise this method would be equivalent to simply using the Monte Carlo truth information from the sample used to study background events and missed events (the NEUT Monte Carlo). The sample used for unfolding is GENIE Monte Carlo with 3.50×10^{21} POT.

The implimentation of unfolding is handled by RooUnfold [74]. Bayesian unfolding is chosen over other unfolding methods as it can be applied iteratively. Choosing zero iterations means that the response matrix is generated using only the Monte Carlo control sample. With each subsequent iteration, the unfolding result from the previous iteration is used as a prior to replace μ_i^{MC} in Eq 4.6.9. This means the data is used in the unfolding procedure, making it less model dependent than the other methods.

The response matrices for unfolding from reconstructed track momentum to true track momentum for the four selections are shown in Fig 4.6.3. Since there aren't significant biases in the reconstruction, the distributions are fairly symmetrical.

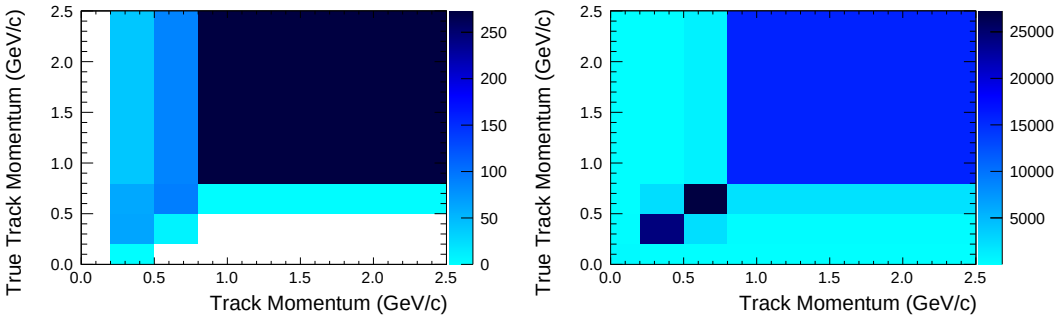

(a) ν_e CC0π **(b)** ν_μ CC0π

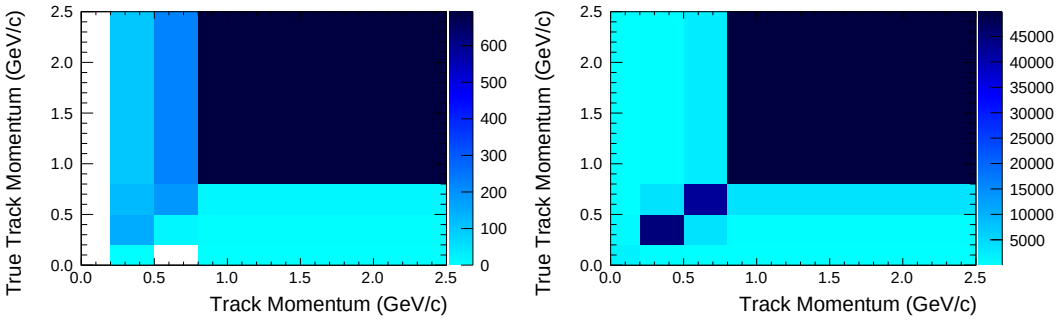

(c) ν_e CC **(d)** ν_μ CC

Figure 4.6.3: The response matrices for converting between reconstructed track momentum and true track momentum for events passing the four selections. These were made with an Monte Carlo sample that is statistically independent from the samples used to study the selections.

The response matrices for unfolding from reconstructed track momentum to neutrino energy for the four selections are shown in Fig 4.6.4. These are significantly different to the response matrices unfolding to true track momentum. This is because the neutrino energy is necessarily larger than the true track momentum, leading to a highly asymmetric response matrix. There are cases where the momentum is reconstructed incorrectly as being larger than the true neutrino energy. These are rare, but are consistent with the momentum resolution.

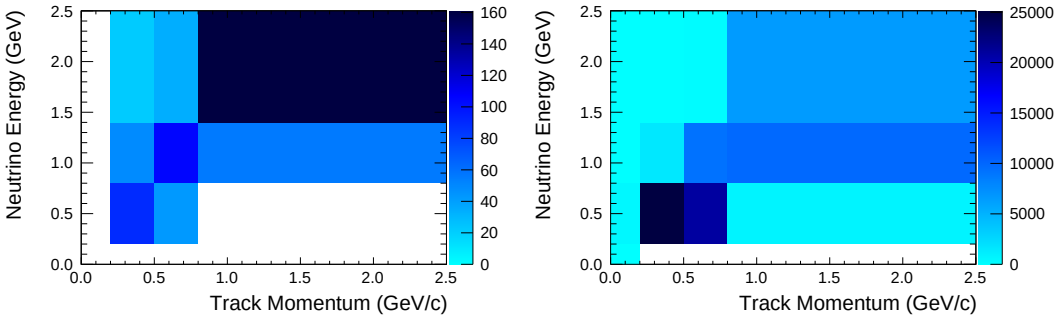

(a) ν_e CC0π **(b)** ν_μ CC0π

(c) ν_e CC **(d)** ν_μ CC

Figure 4.6.4: The response matrices for converting between reconstructed track momentum and neutrino energy for events passing the four selections. These were made with an Monte Carlo sample that is statistically independent from the samples used to study the selections.

As a check of this method, the unfolded distribution for data and fake data can be compared to the true distribution for a Monte Carlo sample. The results of this are shown in Fig 4.6.5 when unfolding from reconstructed track momentum to true neutrino energy.

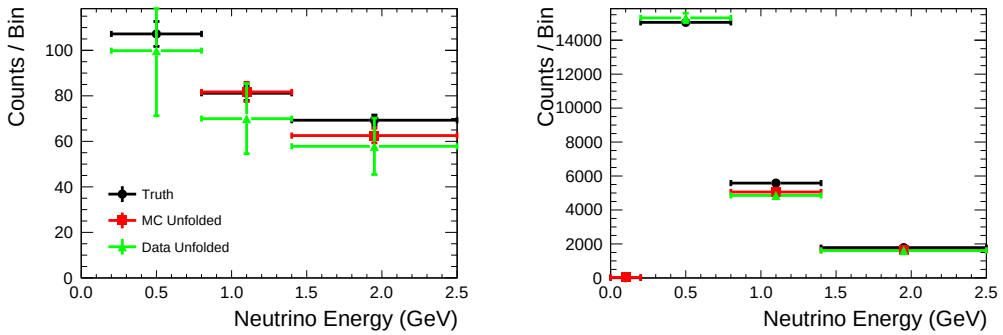

(a) ν_e CC0π **(b)** ν_μ CC0π

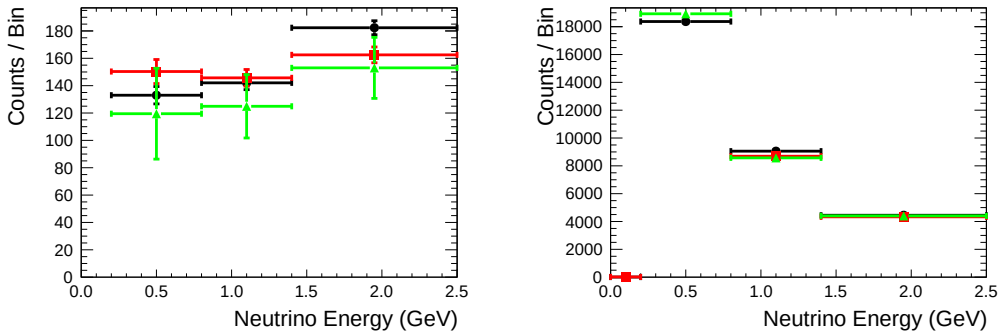

(c) ν_e CC **(d)** ν_μ CC

Figure 4.6.5: The four selections shown in terms of neutrino energy. The black points show the true number of events from the Monte Carlo. The red and green points show the selections in Monte Carlo and data unfolded with a control sample. The Monte Carlo distributions are scaled to the same POT as the data.

The reasonable agreement between the unfolded Monte Carlo and the truth from the Monte Carlo helps to validate the unfolding method. A perfect reproduction of the true distribution is not expected due to statistical and systematic differences between the control sample and the sample used for the selections. Iterating the unfolding will improve the agreement. The issue of the number of iterations

will be addressed shortly. The unfolded distribution of the data agrees well with the true distribution and unfolded distribution from the Monte Carlo. When using a Monte Carlo sample to unfold itself, it was found that the true distribution was reproduced perfectly. These results help validate the implimentation of the unfolding procedure.

The unfolding procedure is applied iteratively. With each sucessive iteration, the data is used to a greater extent in the unfolding procedure. As a consequence of this, the statistical fluctuations on the data has a greater effect with each iteration. The optimum number of iterations to apply is determined by calculating a χ^2 for unfolding based on the difference between the true and unfolded distributions. Since the unfolding isn't expected to reproduce the values from the Monte Carlo, the χ^2 can be quite large. More important is the different χ^2 values as a function of number of iterations. The number of iterations is then chosen by whether the χ^2 of the convergence decreases faster than the effect on the statistical uncertainty increases. Fig 4.6.6 shows the value of the χ^2 of the unfolding divided by the sum of the statistical uncertainty of the bins.

The downward trend shown in Fig 4.6.6 shows that one unfolding iteration is optimum, as the uncertainty on the result grows faster than the χ^2 of the unfolding decreases. In the case of a much larger data set, this may not be the case.

The issue of model dependencies is addressed in Fig 4.6.7. This shows two different models being used to unfold data from reconstructed track momentum to neutrino energy for the four selections. If the results of unfolding data using a GENIE sample, shown in black, and a NEUT sample, shown in red, show significant differences, then the models have a large impact on the result. The points do agree reasonably well, which is a good sign. However, it is not true that similar results mean that the result is not model independent, as the two models may be incorrect in the same way.

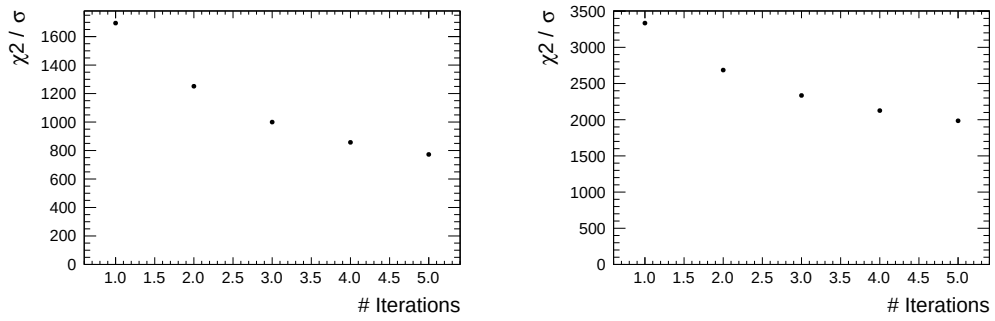

(a) ν_e CC0π **(b)** ν_μ CC0π

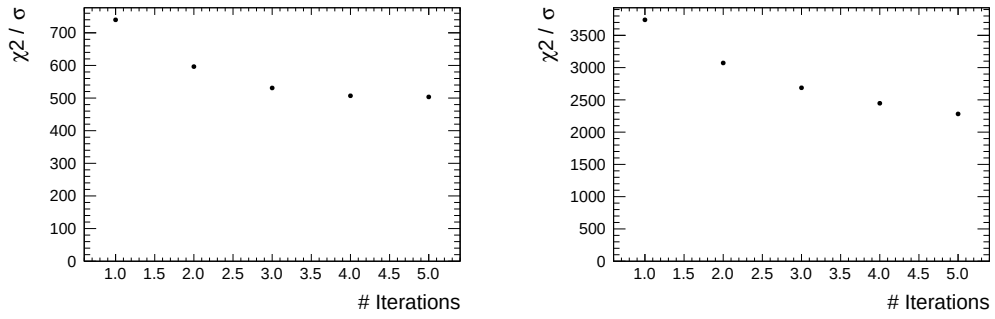

(c) ν_e CC **(d)** ν_μ CC

Figure 4.6.6: The χ^2 of the unfolding procedure on data divided by the statistical uncertainty on the result of the unfolding with the number of unfolding iterations.

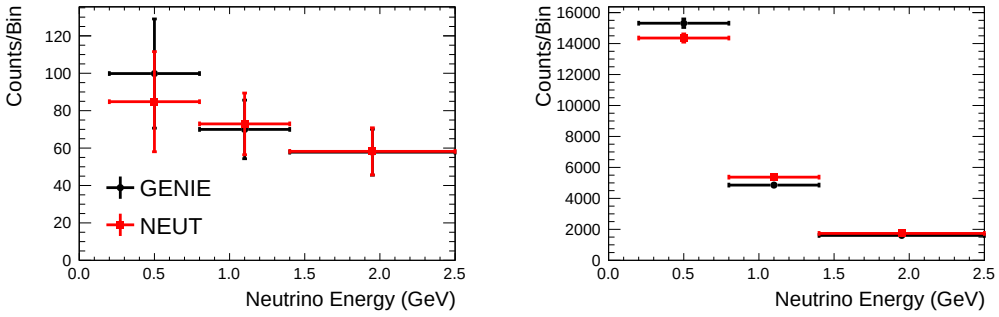

(a) ν_e CC0π **(b)** ν_μ CC0π

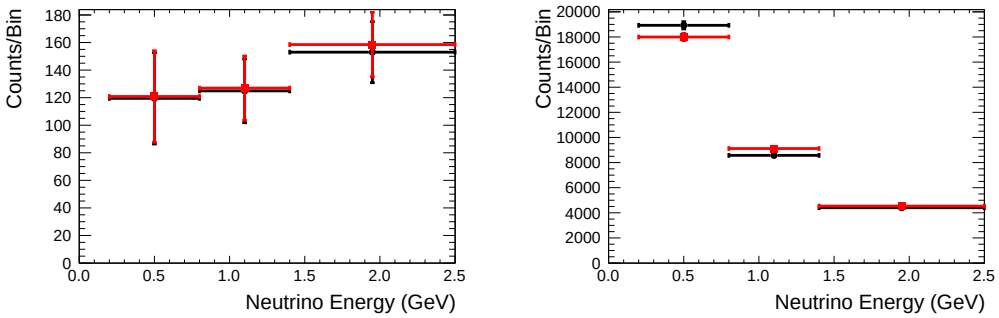

(c) ν_e CC **(d)** ν_μ CC

Figure 4.6.7: A comparison of how two different models can affect the results of unfolding for the four selections. The points show data unfolded with a GENIE Monte Carlo sample (black) and a NEUT Monte Carlo sample (red). The uncertainties are statistical only.

4.6.3 Binning

The binning to use for each variable is determined by studying the distribution of events with the Monte Carlo. The choice of binning is determined by two factors; maintaining enough statistics in each bin to ensure a relatively low statistical error $\mathcal{O}(10\%)$, and having a roughly equal number of events across each bin. The latter is difficult as the distributions of events are sharply peaked in all the variables being studied. The bins chosen due to these criteria will be large enough that the measurement resolution will not have a significant effect.

Since there are far more events for the ν_μ selections than for the ν_e selections, it would be ideal to use finer binning for these selections and the ν_μ single ratio. However, when taking the ν_e to ν_μ double ratio, the statistics of the ν_e samples are far more important. So the binning chosen is based on what is optimum for the ν_e selections.

4.6.4 Method Test

As a check of this method, the cross sections are calculated using Eq 4.6.4 with the NEUT Monte Carlo sample and the data, then compared with the Monte Carlo predictions given in Sec 4.3. Since the Monte Carlo generators do not calculate cross sections in terms of the final state topology, the CCQE cross section is calculated in place of CC0π for these comparisons. The resulting cross sections are given in Fig 4.6.8 for NEUT simulated data shown as black points, the data shown as red points, with NEUT and GENIE calculations shown as curves in blue and red respectively. These are plotted in terms of true neutrino energy unfolded from reconstructed track momentum using the GENIE sample acting as a control sample. The points from data show full statistical and systematic uncertainties whilst the Monte Carlo points show only statistical uncertainties. A description of how these uncertainties are calculated is given in Sec 4.7

The choice of binning for the cross section plots is important for several reasons. If the bins are too large and encompass areas in with very few events (due to the bin covering a range not possible with the T2K beam), then the division by bin width in Eq 4.6.4 will cause the cross section to be measured at too low a value. On the other hand, if the bins are too small, then the statistical uncertainties will grow rapidly. On top of this, the distributions of events within the bins needs to be considered. If most of the events inside a bin are at the lower end of the bin, then it will pull the measured value of the cross section towards the value at the lower energy. For this reason, the choice of binning used for the cross sections is different than that used for the cross section ratios, as these effects will matter less for the ratios where the statistics are the chief concern.

The Monte Carlo distributions agree quite well with the calculations from the Monte Carlos within the statistical uncertainties. There are statistical fluctuations on the event selections and unfolding control sample that prevent a perfect reproduction of the predicted cross section. The slight disagreement between the NEUT points and the NEUT calculation for the ν_e CC and ν_μ CC cross sections is attributed to model dependency assoicated with unfolding to neutrino energy. However, the general shape and magnitude of the cross sections are roughly as expected. This indicates that the method to extract the cross sections with the unfolding and flux weighting can reproduce the values in the Monte Carlo. The data shows a systematic difference from the Monte Carlo predictions for the ν_e cross sections but agrees reasonably well for the ν_μ cross sections. This indicates a disagreement between the Monte Carlos and the data. Taking the ratios of these will help determine whether this is a problem with a particular contributor to the charged current cross section or whether the total is mismodelled. It is a simple extension to this method to calculate the ratios of the cross sections.

Using unfolding requires the use of a model to determine the distribution of events in some quantity given another. Due to this, unfolding means that the results are dependent on how accurately the models simulate the process. Studying quantities like neutrino energy and four-momentum transferred requires a good understanding of the neutrino cross section and the interactions of secondary

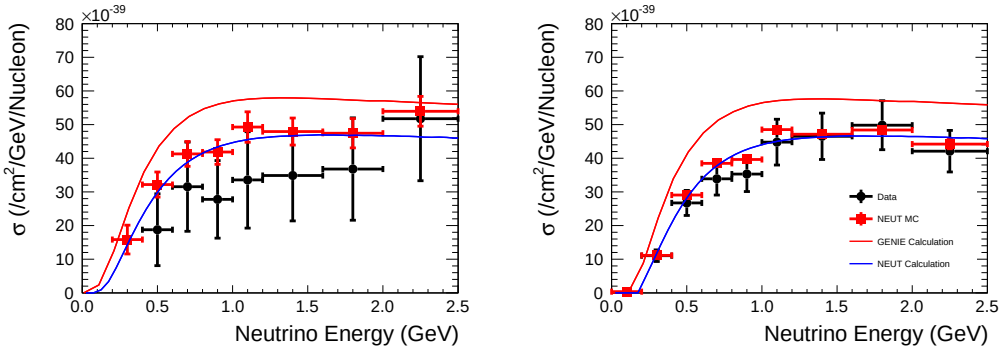

(a) ν_e CCQE **(b)** ν_μ CCQE

(c) ν_e CC **(d)** ν_μ CC

Figure 4.6.8: The ν_e and ν_μ cross sections for CCQE and CC interactions, plotted in terms of neutrino energy unfolded from reconstructed track momentum using a GENIE control sample. The blue and red lines show calculations from the NEUT and GENIE Monte Carlo generators respectively. The red data points show the cross section calculated using events simulated with NEUT with statistical uncertainties only and the black points show data with full systematic and statistical uncertainties. The calculation of these errors will be described later. The measured values and their uncertainties for data are presented in Tab 4.6.1.

E_ν (GeV)	$\sigma(\nu_e\text{CC})$	$\sigma(\nu_e\text{CCQE})$	$\sigma(\nu_\mu\text{CC})$	$\sigma(\nu_\mu\text{CCQE})$
0 - 0.2	0	0	0	0
0.2 - 0.4	0	0	1.84 ± 0.11	1.67 ± 0.11
0.4 - 0.6	3.34 ± 1.59	2.30 ± 1.21	3.88 ± 0.09	2.90 ± 0.08
0.6 - 0.8	5.32 ± 1.78	3.22 ± 1.24	5.91 ± 0.11	3.34 ± 0.08
0.8 - 1	6.30 ± 1.88	2.83 ± 1.11	7.17 ± 0.17	3.30 ± 0.12
1 - 1.2	9.75 ± 2.79	4.06 ± 1.52	9.55 ± 0.30	3.94 ± 0.20
1.2 - 1.6	10.0 ± 2.4	3.42 ± 1.28	12.0 ± 0.4	4.48 ± 0.23
1.6 - 2	13.3 ± 3.0	4.38 ± 1.65	16.3 ± 0.6	4.63 ± 0.34
2 - 2.5	14.5 ± 3.2	3.1 ± 1.3	19.4 ± 0.8	4.23 ± 0.35

Table 4.6.1: The four measured cross sections (in units of 10^{-38} cm^2/ GeV/ Nucleon) with the total systematic and statistical uncertainty for each bin. The values given are for data. The ν_e cross sections calculated are 0 for 0 - 0.4 GeV. This is due to a lack of events in these bins in data after unfolding, not a lower threshold for interactions. This affects the ν_e results more because there are fewer ν_e in the beam and they tend to have higher energies.

particles within the nucleus. Since these are not well known, it adds uncertainty to the final result. Unfolding to lepton momentum is safer as the track momentum is directly measurable in the detector and so do not rely on nuclear models or cross section models to extract the results. Also, comparisons between data and Monte Carlo distributions for reconstructed track momentum and angle help validate the results. Consequently, the results are classified as either model dependent for neutrino energy and four-momentum transfer, or model independent for track momentum and track angle.

4.7 Uncertainties

The uncertainties on the cross sections or ratios can be broken down into 5 uncorrelated types: statistical, flux, cross section, final state interactions (FSI), and detector uncertainties. These are calculated separately as they won't have any affect on each other. The calculation of the statistical uncertainties is given in Sec 4.7.1. The other four are calculated using a similar procedure as described in Sec 4.7.2.

The individual sources of uncertainty that contribute to the flux, detector, cross section and FSI uncertainties are described in Sec 4.7.3 - 4.7.6. The individual components of these uncertainties are treated as correlated when calculating the covariance and error matrices, otherwise the uncertainties would be overestimates.

4.7.1 Statistical Uncertainties

The statistical uncertainties on the selections are treated as the square root of the number of events in each bin. When taking the event ratios, the statistical uncertainties are calculated using Binomial statistics for cases where one selection is a subset of the other (i.e. CC0π to CC) or Poisson statistics for the double ratios.

The calculations of these uncertainties for ratio n_1/n_2 are shown in Eqs 4.7.1 and 4.7.2 for Binomial and Poisson uncertainties respectively.

$$\sigma_B = \frac{1}{n_2}\sqrt{n_1\left(1-\frac{n_1}{n_2}\right)} \tag{4.7.1}$$

$$\sigma_P = \frac{n_1}{n_2}\sqrt{\left(\frac{1}{n_1}+\frac{1}{n_2}\right)} \tag{4.7.2}$$

The uncertainties on the efficiencies and purities have to be taken into account when weighting the selections. These can also be described by binomial statistics (Eq 4.7.1). These are added in quadrature with the statistical uncertainties on a selection or a ratio.

The statistical uncertainty when unfolding is handled by the RooUnfold package. An uncertainty is calculated for the unfolding by repeatedly varying the covariance matrix used to relate the reconstructed quantity to the true quantity. These variations are propagated to the unfolding result and an uncertainty calculated by comparing to the nominal result. This is similar to the method used to propagate the systematic uncertainties in Sec 4.7.2. For a single selection, the statistical uncertainty in each bin post-unfolding is calculated as the square root of the number of events in that bin added in quadrature with unfolding uncertainty. This uncertainty is then propagated through the ratios with the uncertainties on the purities and efficiencies.

A breakdown of fractional statistical uncertainties on the selections and ratios, and the efficiencies and purities is summarised in Tab 4.7.1 for unbinned events.

Analysis	Selected	Purity	Efficiency	Total
ν_e CC0π	0.057	0.0065	0.0056	0.057
ν_e CC	0.053	0.0038	0.0061	0.053
ν_μ CC0π	0.011	0.00078	0.0011	0.011
ν_μ CC	0.0065	0.00058	0.00046	0.0065
ν_e CC0π/ν_e CC	0.018	0.0075	0.0083	0.021
ν_μ CC0π/ν_μ CC	0.0031	0.00097	0.0012	0.0035
DR	0.019	0.0075	0.0084	0.022

Table 4.7.1: A summary of the fractional statistical uncertainties on the number of selected events and the purity and the efficiency for the four selections and ratios. No binning is used for these calculations and therefore unfolding is also unused (unfolding doesn't change the total number of events). The sample used for the selections is the full data set, whereas the efficiency and purity calculations are done using the full NEUT Monte Carlo sample.

4.7.2 Systematic Uncertainty Propagation

For each source of systematic uncertainty, a fractional covariance matrix is calculated. This relates how each flavour and energy bin is affected by changes in the systematic parameters and how the changes in each bin affects the other bins. An error matrix is then calculated by Cholesky Decomposing the covariance matrix [75], which is then used to propagate the uncertainties to the event selections and interaction cross section ratios.

For the flux uncertainty, a fractional covariance matrix is provided by the T2K beam group. For the detector, cross section and FSI uncertainties, the covariance matrices have to be calculated as part of this work. A series of different weights are calculated for each event using a Gaussian distribution with a width based on the results of separate T2K analyses. An example of such is given in Sec 3.3 where the calculated uncertainties correspond to the width of the gaussian. The detector, cross section and FSI uncertainties have multiple sources of

uncertainty contributing to the total, so the events weights are calculated by randomly throwing each variable simultaneously. The different sources are described in the following sections.

The covariance matrix is then calculated as in Eq 4.7.3 for n calculated weights and b bins of energy and flavour. χ and w are the nominal and weighted numbers of events in each bin of energy and flavour respectively.

$$C_{bb} = \sum_{i=0}^{n} \left[\sum_{j=0}^{b} \sum_{k=0}^{j} (\chi_j - w_{i,j})(\chi_k - w_{i,k}) \right] \tag{4.7.3}$$

For the detector, cross section and FSI uncertainties, 1,000 weights were used to calculate the fractional covariance matrices. The resulting matrices are shown in Fig 4.7.1. The binning used is taken from the covariance matrix provided by the T2K beam group for the neutrino flux uncertainty. This matrix contains 25 neutrino energy bins for the flux in the ND280; 11 ν_μ bins, 5 $\bar{\nu}_\mu$ bins, 7 ν_e bins, and 2 $\bar{\nu}_e$ bins. The error matrices resulting from Cholesky Decomposing the fractional covariance matrix are shown in Fig 4.7.2.

The systematic uncertainties for a selection are estimated by creating many toy experiments where the number of events in each bin is weighted (thrown) for each neutrino species. The resulting distributions for each toy experiment are then compared to the nominal distribution to calculate the uncertainty. A vector of random numbers from a gaussian distribution of mean 0 and width 1 is multiplied by the relevant error matrix to get the weight, $f_{\nu iE}$, for each toy experiment, i, for each neutrino flavour, ν, for a particular neutrino energy, E.

To calculate the flux uncertainty in terms of any variable, x, not just neutrino energy, a weight for each bin in x is needed. To do this, a 2D distribution of x against neutrino energy, E, is made for each neutrino type. For each bin in x, all the energy bins are weighted by $f_{\nu iE}$ and then summed. This gives the total weight to be applied for that variable for that neutrino species. Thus the weights

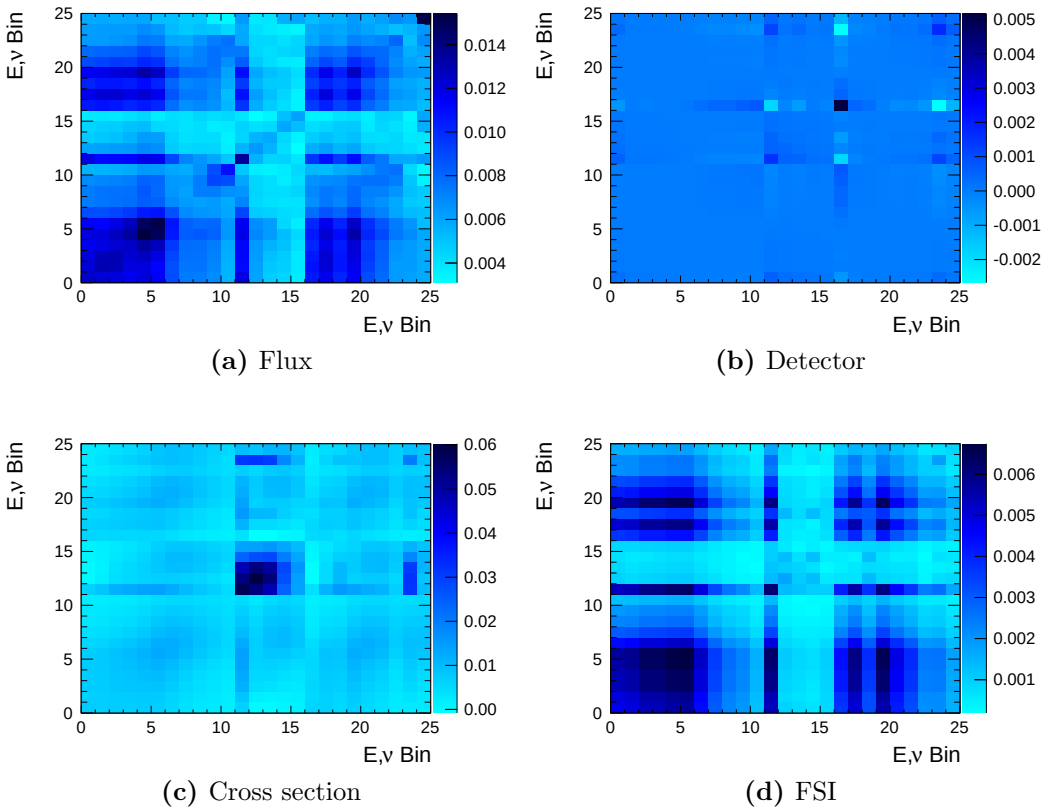

(a) Flux **(b)** Detector

(c) Cross section **(d)** FSI

Figure 4.7.1: The covariance matrices used to propagate the systematic uncertainties to the event selections and cross section ratios. The 25 bins are bins of neutrino energy and flavour; 11 ν_μ bins, 5 $\bar{\nu}_\mu$ bins, 7 ν_e bins, and 2 $\bar{\nu}_e$ bins. The binning was chosen based on the flux covariance matrix provided by the T2K beam group.

for each bin, $W_{\nu i}$, for neutrino flavour ν and toy experiment i, are calculated as in Eq 4.7.4 where y_ν is the number of events in the energy bin of the 2D histogram. For n toy experiments, the flux uncertainty, σ, is given by Eq 4.7.5 where x_ν is the number of events in the selection. In Eq 4.7.5 the calculation of the uncertainty is simply the standard deviation from the mean where the formula is modified to sum each of the neutrino flavours that contribute to the number of events for each toy.

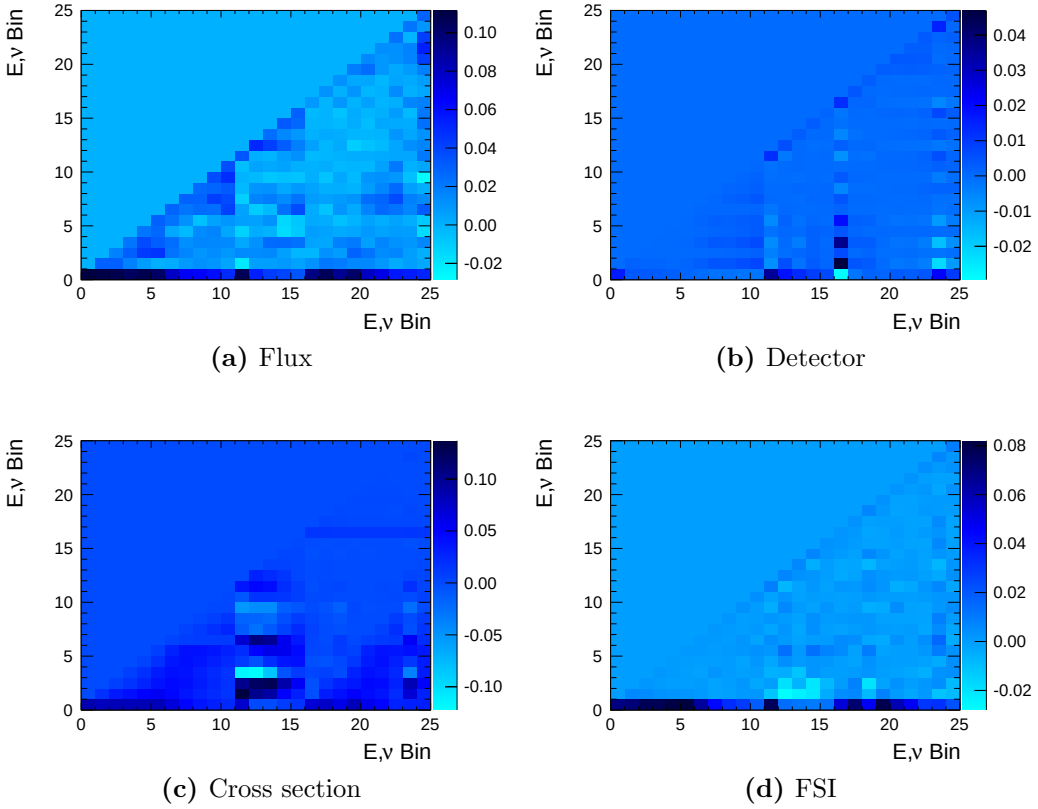

(a) Flux **(b)** Detector

(c) Cross section **(d)** FSI

Figure 4.7.2: The error matrices calculated by Cholesky Decomposing the covariance matrices shown in Fig 4.7.1. These are used when generating the different toy experiments.

$$W_{\nu i} = \sum_{E} f_{\nu i E} y_{\nu} \tag{4.7.4}$$

$$\sigma = \sqrt{\frac{1}{n}\sum_{i=1}^{n}\left[\sum_{\nu}\Big(x_{\nu} - x_{\nu}(1 + W_{\nu i})\Big)\right]^{2}} \tag{4.7.5}$$

For the ratios, the same procedure is used where for each toy the contribution of each neutrino type to both selections is weighted by the same amount. Likewise for the double ratio. This is described in Eq 4.7.6 for a single ratio where x_{ν} and y_{ν} are the number of events in the first and second selection respectively with

neutrino parent, ν.

$$\sigma = \sqrt{\frac{1}{n}\sum_{i=1}^{n}\left[\frac{\sum_\nu x_\nu}{\sum_\nu y_\nu} - \frac{\sum_\nu x_\nu W_{\nu i}}{\sum_\nu y_\nu W_{\nu i}}\right]^2} \tag{4.7.6}$$

The uncertainties are propagated in a similar manner when considering the unfolded distributions. The difference is that the number of events in each bin is weighted, then unfolded, then compared with the nominally unfolded value. If the number of events in a bin is represented by x for the pre-unfolded distribution, then the number of events in a bin of the unfolded distribution is denoted $\mathcal{U}(x)$. In addition, the response matrix used to perform the unfolding is thrown using the same tweaks used to throw the selections for each toy. The calculations of the uncertainties in the unfolded distributions are then described by Eq 4.7.7 and by Eq 4.7.8 for the ratios of unfolded distributions.

$$\sigma = \sqrt{\frac{1}{n}\sum_{i=1}^{n}\left[\sum_\nu \Big(\mathcal{U}(x_\nu) - \mathcal{U}(x_\nu(1+W_{\nu i}))\Big)\right]^2} \tag{4.7.7}$$

$$\sigma = \sqrt{\frac{1}{n}\sum_{i=1}^{n}\left[\frac{\sum_\nu \mathcal{U}(x_\nu)}{\sum_\nu \mathcal{U}(y_\nu)} - \frac{\sum_\nu \mathcal{U}(x_\nu W_{\nu i})}{\sum_\nu \mathcal{U}(y_\nu W_{\nu i})}\right]^2} \tag{4.7.8}$$

4.7.3 Flux Uncertainties

The flux uncertainty is the uncertainty on the number and energy of each type of neutrino in the beam. Mismodeling the neutrino flux could cause rate and shape differences in the results. The NA61/SHINE experiment [76] at CERN provides constrains on the T2K flux [77], which helps to reduce the uncertainties on T2K analyses.

NA61/SHINE is an experiment designed to study hadron production in hadron-proton, hadron-nucleus and nucleus-nucleus collisions. It uses several different

targets for studying these collisions including a replica of the T2K target. The energy of the proton beam can be matched to the 31 GeV used by T2K [76]. The results from NA61/SHINE are used to determine the uncertainty on several of the different components to the total flux uncertainty [77].

The individual sources of uncertainty that lead to the flux uncertainty in the ND280 are given below. These are all included in the fractional covariance matrix shown in Fig 4.7.1.

1. **Pion production.**
   The rate of pion production when the proton beam hits the target has a significant effect on the flux of muon neutrinos in the beam. This would have a large effect on the ν_e/ν_μ ratios.

2. **Kaon production.**
   The rate of kaon production when the proton beam hits the target has a significant effect on the flux of electron neutrinos in the beam. This would have a large effect on the ν_e/ν_μ ratios.

3. **Secondary nucleons.**
   The amount of secondary nucleons further affects the amount of pions and kaons, and therefore the flux of electron and muon neutrinos.

4. **Production cross sections.**
   This is the total cross section of protons interacting with the target. It mostly affects the beam flux normalisation with a slight effect on the shape. Consequently, it shouldn't affect the ratios much.

5. **Beam angle.**
   The off-axis angle of the neutrino beam significantly affects the flux and energy of neutrinos in the ND280 (see Fig 2.2.4).

6. **Protons on target.**
   If the number of protons in the proton beam is modelled incorrectly, it would change the flux of neutrinos but not the energy spectrum or the ratio of ν_e to ν_μ in the beam.

7. **Horn alignment.**
   If the magnetic horns focus the beam differently to expectation, then it could change the off-axis angle and width of the beam, altering the neutrino flux significantly.

8. **Horn current.**
   The operating current of the focusing horns affects how focused (narrow) the neutrino beam is. It could potentially affect the energy spectrum of the neutrino beam.

4.7.4 Detector Uncertainties

The detector uncertainties relate to the performance of the detector and how it is modelled. These include reconstruction failures, detector inefficiencies and smearing of measured values from the true values. These can effect both the rate and shape of the cross sections and the ratios of the cross sections.

The sources of uncertainty associated with the detector are detailed below. The uncertainties of these individual systematics are determined with custom T2K analyses (such as the one described in Sec 3.3) and the results are used to generate event weights for the parameter affected by the systematic. Additional detail on all of these can be found in [72]. When calculating the covariance matrix for the detector systematics, all of these parameters are thrown simultaneously to create a combined weight for each toy experiment.

1. **Magnetic field distribution.**
   If the distribution of the magnetic field is not modelled properly then it would affect the measured momentum of a track. Refer back to Fig 2.2.9 for the variation in magnetic field strength in a TPC.

2. **Momentum measurement scale.**
   The measurement of the momentum of a track depends on the absolute strength of the magnetic field. This is different to the magnetic field distribution systematic but can similarly affect the momentum measurements.

3. **Momentum resolution.**
   There is a difference found in data and Monte Carlo for the momentum resolution of a track as measured using the curvature of the track. This systematic is applied to take this into account by smearing the reconstructed momentum in the Monte Carlo. The effect changes as a function of momentum but is typically 5% - 10%. The potential effect of this uncertainty is a possible change in shape for the extracted interaction cross section ratios.

4. **Momentum range resolution.**
   This systematic uncertainty is similar to the mometum resolution systematic but concerns the momentum resolution determined using the range of the track. It has similar consequences of potentially changing the shape of an extracted interaction cross section.

5. **Particle identification in the TPCs.**
   Uncertainties on the measured dE/dx pulls in the TPCs could affect the relative numbers of different particles selected.

6. **Particle identification in the FGDs.**
   An incorrectly identified track in the FGD could change how the event is classified by incorrectly reconstructing the number of protons leaving the interaction vertex.

7. **Energy resolution in the ECals.**
   If the energy of an ECal segment is incorrectly calculated it could change the measured momentum of the track and the number of selected events of different particles. The ν_μ selections do not use the ECals and so this uncertainty will only affect the ν_e selection.

8. **Charge confusion.**
   For very straight tracks, backwards-going or highly curved tracks, the electric charge can be reconstructed incorrectly. This will change the number of background events in the selection and the number of missed signal events.

9. **TPC track reconstruction efficiency.**
   This concerns the efficiency of reconstructing an isolated TPC object. If

this is mismodelled then the relative number of background events will be different between data and Monte Carlo.

10. **FGD track reconstruction efficiency.**
    If the efficiency of reconstructing FGD objects is different in data and Monte Carlo, then the relative number of events rejected by the FGD veto cuts will be different and the number of background events in the selections will be different. It could also affect the reconstruction of the topology of the event by having a different rate of missed proton tracks in data and Monte Carlo.

11. **FGD to TPC track matching efficiency.**
    If the efficiency of matching a track across an FGD and a TPC is not modelled correctly in the simulation, then the number of missed signal events will be incorrecly calculated.

12. **Number of OOFV background events.**
    For a description of the different types of OOFV background events refer back to Sec 4.5.3. Most of these are caused by some sort of reconstruction failure and so have reconstruction-related uncertainties applied to them. The largest contributor to the OOFV background is events that interact upstream of the target FGDs, typically the PØD, ECals or magnets. The interaction cross sections on the heavy targets in these modules is poorly understood and so have a large uncertainty associated with them. This systematic uncertainty should have a much larger affect on the ν_e selections than the ν_μ selections since the OOFV background is much larger.

13. **Pile up.**
    This systematic affects the cuts designed to veto interactions upstream of the target FGD. The pile up is the number of interactions in the detector within a beam spill. If this is miscalculated for the simulation then the number of events rejected by the veto cuts will be different for data and Monte Carlo.

14. **The mass of the FGD.**
    If the known mass of the FGD is incorrect, then any extracted interaction cross section on the FGDs will be scaled to the wrong number of nucleons. Due to engineering tolerances involved in production the mass is not perfectly known. A previous study has shown the uncertainty on this is 0.67% [80]. For the ratio of interaction cross sections on the same target, this should completely cancel out.

15. **Michel electron reconstruction efficiency**
    The reconstruction efficiency for decay electrons in the FGD is relevant for identifying background events due to low-momentum pions. If this is mismodelled then the number of background events due to other particles will be different for data and Monte Carlo.

16. **TPC clustering efficiency.**
    This is related to the probability of finding a group of single TPC hits (a cluster) that corresponds to a track in the TPC. A difference in efficiency for data and Monte Carlo would cause a different fraction of events to pass the criteria on the number of TPC hits in data and Monte Carlo.

17. **ECal object reconstruction efficiency**
    This concerns the efficiency of reconstructing an ECal object, particularly the cuts to veto various backgrounds originating in the ECals and the PID for the ν_e selection. If the efficiency is modelled incorrectly, then the background contributions to the selections will be different for Monte Carlo and the data.

18. **Particle identification in the ECals.**
    Uncertainties on the performance of the ECal PID variables will affect the numbers of background events in the selection and the number of missed signal events. Since the ν_μ selection does not use ECal information, this should only affect the ν_e selection.

19. **TPC to ECal track matching efficiency.**
    The number of missed signal events in the selections could be mismodelled

due to a miscalculation of the efficiency of matching a track between a TPC and an ECal. A detailed description of how this is calculated is given in Sec 3.3. This should only affect the ν_e selections as the ν_μ selections don't use ECal information.

20. **FGD to ECal track matching efficiency.**
    This is similar to the TPC to ECal track matching systematics but concerns FGD track matching. This shouldn't affect any of the selections as none of them include tracks with this topology.

21. **Pion secondary interactions.**
    A pion produced in a neutrino interaction can undergo an interaction with a nucleus after travelling away from the neutrino interaction vertex. Possible interaction types are elastic scattering, absorption, and charge exchange. These mechanisms are not well understood and make it difficult to identify pion tracks. Consequently, the amount of pion background events that are rejected will not be well understood.

4.7.5 Cross section Uncertainties

The cross section uncertainty relates to how likely a neutrino is to interact within the detector and the topology of the interaction. This is dependent on the flavour and the type of interaction the neutrino undergoes.

The weights calculated for an individual cross section uncertainty are based on previous measurements of neutrino interaction cross sections. The Gaussian used to generate the weights has a width that is related to the uncertainty on the previous measurements. Where these measurements show inconsistencies or disagreement with the models, the range of weights calculated is larger leading to a larger uncertainty on this analysis. NEUT is used to calculate a total weight for the cross section uncertainty for each event. These weights are then used to calculate the covariance matrix given in Fig 4.7.1. The most important source of

external data is from the MiniBooNE experiment [78]. A more detailed description of how this is used is given in [79].

The sources of uncertainty in neutrino cross sections that can contribute significantly to the analysis are listed below.

1. **The axial mass in Quasi-Elastic interactions.**
   The axial mass essentially acts as an effective radius of a nucleon and affects the interaction probability as a function of Q^2.

2. **Fermi Momentum in RFG model.**
   The Fermi momentum used in the Relativistic Fermi Gas (RFG) model of the nucleus. This has a small effect on the shape and normalisation of the cross section.

3. **Spectral Function model differences.**
   A spectral function model is an alternative method to model neutrino interactions. This uncertainty takes into account the differences between the RFG model and the spectral function model.

4. **The axial mass in Resonance interactions.**
   In principle there is good reason to expect this to be the same as the QE axial mass, but is often treated separately in order to get good agreement with data.

5. **Interaction mode normalisations.**
   The modelling of the different interaction modes is constrained by cross section results from other analyses from T2K and other experiments. Poor constraints from the data or disagreements between results contribute to this uncertainty.

6. **Pion production in resonance interactions.**
   The spectrum of pion production in resonance interactions does not agree well between data and Monte Carlo. This could change the topology of events seen in the detector.

4.7.6 Uncertainties on Final State Interactions

Final State Interactions (FSI) concern the particles produced in the neutrino interactions. If one of these particles undergoes an interaction within the nucleus then it will affect the observed final state in the detector. If these processes are not modelled correctly it could change the shape and size of the measured cross section. This uncertainty is seperate from the detector uncertainties as they apply to interactions within the nucleus before the particles have any chance to show up in the detector.

The probability of a particle interacting within the nucleus is calculated by allowing the particle to travel through the nucleus at intervals and allowing it to interact at each step. This is based on external data from proton and pion-nucleus scattering experiments for each interaction type. The weights calculated for FSI uncertainties are based on the uncertainty of the calculated probability of interaction within the nucleus. As with the cross section uncertainties, the most important source of external data is from the MiniBooNE experiment [78] with a more detailed description of how this is used given in [79].

The sources of FSI uncertainty are detailed below.

- **Nucleon elastic scattering**
  The momentum and angle of an outgoing nucleon being changed due to scattering within the nucleus would change the topology of the event and potentially affect the shape of the measured cross section ratios.

- **Delta resonance production**
  A particle traversing the nucleus can excite a proton to a higher energy state, which will then decay to a charged pion. This could cause CCQE events to be reconstructed as CCnQE (Charged Current not Quasi-Elastic) events.

- **Pion inelastic scattering.**
  Similarly to nucleon scattering, the reconstructed final state can be affected

by pions rescattering within the nucleus. This should not affect the analysis significantly as the pion momentum and angle are not used in the classification of events.

- **Charge exchange.**
  Charge exchange can affect the reconstructed topology of the interaction via interactions such as $\pi^+ + n \rightarrow \pi^0 + p$. This could increase the measured CC0π cross sections.

- **Pion absorption** The absorption of a pion within the nucleus could lead to CCnQE events being classified as CCQE events, causing a change of shape of the cross section ratios. In the case of the CC0π topology, this shouldn't have any affect.

4.7.7 Total Uncertainties

All of the uncertainties are shown in Fig 4.7.3 and Fig 4.7.4 in terms of the reconstructed momentum and angle of the candidate lepton track for the four selections. The uncertainties on the ratios are shown in Fig 4.7.5 and Fig 4.7.6. No unfolding is used in these calculations as these are the two variables used to unfold to other quantities. The total uncertainty for the measured cross section or ratio of cross sections is calculated by adding the different sources of uncertainty in quadrature.

Since the events are broken down into neutrino type, the systematic uncertainties for the CCQE and CC0π topologies will be the same. For this reason, the CCQE uncertainties are not shown.

To understand the shape of the statistical uncertainties in these plots, refer back to the selection plots in Sec 4.5.3 as $\sigma_{\text{stat}} \propto \sqrt{n}$. The uncertainties for the flux, detector, cross section and FSI are based on the error matrices shown in Fig 4.7.2. It is difficult to deconvolute the different error sources to describe the shapes of these plots, however, there is a small general trend of a smaller uncertainty in the

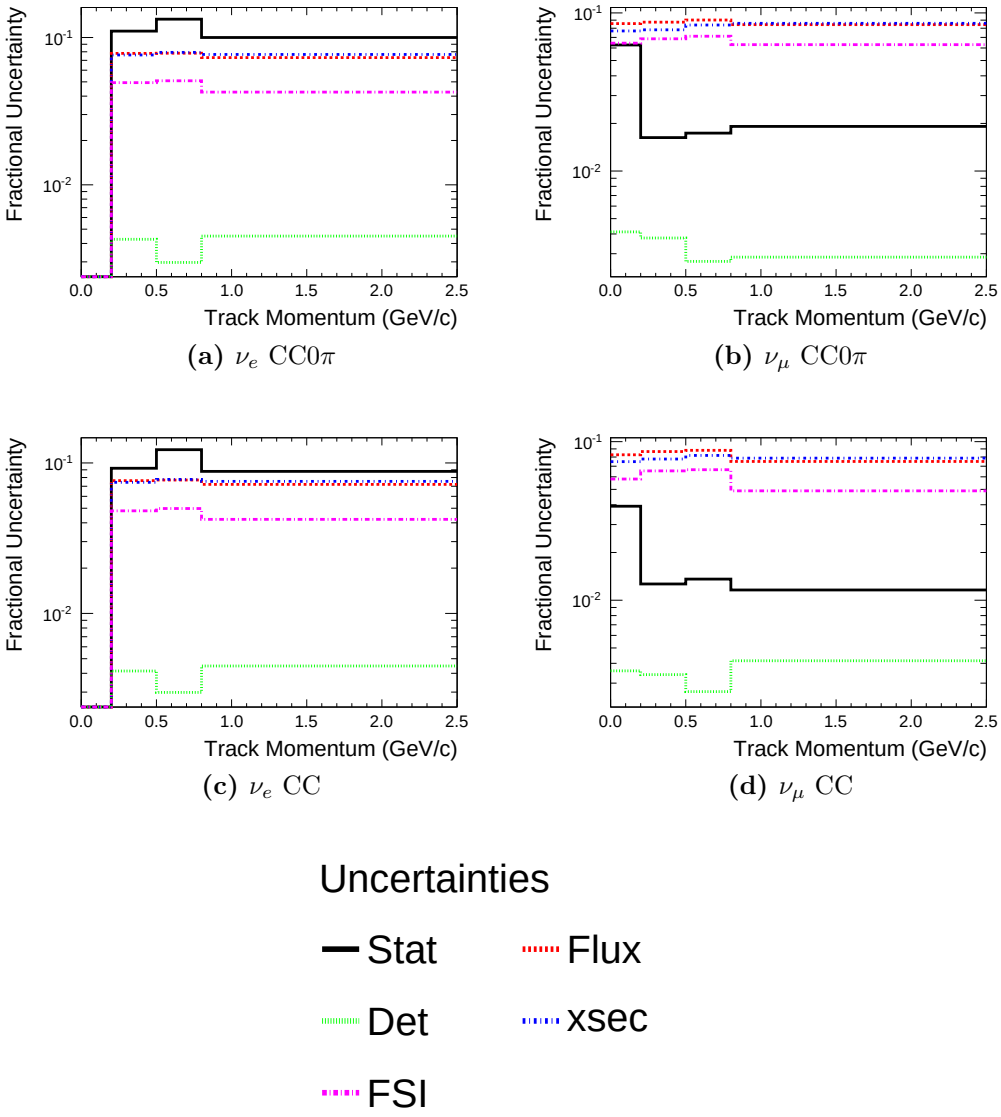

(a) ν_e CC0π **(b)** ν_μ CC0π

(c) ν_e CC **(d)** ν_μ CC

Figure 4.7.3: The different sources of uncertainty for the four selections in terms of the reconstructed momentum of the outgoing candidate lepton.

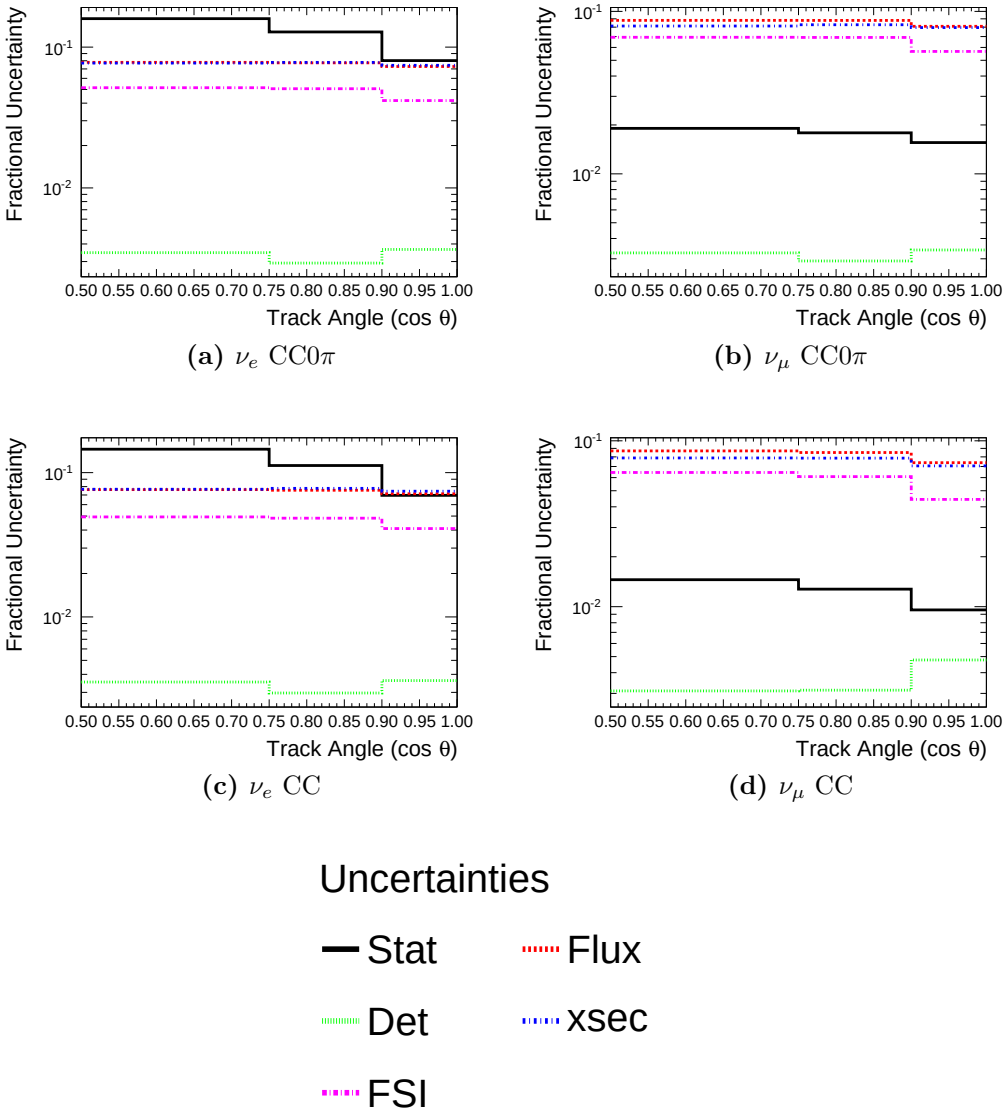

(a) ν_e CC0π **(b)** ν_μ CC0π

(c) ν_e CC **(d)** ν_μ CC

Figure 4.7.4: The different sources of uncertainty for the four selections in terms of the reconstructed angle of the outgoing candidate lepton.

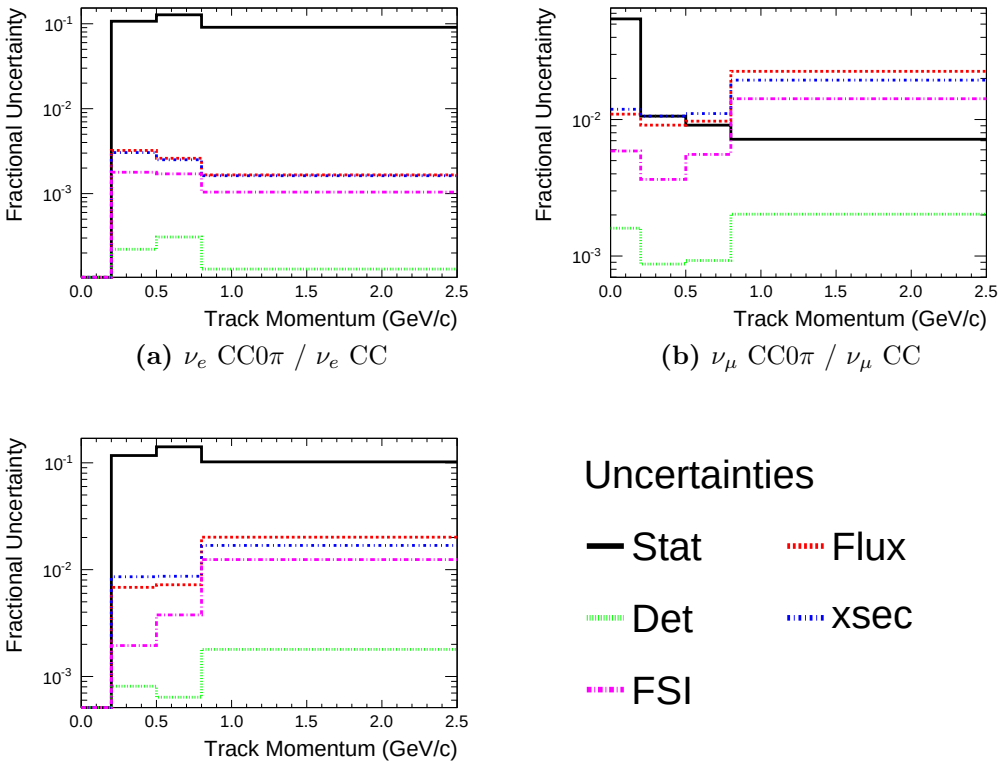

(a) ν_e CC0π / ν_e CC

(b) ν_μ CC0π / ν_μ CC

(c) Double Ratio of (a) and (b)

Figure 4.7.5: The different sources of uncertainty for the ratios in terms of the reconstructed momentum of the outgoing candidate lepton.

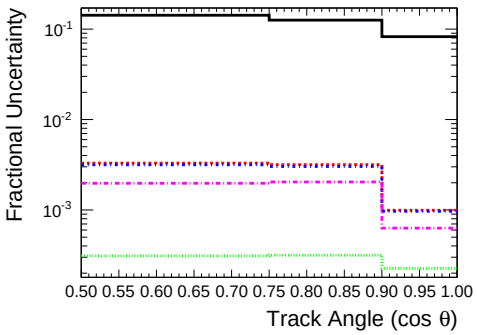

(a) ν_e CC0π / ν_e CC

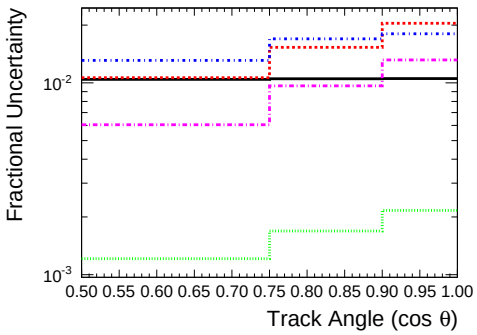

(b) ν_μ CC0π / ν_μ CC

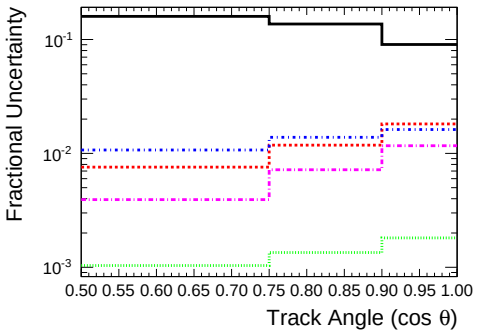

(c) Double Ratio of (a) and (b)

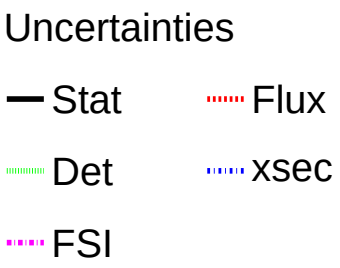

Figure 4.7.6: The different sources of uncertainty for the ratios in terms of the reconstructed angle of the outgoing candidate lepton.

regions where there are fewer background events (higher purity) in the selection. Mostly, the value of the uncertainty does not change much across the bins used. The uncertainties are similar between the CC0π selections and the CC inclusive selections, as they share many of the same events.

As with previous T2K cross section anaylses [17] [18] [19], the flux and cross section uncertainties are dominant at around 10%. The uncertainty due to final state interactions is approximately 6% and the detector uncertainties are $\mathcal{O}(1\%)$. A rough calculation then gives the total systematic uncertainty at $\approx 15\%$ for the four selections.

Each of the four single ratios show different amounts of cancellation for the different sources of uncertainty. For the ν_e CC0π / ν_e CC and ν_μ CC0π / ν_μ CC ratios, the numerator and denominator contain events primarily coming from the same flavour of neutrino. Thus, one would expect the flux and cross section systematic uncertainties to cancel significantly. However, the event topology is very different, so the FSI and detector systematics will cancel to a lesser degree. Since the ν_ℓ CC0π events are a subset of the ν_ℓ CC events, it is reasonable to expect a high degree of cancellation in general for these ratios. This should mean that the double ratio will have a large amount of cancellation for the systematic uncertainties as well, with the statistical uncertainty dominating.

The uncertainties for the unfolded selections are shown in Fig 4.7.7 and Fig 4.7.8 for true track momentum and track angle, and Fig 4.7.9 and Fig 4.7.10 for neutrino energy and four momentum transfered. There is very little event migration when unfolding from reconstructed track momentum or angle to the true quantity. This means that the uncertainties don't change much between the reconstructed and unfolded quantities. For neutrino energy and Q^2 the distributions change significantly, so the uncertainties change more too. The unfolding simply moves events around, and so the total uncertainties for the selections or ratios do not change much when unfolding. The small change in the total uncertainty is due to throwing the response matrix for each toy experiment.

The uncertainties for the ratios are shown in Figs 4.7.11 - 4.7.14 for the four unfolded variables. The same arguments used previously are able to describe the cancellation of the systematic uncertainties for the ratios of unfolded selections.

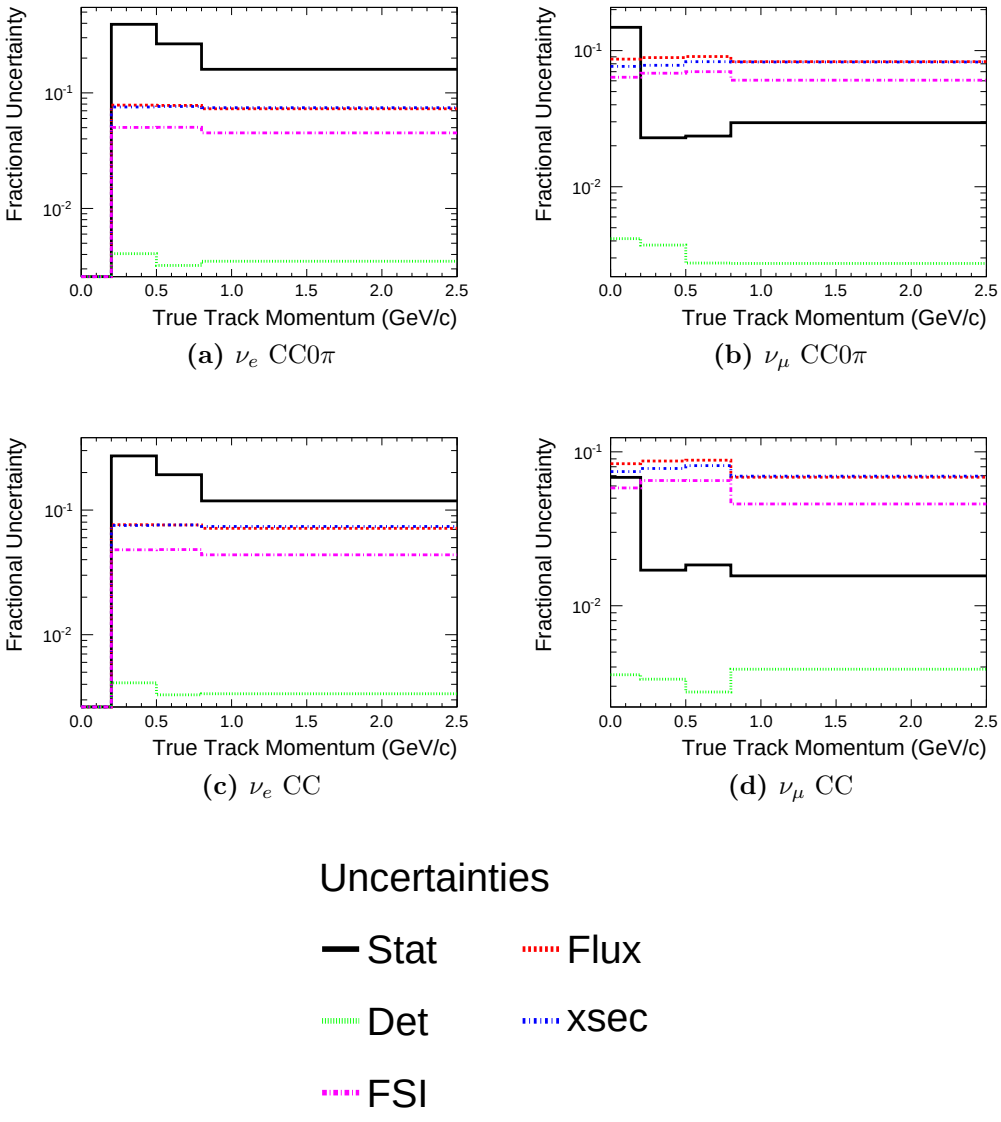

(a) ν_e CC0π **(b)** ν_μ CC0π

(c) ν_e CC **(d)** ν_μ CC

Figure 4.7.7: The different sources of uncertainty for the four selection in terms of the true momentum of the outgoing lepton unfolded from the reconstructed momentum of the outgoing candidate lepton.

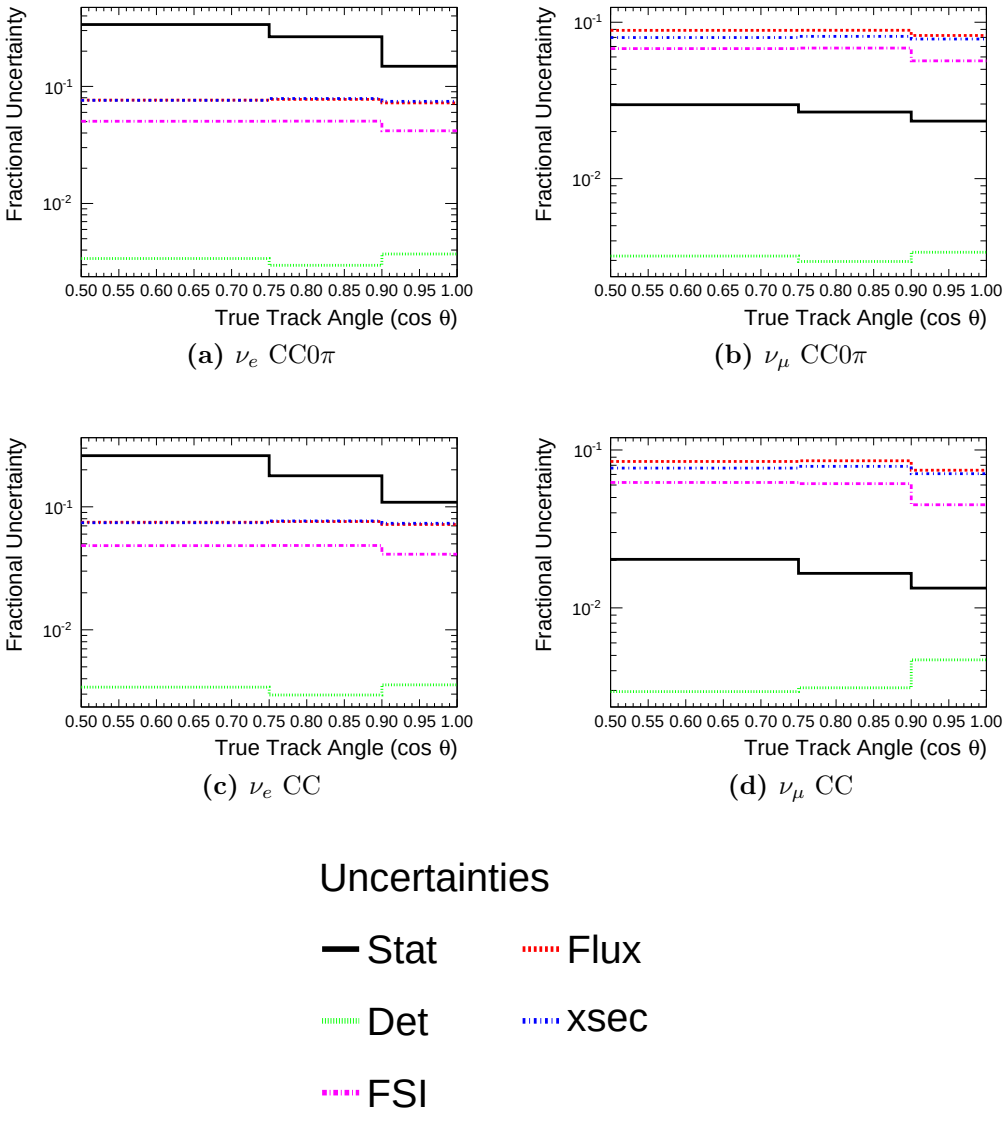

(a) ν_e CC0π **(b)** ν_μ CC0π

(c) ν_e CC **(d)** ν_μ CC

Figure 4.7.8: The different sources of uncertainty for the four selection in terms of the true angle of the outgoing lepton unfolded from the reconstructed angle of the outgoing candidate lepton.

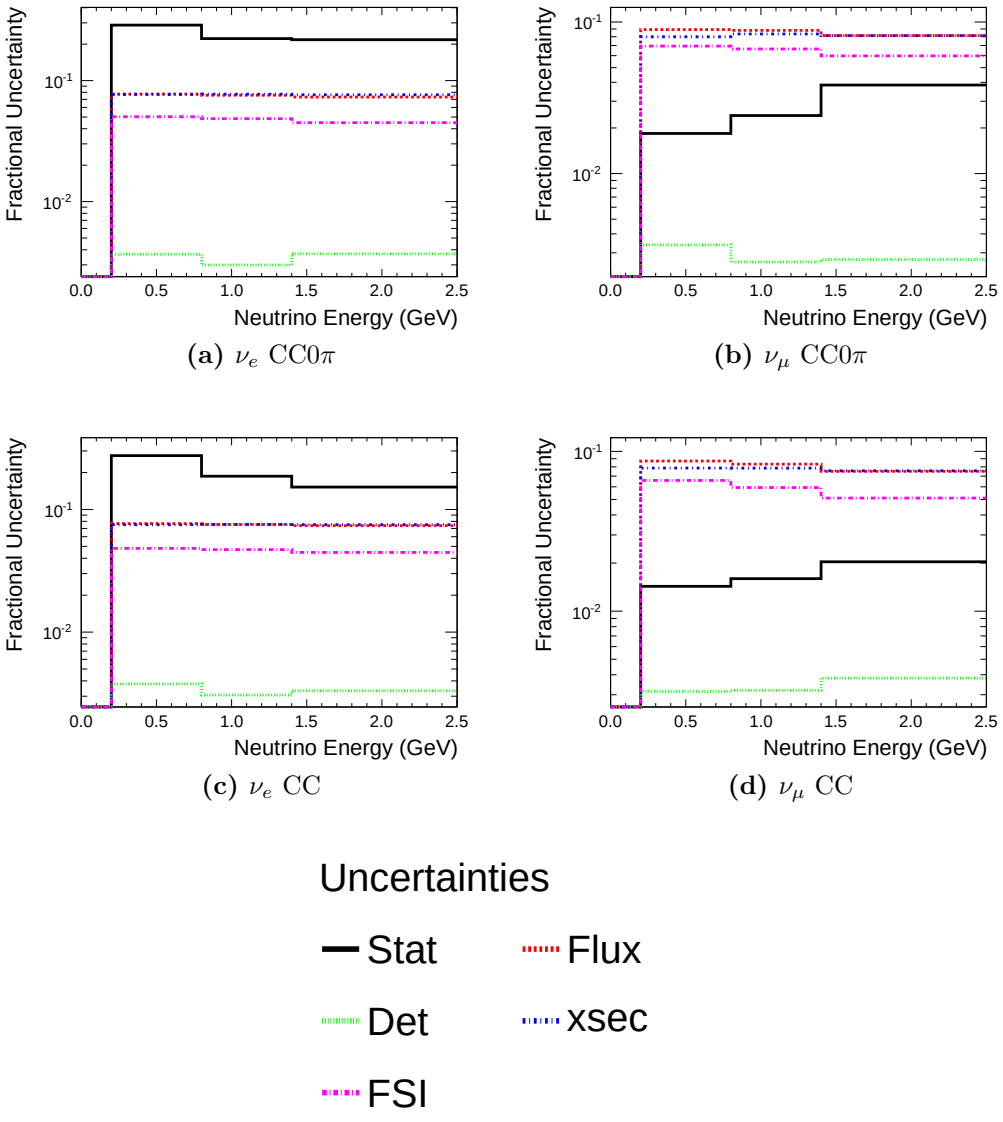

(a) ν_e CC0π **(b)** ν_μ CC0π

(c) ν_e CC **(d)** ν_μ CC

Figure 4.7.9: The different sources of uncertainty for the four selection in terms of the energy of the interacting neutrino unfolded from the reconstructed momentum of the outgoing candidate lepton.

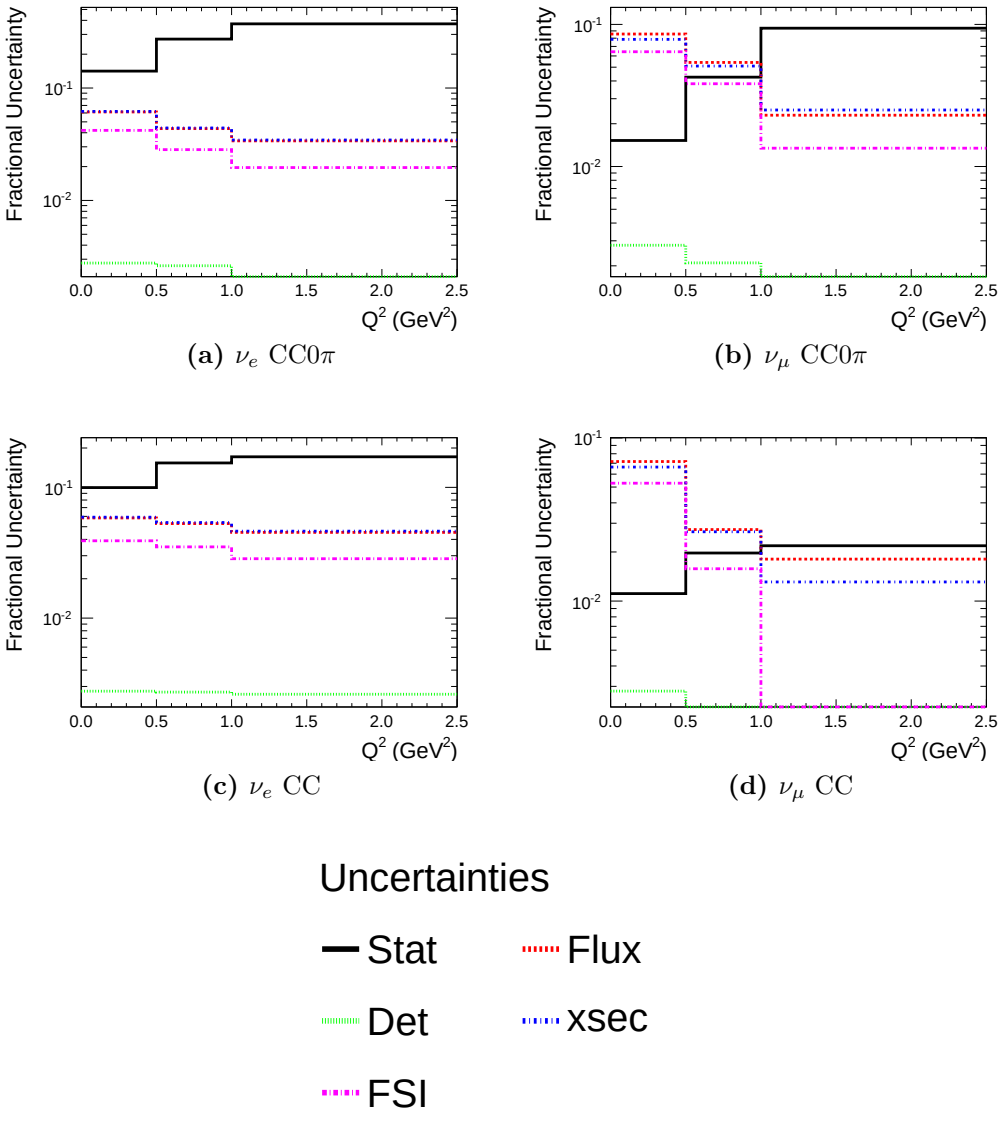

(a) ν_e CC0π **(b)** ν_μ CC0π

(c) ν_e CC **(d)** ν_μ CC

Figure 4.7.10: The different sources of uncertainty for the four selection in terms of the four-momentum transfered in the neutrino interaction unfolded from the reconstructed momentum of the outgoing candidate lepton.

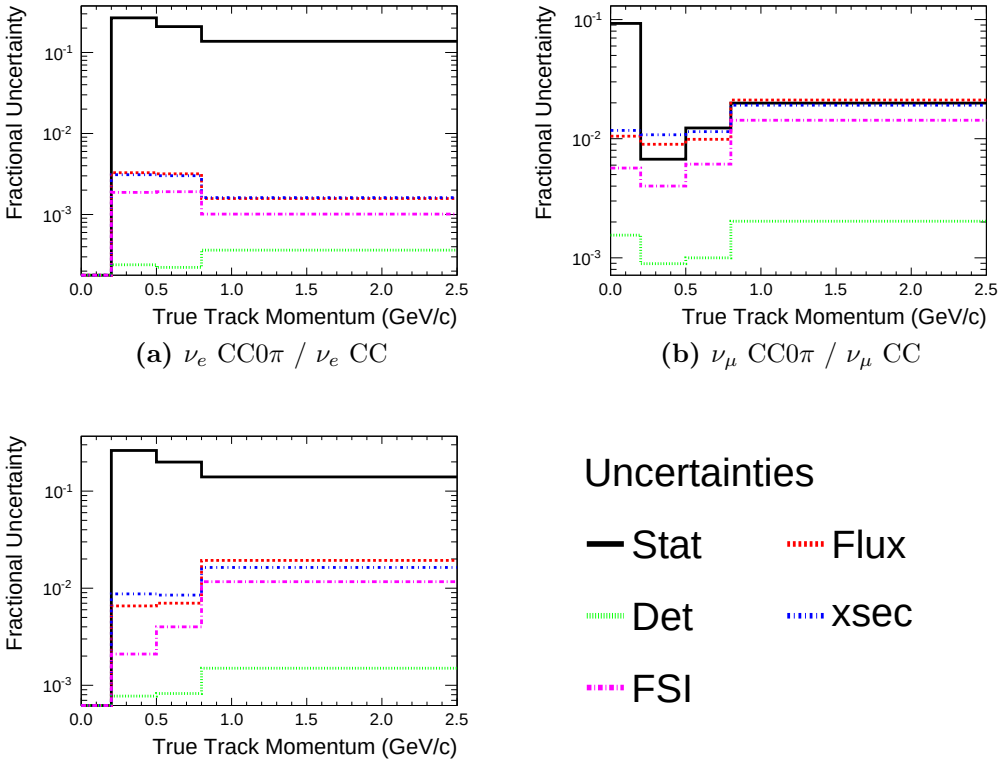

(a) ν_e CC0π / ν_e CC

(b) ν_μ CC0π / ν_μ CC

(c) Double Ratio of (a) and (b)

Figure 4.7.11: The different sources of uncertainty for the ratios in terms of the true momentum of the outgoing lepton unfolded from the reconstructed momentum of the outgoing candidate lepton.

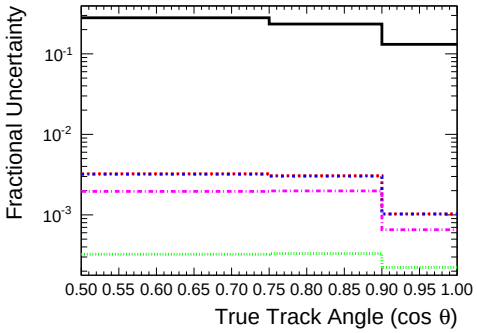

(a) ν_e CC0π / ν_e CC

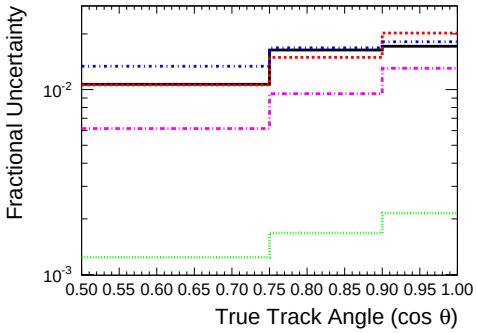

(b) ν_μ CC0π / ν_μ CC

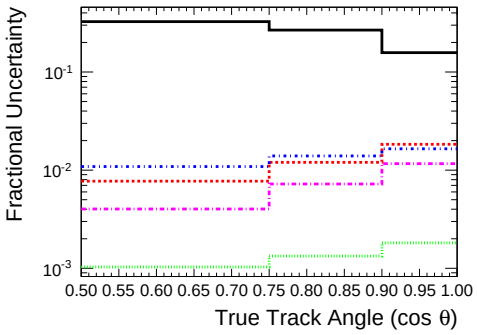

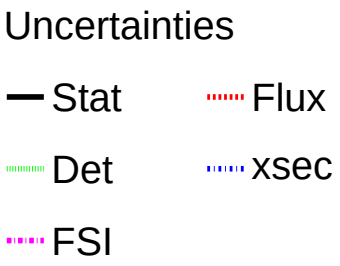

(c) Double Ratio of (a) and (b)

Figure 4.7.12: The different sources of uncertainty for the ratios in terms of the true angle of the outgoing lepton unfolded from the reconstructed angle of the outgoing candidate lepton.

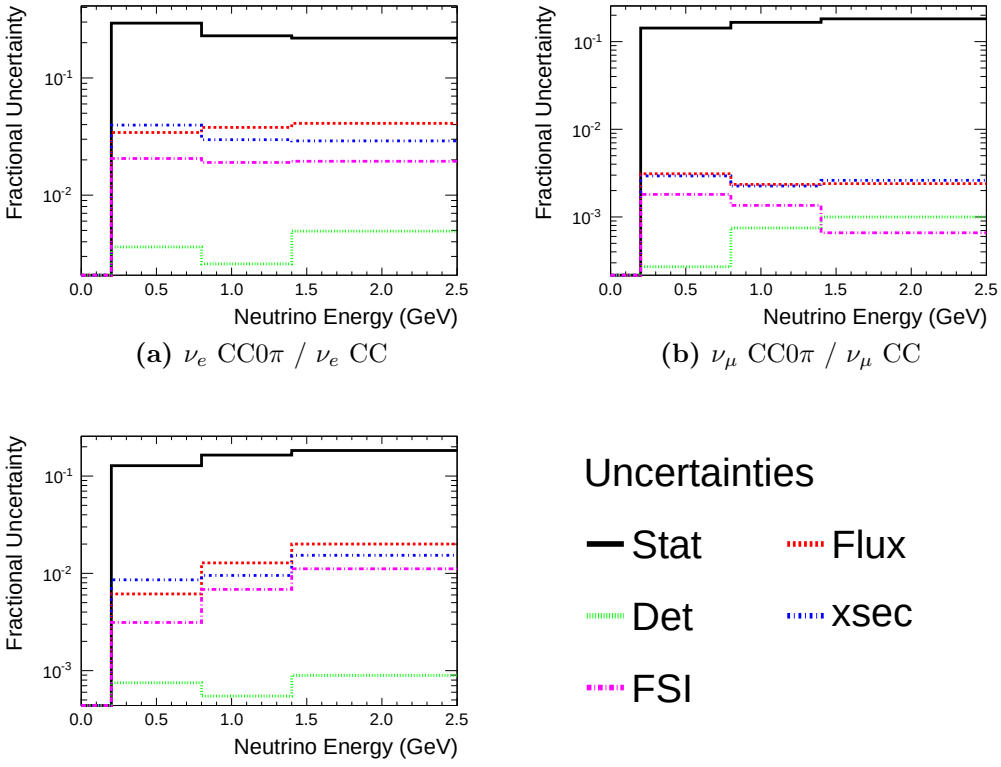

(a) ν_e CC0π / ν_e CC

(b) ν_μ CC0π / ν_μ CC

(c) Double Ratio of (a) and (b)

Figure 4.7.13: The different sources of uncertainty for the ratios in terms of the energy of the interacting neutrino unfolded from the reconstructed momentum of the outgoing candidate lepton.

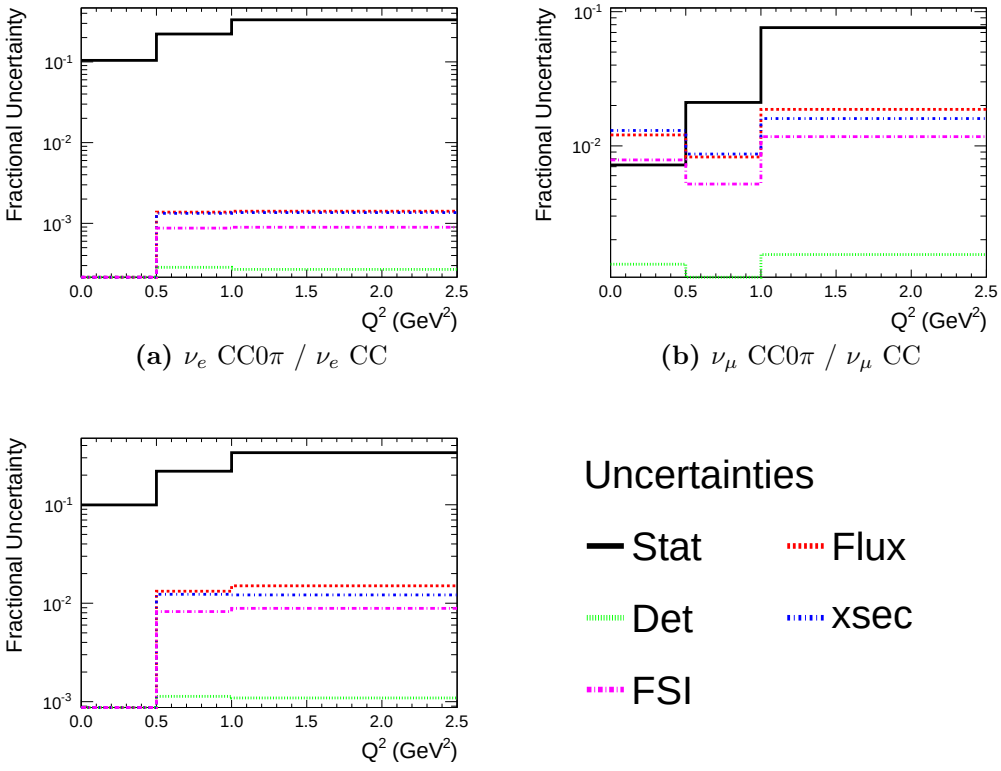

(a) ν_e CC0π / ν_e CC

(b) ν_μ CC0π / ν_μ CC

(c) Double Ratio of (a) and (b)

Figure 4.7.14: The different sources of uncertainty for the ratios in terms of the four-momentum transfered in the neutrino interaction unfolded from the reconstructed momentum of the outgoing candidate lepton.

The statistical uncertainties, flux uncertainties, detector uncertainties, FSI uncertainties and cross section uncertainties are added in quadrature to get the total uncertainty for each selection and ratio. These are summarised in Tab 4.7.2 for each of the selections and cross section ratio analyses. No binning is used when calculating the numbers in Tab 4.7.2. For the uncertainties on the binned selections and cross section ratios, see Tab A.1.3 - Tab A.1.14

Analysis	Statistical	Flux	Detector	Cross section	FSI
ν_e CC0π	0.122	0.076	0.003	0.077	0.048
ν_e CCQE	0.137	0.076	0.003	0.077	0.048
ν_e CC	0.084	0.075	0.003	0.076	0.046
ν_μ CC0π	0.013	0.089	0.003	0.081	0.068
ν_μ CCQE	0.015	0.089	0.003	0.082	0.068
ν_μ CC	0.009	0.084	0.003	0.079	0.060
ν_eCC0π/ν_eCC	0.103	0.002	0.001	0.002	0.001
ν_eCCQE/ν_eCC	0.120	0.002	0.001	0.002	0.001
ν_μCC0π/ν_μCC	0.008	0.010	0.001	0.011	0.007
ν_μCCQE/ν_μCC	0.010	0.010	0.001	0.011	0.006
DR (CC0π)	0.101	0.013	0.001	0.011	0.008
DR (CCQE)	0.125	0.013	0.001	0.011	0.007

Table 4.7.2: A summary of the total fractional uncertainties for the selections and cross section ratios analyses. No binning is used when calculating these numbers. The flux, detector, cross section and FSI uncertainties need to be propagated through the unfolding, so this procedure is used when calculating these numbers despite the data being unbinned.

4.8 Results

4.8.1 Monte Carlo Testing

The cross section ratios are first calculated for the GENIE Monte Carlo sample in terms of neutrino energy and compared with the Monte Carlo calculations given in Sec 4.3. This is the final test of the method that is used to measure the ratios with data. The NEUT sample is used to simulate the selections and calculate the weights for purity, efficiency and flux. The unfolding is performed with the GENIE control sample. As with Fig 4.6.8 the CC0π topology is replaced with a CCQE signal in order to test the results by comparing with the Monte Carlo generators. The results of this are shown in Fig 4.8.1 with total systematic and statistical uncertainties on the data points and statistical uncertainties only on the Monte Carlo points.

The level of agreement in Fig 4.8.1 shows that the methodology is able to extract the cross section ratios. The distribution of events within the bins affects the single ratios. There tends to be a greater number of events at higher energies, where the CC interaction cross section is dominant. This pushes the two single ratios to lower values for the lower energy bins. The energy spectra can be seen in Figs 4.5.8 - 4.5.11 for the four selections, which should help demonstrate this affect.

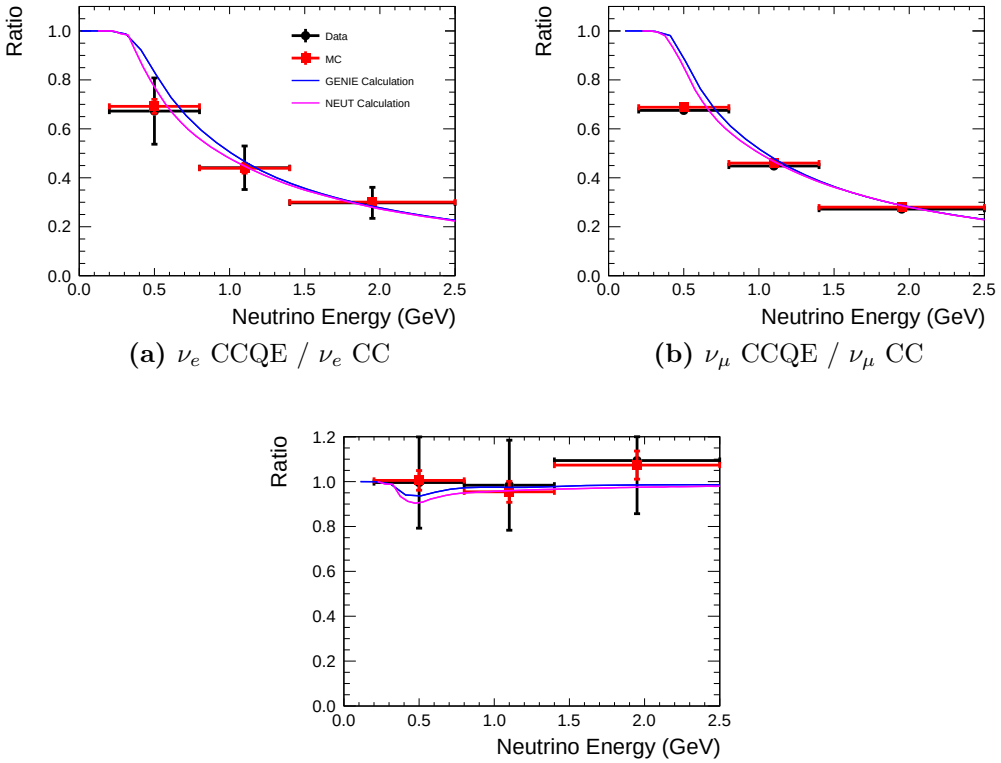

(a) ν_e CCQE / ν_e CC

(b) ν_μ CCQE / ν_μ CC

(c) Double Ratio of (a) and (b)

Figure 4.8.1: The ratios plotted in terms of neutrino energy for a data sample and a NEUT Monte Carlo sample. The unfolding is performed using a GENIE Monte Carlo sample. The red points show the ratio calculated for simulated NEUT events with statistical uncertainties and the black points show data with total statistical and systematic uncertainties. The CC0π cross sections are not shown here because the generators can not calculate the cross sections in terms of final state topologies.

4.8.2 Model Independent Measurement

Following the methodology in Sec 4.6, the ratios of the cross sections can be calculated. A model-independent approach is used by taking the ratios in terms of detector variables. The ratios are shown in Figs 4.8.2 and 4.8.3 in terms of track momentum and track angle. The unfolding procedure described in Sec 4.6.2 is used to take into account missing events and event migration due to the detector performance.

The T2K beam has a wide range of neutrino energies (see Fig 2.2.4). This adds a complication when taking the ratios in terms of other quantities as the neutrino energy is the quantity that is directly related to the cross section. Due to this the ratios presented in Fig 4.8.2 and Fig 4.8.3 are flux-averaged over the energy of the beam instead of a fixed energy.

The coloured areas around the central values correspond to the sizes of the uncertainties on the results for data added in quadrature. The innermost area corresponds to the size of the detector uncertainties on the results. The next layers out include the other sources of systematic uncertainty added in quadrature; the uncertainty on the neutrino interaction cross section and the properties of the interactions, the uncertainty on the neutrino flux, and the uncertainty on the interactions particles can undergo before leaving the nucleus. The outermost area includes the statistical uncertainty on the number of selected events, the scaling factor to correct for missed events and background events and the uncertainty assoicated with unfolding. This culminates in the total uncertainty on the measured ratios.

To interpret the ratios in terms of the momentum of the lepton track, as shown in Fig 4.8.2, one needs to consider the kinematics of the interaction. Interactions with a high momentum outgoing lepton will be due to a high energy incident neutrino, meaning the phase space was large enough to create additional particles. This causes the decrease in the ν_e and ν_μ single ratios at higher lepton momenta. Interactions with very low lepton momentum (removed by the momentum cut for the ν_e selection) will often be caused by a CCnQE interaction just above the threshold for producing particles other than the lepton and causing the lepton to have little momentum. This leads to the dip in the ν_μ single ratios at low lepton momentum.

The double ratios show that at low lepton momentum, a ν_μ is more likely to undergo a CCnQE interaction. These events are likely due to low energy neutrinos, which are less likely to be able to produce additional particles for a ν_μ than a ν_e due to the difference in lepton masses. This explains the dip in the double ratios

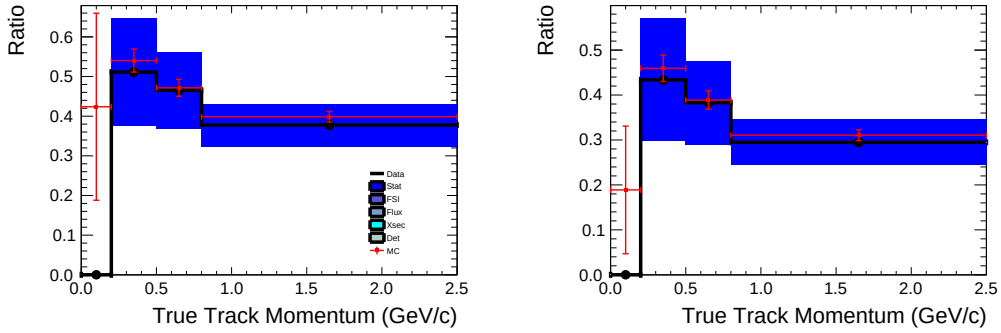

(a) ν_e CC0π / ν_e CC

(b) ν_e CCQE / ν_e CC

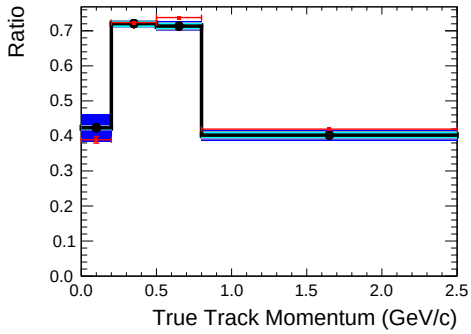

(c) ν_μ CC0π / ν_μ CC

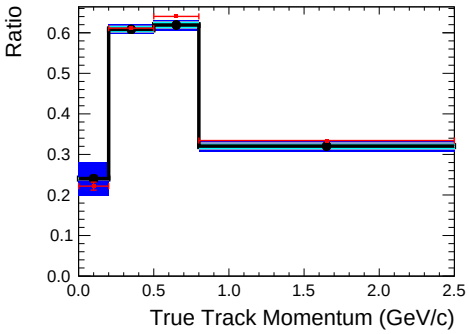

(d) ν_μ CCQE / ν_μ CC

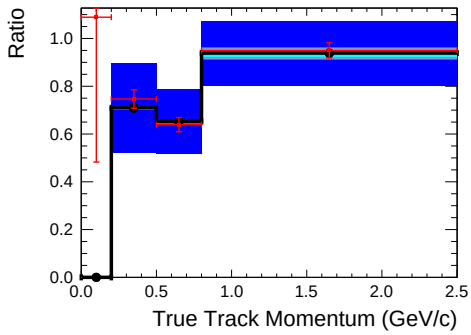

(e) Double Ratio of (a) and (c)

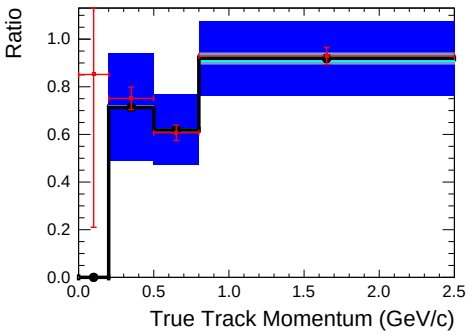

(f) Double Ratio of (b) and (d)

Figure 4.8.2: The ratios plotted in terms of the momentum of the candidate lepton unfolded from the reconstructed momentum of the candidate track. Since the neutrinos in the beam have a wide range of energies, the ratios shown are not for a fixed neutrino energy. Instead, a flux-averaged measurement is presented. The black points show data with the coloured bands representing the size of the different sources of uncertainty on the data. The red points show the ratios calculated for Monte Carlo with statistical uncertainties only.

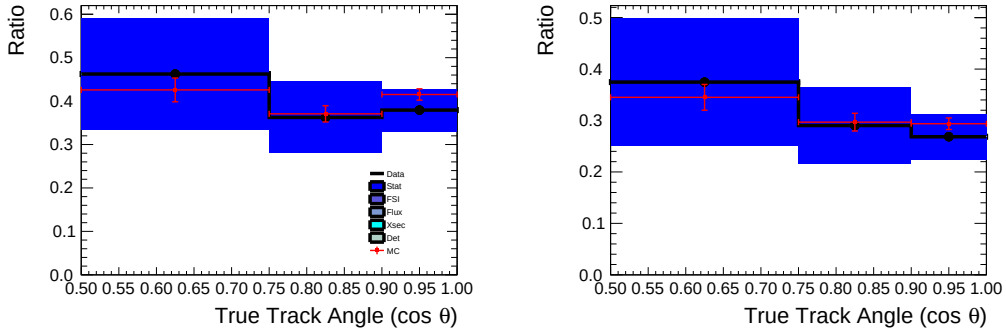

(a) ν_e CC0π / ν_e CC

(b) ν_e CCQE / ν_e CC

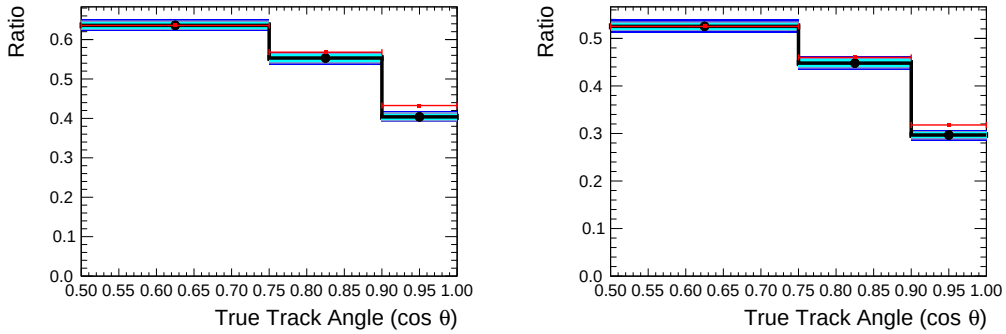

(c) ν_μ CC0π / ν_μ CC

(d) ν_μ CCQE / ν_μ CC

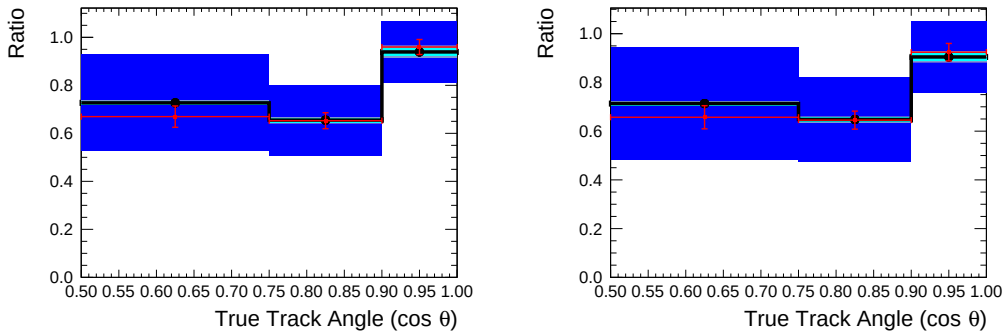

(e) Double Ratio of (a) and (c)

(f) Double Ratio of (b) and (d)

Figure 4.8.3: The ratios plotted in terms of the angle of the candidate lepton unfolded from the reconstructed angle of the candidate track. Since the neutrinos in the beam have a wide range of energies, the ratios shown are not for a fixed neutrino energy. Instead, a flux-averaged measurement is presented. The black points show data with the coloured bands representing the size of the different sources of uncertainty on the data. The red points show the ratios calculated for Monte Carlo with statistical uncertainties only.

for low lepton momenta.

The first bin in plots (a), (b), (e), and (f) in Fig 4.8.2 shows a Monte Carlo data point with large uncertainties and a value of 0 for data. This is due to the cut on reconstructed track momentum at 0.2 GeV/c when selecting ν_e interactions. When unfolding to true track momentum, a very small number of Monte Carlo events are migrated to this first bin. Due to the differences in sample size, there are no data events in this bin and the calculated ratios are 0, leading to the discrepancies. There are too few of these events to do anything meaningful with them.

The ratios in terms of the angle of the lepton track are a little trickier to interpret. At fixed neutrino energy one would expect the single ratios to decrease at more forward going angles, since CCQE (CC0π) interactions tend to be more forward boosted due to less energy being lost in the interaction. However, the ratios in Fig 4.8.3 are for a wide range of energies with the higher energy interactions tending to be very forward boosted. This has the effect that the more forward boosted (higher energies) have a lower fraction of CCQE (CC0π) events compared to larger angles. This particularly affects the ν_μ ratios as a difference in energy will have a larger affect on the angle of the outgoing muon than for an electron, due to its greater mass. These effects show up overall as an increase in the double ratio at higher values of lepton angle.

The differences between the CCQE and CC0π ratios is very small. This is because most CC0π events are CCQE interactions, but all CCQE interactions should result in no pions leaving the nucleus. This means that the CC0π ratios have a very similar shape to the CCQE ratios but with slightly lower values, due to there being a greater number of CC0π events.

4.8.3 Model Dependednt Measurement

It is possible to calculate the ratios shown in Figs 4.8.2 and 4.8.3 in terms of neutrino energy. This is a more interesting quantity from a theoretical perspective but requires an assumption that the models used to describe neutrino interactions are accurate. The Monte Carlo generators NEUT and GENIE can calculate the cross sections in terms of neutrino energy. This can be used to form a prediction for the cross section ratios as described in Sec 4.3. The ratios are therefore presented in Fig 4.8.4 as a cross check of the methodology by comparing the calculated ratios with the ratios found using fake data studies.

As with the ratios in terms of track momentum and track angle, the ratio shown in Fig 4.8.5 is for neutrino energy that is averaged over the flux of neutrinos in the beam. The ratios in terms of neutrino energy are flux-averaged within each bin of neutrino energy.

For interpretation of the results shown in Figs 4.8.4 and 4.8.5 refer back to Sec 2.1.7. These arguements were given for the cross section ratios in terms of neutrino energy, but also apply to the four-momentum transfered since the two variables are very highly correlated. The calculated values and their uncertainties for each of the ratios shown in Figs 4.8.2 - 4.8.5 can be found in Appendix A.1.

The ratios shown in Figs 4.8.2 - 4.8.5 have good agreement between data and Monte Carlo. This indicates that there are not significant differences in ν_e and ν_μ cross sections not due to the different lepton masses. Some caution should be taken when considering the ratios plotted in terms of neutrino energy and four momentum transfer as these use models of processes that are not well understood. For all the ratios, the statistical uncertainties dominate over the systematic uncertainties. These systematic uncertainties are small enough ($\mathcal{O}(1\%)$) that as T2K continues to take data, these ratios could become a powerful tool for studying neutrino interactions.

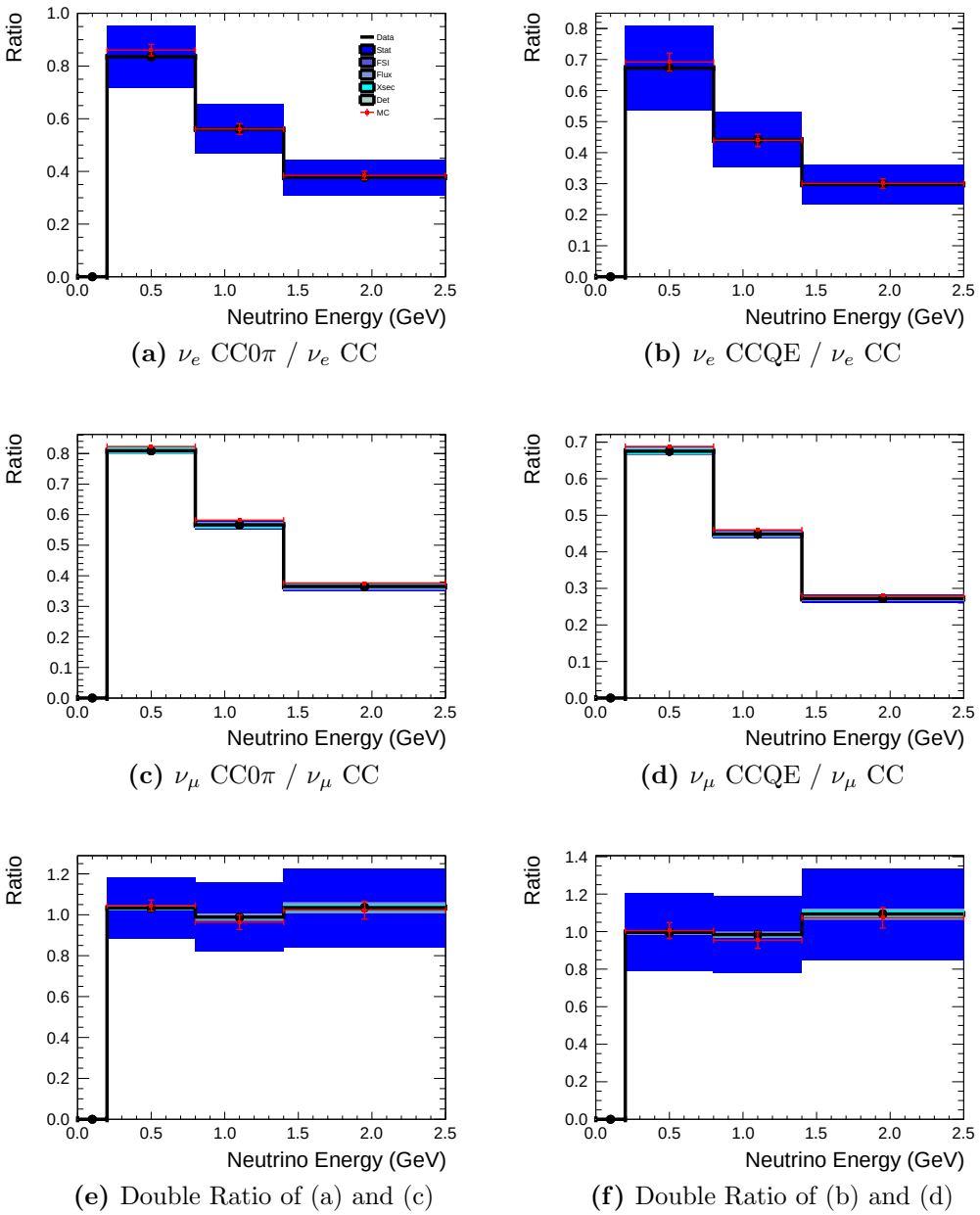

(a) ν_e CC0π / ν_e CC

(b) ν_e CCQE / ν_e CC

(c) ν_μ CC0π / ν_μ CC

(d) ν_μ CCQE / ν_μ CC

(e) Double Ratio of (a) and (c)

(f) Double Ratio of (b) and (d)

Figure 4.8.4: The ratios plotted in terms of the energy of the neutrino unfolded from the reconstructed momentum of the candidate track. The black points show data with the coloured bands representing the size of the different sources of uncertainty on the data. The red points show the ratios calculated for Monte Carlo with statistical uncertainties only.

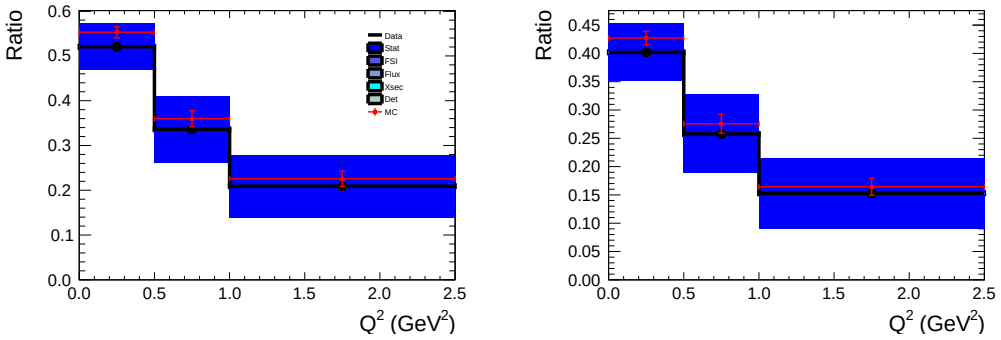

(a) ν_e CC0π / ν_e CC

(b) ν_e CCQE / ν_e CC

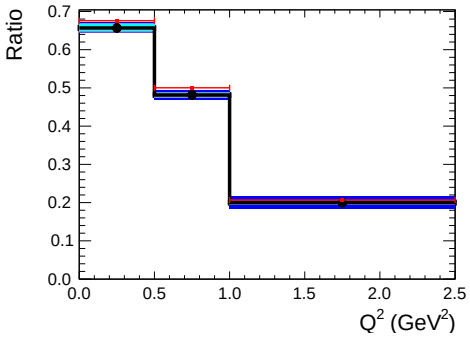

(c) ν_μ CC0π / ν_μ CC

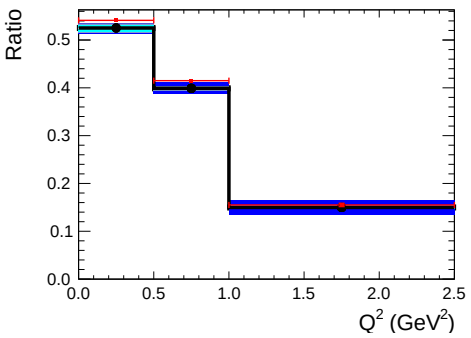

(d) ν_μ CCQE / ν_μ CC

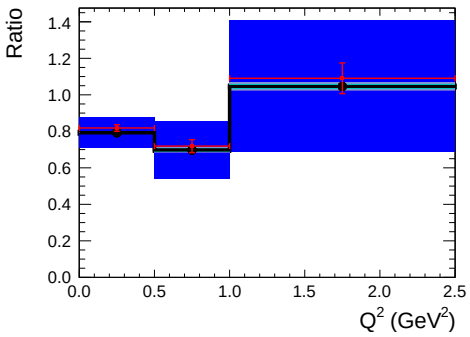

(e) Double Ratio of (a) and (c)

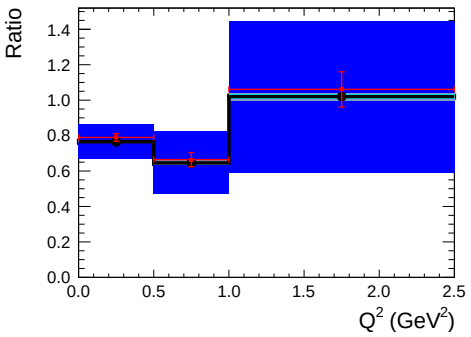

(f) Double Ratio of (b) and (d)

Figure 4.8.5: The ratios plotted in terms of the four-momentum transfered in the neutrino interaction unfolded from the reconstructed momentum of the candidate track. Since the neutrinos in the beam have a wide range of energies, the ratios shown are not for a fixed neutrino energy. Instead, a flux-averaged measurement is presented. The black points show data with the coloured bands representing the size of the different sources of uncertainty on the data. The red points show the ratios calculated for Monte Carlo with statistical uncertainties only.

Chapter 5

Conclusions

The results from a number of service tasks are presented with the combined goal of improving the performance and understanding of the ND280 ECals. These are useful for the T2K collaboration as a whole and for the cross section ratio analysis that is also presented.

Firstly, a calibration of the scintillator bars in the ND280 ECals is performed for T2K runs 4, 5 and 6. The results of this showed a much greater consistency of the ECals when measuring the energy deposited by charged particles had been achieved. This allows the ECals to provide more accurate information and therefore helps reduce the uncertainty on any selection using them. The improvements gained by applying the calibrations can be seen in Fig 3.1.3

A study into the rate of ageing of the ECal scintillator bars is also presented. This parameterises the reduction in light collection efficiency for the bars in the ECals as they age. This reduction was found to be well modelled by an exponential decay as shown in Fig 3.2.5 with approximately 3% loss per year in the first 5 years of running. Extrapolating the exponential fits into the future allows for a prediction of detector performance at later times. The fit parameters can be used to calculate a correction for the ageing of the scintillator. This will affect all future analyses which use the ECals.

Lastly, a study on the systematic uncertainty associated with matching a reconstructed object in a TPC with a reconstructed object in an ECal is given. An uncertainty of 1.0 % was calculated for the Barrel ECals and 0.6 % for the Downstream ECal. Electron-like and muon-like tracks are studied separately to be used by different analyses. The uncertainties for electron-like tracks are shown in Fig 3.3.21 and muon-like tracks in Fig 3.3.23. The results of these studies are used in the cross section ratio analysis when generating the throws for the detector systematics.

For the main analysis of this thesis, cut-based selections were used to determine the number of electron and muon neutrinos interacting within the FGD1 fiducial volume in the ND280. From these, the neutrino interaction cross sections on

Carbon and several different ratios of the cross sections were calculated. This was motivated by a need to test the Standard Model and the NEUT and GENIE Monte Carlo generators. Taking the ratios of the cross sections was shown to have a significant amount of cancellation of the uncertainties on the measurement compared to directly measuring the cross sections. This meant a precise test of the models could be performed. To achieve this, the cross section ratios were calculated for data and the Monte Carlo generators then compared to each other. Any significant difference would be indicative of Physics beyond the Standard Model.

The main challenge of the analysis was the calculation of the uncertainties and to what degree they would cancel out when taking the ratios of the cross sections. Many toy experiments were generated where the values associated with each source of uncertainty were thrown. These were propagated through the unfolding procedure and the standard deviation of the results of all the toys was calculated to give the systematic uncertainty. It can be seen in Figs 4.7.11 - 4.7.14 compared with Figs 4.7.7 - 4.7.10 that the systematic uncertainties do decrease when taking the ratios. The statistical uncertainties become dominant for the ratios, meaning the analyses are statistically limited. With more ND280 data, very precise tests of the neutrino generators could be performed.

In general the data shows no significant deviation from the Monte Carlos for any of the ratios being tested. There are data values that deviate from the Monte Carlo values within their uncertainties, but this is to be expected for multiple ratios plotted in terms of several different properties of the interactions. The limited statistics mean the uncertainties are too large to determine whether there are effects beyond the differences in final state lepton mass that can affect ν_e and ν_μ cross sections. With greater statistics, this method could prove to be a powerful probe of neutrino interaction cross sections.

Appendix A

A.1 Appendix

	ν_e CC0π / ν_e CC	ν_μ CC0π / ν_μ CC	DR (CC0π)
p_ℓ (GeV/c)			
0 - 0.2	0	0.42 ± 0.04	0
0.2 - 0.5	0.51 ± 0.14	0.72 ± 0.01	0.71 ± 0.19
0.5 - 0.8	0.47 ± 0.10	0.71 ± 0.01	0.65 ± 0.19
0.8 - 2.5	0.38 ± 0.05	0.40 ± 0.02	0.94 ± 0.14
θ_ℓ ($\cos\theta$)			
0.5 - 0.75	0.46 ± 0.13	0.64 ± 0.02	0.73 ± 0.20
0.75 - 0.9	0.36 ± 0.08	0.55 ± 0.02	0.66 ± 0.15
0.9 - 1	0.38 ± 0.05	0.40 ± 0.01	0.94 ± 0.13
E_ν (GeV)			
0 - 0.2	0	0	0
0.2 - 0.8	0.84 ± 0.12	0.81 ± 0.01	1.03 ± 0.15
0.8 - 1.4	0.56 ± 0.09	0.57 ± 0.01	0.99 ± 0.17
1.4 - 2.5	0.38 ± 0.07	0.37 ± 0.01	1.04 ± 0.19
Q^2 (GeV^2)			
0 - 0.5	0.52 ± 0.05	0.66 ± 0.01	0.79 ± 0.08
0.5 - 1	0.34 ± 0.07	0.48 ± 0.02	0.70 ± 0.15
1 - 2.5	0.21 ± 0.07	0.20 ± 0.02	1.05 ± 0.36

Table A.1.1: A summary of the values of the ratios and the total uncertainties for the ratios in terms of lepton momentum, lepton angle, neutrino energy, and four-momentum transfered. The ratios are calculated using a CC0π signal.

	ν_e CCQE / ν_e CC	ν_μ CCQE / ν_μ CC	DR (CCQE)
p_ℓ (GeV/c)			
0 - 0.2	0	0.24 ± 0.04	0
0.2 - 0.5	0.43 ± 0.14	0.61 ± 0.01	0.71 ± 0.23
0.5 - 0.8	0.38 ± 0.09	0.62 ± 0.01	0.62 ± 0.15
0.8 - 2.5	0.30 ± 0.05	0.32 ± 0.01	0.92 ± 0.16
θ_ℓ ($\cos\theta$)			
0.5 - 0.75	0.38 ± 0.12	0.53 ± 0.02	0.71 ± 0.23
0.75 - 0.9	0.29 ± 0.08	0.45 ± 0.01	0.65 ± 0.17
0.9 - 1	0.27 ± 0.04	0.30 ± 0.01	0.91 ± 0.15
E_ν (GeV)			
0 - 0.2	0	0	0
0.2 - 0.8	0.67 ± 0.14	0.68 ± 0.01	1.00 ± 0.20
0.8 - 1.4	0.44 ± 0.09	0.45 ± 0.01	0.98 ± 0.20
1.4 - 2.5	0.30 ± 0.06	0.27 ± 0.01	1.09 ± 0.24
Q^2 (GeV^2)			
0 - 0.5	0.40 ± 0.05	0.53 ± 0.01	0.77 ± 0.10
0.5 - 1	0.26 ± 0.07	0.40 ± 0.02	0.65 ± 0.18
1 - 2.5	0.15 ± 0.06	0.15 ± 0.02	1.02 ± 0.43

Table A.1.2: A summary of the values of the ratios and the total uncertainties for the ratios in terms of lepton momentum, lepton angle, neutrino energy, and four-momentum transfered. The ratios are calculated using a CCQE signal.

Bin	Statistical	Flux	Detector	Cross section	FSI	Total
Momentum (GeV/c)						
0.00 - 0.20	0.00	7.74	0.43	7.46	5.00	11.86
0.20 - 0.50	39.41	7.73	0.41	7.48	5.01	41.16
0.50 - 0.80	26.48	7.74	0.32	7.60	5.05	29.06
0.80 - 2.50	16.80	7.42	0.36	7.58	4.58	20.40
Total	12.41	7.56	0.31	7.60	4.77	17.08
Angle (cos θ)						
0.50 - 0.75	34.40	7.87	0.34	7.75	5.13	36.49
0.75 - 0.90	26.44	7.78	0.29	7.85	5.04	29.10
0.90 - 1.00	15.56	7.30	0.36	7.45	4.17	19.19
Total	12.55	7.50	0.32	7.60	4.53	17.09
Energy (GeV)						
0.00 - 0.20	0.00	0.00	0.00	0.00	0.00	0.00
0.20 - 0.80	29.05	7.85	0.37	7.72	5.08	31.48
0.80 - 1.40	22.61	7.71	0.30	7.80	4.92	25.61
1.40 - 2.50	21.90	7.45	0.37	7.74	4.56	24.82
Total	12.62	7.65	0.31	7.75	4.83	17.36
Q^2 (GeV^2)						
0.00 - 0.50	13.31	7.65	0.31	7.70	4.75	17.82
0.50 - 1.00	26.70	7.58	0.32	7.69	4.64	29.18
1.00 - 2.50	36.86	7.58	0.32	7.68	4.63	38.68
Total	12.09	7.63	0.31	7.70	4.73	16.92

Table A.1.3: The statistical, flux, detector, cross section, FSI percentage uncertainties for the ν_e CC0π selection when unfolded from a either reconstructed track momentum or reconstructed track angle to lepton momentum, lepton angle, neutrino energy, and four-momentum transfered. The total uncertainties are the other sources added in quadrature. These numbers were calculated for real data.

Bin	Statistical	Flux	Detector	Cross section	FSI	Total
Momentum (GeV/c)						
0.00 - 0.20	0.00	7.76	0.42	7.55	4.96	11.92
0.20 - 0.50	44.91	7.76	0.41	7.57	4.97	46.47
0.50 - 0.80	29.66	7.78	0.32	7.69	5.02	32.01
0.80 - 2.50	18.13	7.44	0.36	7.64	4.54	21.52
Total	13.60	7.59	0.31	7.64	4.74	17.98
Angle (cos θ)						
0.50 - 0.75	36.63	7.79	0.35	7.83	5.12	38.60
0.75 - 0.90	29.45	7.68	0.29	7.93	5.02	31.85
0.90 - 1.00	17.06	7.19	0.37	7.52	4.16	20.41
Total	14.05	7.39	0.33	7.66	4.53	18.20
Energy (GeV)						
0.00 - 0.20	0.00	0.00	0.00	0.00	0.00	0.00
0.20 - 0.80	30.96	7.81	0.37	7.64	5.02	33.22
0.80 - 1.40	24.62	7.66	0.31	7.71	4.86	27.35
1.40 - 2.50	24.72	7.38	0.38	7.69	4.48	27.29
Total	14.33	7.61	0.31	7.67	4.78	18.58
Q^2 (GeV^2)						
0.00 - 0.50	15.75	7.61	0.31	7.73	4.86	19.73
0.50 - 1.00	31.94	7.51	0.32	7.71	4.72	34.04
1.00 - 2.50	44.18	7.50	0.32	7.71	4.72	45.71
Total	14.02	7.59	0.31	7.72	4.83	18.36

Table A.1.4: The statistical, flux, detector, cross section, FSI percentage uncertainties for the ν_e CCQE selection when unfolded from a either reconstructed track momentum or reconstructed track angle to lepton momentum, lepton angle, neutrino energy, and four-momentum transfered. The total uncertainties are the other sources added in quadrature. These numbers were calculated for real data.

Bin	Statistical	Flux	Detector	Cross section	FSI	Total
Momentum (GeV/c)						
0.00 - 0.20	0.00	7.45	0.33	7.55	4.60	11.57
0.20 - 0.50	26.83	7.60	0.41	7.53	4.79	29.29
0.50 - 0.80	19.57	7.62	0.33	7.66	4.83	22.87
0.80 - 2.50	11.48	7.35	0.34	7.65	4.47	16.26
Total	8.50	7.46	0.31	7.64	4.61	14.41
Angle ($\cos\theta$)						
0.50 - 0.75	25.21	7.74	0.35	7.61	4.93	27.89
0.75 - 0.90	18.15	7.66	0.30	7.69	4.83	21.70
0.90 - 1.00	10.34	7.27	0.36	7.34	4.11	15.19
Total	8.24	7.42	0.32	7.48	4.43	14.09
Energy (GeV)						
0.00 - 0.20	0.00	0.00	0.00	0.00	0.00	0.00
0.20 - 0.80	27.52	7.70	0.38	7.51	4.79	29.94
0.80 - 1.40	18.57	7.60	0.31	7.60	4.70	21.96
1.40 - 2.50	15.01	7.44	0.34	7.57	4.46	18.92
Total	8.58	7.53	0.31	7.57	4.60	14.45
Q^2 (GeV^2)						
0.00 - 0.50	10.46	7.46	0.31	7.53	4.64	15.60
0.50 - 1.00	15.68	7.41	0.31	7.55	4.57	19.46
1.00 - 2.50	17.33	7.40	0.31	7.54	4.56	20.81
Total	8.60	7.45	0.31	7.53	4.61	14.40

Table A.1.5: The statistical, flux, detector, cross section, FSI percentage uncertainties for the ν_e CC selection when unfolded from a either reconstructed track momentum or reconstructed track angle to lepton momentum, lepton angle, neutrino energy, and four-momentum transfered. The total uncertainties are the other sources added in quadrature. These numbers were calculated for real data.

Bin	Statistical	Flux	Detector	Cross section	FSI	Total
Momentum (GeV/c)						
0.00 - 0.20	13.96	8.66	0.41	7.65	6.39	19.22
0.20 - 0.50	2.26	8.86	0.37	7.83	6.83	13.84
0.50 - 0.80	2.38	9.08	0.27	8.27	7.01	14.34
0.80 - 2.50	2.78	8.61	0.28	8.50	6.30	13.92
Total	1.56	8.87	0.29	8.11	6.79	13.89
Angle ($\cos\theta$)						
0.50 - 0.75	2.71	8.99	0.33	7.94	6.87	14.09
0.75 - 0.90	2.40	8.98	0.29	8.07	6.83	14.09
0.90 - 1.00	2.30	8.27	0.33	7.81	5.69	12.93
Total	1.47	8.75	0.29	7.91	6.41	13.51
Energy (GeV)						
0.00 - 0.20	0.00	8.47	0.42	7.67	6.42	13.11
0.20 - 0.80	1.71	8.81	0.34	8.04	6.98	13.93
0.80 - 1.40	2.39	8.68	0.26	8.40	6.69	14.02
1.40 - 2.50	3.94	8.40	0.28	8.57	6.31	14.12
Total	1.36	8.75	0.29	8.16	6.83	13.85
Q^2 (GeV^2)						
0.00 - 0.50	1.54	8.80	0.30	8.18	6.86	13.92
0.50 - 1.00	4.27	8.72	0.26	8.41	6.66	14.47
1.00 - 2.50	9.41	8.55	0.27	8.54	6.46	16.63
Total	1.37	8.80	0.29	8.21	6.84	13.91

Table A.1.6: The statistical, flux, detector, cross section, FSI percentage uncertainties for the ν_μ CC0π selection when unfolded from a either reconstructed track momentum or reconstructed track angle to lepton momentum, lepton angle, neutrino energy, and four-momentum transfered. The total uncertainties are the other sources added in quadrature. These numbers were calculated for real data.

Bin	Statistical	Flux	Detector	Cross section	FSI	Total
Momentum (GeV/c)						
0.00 - 0.20	21.96	8.64	0.42	7.66	6.34	25.61
0.20 - 0.50	2.46	8.80	0.37	7.81	6.78	13.81
0.50 - 0.80	2.46	9.02	0.28	8.27	6.96	14.30
0.80 - 2.50	3.15	8.56	0.28	8.51	6.25	13.96
Total	1.49	8.84	0.29	8.11	6.75	13.85
Angle ($\cos\theta$)						
0.50 - 0.75	3.09	8.84	0.33	8.03	6.92	14.15
0.75 - 0.90	2.81	8.82	0.29	8.17	6.89	14.14
0.90 - 1.00	2.53	8.13	0.34	7.85	5.71	12.92
Total	1.56	8.61	0.30	7.97	6.46	13.49
Energy (GeV)						
0.00 - 0.20	0.00	8.56	0.42	7.65	6.36	13.13
0.20 - 0.80	1.93	8.84	0.34	7.99	6.86	13.89
0.80 - 1.40	2.66	8.71	0.26	8.40	6.61	14.04
1.40 - 2.50	4.35	8.47	0.29	8.53	6.23	14.22
Total	1.42	8.75	0.30	8.14	6.75	13.80
Q^2 (GeV^2)						
0.00 - 0.50	1.62	8.88	0.30	8.09	6.83	13.92
0.50 - 1.00	4.79	8.78	0.27	8.38	6.64	14.64
1.00 - 2.50	11.20	8.64	0.27	8.51	6.43	17.72
Total	1.46	8.87	0.30	8.12	6.81	13.90

Table A.1.7: The statistical, flux, detector, cross section, FSI percentage uncertainties for the ν_μ CCQE selection when unfolded from a either reconstructed track momentum or reconstructed track angle to lepton momentum, lepton angle, neutrino energy, and four-momentum transfered. The total uncertainties are the other sources added in quadrature. These numbers were calculated for real data.

Bin	Statistical	Flux	Detector	Cross section	FSI	Total
Momentum (GeV/c)						
0.00 - 0.20	7.30	8.34	0.36	7.54	5.90	14.65
0.20 - 0.50	1.66	8.68	0.34	7.85	6.59	13.54
0.50 - 0.80	1.68	8.74	0.28	8.20	6.60	13.79
0.80 - 2.50	1.62	7.60	0.41	7.88	5.00	12.15
Total	0.98	8.39	0.32	7.90	6.03	13.05
Angle (cos θ)						
0.50 - 0.75	2.13	8.60	0.31	7.89	6.51	13.54
0.75 - 0.90	1.69	8.39	0.31	7.86	6.15	13.15
0.90 - 1.00	1.27	7.28	0.47	7.08	4.52	11.19
Total	0.95	7.96	0.37	7.48	5.43	12.24
Energy (GeV)						
0.00 - 0.20	0.00	8.33	0.37	7.44	5.79	12.58
0.20 - 0.80	1.45	8.69	0.32	7.83	6.48	13.45
0.80 - 1.40	1.64	8.37	0.32	7.89	5.88	13.03
1.40 - 2.50	2.10	7.81	0.39	7.85	5.17	12.41
Total	0.86	8.44	0.32	7.84	5.99	13.01
Q^2 (GeV^2)						
0.00 - 0.50	1.11	8.47	0.31	7.87	6.17	13.15
0.50 - 1.00	1.94	8.02	0.35	7.93	5.57	12.73
1.00 - 2.50	2.15	7.83	0.37	7.91	5.33	12.53
Total	0.90	8.33	0.32	7.88	5.99	12.98

Table A.1.8: The statistical, flux, detector, cross section, FSI percentage uncertainties for the ν_μ CC selection when unfolded from a either reconstructed track momentum or reconstructed track angle to lepton momentum, lepton angle, neutrino energy, and four-momentum transfered. The total uncertainties are the other sources added in quadrature. These numbers were calculated for real data.

Bin	Statistical	Flux	Detector	Cross section	FSI	Total
Momentum (GeV/c)						
0.00 - 0.20	0.00	0.00	0.00	0.00	0.00	0.00
0.20 - 0.50	25.96	0.33	0.02	0.32	0.19	25.97
0.50 - 0.80	20.48	0.32	0.02	0.31	0.19	20.48
0.80 - 2.50	14.04	0.16	0.04	0.16	0.10	14.04
Total	10.21	0.00	0.00	0.00	0.00	10.21
Angle (cos θ)						
0.50 - 0.75	27.99	0.33	0.03	0.31	0.20	27.99
0.75 - 0.90	23.46	0.31	0.03	0.30	0.20	23.47
0.90 - 1.00	13.33	0.10	0.02	0.10	0.07	13.33
Total	10.73	0.24	0.03	0.23	0.15	10.74
Energy (GeV)						
0.00 - 0.20	0.00	0.00	0.00	0.00	0.00	0.00
0.20 - 0.80	13.61	0.31	0.03	0.30	0.18	13.62
0.80 - 1.40	16.50	0.23	0.07	0.23	0.14	16.51
1.40 - 2.50	18.18	0.24	0.10	0.26	0.07	18.18
Total	10.41	0.22	0.06	0.21	0.13	10.42
Q^2 (GeV^2)						
0.00 - 0.50	10.01	0.00	0.00	0.00	0.00	10.01
0.50 - 1.00	21.94	0.15	0.03	0.14	0.09	21.94
1.00 - 2.50	33.06	0.15	0.03	0.15	0.09	33.06
Total	10.12	0.00	0.00	0.00	0.00	10.12

Table A.1.9: The statistical, flux, detector, cross section, FSI percentage uncertainties for the ratio of the ν_e CC0π to ν_e CC selections after unfolding from a either reconstructed track momentum or reconstructed track angle to lepton momentum, lepton angle, neutrino energy, and four-momentum transfered. The total uncertainties are the other sources added in quadrature. These numbers were calculated for real data.

Bin	Statistical	Flux	Detector	Cross section	FSI	Total
Momentum (GeV/c)						
0.00 - 0.20	0.00	0.00	0.00	0.00	0.00	0.00
0.20 - 0.50	31.14	0.33	0.02	0.31	0.19	31.14
0.50 - 0.80	24.30	0.33	0.02	0.30	0.20	24.30
0.80 - 2.50	16.50	0.15	0.04	0.16	0.09	16.50
Total	11.97	0.00	0.00	0.00	0.00	11.97
Angle (cos θ)						
0.50 - 0.75	31.15	0.32	0.03	0.31	0.20	31.16
0.75 - 0.90	26.65	0.30	0.03	0.29	0.20	26.65
0.90 - 1.00	16.76	0.10	0.02	0.10	0.06	16.76
Total	12.25	0.24	0.03	0.23	0.15	12.25
Energy (GeV)						
0.00 - 0.20	0.00	0.00	0.00	0.00	0.00	0.00
0.20 - 0.80	20.55	0.31	0.03	0.30	0.18	20.56
0.80 - 1.40	20.42	0.24	0.09	0.24	0.13	20.42
1.40 - 2.50	21.61	0.30	0.12	0.32	0.08	21.62
Total	12.34	0.22	0.06	0.21	0.13	12.35
Q^2 (GeV^2)						
0.00 - 0.50	12.28	0.00	0.00	0.00	0.00	12.28
0.50 - 1.00	26.86	0.13	0.03	0.12	0.08	26.86
1.00 - 2.50	40.40	0.15	0.05	0.16	0.09	40.41
Total	11.99	0.00	0.00	0.00	0.00	11.99

Table A.1.10: The statistical, flux, detector, cross section, FSI percentage uncertainties for the ratio of the ν_e CCQE to ν_e CC selections after unfolding from a either reconstructed track momentum or reconstructed track angle to lepton momentum, lepton angle, neutrino energy, and four-momentum transfered. The total uncertainties are the other sources added in quadrature. These numbers were calculated for real data.

Bin	Statistical	Flux	Detector	Cross section	FSI	Total
Momentum (GeV/c)						
0.00 - 0.20	9.28	1.04	0.15	1.17	0.56	9.43
0.20 - 0.50	0.67	0.89	0.09	1.08	0.40	1.61
0.50 - 0.80	1.23	1.00	0.10	1.15	0.61	2.05
0.80 - 2.50	1.99	2.18	0.20	1.92	1.40	3.79
Total	0.75	1.05	0.12	1.18	0.68	1.88
Angle ($\cos\theta$)						
0.50 - 0.75	1.07	1.06	0.12	1.31	0.61	2.09
0.75 - 0.90	1.64	1.50	0.17	1.67	0.94	2.94
0.90 - 1.00	1.72	2.02	0.21	1.81	1.30	3.47
Total	0.63	1.43	0.16	1.51	0.91	2.36
Energy (GeV)						
0.00 - 0.20	0.00	1.08	0.16	1.19	0.58	1.71
0.20 - 0.80	0.45	0.87	0.09	1.09	0.49	1.55
0.80 - 1.40	1.35	1.34	0.11	1.14	0.82	2.37
1.40 - 2.50	2.84	1.87	0.15	1.56	1.14	3.92
Total	0.66	1.02	0.13	1.09	0.64	1.76
Q^2 (GeV^2)						
0.00 - 0.50	0.72	1.13	0.13	1.28	0.73	2.00
0.50 - 1.00	2.11	1.71	0.17	1.64	1.10	3.36
1.00 - 2.50	7.61	1.79	0.15	1.54	1.12	8.05
Total	0.75	1.29	0.14	1.36	0.85	2.19

Table A.1.11: The statistical, flux, detector, cross section, FSI percentage uncertainties for the ratio of the ν_μ CC0π to ν_μ CC selections after unfolding from a either reconstructed track momentum or reconstructed track angle to lepton momentum, lepton angle, neutrino energy, and four-momentum transfered. The total uncertainties are the other sources added in quadrature. These numbers were calculated for real data.

Bin	Statistical	Flux	Detector	Cross section	FSI	Total
Momentum (GeV/c)						
0.00 - 0.20	17.14	1.03	0.15	1.12	0.55	17.21
0.20 - 0.50	1.48	0.88	0.09	1.04	0.39	2.05
0.50 - 0.80	1.28	0.98	0.10	1.11	0.59	2.05
0.80 - 2.50	2.40	2.19	0.20	1.89	1.37	4.00
Total	0.95	1.05	0.12	1.14	0.67	1.94
Angle ($\cos\theta$)						
0.50 - 0.75	1.99	1.06	0.12	1.33	0.60	2.69
0.75 - 0.90	2.04	1.50	0.17	1.68	0.94	3.19
0.90 - 1.00	2.07	2.01	0.21	1.81	1.29	3.65
Total	0.98	1.43	0.16	1.52	0.91	2.48
Energy (GeV)						
0.00 - 0.20	0.00	1.08	0.16	1.19	0.59	1.72
0.20 - 0.80	0.95	0.87	0.09	1.08	0.50	1.76
0.80 - 1.40	1.86	1.35	0.10	1.12	0.80	2.69
1.40 - 2.50	3.64	1.85	0.15	1.54	1.13	4.51
Total	1.06	1.01	0.13	1.08	0.62	1.93
Q^2 (GeV^2)						
0.00 - 0.50	1.00	1.15	0.13	1.28	0.74	2.12
0.50 - 1.00	2.86	1.74	0.17	1.65	1.12	3.90
1.00 - 2.50	9.60	1.83	0.15	1.56	1.13	9.97
Total	0.99	1.30	0.14	1.36	0.85	2.29

Table A.1.12: The statistical, flux, detector, cross section, FSI percentage uncertainties for the ratio of the ν_μ CCQE to ν_μ CC selections after unfolding from a either reconstructed track momentum or reconstructed track angle to lepton momentum, lepton angle, neutrino energy, and four-momentum transfered. The total uncertainties are the other sources added in quadrature. These numbers were calculated for real data.

Bin	Statistical	Flux	Detector	Cross section	FSI	Total
Momentum (GeV/c)						
0.00 - 0.20	0.00	0.00	0.00	0.00	0.00	0.00
0.20 - 0.50	26.22	0.65	0.08	0.87	0.21	26.24
0.50 - 0.80	19.92	0.70	0.08	0.84	0.41	19.95
0.80 - 2.50	14.00	1.94	0.16	1.67	1.22	14.28
Total	10.10	0.00	0.00	0.00	0.00	10.10
Angle ($\cos\theta$)						
0.50 - 0.75	29.20	0.77	0.10	1.10	0.40	29.24
0.75 - 0.90	23.15	1.20	0.13	1.39	0.72	23.23
0.90 - 1.00	13.65	1.84	0.18	1.63	1.17	13.92
Total	10.17	1.31	0.14	1.33	0.82	10.37
Energy (GeV)						
0.00 - 0.20	0.00	0.00	0.00	0.00	0.00	0.00
0.20 - 0.80	12.79	0.61	0.07	0.86	0.31	12.84
0.80 - 1.40	16.44	1.26	0.05	0.96	0.68	16.53
1.40 - 2.50	18.31	1.93	0.09	1.51	1.09	18.51
Total	10.23	1.29	0.07	1.07	0.76	10.39
Q^2 (GeV^2)						
0.00 - 0.50	9.97	0.00	0.00	0.00	0.00	9.97
0.50 - 1.00	21.92	1.57	0.13	1.45	0.96	22.05
1.00 - 2.50	33.82	1.67	0.12	1.34	0.98	33.90
Total	9.96	0.42	0.00	0.39	0.08	9.98

Table A.1.13: The statistical, flux, detector, cross section, FSI percentage uncertainties for the double ratio of the four selections after unfolding from a either reconstructed track momentum or reconstructed track angle to lepton momentum, lepton angle, neutrino energy, and four-momentum transfered (with a CC0π signal used). The total uncertainties are the other sources added in quadrature. These numbers were calculated for real data.

Bin	Statistical	Flux	Detector	Cross section	FSI	Total
Momentum (GeV/c)						
0.00 - 0.20	0.00	0.00	0.00	0.00	0.00	0.00
0.20 - 0.50	31.57	0.65	0.08	0.86	0.21	31.59
0.50 - 0.80	23.97	0.69	0.08	0.84	0.39	24.00
0.80 - 2.50	16.17	1.98	0.15	1.70	1.21	16.42
Total	12.74	0.00	0.00	0.00	0.00	12.74
Angle ($\cos\theta$)						
0.50 - 0.75	32.62	0.77	0.10	1.07	0.40	32.65
0.75 - 0.90	26.76	1.19	0.13	1.36	0.72	26.84
0.90 - 1.00	15.85	1.82	0.18	1.60	1.17	16.07
Total	11.85	1.29	0.14	1.30	0.82	12.02
Energy (GeV)						
0.00 - 0.20	0.00	0.00	0.00	0.00	0.00	0.00
0.20 - 0.80	20.57	0.61	0.07	0.87	0.30	20.60
0.80 - 1.40	20.55	1.31	0.05	0.93	0.65	20.62
1.40 - 2.50	21.81	1.96	0.09	1.52	1.08	21.98
Total	11.98	1.30	0.06	1.04	0.74	12.12
Q^2 (GeV^2)						
0.00 - 0.50	12.72	0.00	0.00	0.00	0.00	12.72
0.50 - 1.00	27.22	1.59	0.13	1.49	0.99	27.32
1.00 - 2.50	41.69	1.71	0.11	1.37	0.99	41.76
Total	12.26	0.54	0.00	0.50	0.22	12.28

Table A.1.14: The statistical, flux, detector, cross section, FSI percentage uncertainties for the double ratio of the four selections after unfolding from a either reconstructed track momentum or reconstructed track angle to lepton momentum, lepton angle, neutrino energy, and four-momentum transfered (with a CCQE signal used). The total uncertainties are the other sources added in quadrature. These numbers were calculated for real data.

Bibliography

[1] B. T. Cleveland, T. Daily, R. Davis, Jr., J. R. Distel, K. Lande, C. K. Lee, P. S. Wildenhain and J. Ullman, ISNC4-1997-85. 2

[2] Y. Suzuki, Nucl. Phys. Proc. Suppl. **38** (1995) 54. doi:10.1016/0920-5632(94)00733-C 2

[3] K. S. Hirata *et al.* [Kamiokande-II Collaboration], Phys. Lett. B **280** (1992) 146. doi:10.1016/0370-2693(92)90788-6 2

[4] Y. Fukuda *et al.* [Kamiokande Collaboration], Phys. Lett. B **335** (1994) 237. doi:10.1016/0370-2693(94)91420-6 2

[5] Q. R. Ahmad *et al.* [SNO Collaboration], Phys. Rev. Lett. **87** (2001) 071301 doi:10.1103/PhysRevLett.87.071301 [nucl-ex/0106015]. 2

[6] Y. Fukuda *et al.* [Super-Kamiokande Collaboration], Phys. Rev. Lett. **81** (1998) 1562 doi:10.1103/PhysRevLett.81.1562 [hep-ex/9807003]. 2

[7] B. Pontecorvo, Sov. Phys. JETP **26** (1968) 984 [Zh. Eksp. Teor. Fiz. **53** (1967) 1717]. 2, 16

[8] K. A. Olive *et al.* [Particle Data Group Collaboration], Chin. Phys. C **38** (2014) 090001. doi:10.1088/1674-1137/38/9/090001 vii, xxii, 2, 3, 12

[9] E. Richard *et al.* [Super-Kamiokande Collaboration], arXiv:1510.08127 [hep-ex]. 2

[10] B. Aharmim *et al.* [SNO Collaboration], Phys. Rev. C **88** (2013) 025501 doi:10.1103/PhysRevC.88.025501 [arXiv:1109.0763 [nucl-ex]]. 2

[11] A. Suzuki, Eur. Phys. J. C **74** (2014) no.10, 3094 doi:10.1140/epjc/s10052-014-3094-x [arXiv:1409.4515 [hep-ex]]. 2

[12] M. G. Aartsen *et al.* [IceCube Collaboration], Phys. Rev. D **91** (2015) no.7, 072004 doi:10.1103/PhysRevD.91.072004 [arXiv:1410.7227 [hep-ex]]. 2

[13] F. P. An *et al.* [Daya Bay Collaboration], Chin. Phys. C **37** (2013) 011001 doi:10.1088/1674-1137/37/1/011001 [arXiv:1210.6327 [hep-ex]]. 2

[14] J. H. Choi *et al.* [RENO Collaboration], arXiv:1511.05849 [hep-ex]. 2

[15] A. de Gouvea *et al.* [Intensity Frontier Neutrino Working Group Collaboration], arXiv:1310.4340 [hep-ex]. vii, 3

[16] M. C. Gonzalez-Garcia, M. Maltoni and T. Schwetz, arXiv:1512.06856 [hep-ph]. 3

[17] K. Abe *et al.* [T2K Collaboration], Phys. Rev. D **92** (2015) no.11, 112003 doi:10.1103/PhysRevD.92.112003 [arXiv:1411.6264 [hep-ex]]. vii, 4, 7, 159

[18] K. Abe *et al.* [T2K Collaboration], Phys. Rev. Lett. **113** (2014) no.24, 241803 doi:10.1103/PhysRevLett.113.241803 [arXiv:1407.7389 [hep-ex]]. vii, 4, 5, 7, 159

[19] K. Abe *et al.* [T2K Collaboration], Phys. Rev. D **87** (2013) no.9, 092003 doi:10.1103/PhysRevD.87.092003 [arXiv:1302.4908 [hep-ex]]. vii, 4, 5, 7, 159

[20] A. Masiero, P. Paradisi and R. Petronzio, Phys. Rev. D **74** (2006) 011701 doi:10.1103/PhysRevD.74.011701 [hep-ph/0511289]. 8

[21] S. L. Glashow, Nucl. Phys. **22** (1961) 579. doi:10.1016/0029-5582(61)90469-2 11

[22] S. Weinberg, Phys. Rev. Lett. **19** (1967) 1264. doi:10.1103/PhysRevLett.19.1264 11

[23] S. Weinberg, The Quantum Theory of Fields Volume I: Foundations (Cambridge University Press, Cambridge, 1995) 11

[24] E. C. G. Sudarshan and R. e. Marshak, Phys. Rev. **109** (1958) 1860. doi:10.1103/PhysRev.109.1860.2 13

[25] A. Pich, arXiv:1201.0537 [hep-ph]. 13

[26] C. S. Wu, E. Ambler, R. W. Hayward, D. D. Hoppes and R. P. Hudson, Phys. Rev. **105** (1957) 1413. doi:10.1103/PhysRev.105.1413 14

[27] C. H. Llewellyn Smith, Phys. Rept. **3** (1972) 261. doi:10.1016/0370-1573(72)90010-5 15, 22, 95

[28] C. Berger and L. M. Sehgal, Phys. Rev. D **76** (2007) 113004 doi:10.1103/PhysRevD.76.113004 [arXiv:0709.4378 [hep-ph]]. 18

[29] A. A. Aguilar-Arevalo *et al.* [MiniBooNE Collaboration], Phys. Rev. D **81** (2010) 092005 doi:10.1103/PhysRevD.81.092005 [arXiv:1002.2680 [hep-ex]]. viii, 19, 20

[30] V. Lyubushkin *et al.* [NOMAD Collaboration], Eur. Phys. J. C **63** (2009) 355 doi:10.1140/epjc/s10052-009-1113-0 [arXiv:0812.4543 [hep-ex]]. viii, 19, 20

[31] G. D. Megias, J. E. Amaro, M. B. Barbaro, J. A. Caballero and T. W. Donnelly, Phys. Lett. B **725** (2013) 170 doi:10.1016/j.physletb.2013.07.004 [arXiv:1305.6884 [nucl-th]]. viii, 19, 20

[32] J. A. Formaggio and G. P. Zeller, Rev. Mod. Phys. **84** (2012) 1307 doi:10.1103/RevModPhys.84.1307 [arXiv:1305.7513 [hep-ex]]. vii, 20, 21, 22

[33] V. B. Berestetskii, E. M. Lifshitz and L. P. Pitaevskii, 21

[34] A. Bodek, S. Avvakumov, R. Bradford and H. S. Budd, Eur. Phys. J. C **53** (2008) 349 doi:10.1140/epjc/s10052-007-0491-4 [arXiv:0708.1946 [hep-ex]]. 23, 26

[35] S. Choi *et al.*, Phys. Rev. Lett. **71** (1993) 3927. doi:10.1103/PhysRevLett.71.3927 23

[36] K. Minamisono *et al.*, Phys. Rev. C **65** (2002) 015501. doi:10.1103/PhysRevC.65.015501 29

[37] B. R. Holstein, Phys. Rev. C **29** (1984) 623. doi:10.1103/PhysRevC.29.623 29

[38] M. Day and K. S. McFarland, Phys. Rev. D **86** (2012) 053003 doi:10.1103/PhysRevD.86.053003 [arXiv:1206.6745 [hep-ph]]. viii, 26, 28, 29

[39] Study of QED radiative corrections to charged lepton leg in neutrino-nucleon interactions
Pueh Leng Tan
Ph.D Thesis viii, 26, 27

[40] S. Sarantakos, A. Sirlin and W. J. Marciano, Nucl. Phys. B **217** (1983) 84. doi:10.1016/0550-3213(83)90079-2 26

[41] J. F. Wheater and C. H. Llewellyn Smith, Nucl. Phys. B **208** (1982) 27 [Nucl. Phys. B **226** (1983) 547]. doi:10.1016/0550-3213(82)90187-0 26

[42] T. Kubota and M. Fukugita, doi:10.1142/9789812701756_0029 hep-ph/0410009. 26

[43] M. Fukugita and T. Kubota, Acta Phys. Polon. B **35** (2004) 1687 [hep-ph/0403149]. 26

[44] S. Weinberg, Phys. Rev. **112** (1958) 1375. doi:10.1103/PhysRev.112.1375 28

[45] R. Escribano, S. Gonzalez-Solis and P. Roig, Phys. Rev. D **94** (2016) no.3, 034008 doi:10.1103/PhysRevD.94.034008 [arXiv:1601.03989 [hep-ph]]. 28

[46] M. Oka and K. Kubodera, Phys. Lett. B **90** (1980) 45. doi:10.1016/0370-2693(80)90047-7 29

[47] S. Weinberg, Phys. Rev. Lett. **29** (1972) 1698. doi:10.1103/PhysRevLett.29.1698 30

[48] The T2K public webpage, The T2K collaboration, http://t2k-experiment.org/ viii, 31, 33, 97

[49] S. Nagamiya, PTEP **2012** (2012) 02B001. doi:10.1093/ptep/pts025 viii, 32

[50] T2K collaboration photographs, 2014. URL http://www.t2k.org/docs/photos viii, 33

[51] K. Abe *et al.* [T2K Collaboration], Phys. Rev. D **88** (2013) 3, 032002 doi:10.1103/PhysRevD.88.032002 [arXiv:1304.0841 [hep-ex]]. viii, 34

[52] J. Caravaca, G. Christodoulou, C. Giganti, D. Hadley, E. Larkin, N. McCauley, D. Sgalaberna, B. Smith, P. Stamoulis, C. Wilkinson
Measurement of the electron neutrino beam component in the ND280 Tracker for 2013 analyses
T2K-TN-149 34, 71, 74, 99

[53] K. Abe *et al.* [T2K Collaboration], Nucl. Instrum. Meth. A **659** (2011) 106 doi:10.1016/j.nima.2011.06.067 [arXiv:1106.1238 [physics.ins-det]]. ix, 37, 40, 41, 43, 44, 45, 48, 49, 50

[54] D. Allan *et al.* [T2K UK Collaboration], JINST **8** (2013) P10019 doi:10.1088/1748-0221/8/10/P10019 [arXiv:1308.3445 [physics.ins-det]]. 38, 45, 53, 60

[55] D. Renker and E. Lorenz, JINST **4** (2009) P04004. doi:10.1088/1748-0221/4/04/P04004 38

[56] P. A. Amaudruz *et al.* [T2K ND280 FGD Collaboration], Nucl. Instrum. Meth. A **696** (2012) 1 doi:10.1016/j.nima.2012.08.020 [arXiv:1204.3666 [physics.ins-det]]. 39, 42

[57] N. Abgrall *et al.* [T2K ND280 TPC Collaboration], Nucl. Instrum. Meth. A **637** (2011) 25 doi:10.1016/j.nima.2011.02.036 [arXiv:1012.0865 [physics.ins-det]]. 43

[58] I. Giomataris *et al.*, Nucl. Instrum. Meth. A **560** (2006) 405 doi:10.1016/j.nima.2005.12.222 [physics/0501003]. 43

[59] S. Assylbekov *et al.*, Nucl. Instrum. Meth. A **686** (2012) 48 doi:10.1016/j.nima.2012.05.028 [arXiv:1111.5030 [physics.ins-det]]. 46

[60] S. Aoki *et al.*, Nucl. Instrum. Meth. A **698** (2013) 135 doi:10.1016/j.nima.2012.10.001 [arXiv:1206.3553 [physics.ins-det]]. 47

[61] C. W. Walter, In *Thomas, Jennifer A. (ed.), Vahle, Patricia L. (ed.): Neutrino oscillations* 19-43 [arXiv:0802.1041 [hep-ex]]. 48

[62] V. Senchishin *et al.*, In *La Biodola 1993, Calorimetry in high energy physics* 552-560 60, 61, 66, 69

[63] V. D. Bezuglyi and L. L. Nagornaya In *Soviet Atomic Energy, volume 17 doi:0.1007/BF01650860 60

[64] M. Mathis [MINOS Collaboration], J. Phys. Conf. Ser. **404** (2012) 012039. doi:10.1088/1742-6596/404/1/012039 61, 69

[65] I. Lamont, A. Knight
A Study into the Rate of Degradation of the ECal Scintillator Bars
T2K-TN-268 70

[66] J. Wolcott [MINERvA Collaboration], arXiv:1512.09312 [hep-ex]. 93

[67] R. A. Smith and E. J. Moniz, Nucl. Phys. B **43** (1972) 605 Erratum: [Nucl. Phys. B **101** (1975) 547]. doi:10.1016/0550-3213(75)90612-4, 10.1016/0550-3213(72)90040-5 23, 95

[68] A. Bodek and J. L. Ritchie, Phys. Rev. D **24** (1981) 1400. doi:10.1103/PhysRevD.24.1400 95

[69] Y. Hayato, Acta Phys. Polon. B **40** (2009) 2477. 95

[70] C. Andreopoulos, C. Barry, S. Dytman, H. Gallagher, T. Golan, R. Hatcher, G. Perdue and J. Yarba, arXiv:1510.05494 [hep-ph]. 95

[71] T. Golan, AIP Conf. Proc. **1663** (2015) 030003 doi:10.1063/1.4919467 [arXiv:1402.1608 [hep-ph]]. 95

[72] P. Bartet, S. Bordoni, R. Castillo, G. Catanesi, A. Cervera, L. Cremonesi, A. Fiorentini, L. Haegel, A. Hillairet, A. Izmaylov, J. Kim, J. Lagoda, T. Lindner, L. Magaletti, J. Myslik, C. Nielsen, S. Oser, W. Oryszczak, M. Posiadala-Zezula, Y. Petrov, M. Ravonel, F. Sanchez, E. Scantamburlo, M. Scott, W. Warzycha, J. Wilson, J. Zalipska
ν_μ CC event selections in the ND280 tracker using Run 2+3+4 data
T2K-TN-212 99, 147

[73] G. D'Agostini, Nucl. Instrum. Meth. A **362** (1995) 487. doi:10.1016/0168-9002(95)00274-X 127

[74] T. Adye, Proceedings of the PHYSTAT 2011 Workshop, CERN, Geneva, Switzerland, January 2011, CERN-2011-006, pp 313-318 [arXiv:1105.1160 [physics.data-an]]. 128

[75] A. Cholesky Note sur une mthode de rsolution des quations normales provenant de l'application de la mthode des moindres carrs un systme d'quations linaires en nombre infrieur celui des inconnues 141

[76] N. Abgrall *et al.* [NA61 Collaboration], JINST **9** (2014) P06005 doi:10.1088/1748-0221/9/06/P06005 [arXiv:1401.4699 [physics.ins-det]]. 145, 146

[77] D. Sgalaberna [NA61/SHINE Collaboration], Nucl. Part. Phys. Proc. **273-275** (2016) 2672. doi:10.1016/j.nuclphysbps.2015.10.026 145, 146

[78] A. A. Aguilar-Arevalo *et al.* [MiniBooNE Collaboration], Nucl. Instrum. Meth. A **599** (2009) 28 doi:10.1016/j.nima.2008.10.028 [arXiv:0806.4201 [hep-ex]]. 152, 153

[79] K. Abe *et. al* [T2K Collaboration], Phys. Rev. D **91** (2015) no.7, 072010 doi:10.1103/PhysRevD.91.072010 [arXiv:1502.01550 [hep-ex]] 152, 153

[80] S. Oser
Elemental Composition of the FGD XY Modules
T2K-TN-091 150